Dissertation

Experiments for the Detection of Biosignatures in Ice Grains by Space Missions to Enceladus and Europa

Fabian Klenner

Berlin, November 2020

Submitted for the degree of
Doctor rerum naturalium (Dr. rer. nat.)

Department of Earth Sciences
Freie Universität Berlin

First reviewer:

Prof. Dr. Frank Postberg
Institute of Geological Sciences
Freie Universität Berlin
Malteserstraße 74-100
12249 Berlin
Germany

Second reviewer:

Prof. Dr. Jürgen Schmidt
Astronomy Research Unit
University of Oulu
PL 3000
90014 Oulu
Finland

Date of defence: February 12, 2021

Somewhere, something incredible is waiting to be known.

- Unknown, often attributed to Carl Sagan -

Kurzfassung

Der Saturnmond Enceladus stößt Partikel aus Wassereis, die sich aus unterirdischem Ozeanwasser gebildet haben, in das Weltall. Eine ähnliche kryovulkanische Aktivität findet vermutlich auch auf dem Jupitermond Europa statt. Die ausgetoßenen Eispartikel können mit vorbeifliegenden Raumsonden mit Einschlagsionisations-Massenspektrometern analysiert werden, um die Habitabilität der unterirdischen Ozeane zu untersuchen. Ein Urtyp solcher Massenspektrometer, der Cosmic Dust Analyzer (CDA) auf der Cassini Raumsonde, untersuchte einzelne Eisteilchen in Enceladus' Plume und in Saturn's E Ring. Der SUrface Dust Analyzer (SUDA), der bereits für die anstehende Europa Clipper Mission gebaut wird, wird die Eispartikel in Europa's Umgebung analysieren. Die Interpretation der im Weltall stattfindenden Messungen erfordert erdgebundene Kalibrationen. Diese Dissertation befasst sich deshalb mit erdgebundenen Analogexperimenten und besteht aus zwei miteinander verbundenen Projekten.

Das Erscheinungsbild der aufgenommenen Einschlagsionisations-Massenspektren hängt nicht nur von der Zusammensetzung der Eispartikel sondern auch von deren Einschlagsgeschwindigkeit auf das Massenspektrometer ab. Im *ersten Projekt* werden Massenspektren von Wassereispartikeln mit typischen Einschlagsgeschwindigkeiten zwischen 4 und 21 km/s mit einem Analogexperiment im Labor simuliert, mit dem es zudem möglich ist, Variationen in der Zusammensetzung der Eispartikel nachzustellen. In diesem laserinduzierten Flüssigstrahl-Desorptions (LILBID) Prozess wird ein wenige Mikrometer breiter Wasserstrahl mit einem gepulsten Infrarot-Laser bei geeigneten Energien und Wellenlängen beschossen. Die entstandenen Ionen werden anschließend mit einem Flugzeit-Massenspektrometer (ToF-MS) untersucht. Die drastischen Unterschiede im Erscheinungsbild der Eispartikel-Massenspektren, die zuvor in fünf verschiedene Geschwindigkeitsbereiche eingeteilt wurden, können detailgetreu durch das Variieren der Laserenergie und der Verzögerungszeit des Massenspektrometers nachgestellt werden. Mit dem LILBID Experiment können CDA Spektren von Eispartikeln mit Einschlagsgeschwindigkeiten von bis zu 15 km/s quantitativ nachgestellt werden. Spektren höherer Geschwindigkeiten können qualitativ nachgestellt werden. Die experimentellen Parameter, die für diese "Geschwindigkeitskalibration" verwendet wurden, können nun auf Eispartikel angewendet werden, die neben Wasser zahlreiche anderen Substanzen beinhalten, wie sie bereits in Enceladus' Plume und Saturn's E Ring gefunden wurden.

Mit dem LILBID Versuchsaufbau im Labor wurden bereits über 10.000 Analogspektren von mehr als 200 verschiedenen organischen und anorganischen Substanzen, in Wasser gelöst oder suspendiert, aufgenommen. Diese große Datenmenge lässt sich zunehmend umständlicher sortieren, prozessieren und interpretieren, was auch den Vergleich mit den Daten aus dem Weltall erschwert. Das Vergleichen der Massenspektren der Eispartikel mit den LILBID Laborspektren musste bisher manuell für individuelle Spektren durchgeführt werden. Innerhalb dieser Arbeit wird eine umfangreiche spektrale Referenzbibliothek entwickelt, die alle aufgenom-

menen LILBID Daten beinhaltet. Diese relationale Datenbank, die auf Structured Query Language (SQL) basiert, ermöglicht es, die Labordaten nach zahlreichen experimentellen Parametern zu filtern, wie zum Beispiel Laserenergie, Verzögerungszeit und Massenlinien in den Spektren. Die LILBID Massenspektren der Referenzbibliothek können nicht nur mit Daten von Raumsonden sondern auch mit jeglicher anderer Art verfügbarer Massenspektren verglichen werden.

Mit dem CDA wurden erfolgreich anorganische und organische Bestandteile von Eispartikel untersucht und es konnten Rückschlüsse auf die Habitabilität von Enceladus' Ozean gezogen werden. Bisher wurden jedoch keine Biosignaturen in außerirdischen Ozeanwelten identifiziert. Im *zweiten Projekt* werden die spektralen Erscheinungsbilder von Aminosäuren, Fettsäuren und Peptiden in Wassereispartikeln mit dem LILBID Experiment simuliert. Die untersuchten organischen Moleküle und ihre Fragmente können in den Massenspektren eindeutig identifiziert werden. Die Moleküle und Fragmente können bis in den ppm oder ppb Bereich nachgewiesen werden, abhängig von der individuellen Molekülspezies und der Polarität des Instruments. Durch das Vergleichen der Laborspektren mit denen von beispielsweise SUDA können diese organischen Biomarker zukünftig in Eispartikeln von außerirdischen Ozeanwelten nachgewiesen werden.

Während das Aufspüren von Peptiden ein deutlicher Hinweis auf vorhandene biologische Prozesse wäre, können Aminosäuren und Fettsäuren abiotisch oder biotisch entstehen. Die Unterscheidung von abiotischen und biotischen Signaturen von Aminosäuren und Fettsäuren in Ozeanwelten ist für die Suche nach Leben auf diesen Welten entscheidend. Deshalb werden die spektralen Erscheinungsbilder und Nachweisgrenzen von Aminosäuren und Fettsäuren in Proportionen untersucht, wie sie für entweder abiotische oder biotische Prozesse repräsentativ ist. Um ein realistisches Szenario zu simulieren, werden die Analyten mit zahlreichen zusätzlichen organischen und anorganischen Substanzen gemischt, wie sie in Eisteilchen von Enceladus erwartet werden, die sich aus einem Ozean gebildet haben, der mit einem Gesteinskern wechselwirkte. Abiotische und biotische spektrale Fingerabdrücke von Aminosäuren und Fettsäuren können sogar in diesen anspruchsvollen Matrizen zuverlässig identifiziert und voneinander unterschieden werden. In den salzreichen Matrizen bilden die organischen Moleküle charakteristische kationische Natriumkomplexe. Die organischen Biosignaturen können bis in den ppm oder ppb Bereich nachgewiesen werden, abhängig von den pK_S Werten der organischen Substanzen und der Salinität der Eispartikel. Die Experimente legen nahe, dass "Überlebenswahrscheinlichkeit" und Ionisierungseffizienz der komplexen organischen Moleküle während der Einschlagsionisation eines Eispartikels signifikant erhöht sind, wenn die Moleküle von einer Wassereismatrix geschützt werden. Anwendung der "Geschwindigkeitskalibration" des ersten Projektes auf diese Messungen zeigt, dass Einschlagsgeschwindigkeiten der Eispartikel von 3 - 8 km/s (optimal sind 4 - 6 km/s) am besten geeignet sind, eingeschlossene Aminosäuren, Fettsäuren und Peptide mit weltraumgestützten Massenspektrometern zu detektieren und dabei zwischen abiotischen und biotischen Signaturen in den aufgenommenen Massenspektren zu unterscheiden.

Abstract

Cryovolcanically active ocean worlds, such as Saturn's moon Enceladus and potentially Jupiter's moon Europa, eject water ice grains formed from subsurface water into space. The ejected ice grains can be analyzed by impact ionization mass spectrometers on-board spacecraft, thereby exploring the habitability of the subsurface oceans during flybys. An archetype of such mass spectrometers, the Cosmic Dust Analyzer (CDA) on-board the Cassini spacecraft, sampled individual ice grains from Enceladus in the Enceladean plume and Saturn's E ring. The SUrface Dust Analyzer (SUDA) instrument, being built for the upcoming Europa Clipper mission, will analyze ice grains in Europa's vicinity. Interpreting the spaceborne measurements requires terrestrial calibration and this PhD thesis therefore deals with terrestrial analogue experiments and comprises two conjoint projects.

The appearance of recorded impact ionization mass spectra is a function of not only composition but also impact speed (i.e. kinetic energy) of the ice grains onto the mass spectrometer's metal target. In the *first project*, mass spectra of water ice grains as recorded by the CDA at typical impact speeds ranging between 4 and 21 km/s are simulated using a laboratory analogue experiment which is capable of reproducing compositional variations of the ice grains. In this Laser-Induced Liquid Beam Ion Desorption (LILBID) process, a µm-sized liquid water beam is irradiated by a pulsed infrared laser at suitable energies and wavelengths. The created ions are subsequently analyzed in a Time-of-Flight mass spectrometer (ToF-MS). Categorizing the ice grain mass spectra into five different speed regimes, the significantly varying spectral appearances can be accurately reproduced by tuning the laser energy and the delay time of the mass spectrometer's gating system. The LILBID facility is capable of quantitatively reproducing CDA spectra of ice grains at impact speeds up to 15 km/s. Above that speed a qualitative match is achieved. The experimental parameters used for this "speed calibration" can now be applied to ice grains carrying a wide variety of non-water compounds as observed in the Enceladean plume and Saturn's E ring.

More than 10,000 laboratory analogue spectra of over 200 different organic and inorganic compounds dissolved or suspended in water have been recorded with the LILBID facility. The enormous amount of data are increasingly challenging to sort, process, interpret and eventually compare to the data from space. Thus far, manual comparison of ice grain and LILBID mass spectra has been required. As part of the research presented here, a comprehensive spectral reference library containing all recorded data from the LILBID facility has been developed. This relational database is based on Structured Query Language (SQL) and enables filtering the laboratory data for scores of experimental parameters, such as laser energy and delay time, as well as mass lines in the spectra. The LILBID mass spectra in the reference library can be compared not only to data from space missions but also to any kind of available mass spectral data.

The CDA has proven to be very successful in analyzing inorganic and organic ice grain constituents to characterize the habitability of Enceladus' ocean. Hitherto biosignatures have not been identified in extraterrestrial ocean environments. In the *second project*, the mass spectral appearances of amino acids, fatty acids, and peptides in water ice grains have been simulated using the LILBID facility. The investigated organic molecules and their fragments are clearly identifiable in the mass spectra and their detection limits are determined to be at the ppm or ppb level, depending on the molecular species and instrument polarity. By comparing the laboratory spectra with e.g. SUDA spectra, these key organic molecules can be recognized in ice grains from extraterrestrial ocean worlds.

While the detection of peptides would strongly indicate extant biological processes, amino acids and fatty acids can be either produced abiotically or biotically. Discriminating between abiotic and biotic signatures of amino acids and fatty acids on ocean worlds is crucial for the search for life and its emergence on these bodies. Therefore, the mass spectral appearances and detection limits of amino acids and fatty acids, in proportions representative of either abiotic or biotic formation processes, have been investigated in matrices realistic for extraterrestrial subsurface oceans. The analytes are mixed with numerous additional organic and inorganic background compounds suitable for ice grains formed from Enceladean ocean water which has interacted with a rocky core. Differing abiotic and biotic mass spectral fingerprints of amino acids and fatty acids can be reliably identified and distinguished from each other, even under these demanding matrix conditions. In a salty matrix, the organics form characteristic sodiated molecular cations. Detection limits of the organic biosignatures are at the ppm or ppb level, strongly dependent on the pK_a values of the organics and the salinity of the ice grains. The conducted experiments suggest that the survivability and ionization efficiency of large organic molecules during impact ionization of an ice grain is significantly improved when the molecules are protected by a frozen water matrix. Applying the "speed calibration" of the first project to these measurements shows that ice grain encounter velocities of 3 - 8 km/s, with an optimal window at 4 - 6 km/s, are most appropriate to detect encased amino acids, fatty acids, and peptides with a spaceborne mass spectrometer, and in turn discriminate between abiotic and biotic signatures in the resulting mass spectra.

Contents

List of Figures

I Introduction

II. Developing a reference library for impact ionization mass spectrometers

III. Experiments with amino acids, fatty acids, and peptides for the detection of biosignatures in ice grains from extraterrestrial ocean worlds

IV. Conclusions and outlook

Appendices

List of Tables

I. Introduction

II. Developing a reference library for impact ionization mass spectrometers

III. Experiments with amino acids, fatty acids, and peptides for the detection of biosignatures in ice grains from extraterrestrial ocean worlds

Appendices

I. Introduction

1 Thesis structure

THIS CUMULATIVE DISSERTATION is divided into four consecutive parts. The introductory Part I containing chapters 1 to 6 provides a framework for this thesis. Parts II (chapters 7 and 8) and III (chapters 9 and 10) present the methods and results as well as comprehensive discussions. Chapters 7, 9, and 10 comprise three peer-reviewed published articles. The text of these chapters is given as published. Chapter 8 is a manuscript in preparation for submission to a peer-reviewed journal.* Part IV, containing chapters 11 and 12, discusses the major results of Parts II and III, draws overall conclusions and gives an outlook about ongoing and future work. Appendices A, B, and C provide supplementary information to Parts II and III. Appendix D lists published articles, to which the PhD candidate has contributed, in addition to those in Parts II and III. Appendix E lists conference abstracts, which rely on the published articles in Parts II and III. All references cited can be found in the bibliography. The contents of Parts I to IV are briefly summarized below.

**The PhD candidate's contributions to these four articles can be found in chapter 6.3.*

Part I: Introduction

After giving a general overview about the structure of this thesis (chapter 1), chapter 2 introduces the Cassini mission, the Cosmic Dust Analyzer (CDA) instrument and the Saturnian System, and is followed by chapter 3, which focuses on Saturn's moon Enceladus and the proposed Enceladus Life Finder mission. Chapter 4 is dedicated to Jupiter's moon Europa, the upcoming Europa Clipper mission and the SUrface Dust Analyzer (SUDA), an instrument similar to CDA, but with superior performance. Chapter 5 explains the significance of laboratory laser induced analogue experiments at Freie Universität Berlin for space instruments like CDA and chapter 6 completes the introduction by explaining the research aims of this thesis as well as the PhD candidate's contributions to the scientific articles within Parts II and III.

Part II: Developing a reference library for impact ionization mass spectrometers

Previous work (e.g. Postberg et al., 2009a; Zou et al., 2020) has shown that compositional variations as seen in ice grain mass spectra recorded by e.g. CDA in space can be reproduced with laboratory laser-based analogue experiments, but did not consider variations in the impact speeds of the ice grains onto the detector's target plate. Chapter 7 deals with the accurate laboratory reproduction of water ice grain mass spectra at different impact speeds in space and proves that laser desorption in the laboratory can be considered to be an appropriate analogue for the impact ionization process of ice grains in space. Chapter 7 paves the way for chapter 8, which describes the development of a comprehensive mass spectral reference library containing $>$ 10,000 analogue mass spectra, which mimic variable ice grain compositions at different impact speeds. The mass spectra in the spectral reference library can be compared with past and future space mission data and thereby significantly improve analyses of ice grain mass spectra recorded in space.

Part III: Experiments with amino acids, fatty acids, and peptides for the detection of biosignatures in ice grains from extraterrestrial ocean worlds

Chapter 9 is concerned with recording and analyzing laboratory mass spectra of amino acids, fatty acids, and peptides in a water matrix. This chapter predicts the mass spectral appearance and detection limits of these biologically important molecules as they can potentially be incorporated in ice grains emitted by ocean-bearing moons and then encountered in space. In chapter 10, the relative abundances of various amino acids and fatty acids representative of either abiotic or biotic chemistry are investigated and other organic and inorganic background compounds, as expected in a realistic ocean world scenario, are added to the water matrix. In this chapter, it is demonstrated to what extend biotic and abiotic signatures in the mass spectra can be detected and distinguished from each other and the detection limits of amino acids and fatty acids in the presence of a complex organic and inorganic background matrix are determined. Building on chapters 7 and 9, optimal encounter velocities for spacecraft flying by ocean-bearing moons for astrobiology investigations are recommended in chapter 10.

Part IV: Conclusions and outlook

Chapter 11 summarizes and discusses major conclusions and addresses open questions emerging from this thesis. Chapter 12 gives a brief summary about ongoing laboratory campaigns and provides an outlook about future work.

2 Exploring the Saturnian System with Cassini-Huygens

2.1 The Cassini-Huygens mission

The Cassini-Huygens spacecraft was launched on board a Titan 4B Centaur rocket from Cape Canaveral Air Force Station on October 15, 1997 as a collaborative flagship mission of the National Aeronautics and Space Administration (NASA), the European Space Agency (ESA) and the Agenzia Spaziale Italiana (ASI). The spacecraft was named after Giovanni Domenico Cassini, who was the first to observe Saturn's rings, and Christiaan Huygens, who discovered Saturn's moon Titan. The naming of the spacecraft already points to two mission goals: Understanding the structure and dynamics of Saturn's ring system and Titan's atmosphere and surface. Other mission objectives were to investigate Saturn's atmosphere and magnetosphere, the nature of the dark material on Iapetus, and Saturn's icy satellites. The icy moon Enceladus itself was not a primary mission target, but Cassini's discoveries made Enceladus one of the most interesting objects in the Solar System (see section 3.1). Cassini-Huygens entered into an orbit around Saturn on July 1, 2004 after traveling 3.5 billion kilometers and executing gravitational assists using Venus, Earth and Jupiter (Figure 2.1). A detailed description of the Cassini-Huygens mission and the spacecraft can be found in the literature (Henry, 2002; Matson et al., 2002; Spilker, 2018; Spilker, 2019; NASA(url1), 2020).

The Cassini-Huygens spacecraft (Figure 2.2) was 6.8 m tall and 4.0 m wide, including the Cassini orbiter and the Huygens lander. Its total launch mass was 5712 kg, of which 2978 kg was propellant. Electrical power for the spacecraft's instruments and on board systems was generated by three radioisotope thermoelectric generators (RTGs). Each unit used heat produced by 10.9 kg of plutonium-238 (^{238}Pu) to generate 300 W electrical power at the beginning of the mission. To achieve its mission goals, the orbiter was equipped with twelve instruments; the lander had six instruments. The twelve instruments of the Cassini orbiter were as follows:

Cassini Plasma Spectrometer (CAPS): In situ plasma measurements by sampling ions and electrons (Young et al., 2004).

Composite Infrared Spectrometer (CIRS): Remote sensing temperature and composition measurements of surfaces and atmospheres by measuring infrared thermal radiation (Flasar et al., 2004).

Cassini Radar (RADAR): Produced radar maps (remote sensing) to investigate e.g. the roughness of surfaces (Elachi et al., 2004).

Radio Science Subsystem (RSS): Remote sensing measurements of atmospheres, Saturn's ring structure as well as gravity field measurements by sending radio signals to antennas on Earth (Kliore et al., 2004).

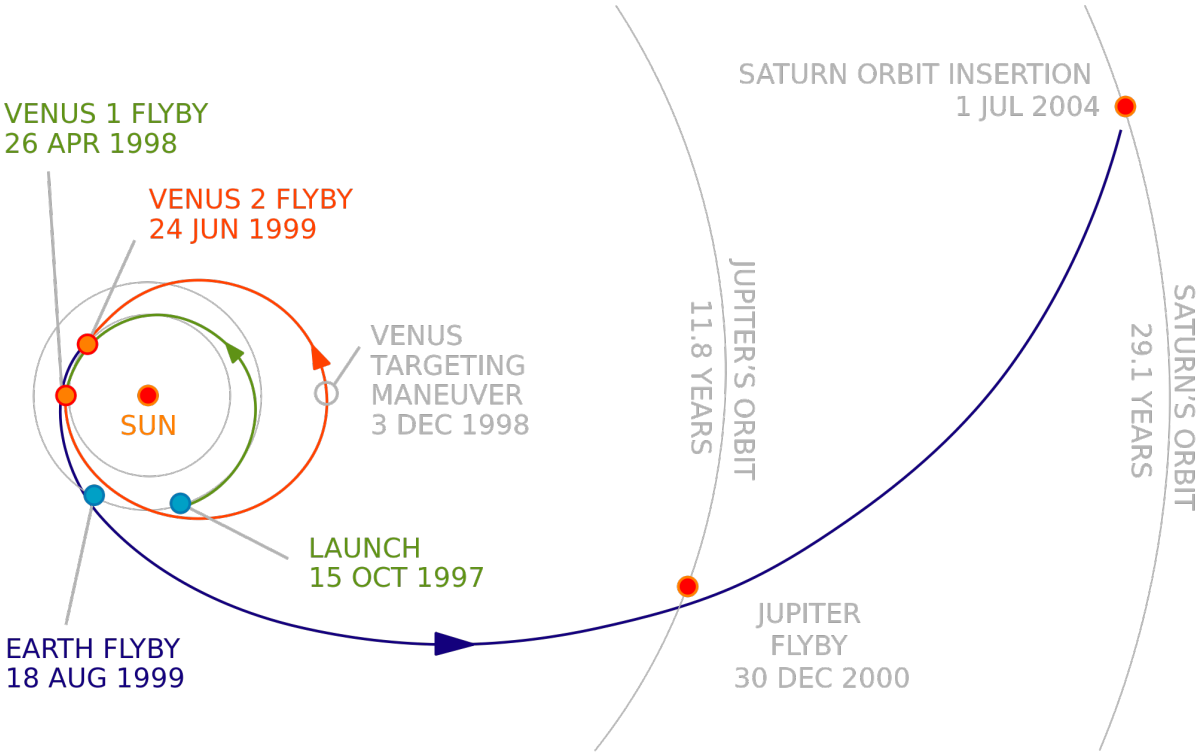

Figure 2.1: *Cassini's interplanetary flight trajectory with launch from Earth on October 15, 1997, followed by gravity assist flybys of Venus, Earth and Jupiter, and Saturn arrival on July 1, 2004. Using the VVEJGA (Venus-Venus-Earth-Jupiter Gravity Assist) trajectory, it took Cassini 6.7 years to arrive at the Saturnian System (Image credit: NASA/JPL-Caltech).*

Magnetometer (MAG): Recorded in situ the direction and strength of magnetic fields around the spacecraft and investigated magnetic interactions with solar wind (Dougherty et al., 2004).

Imaging Science Subsystem (ISS): Took images with two cameras (remote sensing): A wide-angle camera and a narrow-angle camera (Porco et al., 2004).

Visible and Infrared Mapping Spectrometer (VIMS): Took images using infrared and visible light for remote sensing compositional analyses (Brown et al., 2004).

Radio and Plasma Wave Science (RPWS): In situ electric and magnetic field measurements as well as electron density and temperature measurements by receiving and measuring radio signals (Gurnett et al., 2004).

Ion and Neutral Mass Spectrometer (INMS): In situ analyses of encountered gaseous and ionic material (Waite et al., 2004).

Magnetospheric Imaging Instrument (MIMI): Magnetosphere images and in situ magnetic field analyses plus interactions with solar wind (Krimigis et al., 2004).

Cosmic Dust Analyzer (CDA): In situ analyses of encountered dust/ice grains (Srama et al., 2004). Chapter 7 of this thesis utilizes data from the CDA (see section 2.2).

Ultraviolet Imaging Spectrograph (UVIS): Structural and compositional remote sensing analyses by taking images and spectra in the ultraviolet (Esposito et al., 2004).

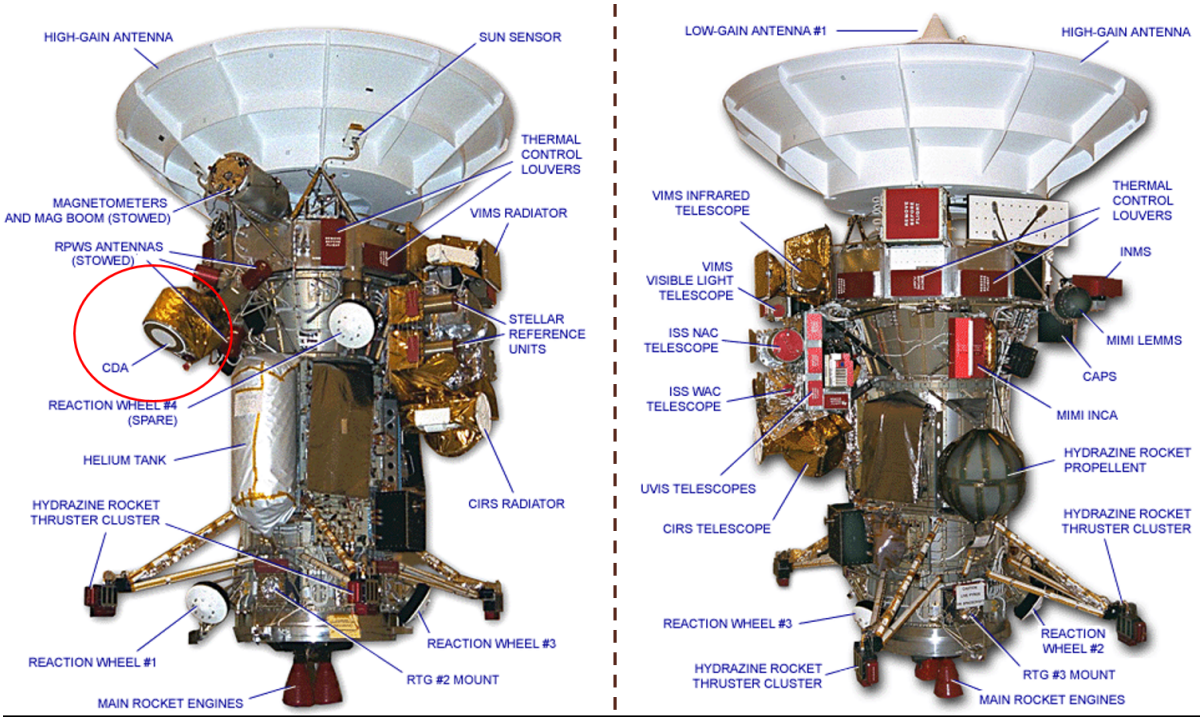

Figure 2.2: *Images of the Cassini orbiter taken during preparation for launch in October 1997. The thermal blanketing was not yet installed, so nearly all spacecraft's components are visible. The spacecraft's Plus-Y Side is shown on the left; The Cosmic Dust Analyzer (CDA) is circled red. The Minus-Y Side is shown on the right (Image credit: NASA).*

The Huygens lander (Lebreton and Matson, 2002), released from the spacecraft on December 25, 2004, followed a ballistic trajectory onto Titan to study the moon's atmosphere and surface. Its landing on January 14, 2005 was the first, and so far only, landing in the outer Solar System. The probe transmitted data for $2^{\mathrm{h}}28^{\mathrm{min}}$ during parachute descent and for another $3^{\mathrm{h}}14^{\mathrm{min}}$ after landing (Lebreton et al., 2005). Cassini's four-year Prime Mission was followed by the two-year Equinox Mission and seven years of exploration during the Solstice Mission. In the last mission phase, the Grand Finale Phase, Cassini passed 22 times between the innermost D ring and Saturn's uppermost atmosphere (Figure 2.6). After 13 years of exploration ($\sim$ half a Saturn year), 2.5 million executed commands, and 635 GB collected science data, the mission was ended by a deliberate plunge into Saturn on September 15, 2017.

Cassini-Huygens' spectacular findings include three dimensional structures in Saturn's dynamic ring system (Schmidt et al., 2009; Hoffmann et al., 2015), a methane-based hydrologic cycle on Titan (Hayes et al., 2018) with methane rain that creates hydrocarbon seas and lakes (Hayes, 2016), and erupting geysers on Enceladus (Porco et al., 2006) that are composed of material derived from a subsurface water ocean and eventually feed Saturn's E ring (Kempf et al., 2010; Mitchell et al., 2015) as described in detail in section 3.1.

2.2 The Cosmic Dust Analyzer (CDA)

One of the instruments on-board Cassini, the Cosmic Dust Analyzer (CDA), was designed to analyze and characterize the micron- and submicron dust particles in the Saturnian System (Srama et al., 2004; Srama et al., 2011). The instrument was 51 cm in length, had a diameter of 45 cm and weighted 17 kg (Figure 2.3, left). The last instrument signal that was conveyed by Cassini to Earth before the spacecraft crashed into Saturn (see section 2.1) was a signal from the CDA (R. Srama, pers. comm., 2017[1]). The CDA determined dust impact rates as well as the compositions, masses (10^{-5}-10^{-9} g), speeds (1-100 km/s), and electric charges (1 fC - 1 pC) of individual particles. The instrument had two independent subsystems: The High Rate Detector (HRD) and the Dust Analyzer (DA). The HRD detected very high impact rates (up to 10^4/s) whereas the DA was built to analyze particle properties. The DA consisted of three subsystems: The EG detector (Entrance Grid) was a charge sensing grid, which measured the charges of traversing particles. The Impact Ionization Detector (IID) was similar to the Ulysses- and Galileo-type detectors (Grün et al., 1992a; Grün et al., 1992b). The third subsystem, the Chemical Analyzer (CA), was a linear Time-of-Flight mass spectrometer (ToF-MS) that produced cationic impact ionization mass spectra from impacting particles with a mass resolution of 20-50 m/Δm (Figure 2.3, right).

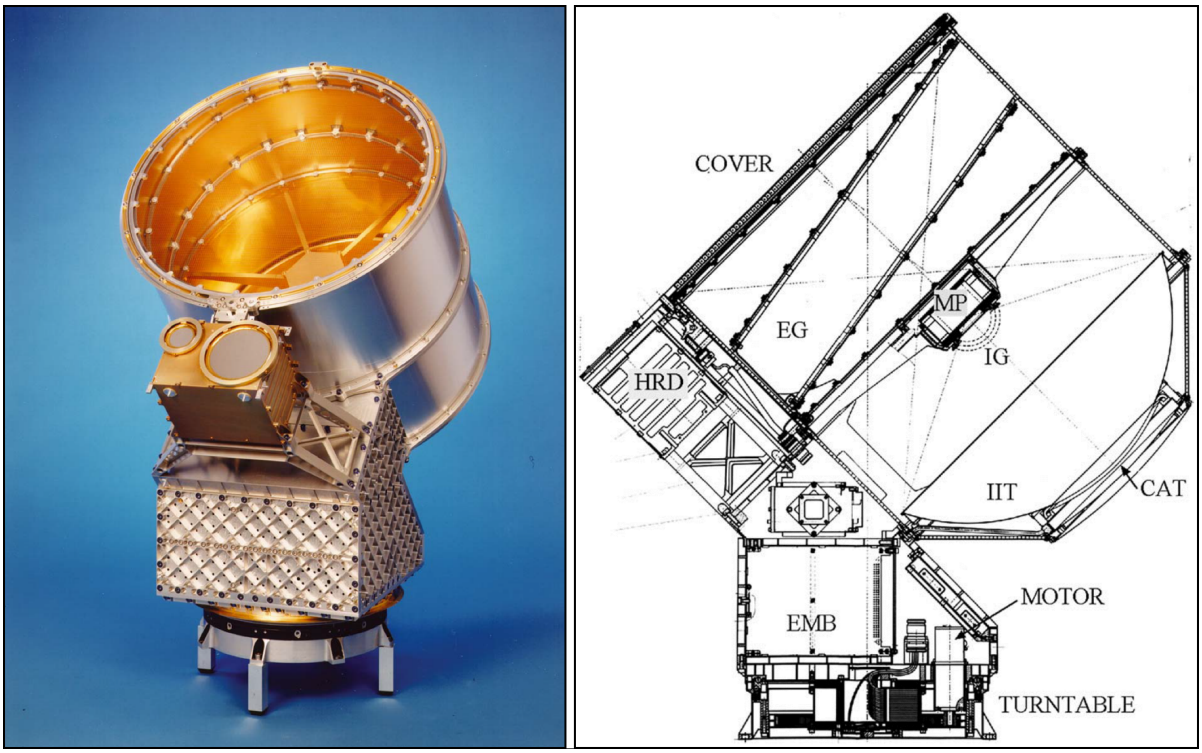

Figure 2.3: *A photograph of the Cosmic Dust Analyzer (CDA) on the left and its technical drawing on the right (adapted from Srama et al., 2004). HRD: High Rate Detector; EG: Entrance Grid; EMB: Electronics Main Box; MP: Multiplier; IG: Ion Grid; IIT: Impact Ionization Target; CAT: Chemical Analyzer Target.*

The space data analyses part of this thesis deals exclusively with CA

[1]Personal communication on October 19, 2017.

mass spectra. A particle entering the CA aperture hit either the Impact Ionization Target (IIT), a big (41 cm in diameter) gold plate, or the Chemical Analyzer Target (CAT), a small (16 cm in diameter) rhodium plate. Mass spectra that are meaningful for compositional analyses were only generated if a particle hit the small rhodium target. An impacting particle at hypervelocity (> 1 km/s) was vaporized and partially ionized after hitting the target plate. Depending on the impact speed, the target material rhodium was excavated and ionized (see chapter 7). During the impact ionization process, which was first described and characterized in the 1960s and 1970s (Friichtenicht, 1964; Auer and Sitte, 1968; Friichtenicht et al., 1971), positively charged cations, negatively charged anions, electrons as well as neutral molecules are created. The cations were accelerated through a strong electric field, which was generated by a potential of -1000 V applied over a distance of 3 mm, towards the multiplier (MP) and cationic mass spectra of the impacting dust/ice grain and the excavated target material were generated (Srama et al., 2004). The QI channel measured the amount of cations moving towards the MP (Figure 2.4).

Recording a mass spectrum was triggered when the QC or QA signals exceeded a specified trigger threshold or when the first abundant cation species (e.g. $[H_3O]^+$) arrived at the MP after impact. Detected cation species are almost exclusively singly charged and the maximum recorded mass is 170-240 u, depending on the trigger mechanism. The QI signal amplitude is proportional to the ion yield of the impact and correlates with particle mass and relative impact speed: $m^\alpha v^\beta$, with α typically 1 and β typically between 3 and 5 (Bedford, 1971; Stübig, 2002; Altobelli et al., 2016). For more details about the impact ionization process and the CAT, see chapter 7 and the literature (Srama et al., 2004; Hillier et al., 2006; Khawaja, 2016; Kempf et al., 2020).

Because of the low mass resolution and the instrument's limited mass range and dynamic range (range from lowest to highest detected signal), a very detailed compositional analysis of impacting ice grains with the CDA is extremely difficult. It is currently technically challenging, if not impossible, to accelerate micron- and sub-micron-sized ice grains to relevant speeds in a laboratory environment (Burchell et al., 1999; Shu et al., 2012; Fielding et al., 2015) and a laser-based laboratory analogue experiment has instead been developed to simulate the impact ionization process of ice grains in space. The laboratory experiment produces spectra with a much higher mass resolution and mass range than the CDA - and with that improves the diagnostic capabilities of the ice dominated mass spectra obtained by space instruments (see chapters 5, 7, and 8).

2.3 Saturn, its rings and moons

Saturn is the second largest planet (Figure 2.5) and has the lowest density (0.687 g/cm^3) among all planets in the Solar System (Helled et al., 2009). Its radius between poles and equator differs by almost 11 % due to a rapid rotation period of about $10^{\mathrm{h}}40^{\mathrm{min}}\pm10^{\mathrm{min}}$ (Gurnett et al., 2007; Read et al., 2009) and quasi-fluid state (Helled and Guillot, 2013). Sat-

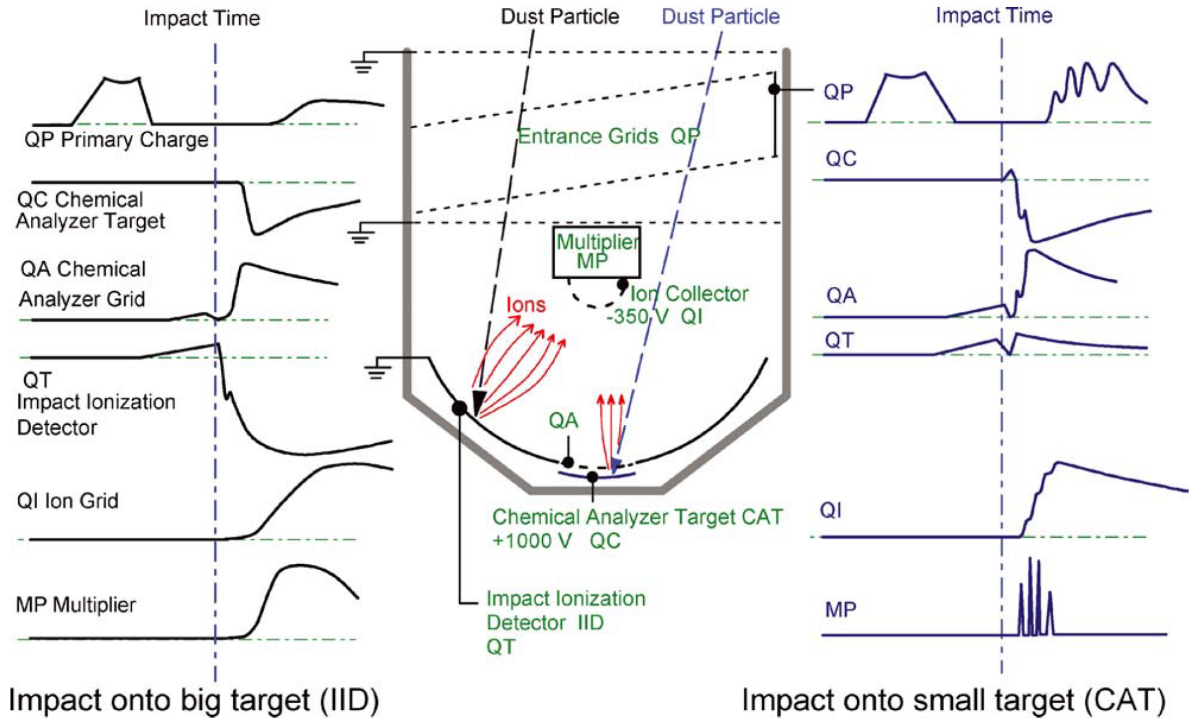

Figure 2.4: *Hypervelocity impact signals of dust/icy grains onto the Impact Ionization Target (left) and onto the Chemical Analyzer Target (right). The latter is made of rhodium. The MP channel generated the Time-of-Flight mass spectra of the impinging grains (figure taken from Srama et al., 2004).*

urn has a large rocky core of 15 - 18 m_E[1] (Fortney et al., 2018; Iess et al., 2019). The core is surrounded by a layer of metallic hydrogen, followed by a helium (He)-saturated layer of liquid molecular hydrogen (H_2), which possibly contains trace amounts of volatiles other than hydrogen and helium (Guillot et al., 2009; Hubbard et al., 2009). This layer gradually turns into the gas phase with decreasing depth. The atmosphere is mainly composed of H and He with small amounts of CH_4 (methane), NH_3 (ammonia), PH_3 (phosphine), and probably H_2S (hydrogen sulfide) and H_2O (water) (Porco et al., 2005). Two characteristic features of Saturn are the Great White Spot and the hexagonal wave. The Great White Spot consists of giant periodic storms. Seasonal changes are believed to be responsible for their occurrences (Sánchez-Lavega et al., 1991). The hexagonal wave is a warm polar vortex around Saturn's North Pole (Godfrey, 1988).

Saturn's most striking feature is the vast ring system (Figure 2.6). It was discovered by Galileo Galilei in 1610 writing in a letter to the Duke of Tuscany that "the planet Saturn is not alone, but is composed of three, which almost touch one another and never move nor change [...] and the middle one (Saturn itself) is about three times the size of the lateral ones" and later describing the rings as "Saturn's ears" (Whitehouse, 2009). Christiaan Huygens observed the rings during the 1650s and suggested that Saturn is surrounded by a solid ring detached from the planet (Huygens, 1659). He was also surprised to see that Saturn had a large moon, now known as Titan. Giovanni Domenico Cassini, in 1675,

[1] $1 m_E = 5.97 \times 10^{24} kg$; m_E: Earth mass.

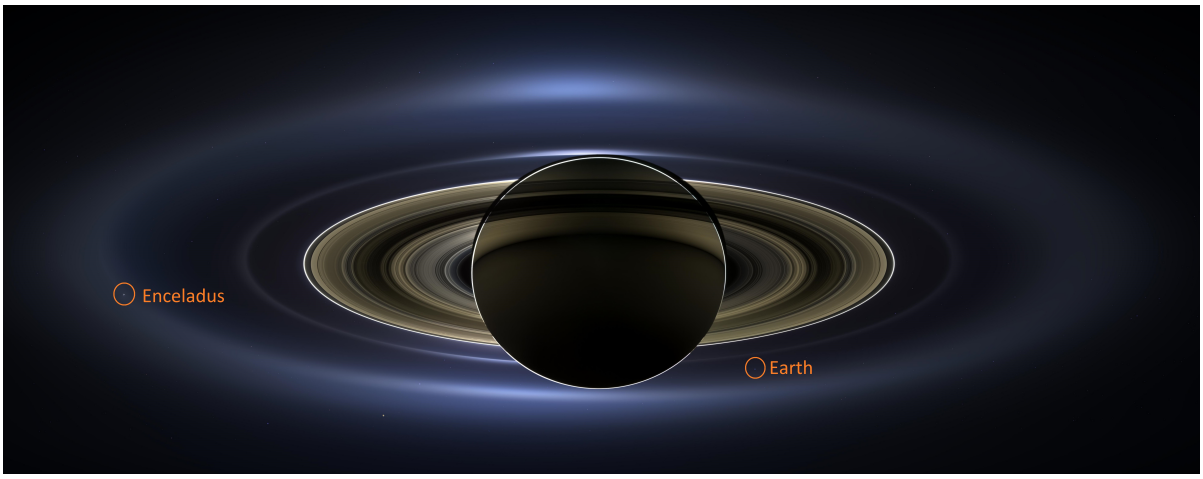

Figure 2.5: *Saturn and its ring system. This panoramic mosaic is a combination of 141 images taken by the Cassini wide-angle camera on July 19, 2013. Enceladus' orbit lies within Saturn's E ring. Earth can be seen in the background. Cassini was approximately 1.2 million kilometers from Saturn and 17 degrees below the ring plane (Image credit: NASA/JPL-Caltech/Space Science Institute).*

discovered that Saturn's ring is composed of numerous smaller rings with gaps between them (Cassini, 1685). James Clerk Maxwell demonstrated in 1859 that the rings must be composed of a large number of particles that independently orbit the planet (Maxwell, 1859). The latest ring discovery was the so-called "Phoebe ring" by Verbiscer et al. (2009). The Phoebe ring is Saturn's outermost, and largest, ring extending from at least 128 R_S[1] to 207 R_S (Verbiscer et al., 2009).

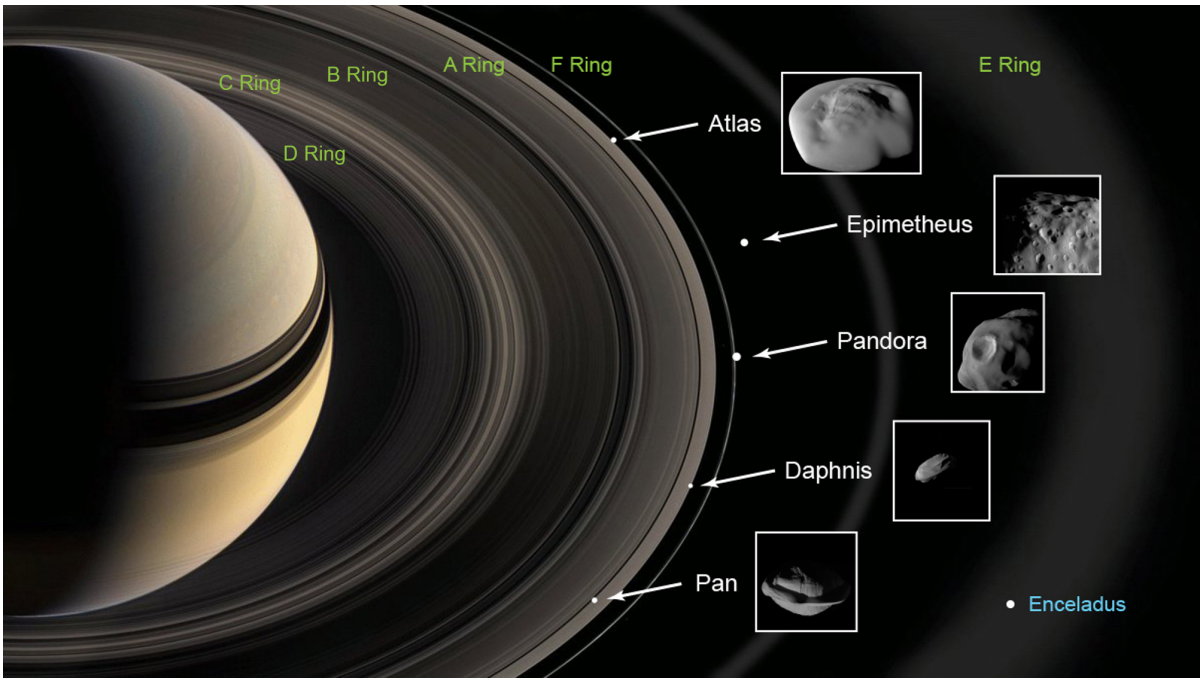

Figure 2.6: *Detailed view of Saturn's ring system and moons orbiting the planet withing the ring system (not to scale; Image credit: NASA/JPL-Caltech).*

Saturn's diffuse E ring, the second outermost ring, extends from ~ 3

[1] 1 R_S = 60,330 km; R_S: Saturnian model radius.

R_S to ~ 20 R_S, thus lies roughly between the orbits of the moons Mimas and Titan. In drastic contrast to Saturn's main A, B, C, and D rings (Cuzzi et al., 2010), the E ring's vertical dimension is at least 0.5 Rs, with a decrease in thickness at 3.95 R_S coincident with Enceladus' orbit (Showalter et al., 1991; Hillier et al., 2007; Nölle, 2020). The E ring is mainly composed of water ice grains (Hillier et al., 2007; Postberg et al., 2008) that have lifetimes of a few tens to a few hundreds of years (Kempf et al., 2018). The ice grains show compositional differences with respect to their distance to Saturn and the ring plane (Nölle, 2020). The Saturnian moon Enceladus was suggested to be the main source of the E ring particles because the edge-on brightness profile of the E ring peaks near the Enceladean mean orbital distance at 3.95 R_S (Baum et al., 1981). In addition to Enceladus, Tethys, another Saturnian moon, was suggested to be a second source of the E ring particles (de Pater et al., 2004).

Saturn has 82 known moons, which vary significantly in size, shape and orbital parameters (Figure 2.7).

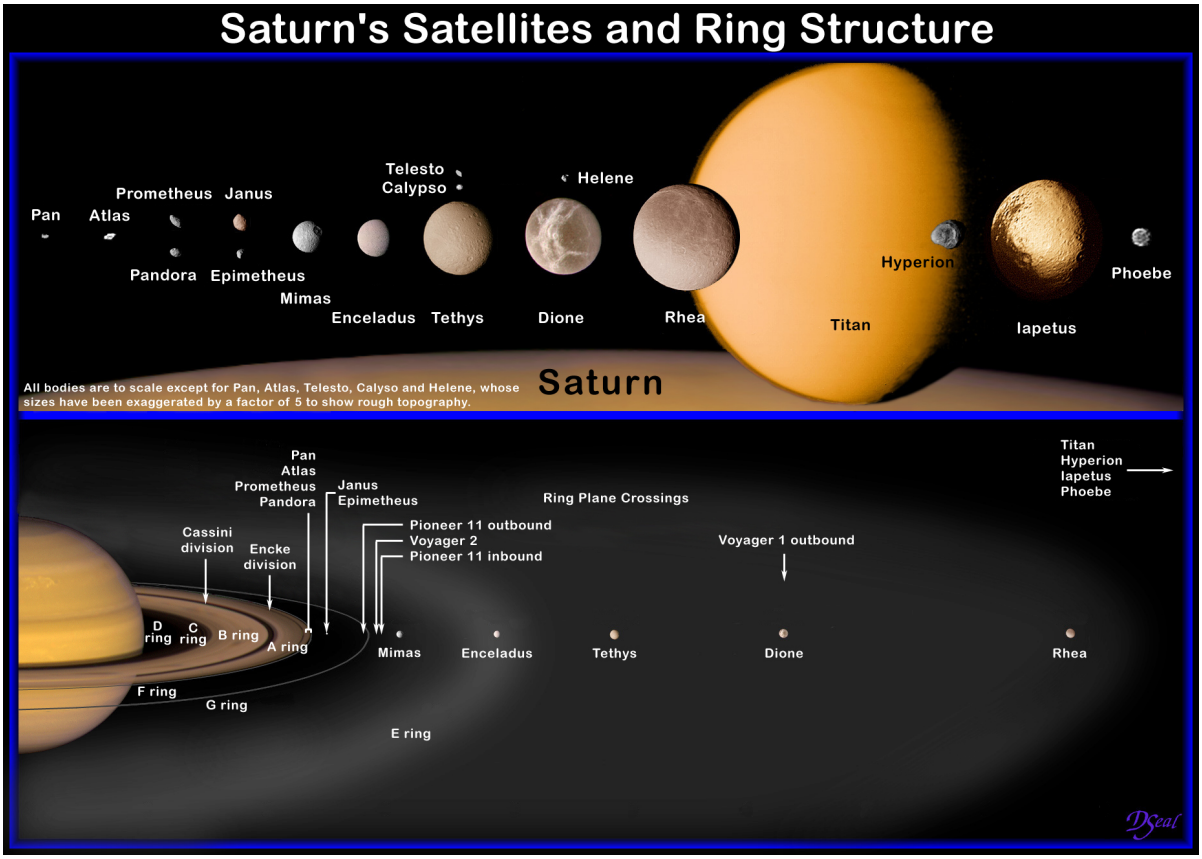

Figure 2.7: *Saturn, some of its rings and satellites to relative scale. The diffuse E ring reaches from Mimas to Titan (Image credit: NASA/JPL-Caltech/David Seal).*

On the one hand, there is Titan, the second largest moon in the Solar System with its dense atmosphere and complex organic chemistry (Griffith et al., 1998; Raulin et al., 2010).[1] On the other hand, there are 58 (out of 82) irregular satellites, which are small (diameter often <10 km) and have distant, inclined, often retrograde orbits (T. Denk, pers.

[1]In June 2019, the Dragonfly mission was selected to fly (launch date: 2026) with a rotorcraft lander to Titan and further explore its habitability (Lorenz et al., 2018).

comm., 2019[1]). Numerous mid-sized icy satellites, for example Enceladus (see section 3.1), complete the diverse population of the Saturnian moons.

[1]Personal communication on October 7, 2019.

3 Saturn's moon Enceladus and the Enceladus Life Finder mission (ELF)

3.1 Enceladus - A hydrothermally active ocean world

Enceladus, discovered by William Herschel in 1789 during the first use of his new reflecting telescope (Herschel, 1790), is one of five mid-sized icy satellites in Saturn's E ring - the others are Mimas, Dione, Tethys and Rhea. The surfaces of the icy moons, except Enceladus, are dominated by impact craters leading to the conclusion that they are geologically inactive for billions of years (Spencer and Nimmo, 2013; Schenk et al., 2018). Enceladus' average diameter is 504 km and its density of 1.6 g/cm^3 (Thomas, 2010) indicates an ice:rock ratio of 60:40 by mass (Schubert et al., 2007). Surface temperatures vary from ∼50 K in the night to ∼80 K during the daytime (Howett et al., 2010).

The earliest hints that Enceladus is unusual compared to other icy moons came from terrestrial telescopic observations obtained from 1912 to 1913 when a magnitude increase of 0.3 in the brightness of Enceladus at 32° southern latitude, which was the maximum declination of the used telescope, was reported (Slipher and Slipher, 1914). The same increase in the brightness of Enceladus' lightcurve at 32° southern latitude was observed in 1972-1973 (Franz and Millis, 1975). Voyager 2 images showed Enceladus' high albedo and that the moon's surface ranges from old, densely cratered regions to geologically young uncratered plains (Smith et al., 1982), as for example in the South Polar Terrain (SPT) region located around 55° southern latitude (Helfenstein, 2010). In this region, Enceladus has four nearly parallel fractures, so-called "Tiger Stripes". Each of the Tiger Stripes, shown in Figure 3.1, is around 130 km long, two to four km wide and separated from their neighbors by approximately 35 km (Spilker, 2018). The Tiger Stripes are, with observed temperatures of up to 200 K, more than 100 K warmer than the surrounding areas (Howett et al., 2011; Goguen et al., 2013). Magnetic field anomalies detected during a flyby in February 2005 (Dougherty et al., 2006) led to a closer flyby of Enceladus (∼168 km from the moon's surface) in July 2005. Images taken by the Cassini Imaging Subsystem (ISS) cameras showed an icy plume erupting from the SPT (Porco et al., 2006) and the High Rate Detector (HRD), a subsystem of the Cassini Cosmic Dust Analyzer (CDA), discovered a significant increase in particle flux (Spahn et al., 2006). Another instrument, the Composite Infrared Spectrometer (CIRS), detected a remarkably high thermal emission of 3 to 7 GW from this region (Spencer et al., 2006). Complementing these results, the Ion and Neutral Mass Spectrometer (INMS) and Ultraviolet Imaging Spectrograph (UVIS) also found evidence of ongoing geologically active processes in the SPT of Enceladus (Waite et al., 2006; Hansen et al., 2006).[1] The moon's famous plume (Figure 3.1), erupting through the Tiger Stripes in the SPT, is composed of material that stems from a liquid subsurface

[1] A compiled global infrared mosaic of Enceladus suggests that the moon's North Polar terrain around 30° northern latitude has recently been geologically active, similar to the SPT activity (Robidel et al., 2020).

water ocean (Collins and Goodman, 2007; Schmidt et al., 2008; Tobie et al., 2008; Postberg et al., 2009a) and actively feeds Saturn's E ring (Kempf et al., 2010; Mitchell et al., 2015). In recent decades spacecraft measurements have revealed that several other objects in the Solar System harbor subsurface oceans beneath insulating ice shells (Fortes, 2000; Zimmer et al., 2000; Hussmann et al., 2006; Nimmo and Pappalardo, 2016; Hand et al., 2020), for example the Jovian moon Europa, which is the target of the upcoming Europa Clipper mission (see section 4.2).

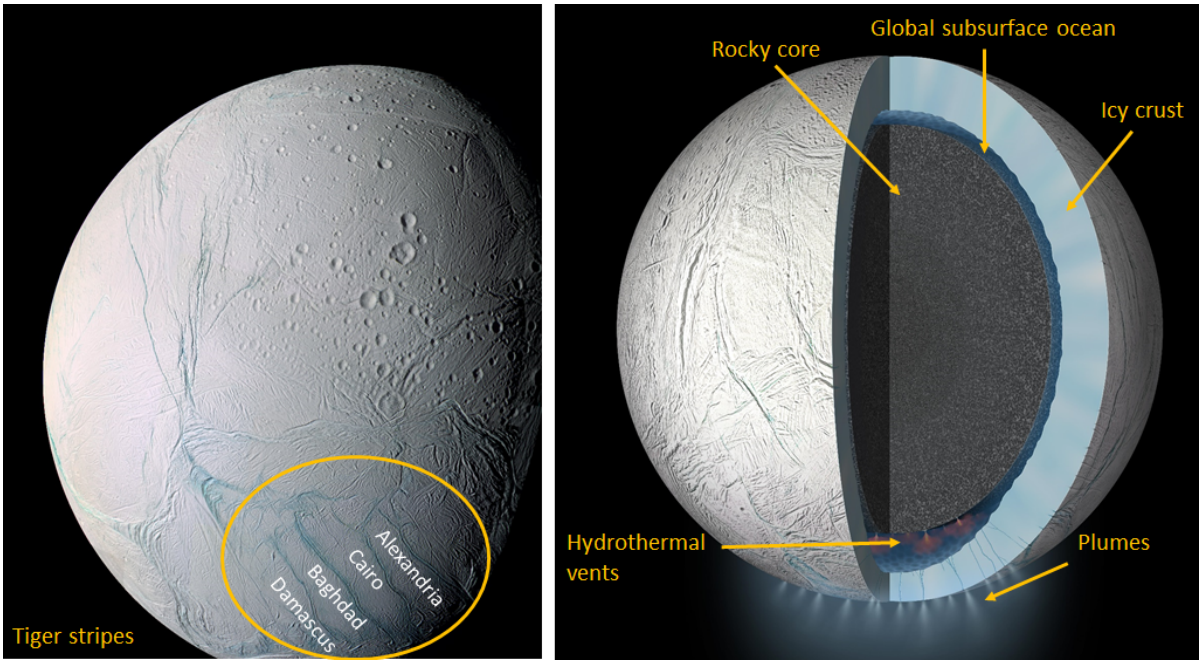

Figure 3.1: *Left: False color mosaic created from 21 frames taken by the Cassini Narrow Angle Camera on March 9 and July 14, 2005. Enceladus' South Polar Terrain (SPT) including the four named Tiger Stripes can be seen at the bottom of the image. Right: Artist's rendering of the approximate interior of Enceladus (to scale). The plume emits gas and ice grains containing salts and organic material into space (Image credit: NASA/JPL-Caltech/Space Science Institute).*

Enceladus' erupted plume material has been sampled by the two mass spectrometers on board Cassini: The INMS (Waite et al., 2004) measured the gaseous material whereas the CDA (Srama et al., 2004) sampled the solid ice grains in the plume. The INMS detected CO_2 (carbon dioxide), simple hydrocarbons, such as CH_4 and C_2H_4 (ethylene), and molecular hydrogen (Waite et al., 2009; Waite et al., 2017). Based on CDA mass spectra, the ice grains can be divided into three main types. The three main spectral types are described as follows: Type 1 ice grains are almost pure water ice with occasional traces of sodium and potassium salts (Postberg et al., 2008; Postberg et al., 2009a; Postberg et al., 2011a). They are relatively homogeneous in composition. Type 2 grains contain significant amounts of organic material. In fact, about 25 % (by number) of the ice grains from Enceladus contain organic material at detectable concentrations (Postberg et al., 2018b). Complex organic macromolecules (Postberg et al., 2018a) as well as oxygen-, nitrogen-bearing, and aromatic compounds (Khawaja et al., 2019), some of which could act as amino acid precursors, were identified in Type 2 grains. Type 3 grains are dominated

by sodium salts at concentrations of about 1 % by mass (Postberg et al., 2008; Postberg et al., 2009a; Postberg et al., 2011a).

A sodium content of 0.05 - 0.2 M (salinity of 0.5 - 2 %) with NaCl as the most abundant dissolved component followed by about half the amount of $NaHCO_3$ and/or Na_2CO_3 and a pH of 8.5 - 12 are inferred for the ocean from CDA and INMS measurements (Postberg et al., 2009a; Postberg et al., 2011a; Glein et al., 2015; Hsu et al., 2015; Postberg et al., 2018b; Glein et al., 2018; Glein and Waite, 2020). Enceladus' global subsurface ocean (Figure 3.1) has a thickness of $\sim$ 20 km, ranging from 30 to 50 km in depth (McKinnon, 2015; Thomas et al., 2016; Hemingway et al., 2018). According to an ocean-ice shell model for Enceladus (Cadek et al., 2016), the ocean's mean density is $\sim$ 1030 kg/m^3 and the ocean amounts to $\sim$ 40 % of the total satellite volume. The same model predicts a core radius of 180 - 185 km and an ice shell thickness in the SPT of 2 - 5 km. The average ice shell thickness over the entire moon is 20 - 30 km (Hemingway et al., 2018). The relatively low core density of 2.4 g/cm^3 (Iess et al., 2014) suggests a predominance of phyllosilicates and a high porosity in a fluffy core (Roberts, 2015). Interior models of Enceladus also work best with a porous core and demonstrate that tidal heating resulting from interactions with Saturn and Dione produces enough heat to maintain the ocean (Choblet et al., 2017; Liao et al., 2020).

The salty Type 3 ice grains (Postberg et al., 2009a; Postberg et al., 2011a), which are thought to represent frozen ocean spray, together with gravity field measurements (Iess et al., 2014) and rotational state measurements (Thomas et al., 2016) strongly indicate that the ocean interacts with the moon's rocky core. In fact, the conditions at the rock-water interface of Enceladus might be similar to those found in alkaline hydrothermal vent systems on Earth (Hsu et al., 2015; Sekine et al., 2015; Tobie, 2015; Waite et al., 2017), for example to those in the Lost City hydrothermal field in the mid-Atlantic ocean (Kelley et al., 2001; Kelley, 2005). Figure 3.2 shows a cross section of a typical hydrothermal vent within the Lost City field. The alkaline hydrothermal vent fluids have temperatures from $60 - 90$°C and a pH of 9 - 11 (Dalai et al., 2016). Chemical reactions between seawater and the mantle peridotite that lies under the oceanic crust drive the hydrothermal activity. Silica as well as H_2 and/or CH_4 are released during these serpentinization reactions (Vance and Melwani Daswani, 2020). Another study on the Von Damm hydrothermal field, which is located on the flanks of the Mid-Cayman Spreading Center (Hodgkinson et al., 2015), indicates that CH_4 is also formed in H_2-rich inclusions (McDermott et al., 2015). H_2 is a likely "fuel" molecule for a methanogenic ecosystem in an ocean (Waite et al., 2017; McKay et al., 2018). Various hydrocarbons and microbial communities can be found in vent fluids from both the Lost City (Konn et al., 2009; Brazelton et al., 2006) and Von Damm (McDermott et al., 2015) fields. Ongoing hydrothermal activity on the ocean-core interface of Enceladus, similar to the Lost City and Von Damm fields, was ultimately concluded from analyses of silica nano grains found in Saturn's E ring (Hsu et al., 2015). These findings are supported by laboratory experiments, in which Enceladus-like hydrothermal reactions were simulated (Sekine et al., 2015). Moreover, the detection of a relatively high

amount (0.4 - 1.4 % by volume) of molecular hydrogen in Enceladus' plume gas (Waite et al., 2017), together with laboratory evidence that complex organic molecules can be derived in Enceladus (Angelis et al., 2020), strengthens the hypothesis of ongoing hydrothermal activity that produces a variety of organic compounds.

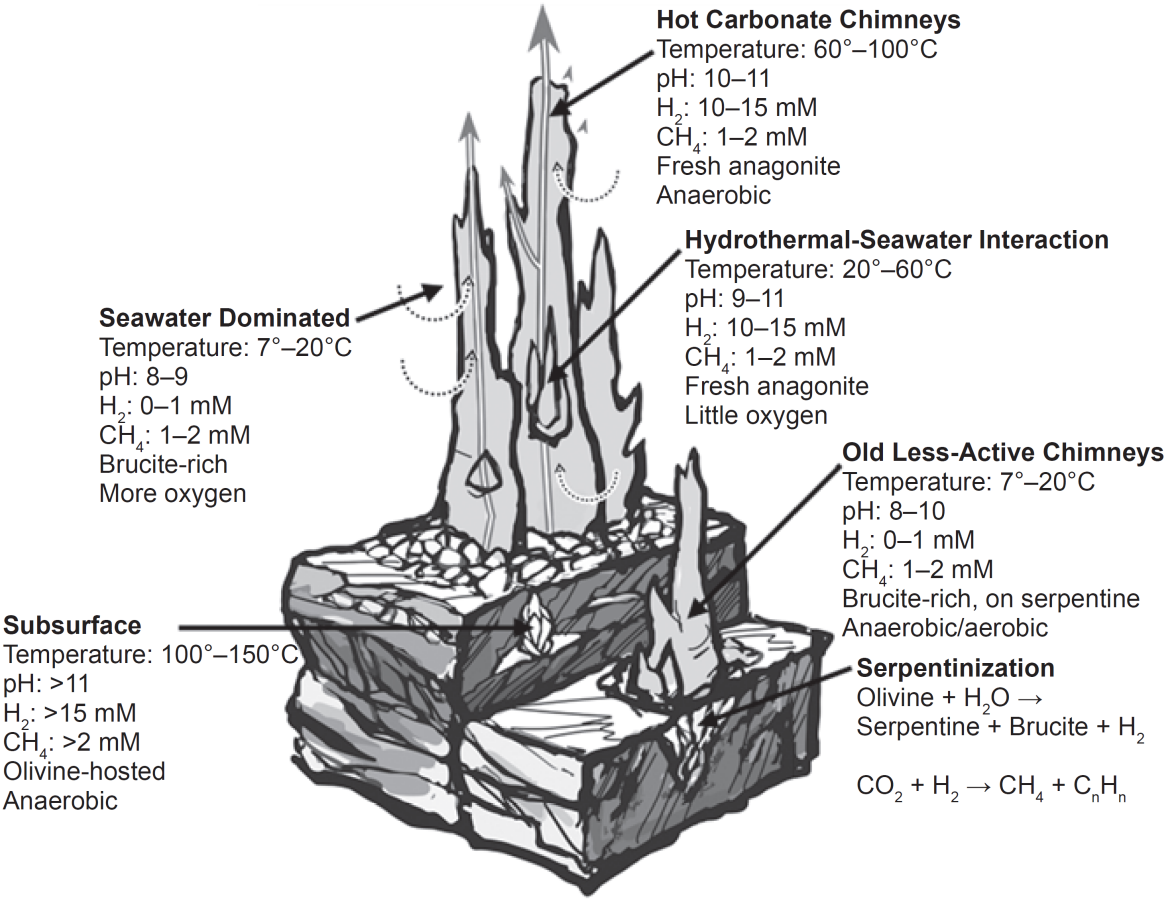

Figure 3.2: *Cross section of geological, geochemical and biological zonation within the Lost City hydrothermal vents. The vents are several tens of meters in height. The combination of H_2 and CH_4 with oxidants in seawater help to support a diverse array of microbial populations within the Lost City field (figure taken from McKay et al., 2018; adapted from Brazelton et al., 2006).*

Noting that there are several other theories about the emergence of life on Earth (Crick and Orgel, 1973; Orgel, 1998; Luisi, 2016; Camprubí et al., 2019; Damer and Deamer, 2020; Preiner et al., 2020), alkaline hydrothermal vent systems are a high-rated candidate for representing the birthplace of life on early Earth (Baross and Hoffman, 1985; Martin et al., 2008). Various organics, for example carboxylic acids, and even RNA have been successfully produced under simulated hydrothermal conditions (Rushdi and Simoneit, 2005; McCollom and Seewald, 2006; Fu et al., 2007; Burcar et al., 2015).

An energy source that produces enough heat to maintain a liquid subsurface ocean, in combination with the recent findings of organic chemistry and ongoing hydrothermal activity, makes Enceladus one of the prime targets for future space missions aiming to search for extraterrestrial life.

3.2 Enceladus Life Finder (ELF) - A future mission concept

Enceladus, with its subsurface ocean in contact with a rocky core, is particularly interesting for the search for life beyond Earth because the Saturnian moon fulfills the three widely accepted requirements for life (as we know it) to originate: Liquid water, an energy source, and organic chemistry (see section 3.1). The plume provides a great opportunity for spacecraft to sample the ejected material and explore the moon's interior in flybys as has been demonstrated by the Cassini spacecraft (see section 2.1). Although Cassini's two mass spectrometers (as well as other instruments) made many discoveries that indicate Enceladus is a promising candidate in which life may originate, the instruments' insufficient mass resolutions and mass ranges do not allow for unambiguous analyses of complex organic molecules and ions. Cassini could also not provide detailed information about the ocean environment (e.g. redox state, available free energy, and exact pH).

The proposed Enceladus Life Finder (ELF) Discovery Mission was designed to further constrain the moon's habitability with more sophisticated instruments by investigating the ejected plume material and thereby the moon's interior in more detail (Figure 3.3). The spacecraft was a solar-powered Saturn orbiter that would have conducted eight science flybys of Enceladus' plume, four for the baseline science and four for follow-up measurements, over three years - plus two more contingency flybys. The orbiter would have flown over all the Tiger Stripes with the closest plume traversal at 50 km altitude (Lunine et al., 2015a; Lunine et al., 2015b; Reh et al., 2016).

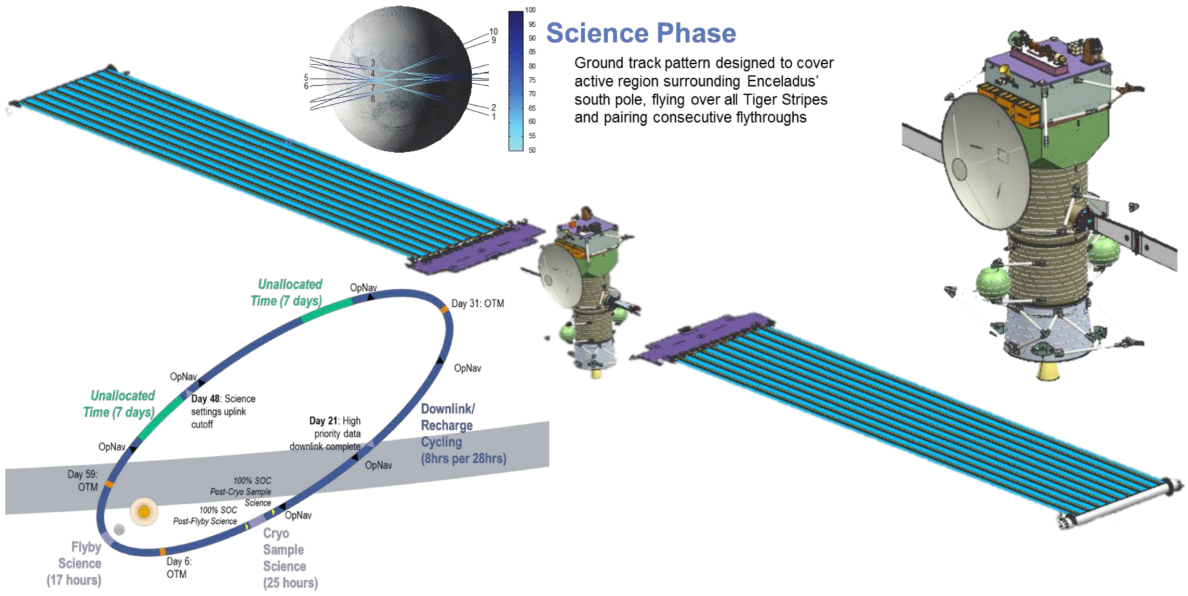

Figure 3.3: *ELF mission design. The orbiter would have performed ten flybys of Enceladus at ∼ 50 km altitude (shown above the spacecraft). The proposed orbit around Saturn is shown on the bottom left (figure taken from Reh et al., 2016).*

The mission design was tightly focused to perform the planned flybys and downlink the data. A 62-day orbit between plume encounters would

have allowed science acquisition, data transmission and battery recharging. The science objectives were geared to investigate the evolution of organics on Enceladus, the moon's habitability and eventually to look for life (Lunine et al., 2015a; Lunine et al., 2015b; Reh et al., 2016).

Science objective 1 - Evolution: ELF would have determined if volatiles, including organics, within Enceladus, have chemically evolved over time and if they have been thermally altered.

Science objective 2 - Habitability: The mission would have provided detailed information about the ocean environment, i.e. temperature, pH, available chemical energy, and oxidation state. ELF would have further quantified the amount of H_2 that was found by Cassini's INMS instrument (Waite et al., 2017).

Science objective 3 - Life: ELF would have investigated whether organics were produced biotically or abiotically through three universal, independent life diagnostic tests (Figure 3.4). Both amino acids and fatty acids exhibit distinct abundance patterns dependent on whether the organics were produced biotically or abiotically (Dorn et al., 2011; Davila and McKay, 2014; Georgiou and Deamer, 2014). ELF's instruments would have looked for these characteristic abundance patterns of amino acids (test 1) and fatty acids (test 2) as described in detail in chapters 9 and 10. The hydrogen and carbon isotope ratios would have been determined (test 3) together with the abundance of methane relative to other alkanes to assess whether the measured values fall in the range for biological processes.

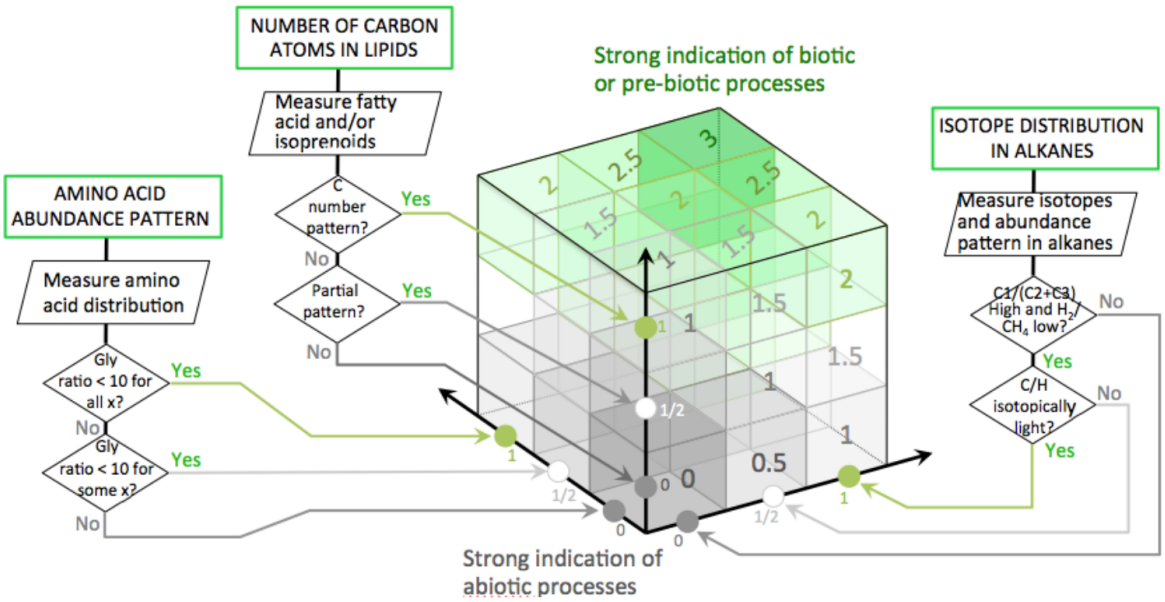

Figure 3.4: *ELF's three independent tests for life to address science objective 3. Positive results for all three tests would have strongly indicated ongoing biotic chemistry on Enceladus. The two tests on the left are the most relevant for this thesis (figure taken from Reh et al., 2016).*

The proposed ELF mission would have built on the heritage of the Cassini orbiter with two Time-of-Flight mass spectrometers in the payload:

MAss Spectrometer for Planetary EXploration (MASPEX): The instrument would have measured species with masses up to 1000 u with a mass resolution, m/Δm, exceeding 25,000, and a sensitivity of ∼ 1 ppt (Figure 3.5A). In addition to analyses of collected plume gases, the instrument would have concentrated species in a cryotrap for post-flyby analyses (Brockwell et al., 2016). The instrument was proposed for several missions, including ELF, and is already being built for the upcoming Europa Clipper mission (see section 4.2).

ENceladus Ice Analyzer (ENIA): Former ENceladus Icy Jet Analyzer (ENIJA), subsequently renamed to ENIA would have been a reflectron-type mass spectrometer with a small aperture and optimized for the high dust densities in the Enceladean plume. It was based on the principle of impact ionization (similar to the CDA and the SUDA; Figure 3.5B). The instrument would have been sensitive to individual micron- and sub-micron sized dust and ice grains impacting onto an iridium target. ENIA would have collected a complete data sequence of cationic or anionic species of masses up to 5000 u with a mass resolution of m/Δm >2000 and a sensitivity down to 100 ppt (Srama et al., 2015a; Srama et al., 2015b). The proposed ELF flyby speeds of 4 - 5 km/s have been found to be optimal for the detection of delicate biomolecules and the discrimination between characteristic biotic and abiotic signatures in the mass spectra as outlined in science objective 3 (see chapters 9 and 10). As for MASPEX, dust detectors have also been proposed for other missions, and indeed incorporated into the Europa Clipper mission (see section 4.2).

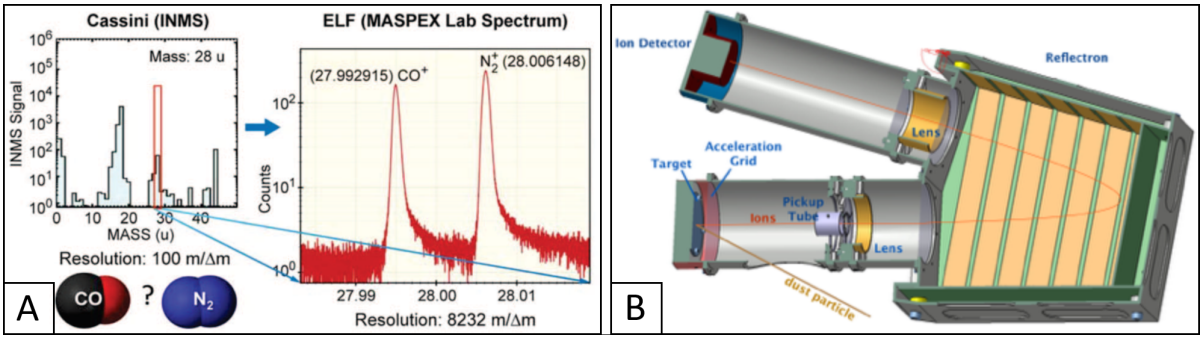

Figure 3.5: *A: Mass spectrum from Cassini's INMS instrument on the left (adapted from Reh et al., 2016). The peak at m/z 28 could represent N_2, CO, C_2H_4, or CH_2N. ELF's MASPEX instrument with its increased mass resolution (on the right) resolves all the species (C_2H_4 would be off the figure to the right). B: Design of ELF's ENIA instrument (adapted from Srama et al., 2015a). An impacting dust/ice grain hits the target plate. Created cations or anions are accelerated through the pickup tube, reflected by the reflectron and subsequently detected.*

4 Jupiter's moon Europa and the Europa Clipper mission

4.1 Europa - another active ocean world?

Europa was discovered together with three other moons - Io, Ganymede, and Callisto - in January 1610 by Galileo Galilei, when he observed Jupiter through a telescope with a magnifying capability of 20 × (Galilei, 1610). Galilei named the four observed objects as the *Medicean Stars* as they appeared to form a straight line of stars near Jupiter. As the first objects found to orbit a planet other than the Earth, the *Medicean Stars* are today known as the four Galilean moons.

With a diameter of 3124 km (Seidelmann et al., 2007), slightly smaller than Earth's moon (diameter of 3474 km), Europa is the smallest of the Galilean moons. The Jovian moon has a mean density of about 3.0 g/cm^3 and probably consists of a metallic rocky core surrounded by a silicate mantle (Anderson et al., 1998; Gomez Casajus et al., 2020) that is in contact with a global liquid water ocean under an ice crust (Carr et al., 1998; Kivelson et al., 2000; Zimmer et al., 2000; Schubert et al., 2009). The outer shell (= ice and liquid water) has a thickness of 80 - 130 km (Anderson et al., 1998), including a 15 - 30 km thick ice shell on top (Tobie et al., 2003; Billings and Kattenhorn, 2005). Another more recent study suggests the top ice layer to be less than 15 km thick (Hand and Chyba, 2007). Figure 4.1 shows a view of the likely internal structure of Europa.

Magnetometer measurements from the Galileo spacecraft revealed that Europa has an electrically conducting layer lying within 200 km of the surface, with an electric conductivity comparable to or less than that of seawater on Earth (Zimmer et al., 2000). This is strong evidence for a salty subsurface ocean because unsalted water could not account for the measured magnitude of the induced magnetic field and electrical currents in the metallic core are simply too far below the surface. The salt (probably NaCl and/or $MgSO_4$) concentration in the ocean might be even near saturation (Hand and Chyba, 2007). According to a recent model, the ocean probably contains volatiles (mainly H_2O) and its overall composition varies with depth, with the sulfur to chloride ratio (S/Cl) increasing with depth (Melwani Daswani and Vance, 2020). Other Galileo observations indicate that the metallic core makes up between 13 and 45 % of the moon's radius, dependent on the core's composition and the thickness of the water ice-liquid outer shell (Sohl et al., 2002).

Surface temperatures on Europa range between 80 and 130 K (Spencer et al., 1999). The most obvious surface features are cracks and lineaments that are visible on the global scale (Figure 4.2). The remarkably young (30 - 90 Ma) surface (Zahnle et al., 2003; Doggett et al., 2009), reflecting only a small fraction of Europa's history, probably undergoes episodic, sporadic or steady-state resurfacing (Pappalardo et al., 1999), with evidence strongest for sporadic resurfacing (Ojakangas and Stevenson, 1986; Hussmann and Spohn, 2004). Possibly ongoing subduction (Kattenhorn and Prockter, 2014) suggests Europa is the only Solar System body other

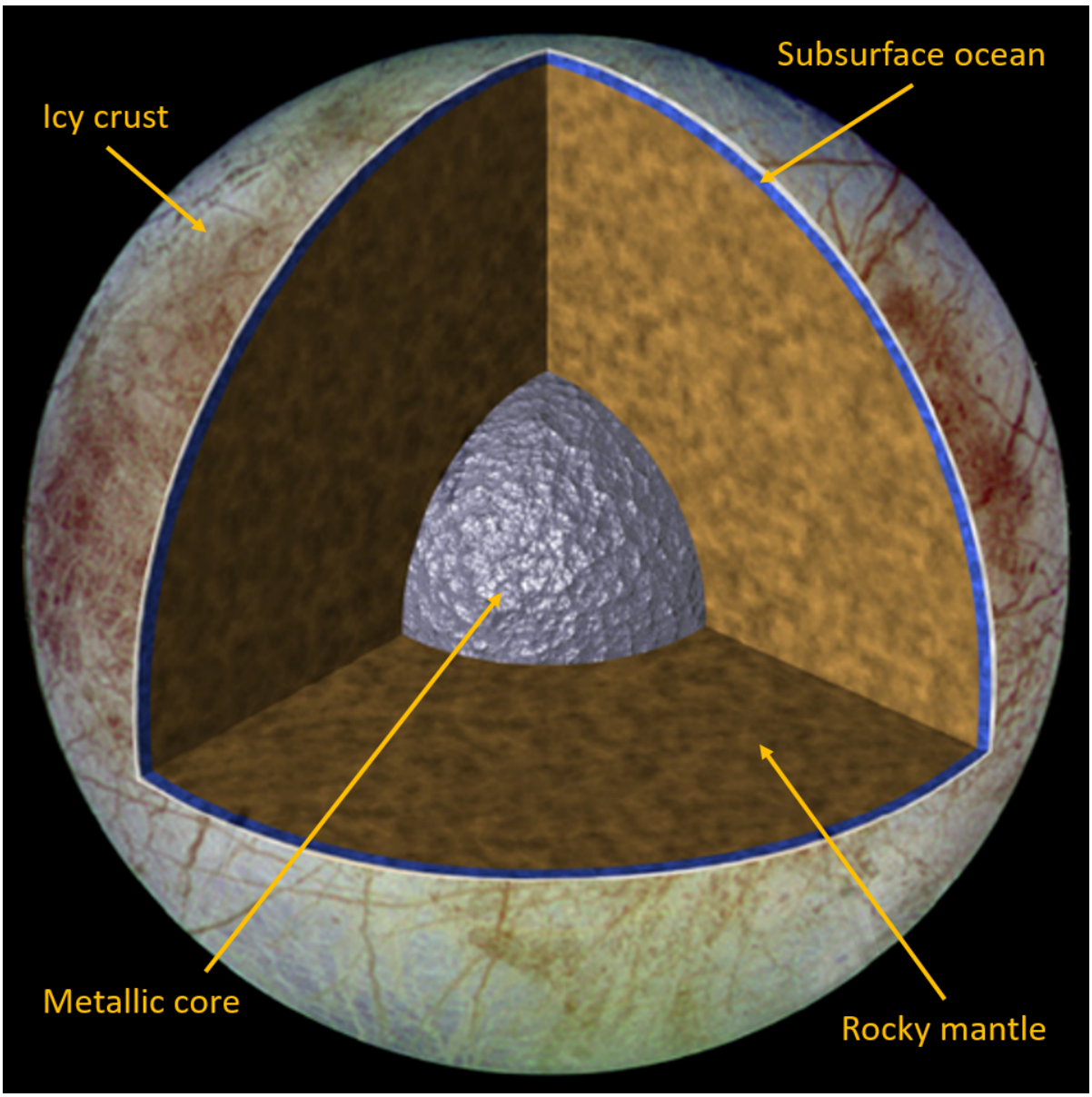

Figure 4.1: *View of the possible internal structure of Europa (approximately to scale). The surface is an image obtained by the Galileo spacecraft in 1996. The interior structure is inferred from magnetic field and gravity measurements from Galileo. It is currently unknown whether Europa has a metallic core (Image credit: NASA/JPL-Caltech).*

than the Earth to exhibit a system of plate tectonics. So-called Chaos regions make up about one quarter of Europa's icy surface (Riley et al., 2000; Collins and Nimmo, 2009). These chaotic regions consist of tilted plates, depressions, blocks, and discontinuous ridges in a disorganized, lumpy matrix (Figure 4.2, yellow circle). Although their formation process is uncertain, these regions probably contribute to downward transport of surface material (Collins and Nimmo, 2009; Schmidt et al., 2011).

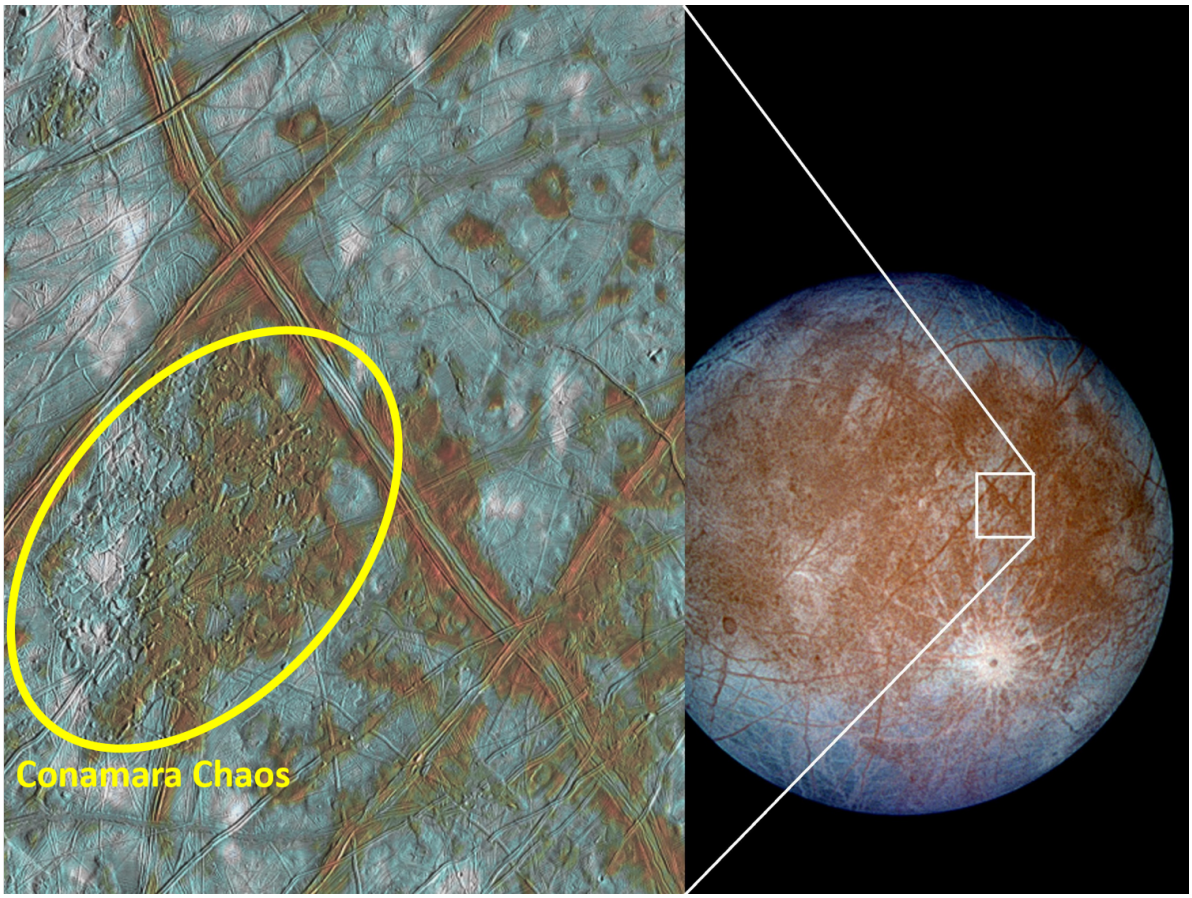

Figure 4.2: *False color image of Europa. The individual images were taken by the Galileo spacecraft from September 1996 to February 1997. The most obvious surface features on Europa are cracks and lineaments suggestive of resurfacing processes (left). One of the so far best studied regions on Europa, Conamara Chaos, is circled yellow. Blueish tones show the icy plains on Europa (right) containing coarse-grained ice (dark blue) and fine-grained ice (light blue; Image credit: NASA/JPL-Caltech/University of Arizona).*

The resurfacing processes (Figure 4.2) imply material exchange from surface to subsurface and vice versa. This material exchange (Soderlund et al., 2020) is of great interest for Europa's astrobiological exploration. Intense radiation from Jupiter converts water and impurities on the surface and shallow subsurface into oxidants whereas seawater, which is actively cycling through rocky material on Europa's seafloor, is expected to be chemically reducing (Hand et al., 2007; Hand et al., 2009; Vance et al., 2016). If mixing between the surface oxidants and the reduced ocean water occurs, there is probably a reduction-oxidation (redox) potential produced within Europa - all known life forms on Earth rely on such redox potentials to extract chemical energy from the environment, enabling cellular maintenance, metabolism, and reproduction

(Nealson, 1997; Russell and Hall, 1997; Halliwell, 2006; Johnson et al., 2008; Howell and Pappalardo, 2020). Indeed, according to a recent model, Europa's ocean exhibits strong transient vertical convection and eddies (Ashkenazy and Tziperman, 2020). Exchange of organic material from the subsurface to the surface (Hand et al., 2009) would also enable a potential future Europa lander (Phillips et al., 2019) to sample organic material accumulated in the shallow subsurface, where potential biomolecules are likely to be preserved (Nordheim et al., 2018).[1]

NaCl and MgCl salts on Europa's surface are believed to be endogenous (Ligier et al., 2016; Trumbo et al., 2019). Europa's seafloor rocks could contain carbonates, phyllosilicates, Fe sulfides, Ca sulfates, and organic compounds (Zolotov and Kargel, 2009). However, chemical information is sparse at present and relies mostly on reasonable assumptions and models.

Europa is, along with Enceladus, Titan, and Mars, among the likeliest bodies in the Solar System to be able to support biological activity (Hand et al., 2009; Shapiro and Schulze-Makuch, 2009). Ground based observations as well as spacecraft data provide strong evidence for an episodically or sporadically active plume on Europa (Roth et al., 2014; Sparks et al., 2016; Sparks et al., 2017; Jia et al., 2018; Huybrighs et al., 2020; Paganini et al., 2020). However, other observations indicate that there is very limited geological activity on Europa (Shemansky et al., 2014). Because of the moon's gravity, a plume on Europa would have a necessarily smaller size than the Enceladean plume, and sampling this putative plume with orbiting spacecraft therefore requires low altitude (<100 km) flybys (Quick et al., 2013; Southworth et al., 2015).

There are numerous existing mission concepts aiming to fly, orbit or land on Europa (Greeley et al., 2009; McEwen et al., 2019; Dachwald et al., 2020; Moore et al., 2020), from which one has been selected to fly and investigate the Jovian moon - the Europa Clipper mission (see section 4.2). With a scheduled launch date in 2024, Europa Clipper will shed light on the Europan plume, the moon's habitability and many other open questions. The spacecraft will have the SUrface Dust Analyzer (SUDA) instrument on-board, an impact ionization mass spectrometer which is more sophisticated than Cassini's CDA (see section 4.3).

4.2 The Europa-Clipper mission

Returning to Europa (Figure 4.3) is the only way to gather crucial data and further investigate the moon's potential plume, its habitability, surface, interior, and vicinity.

A flagship mission managed by NASA's Jet Propulsion Laboratory, the upcoming Europa Clipper spacecraft (Figure 4.4), a Jupiter orbiter, will be flying past Europa about 45 times over its proposed 3.5-year mission. It is important to note that survival of the spacecraft and its in-

[1] Although Europa's surface is strongly affected by Jupiter's harsh radiation, potential biomolecules are likely to be preserved at depths > 1 cm in mid- to high-latitude regions (Nordheim et al., 2018).

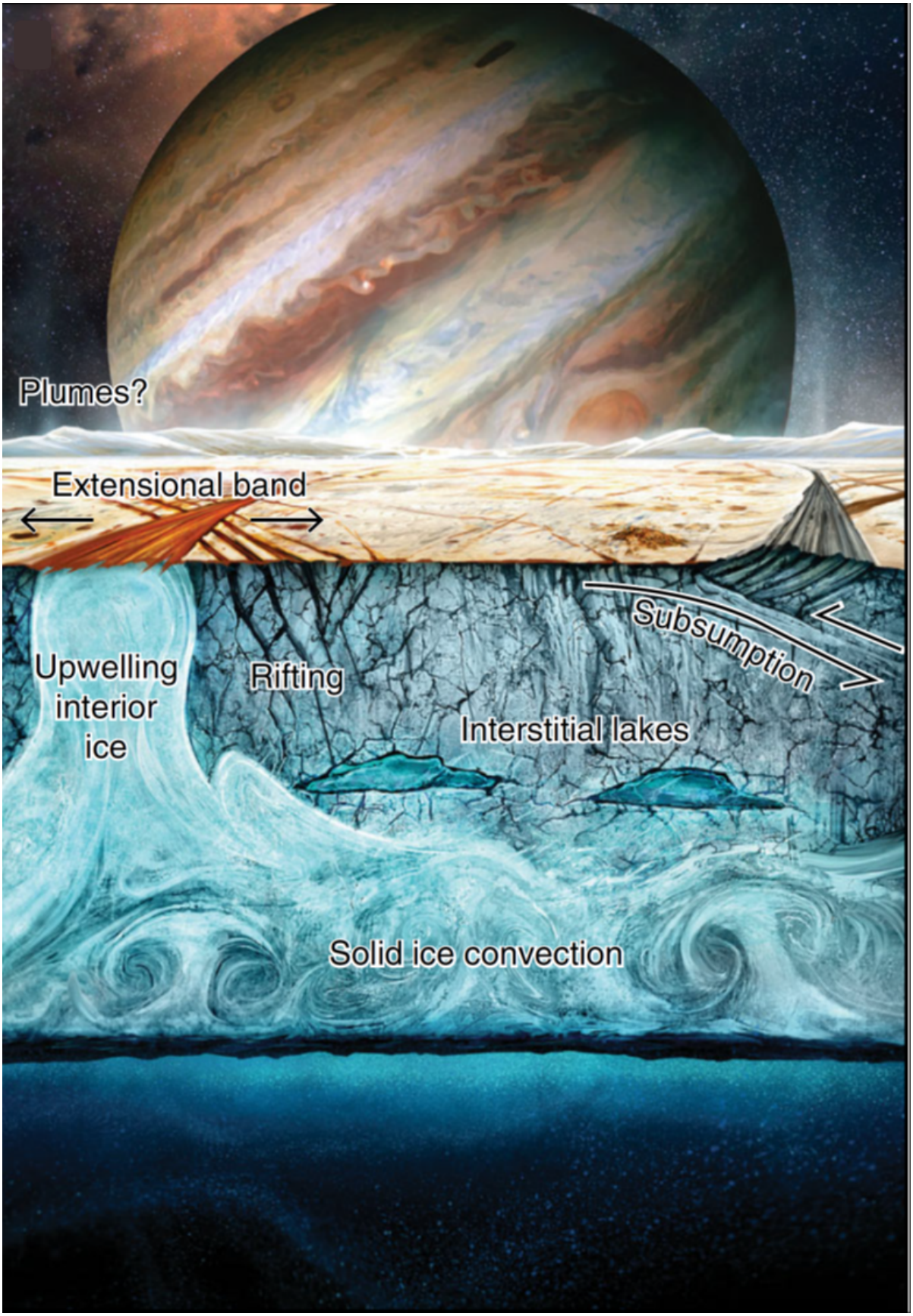

Figure 4.3: *Tectonic and geodynamic processes in Europa's ice shell. These processes may play a role in Europa's habitability (artistic impression by Jeff Nentrup; figure taken from Howell and Pappalardo, 2020).*

struments is expected to be well beyond the planned mission duration.[1] With a payload specifically designed to address Europa's habitability, the launch of the spacecraft is scheduled for 2024, probably aboard a Delta IV rocket. The transit time to the Jovian System is about 6.5 years, using several gravity assists; However, a more expensive direct trajectory without the need for gravity assists, taking less than 3 years, achieved via a Space Launch System (SLS) rocket is also being evaluated. The Europa Clipper spacecraft will be around 6 m height and 22 m wide. It will weigh about 6000 kg including fuel at liftoff (NASA(url2), 2020).

Each of the $\sim$ 45 moon flybys will have a closest approach between 25 and 2700 km from Europa's surface, with most of them being below 100 km. After each approach the spacecraft will transmit its trove of data back to Earth. A key feature of the mission concept is that the spacecraft uses gravitational perturbations from Europa as well as from Ganymede and Callisto to deflect its trajectory, allowing the spacecraft to return to a different closest approach point with each flyby (Howell and Pappalardo, 2020). The flyby paths will therefore build an intersecting web so that nearly the entire moon will be studied from close-up.

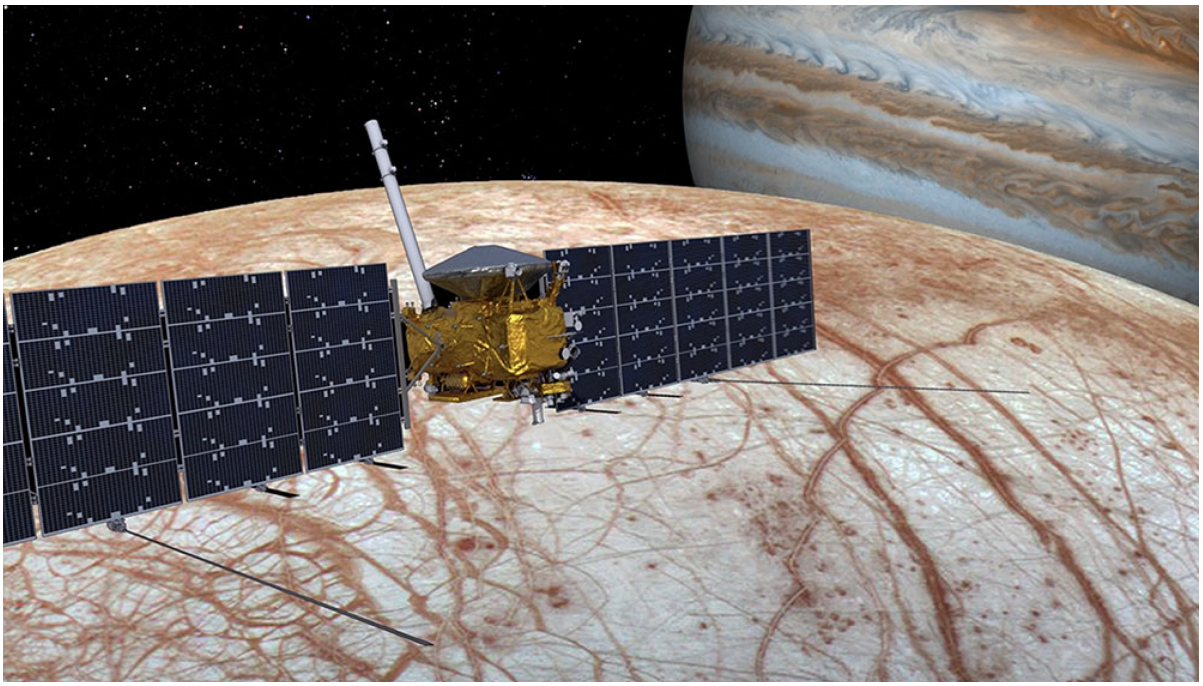

Figure 4.4: *Computer-aided design view of the Europa Clipper spacecraft. Two solar panels extend outward from the spacecraft bus. The silver dome is the primary communication antenna (figure taken from Howell and Pappalardo, 2020).*

The science goal of the mission is to explore Europa's habitability. There are three key science objectives within the scope of the science goal (Pappalardo et al., 2017; Howell and Pappalardo, 2020):

I. Europa's ice shell and subsurface ocean: Characterizing the distribution of Europa's subsurface water, the structure of the ice shell,

[1]The mission lifetime is mostly limited by radiation, but the radiation tolerance of the spacecraft is designed to be twice as much as the expected radiation dose (Andersen et al., 2020). The spacecraft's electronics and instruments will be covered by a thick-walled vault made of aluminum and titanium that acts as a radiation shield.

the ocean's salinity and thickness, the ice shell thickness and heat flow dynamics, and investigating the material exchange among the ocean, ice shell, surface and atmosphere.

II. Composition and chemistry: Characterizing the composition and chemistry of endogenic materials on the surface and in the atmosphere, including a potential plume, determining the role of the plasma and radiation environment, and investigating chemical pathways in the subsurface ocean.

III. Geology and formation of surface features: Localizing sites of most recent geological activity, including a potential plume, characterizing sites of high science interest, and studying the formation and characteristics of landforms, for example erosion and deposition processes.

To address the science objectives, Europa Clipper will be equipped with five remote sensing instruments and four in situ instruments (Pappalardo et al., 2017):

Europa Ultraviolet Spectrograph (Europa-UVS): Investigates the composition, chemistry, and structure of Europa's atmosphere, its surface and any potential plume at ultraviolet wavelengths.

Europa Imaging System (EIS): Consists of a narrow- and a wide-angle camera to map Europa globally at a resolution of 0.5 m/pixel.

Mapping Imaging Spectrometer for Europa (MISE): Operating at wavelengths of 0.8 - 5.9 µm, the instrument examines the inventory and distribution of surface compounds.

Europa Thermal Imaging System (E-THEMIS): Thermal infrared instrument with a resolution of 250 m/pixel to detect thermal hotspots on Europa and characterize the moon's surface and any potential plume.

Radar for Europa Assessment and Sounding: Ocean to Near-surface (REASON): Maps the crust vertically and searches for subsurface water.

Magnetometer: Measures magnetic fields and investigates the subsurface ocean[1]

Plasma Instrument for Magnetic Sounding (PIMS): Investigates the plasma environment and studies the material release from the surface to the atmosphere.

MAss Spectrometer for Planetary Exploration (MASPEX): Analyzes neutral gases and identifies volatiles and key organic compounds in Europa's exosphere and any potential plume. This instrument was also proposed for the Enceladus Life Finder mission (see section 3.2).

[1]NASA decided to replace the planned ICEMAG magnetometer instrument with a less complex magnetometer because of extensive cost overruns.

SUrface Dust Analyzer (SUDA): Maps Europa's surface by analyzing surface ejecta from micrometeoroid impacts and investigates the subsurface ocean by analyzing potentially ejected plume particles. More information about the SUDA instrument can be found in section 4.3. This thesis prepares for the in situ SUDA analyses of surface ejecta (most notably those from fresh plume deposits) and ice particles in any potential Europan plume.

The Europa Clipper mission also complements other missions. Two Europa flybys by ESA's JUpiter ICy moons Explorer (JUICE) spacecraft (Grasset et al., 2013) are planned. Europa Clipper will scout and characterize the moon's surface for potential landing sites for a future Europa lander mission (Phillips et al., 2019), which might follow up on Europa Clipper's discoveries.

The next decades will bring fascinating discoveries about Europa and other bodies believed to host alien oceans within our Solar System. Finding a habitable environment on Europa would greatly expand the possibilities for life beyond Earth.

4.3 The SUrface Dust Analyzer (SUDA)

The SUrface Dust Analyzer (SUDA) aboard the upcoming Europa Clipper spacecraft (see section 4.2) is a Time-of-Flight mass spectrometer utilizing the principle of impact ionization. SUDA (Figure 4.5) builds on the heritage of the Cosmic Dust Analyzer (CDA) aboard the Cassini spacecraft (see section 2.2). The instrument will determine particle properties, such as compositions, relative velocities, and masses of encountered ice/dust grains in the vicinity of Europa or other Galilean moons.

The basic idea of compositional mapping (Kempf et al., 2009; Postberg et al., 2011b; Kempf et al., 2012) is that moons without an atmosphere are shrouded in tenuous clouds of particles ejected from their surfaces by micrometeoroid bombardment (Krüger et al., 2000; Sremčević et al., 2005; Miljković et al., 2012). A typical interplanetary micrometeoroid impact (10^{-8} kg) on a Jovian moon produces a large number of particles with a total mass in the order of a few thousand times that of the impactor (Koschny and Grün, 2001). The ejecta particles can reach altitudes of hundreds of kilometers. Most of the particles that move on ballistic trajectories re-collide with the moon and, thus, create an almost isotropic dust exosphere around the moon (Krivov et al., 2003; Sremčević et al., 2005). These dust particles can be analyzed in spacecraft flybys.

SUDA's entrance grids detect ejecta particles via the charges they carry, from which, coupled with information of the grid layout, impact velocities can be derived. By knowing the particle velocity, spacecraft trajectory and instrument pointing, SUDA's in situ chemical measurements of individual particles can be linked to their sites of origin on Europa's surface. In this way, as these particles are direct samples from the icy surface, SUDA will map Europa's surface by characterizing the particle population in the moon's thin exosphere. In addition to compositional mapping of Europa's surface, the instrument may directly measure freshly ejected material in Europa's potential plume and investigate the

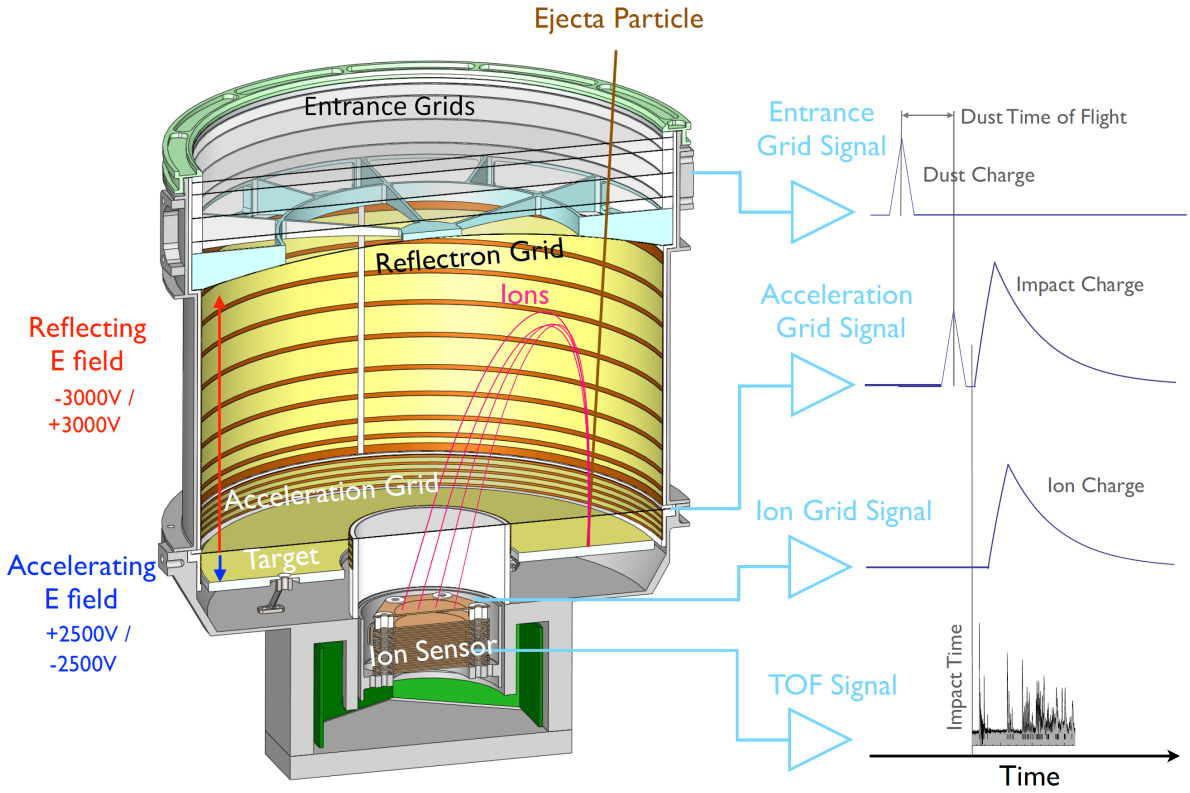

Figure 4.5: *Functional principle of the SUrface Dust Analyzer (SUDA). An incoming ejecta particle enters the aperture through the entrance grids and hits the iridium target. The created cations or anions are accelerated and reflected towards the ion sensor. Impact ionization Time-of-Flight mass spectra (Figure 4.6) are then generated (figure adapted from Kempf et al., 2014).*

plasma environment of Europa. The instrument will also identify particles emitted by Io's volcanoes as these particles, consisting of sodium and potassium chlorides and sulfates, make up the majority of Jovian stream particles (Fegley Jr and Zolotov, 2000; Graps et al., 2000; Postberg et al., 2006; Hillier et al., 2018).

SUDA (Kempf et al., 2014; Kempf et al., 2019) is a compact (26.8 cm × 25.0 cm × 17.1 cm) instrument with a weight of about 14 kg (including radiation shielding) and a sensitive area of 225 cm^2. The instrument has a dual polarity capability as it is sensitive to cations and anions with masses of up to 500 u. The incoming particles enter the aperture through the entrance grids, hit the iridium (Ir) target, which is held at ± 2.5 kV, and become reflected towards the ion sensor (Figure 4.5). Ir is chemically inert and has a double mass peak at m/z 191 and m/z 193, which should be easily distinguishable from mass peaks of the ice or dust material. Unlike Cassini's linear ToF-MS (Cameron and Eggers Jr, 1948; Opsal et al., 1985) CDA (section 2.2), Europa Clipper's SUDA is a reflectron ToF-MS (Mamyrin et al., 1973; Mamyrin, 2001). The reflectron diminishes the influence of the ions' kinetic energy distribution acquired upon impact on their times of flight, as well as provides a longer path length, and thus significantly increases an instrument's mass resolution, which is 150 - 300 m/Δm for SUDA. Performance parameters of SUDA compared to CDA can be found in Table 4.1. As with the CDA, recording of the impact ionization mass spectra (Figure 4.6) is triggered by either the impact-generated charge pulse or ions arriving at the multiplier.

Table 4.1: Comparison of performance parameters of SUDA with those of CDA.

Parameter	**CDA**	**SUDA**
Time-of-Flight type	linear	reflectron
Mass resolution [m/Δm]	20-50	150-300
Detectable mass range	up to 220 u	up to 500 u
Polarity capability	cations	cations and anions
Entrance grids	no velocity sensor	velocity sensor

Near closest approach, during each flyby, SUDA will be capable of detecting tens of ejected surface particles per second with sizes between ∼ 200 nm and 10 µm (Kempf et al., 2014), each particle likely to contain a wide variety of organic and/or inorganic compounds. The instrument will be capable of detecting trace amounts (< 1 ppm) of salts and organics (see chapter 9) and even discriminate between abiotic and biotic chemistry in the Europan subsurface ocean (see chapter 10) by analyzing any encountered plume material during Europa Clipper's low velocity (4 - 4.5 km/s) flybys, assuming that the plume material is formed from subsurface ocean water. SUDA is currently being manufactured and instrumentation tests are ongoing (S. Kempf, pers. comm., 2020[1]).

[1]Personal communication on October 21, 2020.

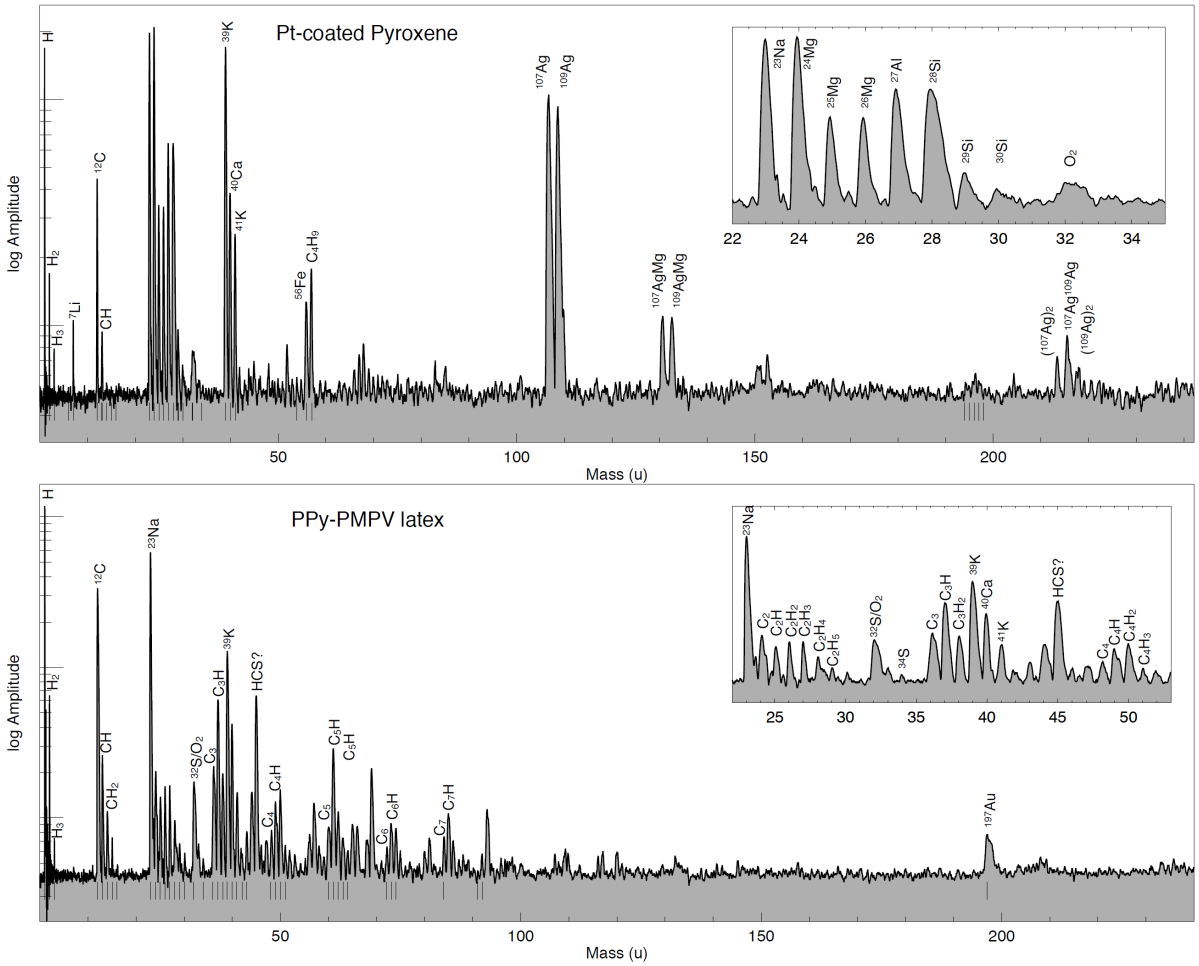

Figure 4.6: *Example mass spectra of a pyroxene particle impacted on a silver target and a latex particle impacted on a gold target recorded with an early laboratory model of the SUrface Dust Analyzer (SUDA). The increased mass resolution compared to Cosmic Dust Analyzer mass spectra (Figure 7.3) is obvious (figure taken from Kempf et al., 2014).*

5 The significance of laser induced analogue experiments

Established in the mid 1980s (Karas et al., 1985; Karas et al., 1987), Matrix-Assisted Laser Desorption and Ionization (MALDI) is a soft ionization method that is used to ionize delicate organic molecules with minimal fragmentation (Figure 5.1). MALDI is a three step process: I. The analyte is mixed with a suitable matrix and applied to a metal plate. II. A pulsed laser irradiates the solid sample creating cations, anions, electrons, and neutral molecules. III. The cations and anions can be accelerated and analyzed with a commercial mass spectrometer.

More recently, it has been shown that not only solid but also liquid matrices are well suited to the soft ionization of organic molecules (Kleinekofort et al., 1996a; Kleinekofort et al., 1996b; Wattenberg et al., 1999). Instead of mounting a solid sample onto a metal plate, the liquid sample is injected into a vacuum and hit by the pulsed laser. This technique is known as Free Liquid Matrix Assisted Laser Desorption and Ionization (FL-MALDI) or Laser Induced Liquid Beam/Bead Ion Desorption (LILBID). In this thesis, 'LILBID' has been used throughout. Detailed information about the LILBID setup and the LILBID ionization mechanism can be found in chapters 7 and 8 and in the literature (Charvat and Abel, 2007; Wiederschein, 2009; Beinsen, 2011; Wiederschein et al., 2015; Stolz, 2016).

MALDI and LILBID have found numerous applications in organic biochemistry for ionizing large macromolecules and identifying proteins (Morgner et al., 2006; Morgner et al., 2007; Peetz et al., 2018). The techniques are also used in medicine in the diagnoses of diseases (Patel, 2015; Sim et al., 2015), especially in pancreatic cancer research (Grüner et al., 2012; Padoan et al., 2013; Zhong et al., 2015). Further applications are in microbiology, bacteriology, parasitology, and polymer chemistry (Seng et al., 2009; Pasch and Schrepp, 2013; Laroche et al., 2017). In recent years, the LILBID technique has been optimized for applications in space sciences to simulate impacts of µm-sized ice grains onto mass spectrometers on-board spacecraft, as demonstrated in this thesis and the literature (Postberg et al., 2009a; Postberg et al., 2018a; Beinsen, 2011; Reviol et al., 2012; Wiederschein et al., 2015; Khawaja et al., 2019).

Although micron- and submicron-sized siliceous, metallic and organic grains can be accelerated in electrostatic accelerators to relevant speeds (Burchell et al., 1999; Shu et al., 2012; Mocker et al., 2013; Fielding et al., 2015), the controlled acceleration of µm-sized ice grains to speeds above 3 km/s is technically extremely challenging.[1] Instead, the LILBID technique is employed to simulate accurately the ionization process for ice grains impacting mass spectrometers in space and with that significantly improve analyses of the recorded ice grain mass spectra (see chapters 7 and 8).

[1] Work is underway to accelerate µm-sized ice grains of ocean world relevant compositions (water ice with salt and/or organics) to velocities of up to 5 km/s (Miller et al., 2019; Cable et al., 2020).

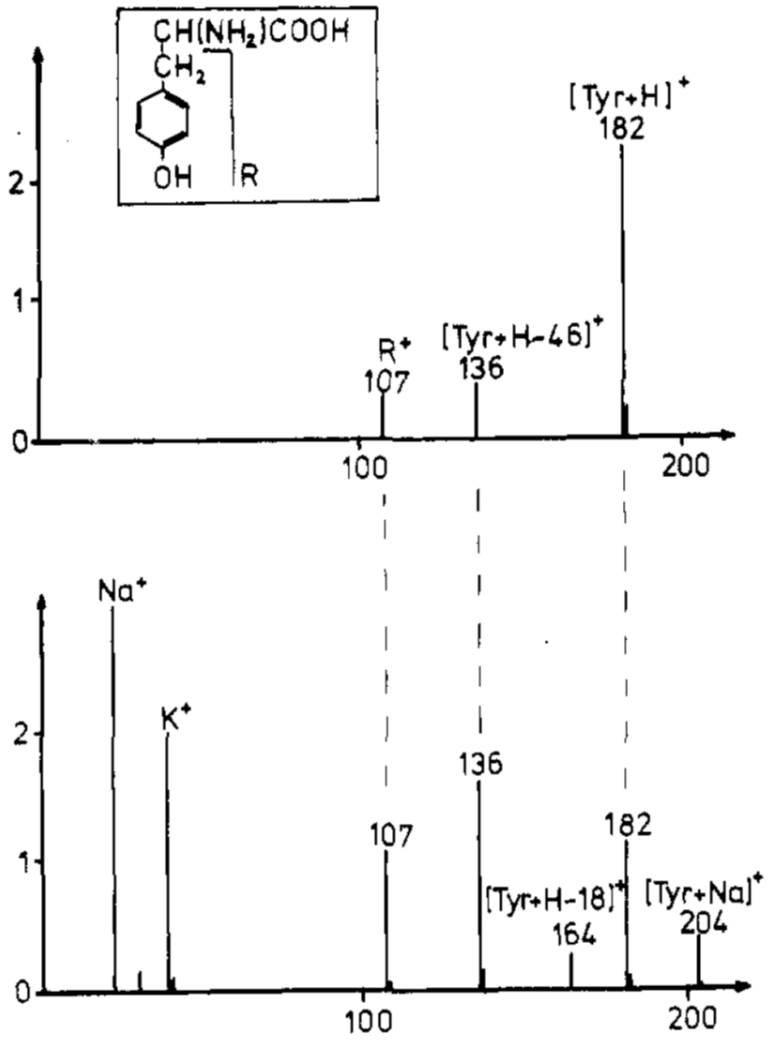

Figure 5.1: *Cationic MALDI mass spectra of tyrosine ionized with an ultraviolet laser at a low laser energy (top) and a significantly higher laser energy (bottom). Higher laser energies fragment the parent molecule, observable at m/z 182, more than lower laser energies. A cation LILBID mass spectrum of tyrosine can be found at the top of Figure B.2 (figure taken from Karas et al., 1985).*

The mass spectral appearance of an ice grain is primarily a function of grain composition and its impact speed onto the spaceborne mass spectrometer. Postberg et al. (2009a) have shown, by analyzing mass spectra of ice grains emitted by Enceladus and comparing them with LILBID mass spectra, that Enceladus' subsurface ocean is salty and contains sodium and potassium salts at concentrations of about 1 % by mass. More recent LILBID analyses have revealed that salt rich ice grains from Enceladus show significant compositional heterogeneity, with two main spectral subtypes representing chloride-rich and carbonate-rich endmember compositions (Zou et al., 2020). As well as salts, various organics have been identified in Enceladus' ocean by comparing ice grain mass spectra from space with laboratory LILBID mass spectra. Some of the detected organics appear to be complex macromolecules (Postberg et al., 2018a) whereas others are low mass with oxygen-, nitrogen-bearing and aromatic functional groups (Khawaja et al., 2019). In addition to compositional variations, different impact speeds of the ice grains, leading to variations in spectral appearance, can be mimicked with the LILBID facility as demonstrated in chapter 7 of this thesis. The successful application of LILBID to data from extraterrestrial ocean worlds makes this laboratory technique essential for the astrobiological exploration of these worlds (Taubner et al., 2020). Organics which are important for life, namely amino acids, fatty acids, and peptides, are investigated with the LILBID facility in chapters 9 and 10 of this thesis, to predict the mass spectral appearance of these delicate organic molecules in impact ionization mass spectra from space if embedded in the ice grains and encountered by spacecraft.

More than 10000 laboratory LILBID mass spectra of over 200 chemical compounds and a wide range of mimicked impact speeds are already archived in a spectral reference library as explained in chapter 8 and numerous laboratory LILBID campaigns are currently ongoing (see chapter 12). The huge variety of recorded and archived LILBID spectra can be compared with existing and future impact ionization mass spectra of ice grains recorded in space. This makes the LILBID facility invaluable for future space missions to ocean worlds in the Solar System (see sections 3.2 and 4.2).

6 Research aims and personal contribution

THIS THESIS FOCUSES on the accurate simulation of spectra produced by µm-sized ice grains impacting spaceborne mass spectrometers at different impact speeds using the laboratory LILBID facility (chapter 7) and the development of a spectral reference library containing laboratory LILBID analogue spectra (chapter 8). With the LILBID facility, bioessential organic molecules (amino acids, fatty acids, and peptides) are investigated to assess whether these molecules can potentially be detected in ice grains from habitable icy moons (chapter 9). Building on the results presented in chapter 9, the ability of a spaceborne mass spectrometer to detect and discriminate between characteristic abiotic and biotic signatures of organic molecules in encountered ice grains is examined in chapter 10.

6.1 Research framework of this thesis

The PhD candidate started his work in the research group of Planetary Sciences by Space Missions at the Institute of Earth Sciences, Ruprecht-Karls-Universität Heidelberg (Germany) in the framework of German Research Foundation (Deutsche Forschungsgemeinschaft, DFG) project PO 1015/4-1, which is an accompanying project to his PhD supervisor's (Frank Postberg) Heisenberg project PO 1015/3-1 "In-situ-Analyse von Eispartikeln im Sonnensystem: Anwendungen, Methoden, Instrumentenentwicklung". After his PhD supervisor accepted a professorship at Freie Universität Berlin, the PhD candidate, together with the complete research group, changed his affiliation in October 2018 and continued his PhD in the research group of Planetary Sciences and Remote Sensing at the Institute of Geological Sciences, Freie Universität Berlin (Germany) in the framework of European Research Council (ERC) Consolidator Grant 724908-Habitat OASIS under the European Union's Horizon 2020 research and innovation program. The two independent projects DFG PO 1015/4-1 and ERC 724908-Habitat OASIS are complementary.

DFG project PO 1015/4-1

The overall goal of DFG project PO 1015/4-1, which started in 2015, was the chemical characterization of icy moons in the Solar System by in situ mass spectrometry of ice grains ejected by these moons. To achieve this goal, the project was divided into two main sub-projects that brought together data recorded in space (sub-project 1) and laboratory analogue data (sub-project 2).

Sub-project 1 dealt with the composition of Saturn's rings and the chemistry of Enceladus' ocean using data from Cassini's CDA. The objectives of sub-project 1 were subdivided into a) geochemistry of Enceladus, b) compositional profile of dust in Saturn's E ring, and c) composition of Saturn's main rings.

Sub-project 2 was dedicated to the recording of TOF mass spectra with analogue materials. Its objective was the dispersion-ionization of water droplets of diverse composition with an IR-FL-MALDI laser.

ERC Consolidator Grant 724908-Habitat OASIS

The European Union funded Consolidator Grant 724908-Habitat OASIS, awarded to Frank Postberg in 2017, constrains the habitability of oceans on icy moons in the outer Solar System by using in situ mass spectrometry in space and preparing for future space missions using novel approaches. It is divided into two main projects.

Project 1 is a refined data analysis of the Enceladus plume material using novel techniques and is the first ever opportunity to explore in detail a potential ocean habitat outside Earth. After substantially upgrading the laboratory LILBID facility, laser-based analogue experiments are used to acquire mass spectra of a wide variety of analogue materials, enabling qualitative and quantitative analyses of inorganic and organic (including biogenic) compounds embedded in the ice grains. Numerical modelling and geochemical aqueous alteration experiments help to further constrain the habitability of Enceladus and extrapolate the results to other moons with subsurface oceans.

Project 2 leverages the laboratory capabilities from project 1 to create a comprehensive spectral reference library of analogue mass spectra in preparation for upcoming missions visiting icy ocean worlds, in particular NASA's Europa Clipper mission (see section 4.2). Having analogue measurements available early in the missions will be critical for realizing their full potential.[1]

6.2 Motivation and scientific objectives

The classical view that a planetary body needs liquid water at its surface to be habitable has been challenged by the discoveries of vast subsurface water oceans in some icy moons of Jupiter and Saturn. Saturn's moon Enceladus (see section 3.1) and Jupiter's moon Europa (see section 4.1) are considered as prime candidates for harboring alien life within their oceans because the moons' rocky cores, potential sources of heat and bioessential elements, are in direct contact with their subsurface oceans. Enceladus maintains a cryovolcanic plume formed from its subsurface ocean and a similar phenomenon is suspected to occur on Europa. The plumes enable mass spectrometers aboard spacecraft to sample the emitted material, thereby exploring the moon's geochemistry and habitability.

The Cosmic Dust Analyzer (CDA) mass spectrometer aboard the Cassini-Huygens spacecraft (see sections 2.1 and 2.2) sampled ice grains emitted by Enceladus' plume until September 2017. Detailed analysis of the data from space requires terrestrial calibration using laboratory analogue experiments (see chapter 5). Comparison of laboratory LILBID analogue spectra with those recorded in space delivered spectacular findings. Enceladus' ocean is salty and feeds Saturn's diffuse E ring (Postberg et al., 2008; Postberg et al., 2009a; Postberg et al., 2011a). Hydrothermal activity within the moon was discovered by the detection of nano-silica particles in the E ring (Hsu et al., 2015). Subsequently,

[1] More information about the Habitat-OASIS (Habitability of Oceans and Aqueous Systems on Icy Satellites) project can be found through www.cordis.europa.eu/project/id/724908 and www.geo.fu-berlin.de/en/geol/fachrichtungen/planet/projects/habitat_oasis/index.html.

organic molecules were found in the emitted ice grains, including complex organic macromolecules (Postberg et al., 2018a) and potential amino acid precursors (Khawaja et al., 2019). The presence of these organic molecules together with liquid water, which interacts with a rocky core via hydrothermal vents, make Enceladus increasingly interesting in the search for life beyond Earth.

The overall goal of this thesis is to prepare for future space missions to extraterrestrial ocean worlds and improve the analysis of ice grain mass spectra recorded in space. To achieve this goal, this thesis addresses four major science objectives:

1. Laboratory LILBID experiments have been successfully used to reproduce compositional variations in the encountered ice grains, which consist of water, salts, and/or organics. The mass spectral appearance of the ice grains is a function of not only grain composition but also the impact speeds of the grains onto a mass spectrometer's target. Ice grains with higher speeds have higher kinetic energies and the grain's molecular constituents fragment more upon impact than those in ice grains at lower speeds. Chapter 7 therefore addresses the following question:

Can variations in the mass spectral appearance caused by differing impact speeds of ice grains onto space detectors be reproduced in the laboratory using LILBID?

2. A detailed evaluation of the laboratory LILBID spectra and subsequent comparison with spectra from space was very time consuming and had to be performed manually for individual spectra. Consequently, much of the data from space have not yet been investigated. A spectral reference library containing all past and future recorded laboratory analogue spectra will help remedy this problem. Future impact ionization mass spectra of ice grains from space will be able to be investigated more time-effectively by comparing them with already existing LILBID spectra in a comprehensive library. Hence, chapter 8 describes

the development of a comprehensive spectral reference library for existing and future LILBID mass spectra.

3. Organics have been found in ice grains from Enceladus (Postberg et al., 2018a; Khawaja et al., 2019), of which potential amino acid precursors are the most relevant for this thesis. The question therefore arises whether amino acids as well as other potentially biogenic molecules, such as fatty acids and peptides, could also be detected using impact ionization. These molecules are probably undetectable by Cassini's CDA due to its insufficient performance (see section 2.2), but future instruments with superior performance, such as SUDA (section 4.3) or ENIA (section 3.2) may provide the possibility for detecting these potentially biogenic molecules in ice grains. The laboratory LILBID setup can be used to predict the mass spectral appearance of any soluble substance, if it is embedded in the

ice grains and encountered by a spacecraft-based mass spectrometer. Chapter 9 therefore considers the following question:

Will future impact ionization mass spectrometers be able to detect bioessential organic molecules, such as amino acids, fatty acids, and peptides, in ice grains emitted into space? If so, how sensitive are these instruments to these organics, i.e. what are the detection limits?

4. Amino acids and fatty acids can be formed either abiotically or biotically. Both abiotic and biotic chemistry, as occurring on Earth, create fundamentally different abundance ratios of different amino acids and fatty acids. Enceladus' ocean is known to be salty and contains inorganic as well as organic compounds. This is likely also the case for Europa. These matrix compounds affect the appearance of amino acids and fatty acids in impact ionization mass spectra. To ensure a detection of unambiguously biotically produced amino acids and/or fatty acids, a distinct biotic abundance pattern of different amino acids and/or fatty acids (biosignature) has to be found in the mass spectra, even under demanding, ocean world like matrix conditions. Chapter 10 is therefore concerned with the following questions:

Will future impact ionization mass spectrometers be able to detect and discriminate between abiotic and biotic signatures of amino acids and fatty acids if mixed with a number of other organic and inorganic compounds in ice grains emitted from ocean worlds such as Enceladus and Europa? If so, what encounter speeds of spacecraft with the ice grains are most suitable for the detection of such acids?

6.3 Personal contribution

This cumulative dissertation comprises three peer-reviewed articles, published in international scientific journals, and one manuscript, which is in preparation for submission to a peer-reviewed international scientific journal. Each of these articles forms a separate chapter within Parts II (chapters 7 and 8) and III (chapters 9 and 10) of this thesis. The PhD candidate is first author of all four articles, sharing the first authorship of one of these articles. The work for the articles was carried out jointly with several colleagues affiliated with various German and American institutions. Part II provides the methodological background for Part III, which is the primary planetological work of this thesis. The results of the three published articles were presented in numerous oral and poster presentations at international conferences and workshops. A complete list of conference/workshop appearances is given in appendix E. The two published articles forming Part III were covered by international press and media.[1] Parts I (chapters 1 - 6) and IV (chapters 11 and 12) were additionally written for this thesis solely by the PhD candidate.

[1]For example FU Berlin, Welt, and El Diario De Santiago.

The three published articles and the manuscript in preparation forming Parts II and III of this thesis are listed below:

1. **Klenner, F.**, Postberg, F., Hillier, J., Khawaja, N., Reviol, R., Srama, R., Abel, B., Stolz, F., and Kempf, S. (2019). Analogue spectra for impact ionization mass spectra of water ice grains obtained at different impact speeds in space. *Rapid Communications in Mass Spectrometry*, 33(22):1751–1760. DOI: 10.1002/rcm.8518.

2. **Klenner, F.**, Postberg, F., Hillier, J., Khawaja, N., Reviol, R., Stolz, F., Cable, M.L., Abel, B., and Nölle, L. (2020). Analog experiments for the identification of trace biosignatures in ice grains from extraterrestrial ocean worlds. *Astrobiology*, 20(2):179–189. DOI: 10.1089/ast.2019.2065.

3. **Klenner, F.**[*], Postberg, F.[*], Hillier, J., Khawaja, N., Cable, M.L., Abel, B., Kempf, S., Glein, C.R., Lunine, J.I., Hodyss, R., Reviol, R., and Stolz, F. (2020). Discriminating abiotic and biotic fingerprints of amino acids and fatty acids in ice grains relevant to ocean worlds. *Astrobiology*, 20(10):1168–1184. DOI: 10.1089/ast.2019.2188.

[*] *Shared first authors.*

4. **Klenner, F.**, Umair, M., Walter, S.H.G., Khawaja, N., Hillier, J., Nölle, L., Zou, Z., Abel, B., and Postberg, F. Developing a Laser Induced Liquid Beam Ion Desorption spectral reference library for spaceborne mass spectrometers. In preparation.

Article 1 forms chapter 7. The research presented in this article was conducted within the framework of two projects funded by DFG and ERC, respectively (section 6.1), at Freie Universität Berlin and Ruprecht-Karls-Universität Heidelberg. As first (and corresponding) author of this article, the PhD candidate carried out a literature survey, performed all laboratory experiments, analyzed the data, interpreted and discussed the results, prepared the figures and the table. The PhD candidate wrote preliminary versions of this article, composed the final version together with Frank Postberg and Jon Hillier, and managed the manuscript through the peer-review process under the supervision of Frank Postberg. The used Cassini CDA mass spectra were provided by Frank Postberg. The research idea and experimental concept were provided by Frank Postberg and Sascha Kempf. All co-authors contributed to discussions and provided valuable comments. The language was improved mainly by Jon Hillier.

Article 2 forms chapter 9. The research presented in this article was conducted within the framework of two projects funded by DFG and ERC, respectively (section 6.1), at Freie Universität Berlin, Ruprecht-Karls-Universität Heidelberg, and Universität Leipzig. As first (and corresponding) author of this article, the PhD candidate carried out a literature survey, performed $\sim$ 95 % of the laboratory experiments (other experiments were performed by René Reviol and Ferdinand Stolz), analyzed the data, interpreted and discussed the results, prepared the figures, the tables, and the supplementary

material (appendix B). The PhD candidate wrote preliminary versions of this article, composed the final version together with Frank Postberg and Jon Hillier, and managed the manuscript through the peer-review process under the supervision of Frank Postberg. Morgan Cable provided major contributions to the introduction section. The research idea and experimental concept were provided by Frank Postberg and Morgan Cable. All co-authors contributed to discussions and provided valuable comments. The language was improved mainly by Jon Hillier.

Article 3 forms chapter 10. The research presented in this article was conducted within the framework of two projects funded by DFG and ERC, respectively (section 6.1), at Freie Universität Berlin, Ruprecht-Karls-Universität Heidelberg, and Universität Leipzig. The PhD candidate is corresponding author and shares the first authorship of this article with Frank Postberg. The PhD candidate carried out a literature survey, performed $\sim$ 90 % of the laboratory experiments (other experiments were performed by René Reviol and Ferdinand Stolz), analyzed the data, interpreted and discussed the results, prepared the figures, the tables, and the supplementary material (appendix C), and managed the manuscript through the peer-review process under the supervision of Frank Postberg. The article was written by the PhD candidate and Frank Postberg with substantial contribution from Jon Hillier. Frank Postberg and Morgan Cable provided calculations and concentrations for the background compounds used in the abiotic amino acid solution. Some of the mass spectra were baseline corrected by Sascha Kempf. The research idea and experimental concept were provided by Frank Postberg, Morgan Cable, and Christopher Glein. All co-authors contributed to discussions and provided valuable comments. The language was improved mainly by Jon Hillier.

Article 4 forms chapter 8. The research presented in this manuscript was conducted within the framework of two projects funded by DFG and ERC, respectively (section 6.1), at Freie Universität Berlin and Ruprecht-Karls-Universität Heidelberg. As first (and corresponding author) of this manuscript, the PhD candidate carried out a literature survey, led the development of the database, wrote the entire manuscript, prepared most of the figures (one figure was prepared by Sebastian Walter). The PhD candidate prepared the supplementary information (appendix A) and provided $\sim$ 80 % of the laboratory data for the database (most of the other data were provided by Zenghui Zou and Lenz Nölle). The PhD candidate conducted the data cleaning together with Muhammad Umair. The database itself was developed by Muhammad Umair. Sebastian Walter improved the database and made it internally accessible. The used Cassini CDA spectrum was provided by Nozair Khawaja. The research idea for the database was provided by the PhD candidate and Frank Postberg. Frank Postberg, Jon Hillier, Sebastian Walter, and Nozair Khawaja provided valuable comments to the manuscript. All co-authors contributed to discussions.

Other published articles, to which the PhD candidate has contributed during the time of his PhD, in addition to the four articles described above, are listed in appendix D.

II. Developing a reference library for impact ionization mass spectrometers

7 Analogue spectra for impact ionization mass spectra of water ice grains obtained at different impact speeds in space[1]

Summary

This is the abstract of the original publication and is titled "Summary" here to separate it from the overall abstract of this thesis given on page vii.

DETECTING ICE GRAINS with impact ionization mass spectrometers in space provides information about the compositions of ice grains and their sources. Depending on the impact speeds of the ice grains onto the metal target of a mass spectrometer, ionization conditions can vary substantially, resulting in changes to the appearance of the resulting mass spectra. Here we accurately reproduce mass spectra of water ice grains, recorded with the Cosmic Dust Analyzer (CDA) on board the Cassini spacecraft at typical impact speeds ranging between 4 km/s to 21 km/s, with a laboratory analogue experiment. In this Laser-Induced Liquid Beam Ion Desorption (LILBID) approach, a µm-sized liquid water beam is irradiated with a pulsed infrared laser, desorbing charged analyte and solvent aggregates and isolated ions, which are subsequently analyzed in a time-of-flight (TOF) mass spectrometer. We show that our analogue experiment can reproduce impact ionization mass spectra of ice grains obtained over a wide range of impact speeds, aiding the quantitative analyses of mass spectra from space. Spectra libraries created with the LILBID experiment will be a vital tool for inferring the composition of ice grains from mass spectra recorded by both past and future impact ionization mass spectrometers (e.g. the SUrface Dust Analyzer (SUDA) onboard NASA's Europa Clipper Mission or detectors on a future Enceladus Mission).

Keywords: Cassini, Enceladus, Ice analogue, Mass spectrometry, Ocean worlds

[1]This chapter is published as: Klenner, F., Postberg, F., Hillier, J., Khawaja, N., Reviol, R., Srama, R., Abel, B., Stolz, F., and Kempf, S. (2019). Analogue spectra for impact ionization mass spectra of water ice grains obtained at different impact speeds in space. *Rapid Communications in Mass Spectrometry*, 33(22):1751–1760. DOI: 10.1002/rcm.8518

7.1 Introduction

Dust detectors have played an important role in spacecraft payloads since at least the Pioneer 8 mission, probing in situ not only mineral dust but also ice grains (Berg and Richardson, 1969; Brownlee et al., 1996; Drolshagen et al., 2001; Grün et al., 1992b; Grün et al., 1992a; Kissel et al., 1986). Later 'active' detectors produce information about the grains' compositions and, therefore, provide insights into the compositions of the sources from which the grains were emitted (Hillier et al., 2007; Hsu et al., 2015; Kempf et al., 2008; Khawaja et al., 2019; Postberg et al., 2008; Postberg et al., 2009a; Postberg et al., 2011a; Postberg et al., 2018a; Tobie, 2015). Ice grains striking a detector's target plate, at speeds above approximately 1 km/s, form impact clouds containing ions and electrons, together with neutral atoms, molecules and macroscopic fragments. Charged particles (electrons, atomic ions and molecular ions) are, polarity dependent, separated and accelerated through a strong electric field towards a detector. Depending on the complexity of the mass spectrometer used, they may pass through either a field-free (or near field-free in the case of the Cosmic Dust Analyzer (CDA)) or a reflectron (Mamyrin, 1994) region. The ions' arrival times are proportional to their mass-to-charge ratios, thus forming time-of-flight mass spectra. In contrast to spaceborne neutral gas mass spectrometers, where ionization occurs in a controlled way using electrons with well-constrained energies (Balsiger et al., 2007; Barabash et al., 2013; Waite et al., 2004), impact ionization relies on the kinetic energy delivered by the impact. The impact speeds of ice grains in space may vary drastically (<5 to >20 km/s), resulting in variations in the energy available for disrupting and ionizing molecular and atomic species. The resulting mass spectra can therefore appear very different, even if the grains are identically composed, with higher mass water cluster ions decreasing in abundance as the impact energy increases. Laboratory analogue experiments in which water ice targets are exposed to high-velocity dust particles, producing these water clusters of the form $[(H_2O)_nH_3O]^+$ show similar variations, with fewer larger (higher n) clusters surviving as the impact velocity increases (Timmermann and Grün, 1991). The reduction in high-mass molecular clusters is primarily linked to the change in impact plasma conditions, with more destructive collisions and a shortening of the timescales over which clustering can occur, with higher energy, faster expanding clouds experiencing longer clustering mean free paths over shorter times, prior to acceleration and detection.

In contrast to siliceous, metallic, or organic grains, micron- and submicron-sized ice grains can currently not be accelerated in an electrostatic dust accelerator facility to relevant speeds (Burchell et al., 1999; Fielding et al., 2015; Goldsworthy et al., 2003; Hasegawa et al., 2001; Mocker et al., 2010; Shu et al., 2012; Stübig, 2002). Previous studies (Postberg et al., 2009a; Beinsen, 2011) have shown that CDA impact ionization mass spectra of ice grains with varying minor compositional differences can be reproduced with laboratory analogue experiments in which a pulsed infrared laser intercepts an ultra-thin water beam or water droplets. However, those studies did not consider the role impact speed plays in determining spectral appearance. The collisional behav-

ior of ions and neutrals within the expanding plasma cloud, leading to recombination, ionization, fragmentation and/or clustering, is a function of the impact cloud expansion speed, energetics and the number density of interacting species within it (Hornung and Kissel, 1994). Typically, four factors determine the initial composition and dynamics of the cloud of ions and neutrals generated during an impact: impact speed, particle mass, and particle and target composition. Although particle mass also influences the total amount of charge generated by an impact (Bedford, 1971), the clearly dominant factor here is impact speed (total impact charge typically scales proportionally to $m^{\alpha}v^{\beta}$, with α typically near one and β varying between approximately 3 and 5 with target and projectile composition (Stübig, 2002; Bedford, 1971)). Impact ionization also primarily occurs at shock fronts, for which the controlling factor is energy per unit mass, and hence is impact speed dependent. To improve the compositional analyses of ice grains and their planetary sources an analogue experiment should be able to simulate the varying ionization and clustering conditions that occur at different impact speeds.

Building on the work of Postberg et al (2009a), here we adapt laser desorption analogue experiments to mimic a wide range of feasible impact speeds, establishing an experimental methodology to predict and reproduce mass spectra generated by ice grains in the future. This will improve quantitative compositional analysis of mass spectra produced by impact ionization mass spectrometers on board not only Cassini (Srama et al., 2004), but also on future spacecraft intended to investigate icy moons, such as the Europa Clipper and Enceladus missions (Kempf et al., 2012; Reh et al., 2016; Postberg et al., 2011b; Mitri et al., 2018; Lunine et al., 2015a).

7.2 Experimental

7.2.1 Scientific approach

Spaceborne impact ionization mass spectrometers form projectile ions from micrometer-sized ice grains as the grains impact onto targets (Figure 7.1A). In the case of Cassini's CDA, ice particles impinge onto a rhodium target, vaporizing and ionizing speed-dependent fractions of both projectile and target. At the low impact speeds considered here, there is no evidence of the generation of multiply charged ions during this process. A 1000 V potential difference, between the impact target (+1000 V) and a grid held at 0 V, approximately 3 mm in front of it, accelerates cations through a near-drift region towards an ion detector, the multiplier, at a distance of 0.23 m. A series of three concentric grids, separated by 0.005 m and held at $\sim$ -350 V, $\sim$ 0.03 m in front of the multiplier, provide only marginal further ion focusing and acceleration. After passing through the grids, the central of which is connected to a charge amplifier and recorder to produce the QI signal (Srama et al., 2004), the ions experience a post acceleration towards the multiplier front electrode, held at $\sim$ -2750 V (Figure 7.1C). The impact speeds of the ice grains may be determined not only by the rise times of the charge signals on the target and/or the ion grids of CDA (Srama et al., 2004), and/or via spectral appearance

(i.e. a decrease in cluster size, appearance of target material ions, production of ions with high ionization energies (Fiege et al., 2014; Postberg et al., 2009b)), but also through dynamical considerations. In this latter technique, the known position of the spacecraft when individual E ring ice grains are detected can be used to estimate the speed of the particle in a circular orbit passing through this point. After subtraction of the known speed of the spacecraft, the likely impact speed for the particle can be estimated. For individual impacts, the error in this derived impact speed, due to uncertainties in the axes, eccentricities and inclinations of the ice grain's orbit, may be large, but is significantly reduced by considering larger ensembles of impacts – summing spectra within speed ranges.

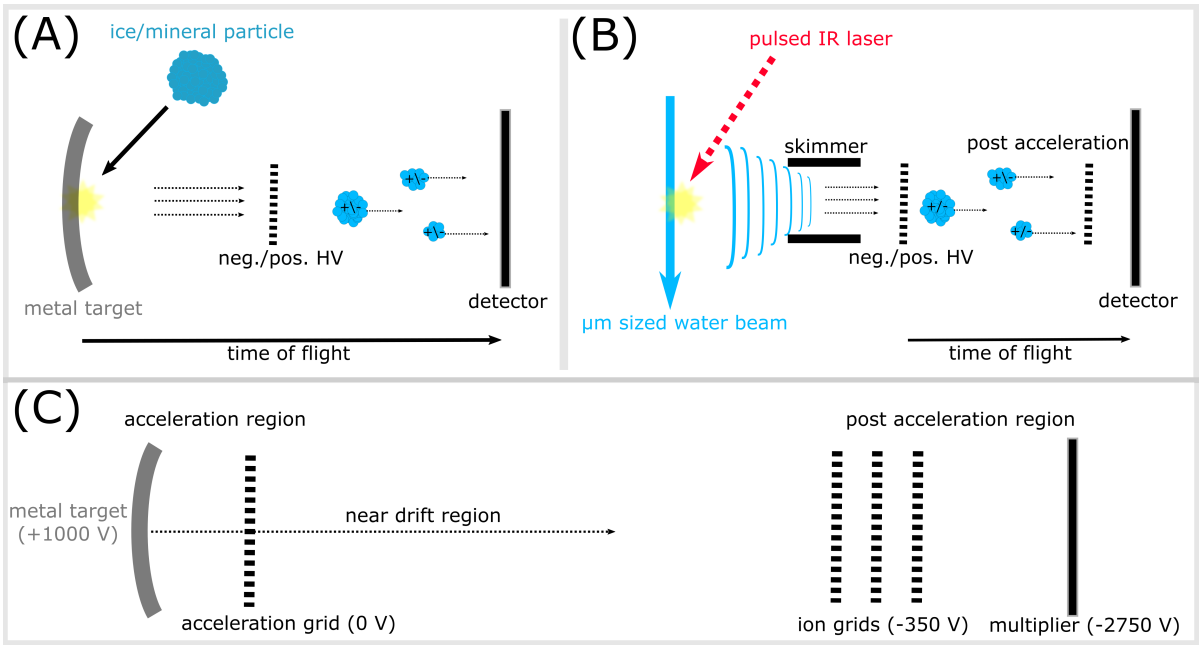

Figure 7.1: *A, Comparison of impact ionization with mass spectrometers in space and B, liquid beam laser desorption for comparable energy impact and dispersion conditions. In (A) ice grains hit a metal target and become partially ionized. In (B) a pulsed infrared laser hits a water beam, which disperses and in turn creates ions and charged aggregates. In both cases the charged ions/aggregates are accelerated by a high voltage potential difference (neg./pos. HV) and detected after a characteristic (mass/charge dependent) time of flight. C, The main acceleration and drift zones within the CDA chemical analyzer mass spectrometer. Voltages are approximate and the regions are not to scale. Instrument recording may be triggered by charges exceeding thresholds on the target, acceleration grids or multiplier.*

In the laser-based analogue experiment, a liquid water beam and dissolved substances therein are primarily ionized by dispersion, a technique known as Laser Induced Liquid Beam Ion Desorption (LILBID; Figure 7.1B) (Karas et al., 1991; Karas et al., 2000). In this process, the energy transferred to the atoms and molecules by the laser is below their nominal ionization potentials, with the formation of charged species accomplished by mechanically breaking up the liquid matrix into charged fragments by laser excitation (Charvat and Abel, 2007; Wiederschein et al., 2015). A similar mechanism may dominate the abundant cation formation from water ice grains at impact speeds as low as 3 km/s observed by Cassini's CDA. The dissociation energy of water (492.2 kJ/mol) (Maksyutenko et al., 2006) is under half its ionization energy (1183 kJ/mol)

(Kovtun, 2015), which is less than that of hydrogen (1312 kJ/mol). It is therefore highly unlikely that significant quantities of $[H_3O]^+$ or $[H]^+$ ions can form by direct ionization at such low impact speeds (Wiederschein et al., 2015). Only at impact speeds >15 km/s are charged water constituents from atomic/molecular collisional ionization observed, as we will demonstrate in this work. Mechanical breakage and collisional ionization almost exclusively produce spectra from singly charged ions in both impact ionization and the laser desorption experiment. In space, the ionization process of water starts from solid ice whereas in the analogue experiment ionization occurs from the liquid phase.

While the mass resolution of CDA is a relatively low 20–50 (m/Δm) (Srama et al., 2004), SUDA's mass resolution reaches ≈ 200 m/Δm and the Enceladus Ice Analyzer (ENIA) is designed to achieve m/Δm > 1000 (Kempf et al., 2012; Reh et al., 2016). With the current analogue experiment we are able to detect cations and anions with a mass resolution of about 800 m/Δm.

The aim of this work is to simulate, in the laboratory, impact ionization mass spectra arising from ice grains hitting a metal target at different impact speeds in space, by variation of both the laser's power density and the delay time of the gated mass spectrometer (see section 7.2.2) to select fractions of the velocity distribution created by the desorption laser. We simulate spectra arising from the impacts of CDA Type 1 E ring ice grains. Type 1 grains are relatively homogeneous in their composition and are almost exclusively composed of water ice with occasional traces of sodium and potassium at the sub-ppm level (Postberg et al., 2009a; Postberg et al., 2011a). These grains are a population, as defined by the appearance of their CDA spectra, detected in Saturn's diffuse E ring (Postberg et al., 2009a). Originating from Enceladus, the grains are believed to have formed via condensation and growth from water vapor expanding into space through fractures in Enceladus' surface (Postberg et al., 2009a; Schmidt et al., 2008; Postberg et al., 2018b). CDA spectra of salt-rich (Type 3) ice grains are discussed in various papers (Postberg et al., 2009a; Postberg et al., 2009b; Postberg et al., 2011a). We therefore assume that the differences between CDA Type 1 spectra recorded at different impact speeds in Saturn's E ring are predominately due to kinetic effects rather than compositional differences. For each investigated speed regime (see below) we averaged over 12–20 individual spectra to further reduce the effects of minor compositional variations within Type 1 grains.

To cover the typical speed range of ice particles relevant for mass spectrometers in space, we examined representative Type 1 CDA mass spectra for five different impact speed regimes: 18–21 km/s; 13–15 km/s; 9–11 km/s; 6.5–8.5 km/s; and 4–6 km/s. As previously mentioned, the impact speeds are determined by subtracting the known spacecraft speed from that of the ice grain, at the point of impact, calculated by assuming that the E ring grains are on circular orbits around Saturn. The natural distribution of orbital eccentricities and inclinations in the E ring will, however, introduce uncertainties in the exact impact speeds, which, as with minor compositional variation, are reduced by averaging over many spectra, over a suitably wide speed range.

To ensure a similar signal-to-noise ratio for all individual spectra at

all speed regimes we used only those with an ion yield, as inferred from CDA's QI signal (Srama et al., 2004), of between 12 fC and 30 fC. In the E ring, CDA recorded many Type 1 spectra outside this range, mostly with lower ion yields. To ensure precise mass calibration of pure water peaks, Type 1 spectra with particularly low sodium and potassium signatures were selected.

7.2.2 Experimental description

The PhD candidate changed his affiliation from Ruprecht-Karls Universität Heidelberg to Freie Universität Berlin. The experimental setup has then also been moved.

Figure 7.2 shows the LILBID experimental setup used in Heidelberg and Leipzig as an analogue for ice grain impacts. An aqueous solution is injected into a high vacuum (5×10^{-5} mbar) through a quartz nozzle (opening radius 6–10 µm). The quartz nozzle is mounted on a threeaxis manipulator and can be precisely adjusted. Flow injection of the tested solutions is accomplished with an injection valve (model MX9925, Rheodyne). An HPLC pump (model 300c, Gynkotek) is employed to keep the flow speed constant at 0.17 mL/min. The liquid flow is stable for ~ 2 mm vertically downward before disintegrating into droplets. To maintain the high vacuum, the liquid is captured by a nitrogen-cooled cryotrap. A second hanging nitrogen-cooled cryotrap freezes vaporized liquid. A pulsed infrared laser (Opolette HE 2731, OPOTEK; 20 Hz, 7 ns pulse length; maximum power density ≈ 1150 MW/cm^2) disperses the water beam. The laser, operating at a wavelength of 2840 nm (chosen to match the absorption frequency of the OH-stretch vibration of water) with a variable pulse energy of up to 4 mJ, is directed and focused onto the liquid through two CaF_2 lenses, a gold mirror and a CaF_2 window. When the water beam absorbs the laser energy, it is heated up and explosively disperses into atomic, molecular and macroscopic fragments.

After passing through a skimmer (a momentum separator resulting in a better-collimated spray of ions), cations or anions are analyzed in a reflectron-type time-of-flight (TOF) mass spectrometer (Kaesdorf) (Mamyrin, 1994). The mass spectrometer operates at approximately 1×10^{-7} mbar and uses the principle of delayed extraction (Figure 7.2) (Charvat and Abel, 2007). The spread in arrival times of the ions in the acceleration/extraction region, due to the field-free drift region (approximately 25 mm in length) between the site of ionization/dispersion and the acceleration region, is a function of the ions' initial velocities. Ion velocities are typically related to their masses and the amount of energy imparted by the laser (Equation 1); a function not only of the maximum applied power density, but also distance away from the site of maximum power density along and through the liquid beam:

$$v_{ini} \sim \sqrt{\frac{E_{laser}}{m}} \tag{1}$$

Within the extraction region itself, the effects of the ions' initial velocity dispersion are further reduced by variations in proximity to the extraction electrodes, with the fast ions having already passed through proportionally more of the extraction region prior to the electrode charging so that the fast ions experience less acceleration than the slow ions when the acceleration electrodes are switched on (Equation 2):

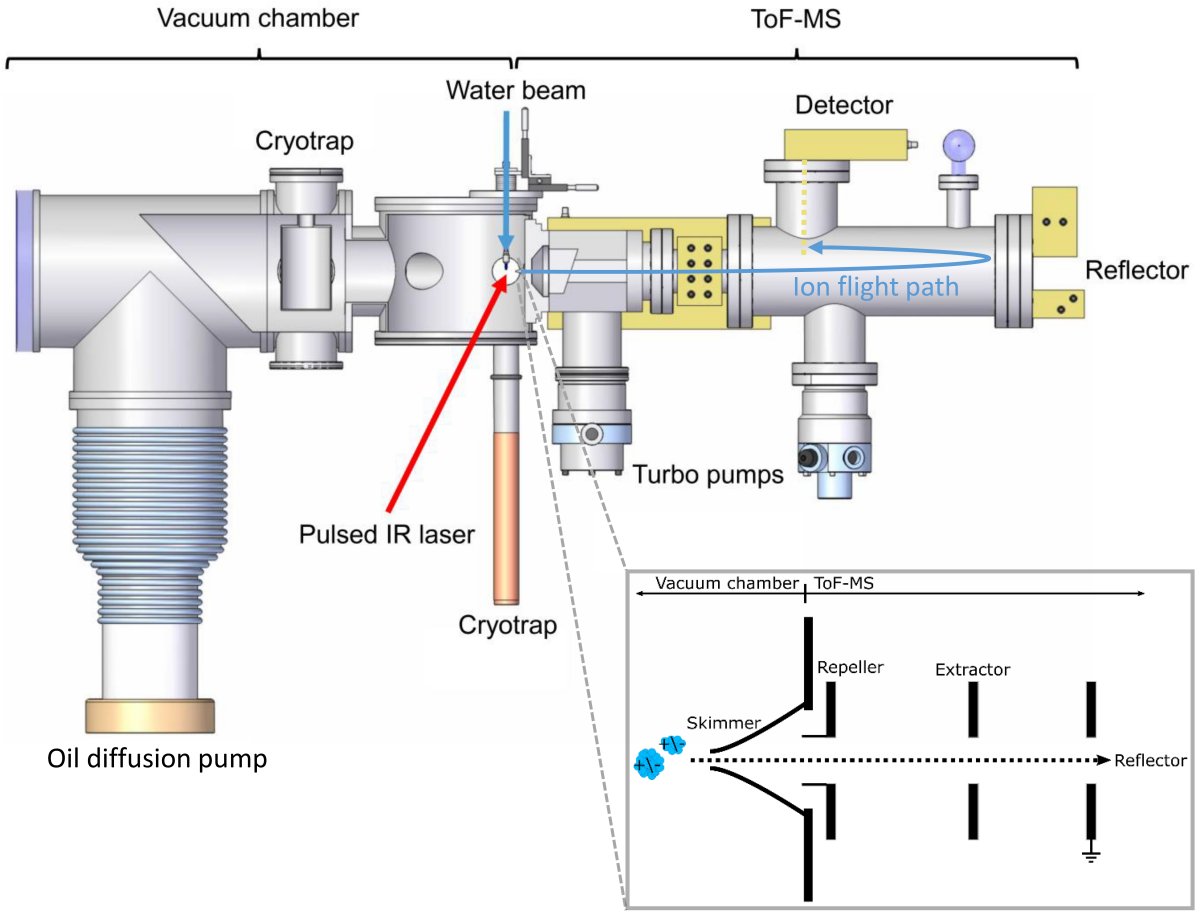

Figure 7.2: *Experimental LILBID-TOF-MS setup for simulating hypervelocity impacts of ice grains onto impact ionization mass spectrometers in space and (inset) a schematic illustrating the instrument configuration underlying the principle of delayed extraction. The start signal occurs when the acceleration electrodes are switched on, the stop signal when the ions reach the detector. The oil diffusion pump shown was later replaced by a turbo pump (adapted from Postberg et al 2018a). See text for further explanation.*

$$U_{fast} < U_{slow} \tag{2}$$

Samples of ions with defined ranges of initial velocities can thus be selected for analysis by the mass spectrometer. With delayed extraction, the acceleration electrodes (repeller and extractor) of the spectrometer are switched on after a predefined delay time for a duration of 30 µs. Late arriving ions are blocked by the repeller electrode and do not enter the mass spectrometer because of the applied electrode potentials (Figure 7.2). Thus, by setting a delay time window, this gated system selects ions dependent on their initial velocity. The delay time is defined by a pulse generator (model DG 535, Stanford Research Systems). The detected (Photonis Chevron MCP-Set) signals are amplified (Preamp 100, Kaesdorf), digitized (12 bit, Acqiris) and then recorded with a LabVIEW controlled computer. Each mass spectrum presented here is the average of 500 individual spectra. NaCl solutions with concentrations of 1×10^{-7} M were used. The NaCl salt (p.a.; Sigma Aldrich) solutions are freshly prepared with doubly distilled and deionized H_2O in 50 mL sample cups. Performing one effective measurement requires a sample volume of ~ 0.5 mL.

7.3 Results

7.3.1 CDA Type 1 spectra characteristics at different impact speed regimes

The averaged CDA Type 1 spectra for each speed regime used in this work are shown in Figure 7.3. At below 15 km/s they show peaks of pure water clusters with masses corresponding to $[(H_2O)_nH_3O]^+$ (n = 0, 1, 2 ...). The averaged spectra exhibit a general amplitude maximum at n = 0 and a monotonous decline from small to large values of n, although in some individual spectra the maximum is reached at n = 1, 2 or 3 at low and intermediate speeds (≤10 km/s). The lower the impact speed and, therefore, the kinetic energy of the impact (assuming equally-sized ice grains), the more abundant are water clusters with larger values of n. Because the ice grains contain traces of sodium and potassium, originally probably in the form of NaCl and KCl (Postberg et al., 2009a), the averaged mass spectra for all speed regimes also show peaks due to sodium water clusters $[(H_2O)_nNa]^+$ and potassium water clusters $[(H_2O)_nK]^+$. Owing to the insufficient mass resolution of CDA, the water cluster peaks of the three different charge-bearing species $[H_3O]^+$, $[K]^+$ and $[Na]^+$ overlap at 19 u $(+18u)_{n+1}$, 39 u $(+18u)_n$, and 23 u $(+18u)_{n+1}$. Because of the dominant pure water cluster peaks ($[(H_2O)_nH_3O]^+$), $[Na]^+$ and $[K]^+$ cluster peaks are often not quantifiable. CDA's target material rhodium is excavated and detectably ionized at impact speeds >9 km/s (Postberg et al., 2009b) and thus $[Rh]^+$ ion signatures are apparent in the three fastest speed regimes in the form of $[Rh]^+$, rhodium dimers $[Rh_2]^+$, and rhodium water clusters $[(H_2O)_{1-4}Rh]^+$.

In CDA spectra of the two fastest speed regimes recorded, above ≈ 13 km/s, $[H]^+$, $[H_2]^+$ and $[H_3]^+$ are created and above ≈ 15 km/s ions

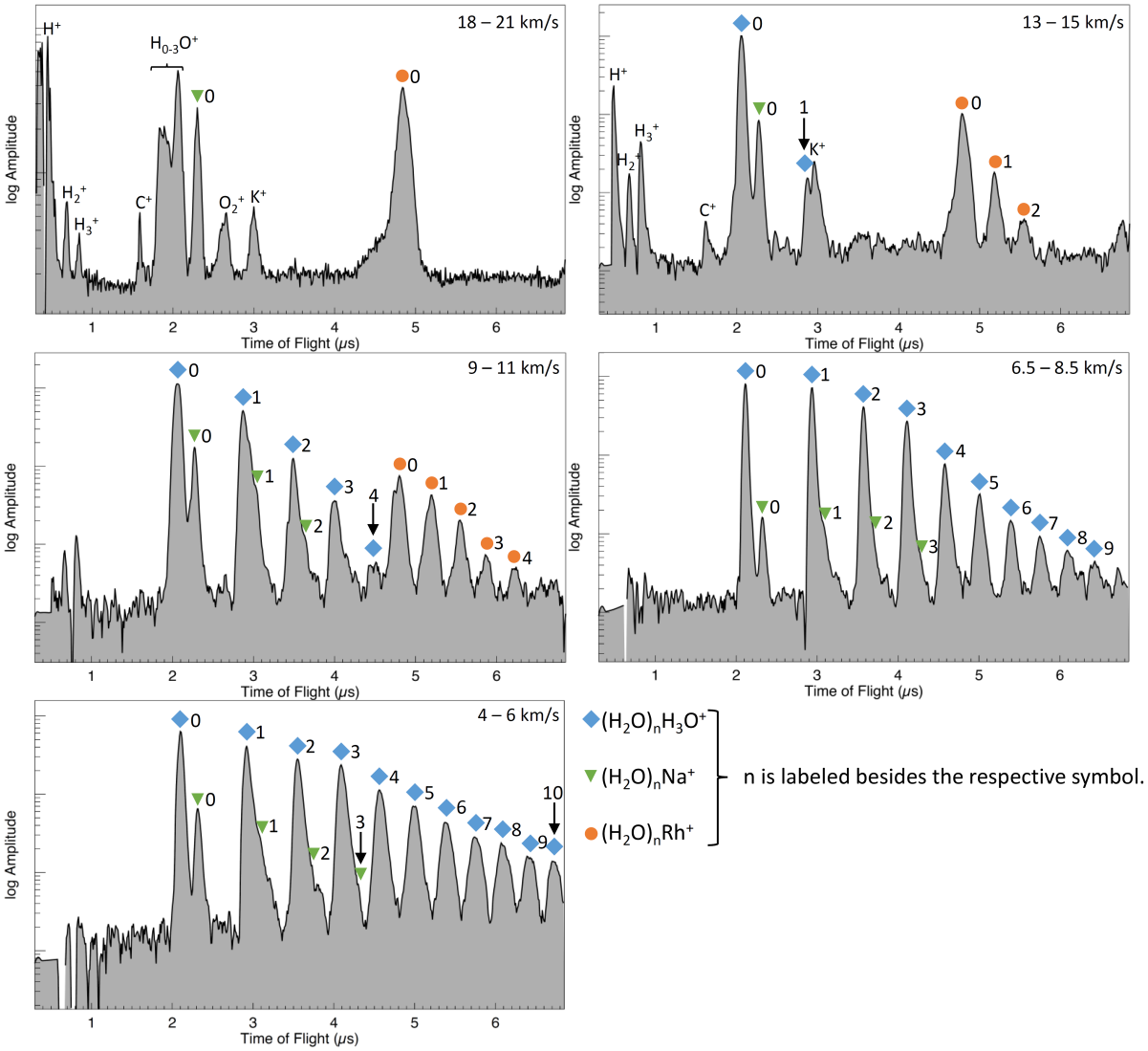

Figure 7.3: *Baseline corrected CDA mass spectra of ice grains at different impact speeds. At the fastest impact speeds (18– 21 km/s) hydronium* $[(H_2O)H]^+$ *(19 u) and elemental* $[Na]^+$ *(23 u) and* $[K]^+$ *peaks (39 u) are observable, whereas no molecular water cluster peaks are detectable. Here dissociation ions are formed from the water molecules, due to the high kinetic energy of the impinging ice grains: Water molecules disintegrate forming hydrogen* $[H]^+$ *(1 u), dihydrogen* $[H_2]^+$ *(2 u), trihydrogen* $[H_3]^+$ *(3 u), oxygen* $[O]^+$ *(16 u), hydroxyl* $[HO]^+$ *(17 u), water* $[H_2O]^+$ *(18 u), and dioxygenyl* $[O_2]^+$ *(32 u) cations. At 13–15 km/s, detectable quantities of molecular dissociation ions do not form and water clusters* $[(H_2O)_nH_3O]^+$ *with* $n = 0$ *and* $n = 1$ *are observable. At 9–11 km/s larger pure water clusters are detected at least up to* $n = 4$ *(91 u) and water sodium clusters up to* $n = 2$ *(59 u), respectively. Due to CDA's relatively low mass resolution, with increasing values of n the K and Na clusters are increasingly difficult to separate from the adjacent pure water clusters and thus might not be identified if present in small quantities. At* $\approx$ *8 km/s pure water clusters usually extend to* $n \geq 7$ *and below 6 km/s water clusters are frequently observable up to the end of CDA's mass range of about 200 u* ($n \geq 10$). *The amplitudes of the pure water cluster peaks and the sodium water cluster peaks decline from lower to higher masses in CDA spectra at all speed regimes. The sequence of nearly exponentially declining amplitudes is interrupted by a "jump" between water clusters with* $n = 3$ *and* $n = 4$. *This is due to the well-known "magic number" stability of* $n = 3$ *water clusters (Andersson et al., 2008; Niedner-Schatteburg and Bondybey, 2000). Above 9 km/s* $[(H_2O)_nRh]^+$ *clusters are frequently observable. The number of water molecules attached to* $[Rh]^+$ *typically corresponds to the number of water molecules in the pure water cluster cation. For example, in the spectrum of 13–15 km/s two water molecules are attached to rhodium (*$[(H_2O)_2Rh]^+$*) and the largest pure water cluster in the spectrum consists of a protonated cluster of two water molecules* $[(H_2O)H_3O]^+$

typical for dissociation and ionization of water molecules ($[OH]^+$, $[OH_2]^+$, $[O]^+$, $[O_2]^+$) start to appear, whereas any water clusters with n $\geq$ 1 start to disappear and are undetectable at $\geq$20 km/s.

7.3.2 Reproducing CDA Type 1 spectra with the analogue experiment

We aim to reproduce the speed-dependent occurrence of water cluster and atomic ions with the laboratory setup, such that both the overall spectral envelope (pattern of peak amplitudes) and appearance and disappearance (within instrument detectability thresholds) of molecular and atomic species are simulated. We use a highly diluted NaCl solution (see section 7.2) without potassium salts and thus K cluster peaks are absent in the analogue spectra, as are Rh-based peaks from the CDA target material. To simulate the fastest two impact speed regimes (18–21 km/s and 13–15 km/ s) a single delay time window at a short delay time, to extract the fastest ions, is sufficient to reproduce CDA spectra. For the next slower speed regime (9–11 km/s) further spectra taken at a longer delay time have to be added to a "fast ion" window as used for 18–21 km/s and 13–15 km/s. For the slowest two speed regimes (6.5–8.5 km/s and 4–6 km/s) a third delay time window at even longer delay times has to be added. In the impact ionization process, ionization and disruption of the water ice grains occur within the acceleration region of the instrument. However, the laboratory laser experiment generates ions in a field-free zone, which then drift into the acceleration region. The apparent production time of the ions is therefore significantly extended, requiring selection (via delay times of the gating system) of ion populations to match those seen in impact ionization experiments. Co-added spectra produced from a mixture of different delay time windows are therefore generated with the LILBID setup (see also section 7.4). The following energy densities and delay times have been used to match the peak patterns produced in the different CDA impact speed regimes:

- **18-21 km/s:** 1150 MW/cm^2 and 4.4 µs
- **13-15 km/s:** 975 MW/cm^2 and 3.2 µs
- **9-11 km/s:** 975 MW/cm^2 and 3.8 µs added to 670 MW/cm^2 and 4.9 µs
- **6.5-8.5 km/s:** 975 MW/cm^2 and 3.8 µs added to 670 MW/cm^2 and 4.9 µs added to 540 MW/cm^2 and 5.7 µs
- **4-6 km/s:** 975 MW/cm^2 and 3.8 µs added to 670 MW/cm^2 and 4.9 µs added to 445 MW/cm^2 and 6.3 µs

Figure 7.4 shows the reproduced CDA spectra resulting from the analogue experiment. Despite the different aggregate states of water, solid in space and liquid in the laboratory, very similar cation mass spectra are produced (Figures 7.3 and 7.4) (Postberg et al., 2009a; Beinsen, 2011). The higher mass resolution of the latter is clearly observable. Peak patterns can be reproduced accurately for impact speeds up to 15 km/s. In

the regime above 18 km/s all ion species can be reproduced but with a poorer quantitative match. Table 7.1 shows a comparison of the relative amplitude ratios of water peaks in CDA spectra with laboratory spectra for impact speeds up to 15 km/s.

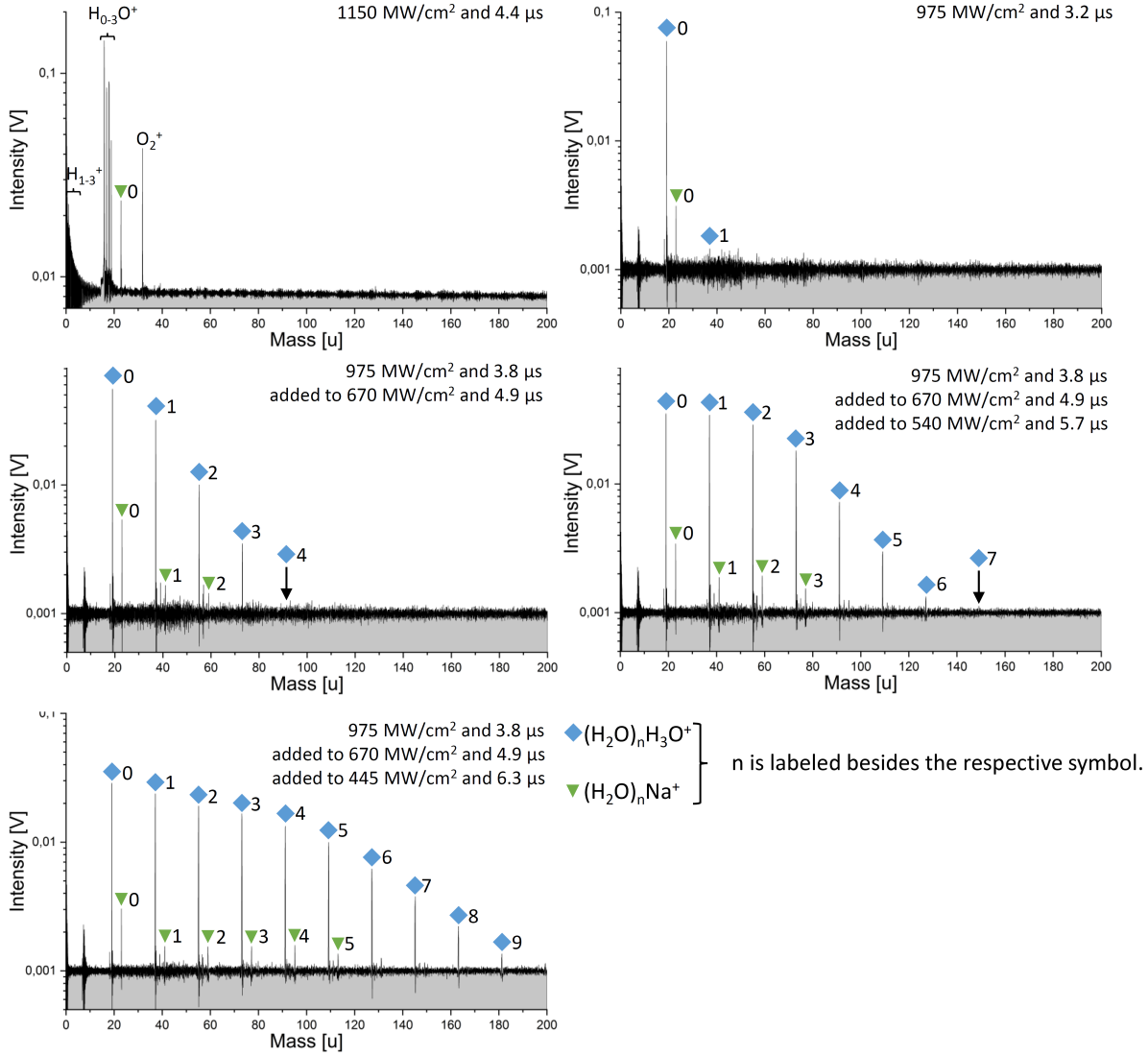

Figure 7.4: *Baseline corrected laboratory analogue spectra of CDA Type 1 spectra for five different speed regimes (Figure 7.3). The panel's positions correspond to the panels in Figure 7.3. A solution of 10^{-7} M NaCl was used to match the sodium content of the selected Type 1 ice grains. In both CDA spectra and laboratory spectra identical ion species are observable in similar quantities.*

7.4 Discussion

We have shown that it is possible to recreate the effects of impact speed on the impact ionization mass spectra of micron and submicron Type 1 E ring ice grains using a laboratory LILBID apparatus. In order to determine salt concentrations within the grains, other Type 1 spectra have been reproduced previously with similar LILBID-MS experiments using a solution of 10^{-6} M NaCl (Postberg et al., 2009a). Here we find somewhat lower concentrations of 1×10^{-7} M yield spectra which better agree with

Table 7.1: A comparison of relative water peak amplitude ratios (normalized to the 19 u signal) of the co-added CDA mass spectra (Figure 7.3) at different impact speeds with laboratory results (Figure 7.4). All peaks apparent in CDA mass spectra are also seen in the laboratory mass spectra, with a near quantitative match of the relative amplitude ratios achieved.

Impact speed [km/s]	**Mass [u]**	**19**	**37**	**55**	**73**	**91**	**109**	**127**	**145**	**163**	**181**	**199**
13-15	**CDA**	100	1.7	-	-	-	-	-	-	-	-	-
	Lab	100	2.4	-	-	-	-	-	-	-	-	-
9-11	**CDA**	100	51.0	15.7	4.6	0.7	-	-	-	-	-	-
	Lab	100	56.4	15.3	5.6	2.1	-	-	-	-	-	-
6.5-8.5	**CDA**	100	92.6	50.6	35.2	8.0	3.1	1.5	1.0	-	-	-
	Lab	100	90.1	68.1	32.7	11.6	5.4	3.1	2.8	-	-	-
4-6	**CDA**	100	60.6	44.7	34.8	17.4	12.2	7.6	4.7	3.6	2.7	1.8
	Lab	100	64.7	39.2	26.0	21.2	16.2	10.4	6.7	4.5	3.1	2.8

those of the selected Type 1 E ring grains, which were biased towards particularly low sodium and potassium contents, in order to rule out resolution-limited, isobaric, peak interference effects in the water cluster peaks in CDA spectra (see section 7.2).

The different phases of water, solid in space and liquid in the laboratory experiment, do not make a noticeable difference to the resulting cation spectra and very similar ensembles of molecular and elemental cations are created, as has also been shown for liquid water and ice in the LILBID approach (Beinsen, 2011; Berkenkamp et al., 1996). The energies required for dispersion of the liquid to form ions and charged aggregates for a given number of molecules (1183 kJ/mol) far exceed the energies required for phase transitions in the H_2O system (vaporization energy of water at 0°C is 45 kJ/mol). The main difference in spectral appearance comes from the higher resolution of the reflectron mass spectrometer used in the laboratory.

There are two processes through which $[(H_2O)_nH]^+$ ions can form in impact clouds or during the LILBID process. The first, for which evidence has been presented by e.g. Wiederschein et al. (2015) for LILBID, is via direct formation of charged fragments. Upon dispersion of a water beam, statistical inhomogeneities in the distribution of charges result in excesses of charges on some fragments. This process does not create abundant $[H]^+$ ions (Figure 7.4). The impinging laser generates a shock wave in the water beam, which travels at approximately 2 km/s (Charvat et al., 2006). This is analogous to the shock wave generated during the impact of an ice grain onto a metal target, although in this latter case a fraction of the available energy is also transferred to the target (Hornung and Kissel, 1994).

Given the lack of $[H]^+$ ions in the CDA spectra at low (<9-11 km/ s) speeds (Figure 7.3), together with the arguments based on impact energies (and speed thresholds) discussed previously (section 7.2), it is likely that ion formation in impact clouds generated by low speed ice grains occurs by the same mechanism, a "top down" dispersion/ fragmentation process for molecular ion production (Wiederschein et al., 2015).

However, with increasingly energetic conditions, and shorter lifetimes, impact clouds from higher speed (>9-11 km/s) impacts show evidence

that clustering, forming larger molecular assemblages from a "bottom up" approach, is occurring as well. The definite clusters, in this instance, are between the target material, Rh, and both hydronium and larger water clusters/fragments. At similar speeds, $[H]^+$ appears in the spectra, preceded at slightly lower speeds by appearance of $[H_2]^+$ and $[H_3]^+$, although it is probable that the hydrogen is, in these cases, also released from the Rh target, in which significant amounts are absorbed (Postberg et al., 2009b). The impact cloud is therefore an environment in which collisional growth can occur, and this process, in addition to fragmentation, is likely to form clusters of water molecules.

Cluster growth is related to the likelihood of ions, or neutrals, encountering other molecules, as the timescale over which suitable conditions exist. It is therefore a function of the number density of neutrals and ions within the impact cloud, together with their size and speed distributions. These will change with time, as the impact cloud expands and clustering (or fragmentation and/or dissociation) occurs. The initial number density of neutrals and ions, and the expansion rate of the impact cloud, are related to the impact conditions, in particular particle mass and impact speed. Of these, impact speed is the dominant characteristic, with the energy density of the impact scaling with kinetic energy, and the total charge generated proportional to $m^{\alpha}v^{\beta}$, where α is typically 1 and β is typically 3–5, depending on particle composition (Stübig, 2002; Bedford, 1971).

In the impact process, with increasing energy densities, molecular dissociation and the formation of atomic (and molecular fragment) ions start to occur. In the LILBID process, the individual photon energy (6.99×10^{-20} J) is too low to directly dissociate the HO-H bond in water (8.19×10^{-18} J) or ionize atomic H (2.18×10^{-18} J). However, with increasing laser power density in the LILBID experiments, the charge density and dispersion speed of the vapor cloud will increase, mimicking the impact plasma shockwave and cloud expansion, until molecular dissociation and ionization of the water molecules start to occur, primarily through collisional processes, leading to the formation of a cationic plasma component composed of e.g. $[H]^+$, $[H_2]^+$, $[H_3]^+$, $[O]^+$, $[O_2]^+$, $[OH]^+$ and $[H_2O]^+$, species dominating CDA spectra above approximately 18 km/s. It is indeed typical that the generation of such ions only occurs above specific speed thresholds in impact ionization at which the localized energy density at the impact site becomes high enough (Fiege et al., 2014). At the lower impact speeds the slow expansion speed, and hence longer impact cloud lifetime, increase the likelihood of any minor $[H]^+$ component clustering, potentially resulting in the same lack of $[H]^+$ that would be seen if fragmentation dominated. For the Type 1 E ring grains, the threshold at which the spectra become dominated by dissociated water ions, and large water clusters become undetectable, is approximately 18 km/s.

Below 15 km/s, by choosing the appropriate delay time windows, a near quantitative match between laboratory and flight spectra can be achieved (Table 7.1). In contrast, the decisive difference between the two fastest speed regimes is the applied laser energy, such that the plasma is either dominated by dissociated atomic or molecular fragment ions (>18

km/s), or stays in the regime where spectra are dominated by larger molecular ions (<15 km/s). The sudden difference in plasma behavior between these two regimes in the LILBID experiment results in a reduced signal to noise if short delay times are used, and hence a longer (4.4 µs) time was selected to maximize the spectral signal. In fact, in general the reproduction of CDA spectra is more difficult in the dissociation regime. While all ion species seen in CDA spectra still show up in the analogue experiment, the quantitative match is worse and ion abundances in the dissociation regime are generally much more variable in both CDA spectra and laboratory spectra. There is a general trend that $[H_{1,2,3}]^+$ and $[H_3O]^+$ form in larger abundances in high speed impact ionization spectra whereas $[O]^+$, $[HO]^+$, $[H_2O]^+$ and $[O_2]^+$ are overrepresented in the laboratory spectra.

Theoretical investigations of the impact ionization process, considering Fe particles impacting metal targets, indicate that at speeds lower than 20 km/s at most $\sim$ 10–15 % of the particles are ionized and do not recombine prior to detection (Drapatz and Michel, 1974), with the majority of the particles remaining neutral, or even in macroscopic fragments. This is likely to also be the case with the water ice grains. In the LILBID experiments, the approx. 100 micron wide gaussian laser power density profile, together with the significant vertical (and horizontal in comparison with the typical size of Type 1 E ring grains) extension of the water beam, will result in a similar variation in energy transfer and ion formation. This issue can be partially overcome by e.g. shooting on individual water droplets, but this method yields highly irreproducible results with our experimental setup. Reducing the length of the water beam by using on-demand nozzles has had some success in mitigating this problem (Morgner et al., 2006), although here we correct for it by the use of appropriate delay time windows.

It is important to note that the measured composition of the impact plasma, and that of the LILBID plasma, is that produced before a "steady state" has been reached via thermalization, with the ion ensemble also having undergone subsequent evolution (e.g. recombination, collisional clustering and fragmentation) during the acceleration/drift periods. Apart from population differences arising from e.g. the extent of the water beam, the main difference between the ion ensembles detected from impact ionization and those arising from the LILBID experiment is due to differences in the electric field environment in which ionization and molecular cluster/fragment formation occurs (imposed by the use of liquid in the LILBID apparatus). Within the CDA, generated ions are collected and accelerated rapidly towards the ion detector (multiplier) as soon as any Debye shielding breaks down and the ions are exposed to the 330 kV/m electric field (Srama et al., 2004). In the LILBID apparatus, ions drift through a completely field-free region after production, prior to entering the mass spectrometer for subsequent acceleration and detection. The speed at which the ions traverse this region is analogous to the speed with which the impact cloud expands, with faster ions having been exposed to the highest energy densities in the water beam. As with impact ionization, these ions tend to have undergone greater fragmentation, less clustering, or even undergone dissociation. Conversely, ions which are

slow to traverse the LILBID drift region are larger and less fragmented (or more clustered, with reduced, thermalized speeds). To simulate the short "snapshot" of the impact plasma sampled by CDA, it is therefore necessary to generate and select suitable populations of ions which have undergone similar energetic conditions in the LILBID experiment. This is achieved by combining variations in laser power density with use of the aforementioned delay time windows.

7.5 Conclusions and outlook

The LILBID laboratory experiment is capable of successfully reproducing impact ionization mass spectra generated by micron- and sub-micron-sized icy dust grains impinging onto spaceborne mass spectrometers over a wide range of impact speeds. The mass spectra of Type 1 ice grains recorded by Cassini's CDA mass spectrometer at impact speeds ranging from 4 to 21 km/s can be reproduced using LILBID-MS by the selection of appropriate laser and ion extraction parameters. The shorter the delay time and the higher the laser's power density, the higher the simulated impact speed. The experimental settings inferred from comparison of this simple spectrum type that match the different speed regimes can now be applied to more complex spectra. Future work will extend these results to produce an accurate speed- and matrix-dependent analysis of CDA salt-rich Type 3 mass spectra. Type 3 mass spectra show characteristic mass spectral features arising from high concentrations of sodium salts (0.5–2 % by mass) (Postberg et al., 2009a; Postberg et al., 2011a). Earlier work (Postberg et al., 2009a) with a similar analogue experiment successfully reproduced co-added CDA Type 3 spectra produced by averaging over a large number of individual impact events but did not consider the effects of considerable variations in grain impact speeds. Compared with Type 1 grains, Type 3 grains bear sodium and potassium salts at much higher concentrations and are thought to be aerosolized samples of Enceladus' subsurface ocean water (Postberg et al., 2009a; Postberg et al., 2011a). In a similar way we can now also investigate the composition of organic-bearing Type 2 ice grains emitted by Enceladus (Khawaja et al., 2019; Postberg et al., 2008; Postberg et al., 2018a), which show characteristic mass spectral features arising from organic compounds, over a wide range of different impact speeds recorded by CDA, giving access to different, speed-dependent spectral fragmentation patterns of the organic molecules.

The broader general goal is to establish a high-resolution, bipolar (cation and anion), spectral library, covering a large sample of organic and inorganic compounds in a water matrix, applicable to future spaceborne impact ionization mass spectrometers. Because the ionization process is intimately linked to the impact speed, spectral appearance is a function not only of composition, but also of impact speed. With this work we have established a standard methodology for the laboratory reproduction of spectra over a wide range of impact speeds, which can be applied to the generation of a spectral library.

Acknowledgements

The authors thank Lenz Nölle and Zenghui Zou for valuable discussions. They acknowledge the work of the scientists and engineers of the Cassini team. The research leading to these results received financial support from the German Research Foundation (DFG) projects PO 1015/2-1, /3-1, /4-1, project AB 63/9-1, and ERC Consolidator Grant 724908-Habitat OASIS.

Handling editor: Pierre Thibault

8 Developing a Laser Induced Liquid Beam Ion Desorption spectral reference library for spaceborne mass spectrometers[1]

Summary

This is the abstract of the manuscript and is titled "Summary" here to separate it from the overall abstract of this thesis given on page vii.

SPACEBORNE IMPACT IONIZATION mass spectrometers, such as the Cosmic Dust Analyzer (CDA) on board the Cassini spacecraft or the SUrface Dust Analyzer (SUDA) being built for the future Europa Clipper mission, are of crucial importance for the compositional investigation of cosmic dust and the exploration of ocean worlds in the Solar System. Analogue experiments on Earth are essential for the interpretation of data produced by these instruments. To date, thousands of laboratory mass spectra recorded with a laser-based analogue experiment for impact ionization mass spectrometers have been recorded. Simulation of impact ionization mass spectra of ice grains of varying composition in space is achieved by a Laser Induced Liquid Beam Ion Desorption (LILBID) approach, in which a µm-sized liquid beam of fully controllable composition is intersected by a pulsed infrared laser. The generated cations or anions are analyzed in a Time-of-Flight (ToF) mass spectrometer. The amount of unsorted raw data is increasingly challenging to sort, process, interpret and compare with data from space. Thus was this has been achieved manually for individual mass spectra because no spectral reference library was available. We here describe the development of a comprehensive bipolar (cations and anions) mass spectral reference library containing data from the laboratory LILBID facility. The relational database is based on Structured Query Language (SQL) and enables filtering of the laboratory data using a wide range of experimental parameters (e.g. analytes, laser energy densities and mass lines). The mass spectra can be compared not only with data from past and future space missions but also mass spectral data generated by other. terrestrial, techniques. The database will be made available for general public in the future.

Keywords: LILBID, Space missions, Database, Analogue experiments, Ice grains, Ocean worlds

[1]This chapter as well as the corresponding supplementary information (appendix A) are a manuscript in preparation for submission with the following authors and working title: Klenner, F., Umair, M., Walter, S.H.G., Khawaja, N., Hillier, J., Nölle, L., Zou, Z., Abel, B., and Postberg, F. Developing a Laser Induced Liquid Beam Ion Desorption spectral reference library for spaceborne mass spectrometers.

8.1 Introduction

Impact ionization mass spectrometers on spacecraft probe in situ dust grains made of refractory material as well as ice grains, thereby providing important information about the grains' compositions and their sources (Kissel et al., 1986; Hillier et al., 2007; Kempf et al., 2008; Postberg et al., 2008; Postberg et al., 2009a; Postberg et al., 2011a; Postberg et al., 2018a; Hsu et al., 2015; Khawaja et al., 2019). In a typical impact ionization mass spectrometer, grains impinge onto the detector's target plate at hypervelocities ($>$ 1 km/s) and form impact clouds of cations, anions, electrons and neutral fragments. The cations or anions, depending on the instrument's polarity, are accelerated through an electric field towards a multiplier, which measures the flux of ions as a function of arrival time and subsequently result in Time-of-Flight (ToF) mass spectra.

Measurements by one such mass spectrometer, the Cosmic Dust Analyzer (CDA; Srama et al., 2004) on board the Cassini spacecraft, showed that a large part of the ice grains, ejected into space in the Saturnian system from Enceladus, were formed from subsurface liquid ocean water from within the icy moon (Postberg et al., 2008; Postberg et al., 2009a; Postberg et al., 2011a). The ice grains therefore provide insights into the chemical and physical properties of the subsurface ocean and the interactions between the ocean and the moon's rocky core (Postberg et al., 2009a; Postberg et al., 2011a; Postberg et al., 2018a; Kempf et al., 2010; Kempf et al., 2018; Hsu et al., 2015; Sekine et al., 2015; Khawaja et al., 2019). Other impact ionization mass spectrometers are currently being built, such as the Surface Dust Analyzer (SUDA; Kempf et al., 2014) or proposed, e.g. the Enceladus Ice Analyzer (ENIA; Srama et al., 2015b; Reh et al., 2016) for future space missions to icy moons in the outer Solar System. Another impact ionization mass spectrometer, selected for a future mission to the asteroid 3200 Phaeton, is the Destiny Dust Analyzer (DDA; Srama et al., 2019). For instrument calibration and data interpretation, laboratory analogue experiments are vital (e.g., chapter 7; Taubner et al., 2020). Accelerating nm- or µm-sized ice grains to relevant speeds in the laboratory is technically challenging, and the Laser Induced Liquid Beam Ion Desorption (LILBID) approach (Kleinekofort et al., 1996a; Kleinekofort et al., 1996b) has therefore been adapted to simulate the impacts of ice grains onto metal targets at different impact speeds in space (see chapter 7). In LILBID analogue experiments for instrument calibration, the compounds mixed with the water matrix and their concentrations are known and therefore compositional and non-compositional variations in mass spectra from space can be reproduced. This makes the LILBID simulation facility an essential tool for the interpretation of future space mission data.

In LILBID a pulsed infrared laser irradiates a µm-sized liquid water beam with substances dissolved therein. The transferred laser energy mechanically disrupts the liquid beam, producing charged fragments (Charvat and Abel, 2007; Wiederschein et al., 2015). The cations and anions are analyzed in a commercial ToF mass spectrometer. Collisional impacts onto space detectors and LILBID create almost exclusively singly charged species (Karas et al., 2000) and the ions' flight times are therefore only

dependent on the ions' masses. The LILBID facility was further adapted (e.g., Beinsen 2011, Stolz 2016) to become a vital tool for exploring the ocean worlds in the Solar System using data from past space missions (Postberg et al., 2009a; Postberg et al., 2011a; Postberg et al., 2018a; Khawaja et al., 2019) as well as preparing for future space missions (this thesis; Taubner et al. 2020). In addition to applications in space, LILBID mass spectrometry is commonly used for structural analyses of organic molecules (Morgner et al., 2006; Morgner et al., 2007; Morgner et al., 2008; Mager et al., 2010; Peetz et al., 2018). Further applications also include the medical field, such as the diagnoses of diseases (Patel, 2015; Sim et al., 2015) and pancreatic cancer research (Grüner et al., 2012; Padoan et al., 2013; Zhong et al., 2015).

Much of the data conveyed from mass spectrometers on spacecraft (e.g., CDA on board Cassini) remains uninvestigated because manual evaluation of the large datasets is required. Laboratory LILBID datasets have also been manually investigated thus far. A complete comparison of e.g. CDA spectra with laboratory LILBID spectra is extremely time consuming, and still in progress. For example, only about 15 % of all CDA mass spectra obtained from July 2004 to September 2017 has so far been investigated and compared with laboratory analogue data. It is therefore clear that an easily accessible and organized database, containing all laboratory LILBID mass spectra, will facilitate the more rapid evaluation of flight data from not only CDA but particularly future spaceborne instruments, such as SUDA (Kempf et al., 2014), ENIA (Srama et al., 2015b; Reh et al., 2016) and DDA (Srama et al., 2019). In contrast to CDA data, the prospective data can then be investigated without any further delay.

Existing databases containing mass spectrometric data created through diverse ionization methods include the NIST Chemistry WebBook (https://webbook.nist.gov/), the mzCloud Advanced Mass Spectral Database (https://www.mzcloud.org/), the MassBank of North America (MoNA; https://mona.fiehnlab.ucdavis.edu/) and a database for oligosaccharides in human milk (Remoroza et al., 2018). However, to the best of our knowledge, no such accessible spectral reference library for LILBID data exists.

We here describe the development and function of a database containing LILBID mass spectra based on a Relational Database Management System (RDBMS) and Structured Query Language (SQL). The frontend to the database enables the sorting and filtering of laboratory LILBID data via a range of parameters adjustable on the experimental setup (e.g. laser energy) as well as parameters that depend on the measured substances (e.g. compositions and concentrations). These parameters are important for the analysis and subsequent interpretation of data from space as, for example, the combination of delay time and laser energy in the LILBID system can be related to the impact speeds of the ice grains onto the spaceborne mass spectrometer (see chapter 7). A peak detection routine applied to all stored data enables queries for certain spectral signals, i.e. single mass lines as well as combinations of mass lines.

The ease and rapidity of interrogating a large library of calibration data, provided through the comprehensive spectral reference library, sig-

nificantly improves analyses of mass spectra from space and thereby aids planning for future space missions. The LILBID data can also be compared rapidly and reliably with many other kinds of available mass spectrometric data. The developed database will continuously be improved as well as be made available for general public in the future.

8.2 Methods

Mass spectra recorded with the LILBID setup are processed and stored in a newly developed mass spectral reference library. The experimental LILBID setup, the data pre-processing, the development of the mass spectral reference library, and the manual data post-processing are described below.

8.2.1 The LILBID facility

Figure 7.2 is shown in the original manuscript and has been removed here to avoid repetition.

The experimental setup used to generate the LILBID mass spectra (Figure 7.2) is described in detail in chapter 7. We therefore only provide a brief overview here.

A liquid water beam (radius of 7-10 µm) containing dissolved, or suspended, substances is injected into a high vacuum (5×10^{-5} mbar) at an adjustable flow rate of 0.15-0.25 mL/min. The liquid beam is irradiated by a pulsed infrared laser (20 Hz, 7 ns pulse length, wavelength $\approx$ 2850 nm) with adjustable pulse energies of up to 4 mJ, heats up due to the energy transferred from the laser, and explosively disperses into atomic, molecular and macroscopic fragments. The created cations or anions, depending on the instrument's polarity, are analyzed in a commercial reflectron-type (Mamyrin, 1994) ToF mass spectrometer at $\approx 10^{-7}$ mbar. In addition to pure water, mixtures of water with organic solvents can be used as matrix solutions and therefore all water soluble and many water insoluble substances can be measured and investigated with the LILBID setup. The mass spectrometer uses the principle of delayed extraction, in which the created ions are extracted as a function of their initial velocities (see chapter 7). The generated mass spectral signals (sampling interval: 1 ns) are amplified, digitized using an 12-bit Analogue to Digital Converter (ADC) and recorded with a LabVIEW®-controlled computer that calibrates the ions' flight times onto a mass scale by using a second order equation (Christian et al., 2000). Typically 300 – 500 mass spectra are averaged to improve the signal-to-noise ratio. The current experimental setup (Figure 7.2) has a mass resolution of between 600 and 800 m/Δm (Full Width at Half Maximum, FWHM).

8.2.2 Data pre-processing

At the time of implementing the data acquisition process using LabVIEW®, use of a database to store the spectra was not foreseen. Instead, a major focus was on the quick and easy manual location of different measurements stored on the hard drive of the analyzing scientist's computer. Therefore it was originally decided to have one line (the "solution" line; Figure A.1) in the header of the recorded raw data files (level-0), which

includes numerous significant parameters, such as the names of the used substances and their concentrations, separated by the "underscore" special character. This line, combined with several other significant experimental parameters that are provided in other header lines, is then used as the filename for the raw data files. This enabled easy manual location of the measurements relevant to certain substances, their concentrations and significant experimental parameters. However, combining different parameters in the same header line of the data files (Figure A.1) turned out to be a major challenge with regards to automatic processing of the data files and this information could not simply be ingested into a RDBMS. Additionally, there were inconsistencies in the naming of the files depending on the respective person performing the measurement. For these reasons, we apply a validation script which checks for the correct number (seven) of underscores in the solution name. If the data file does not pass this first validation script, it has to be manually examined and edited to conform to the right format. The other values from the headers of the mass spectra text files are extracted and re-arranged (data cleaning). The data files are reformatted such that each header line contains information about a single experimental parameter. An example header from a level-1 data file can be found in Figure A.2.

After the file format check and any required manual editing, a peak detection routine is applied to the spectra. The peak detection routine is implemented in Python using the find_peaks_cwt algorithm within the SciPy scientific library. Its general approach is to smooth the data by convolving it using a wavelet transformation and then find relative maxima which appear over sufficient length scales and with suitably high signal-to-noise ratios (https://docs.scipy.org/doc/scipy/reference/signal.html). The peak detection routine calculates a local baseline for a variable number of data points (we use 220 data points) and uses a local percentile rank of 30 for the peak detection threshold. The resulting peak tables are stored in a separate text file on the server, together with graphical plots (PNG format) of the level-1 mass spectra generated using Python Matplotlib. The currently used software versions can be found in Table A.1.

The complete data pre-processing, including data validation, peak detection and plotting of the single raw data spectra, is implemented via a combination of several Python scripts called from a Bash shell script. After data pre-processing the files are ready for ingestion into the database.

8.2.3 The database system

We use a client-server infrastructure as the general system design with the web browser representing the client and an RDBMS together with a web server acting as the backend. The spectrum parameters and extracted peaks are stored as relational tables in a MariaDB instance. An Apache™web server serves as the frontend in the form of a query form with entry fields for several possible parameter filters. After the user enters none, one or several filter parameters and submits the query, the server connects to the database and retrieves the relevant entries. Without entering any filter values and subsequent submission, the server lists

all available entries. As the peak identities are stored in the database, the data can be filtered not only for the experimental parameters used during the measurements but also for the peaks present in the mass spectra. The layout of the user interface allows for adjustable block-wise (10, 25, 50 or all entries per block) browsing of the data. The frontend's web pages are implemented using Hypertext Markup Language (HTML), Hypertext Preprocessor (PHP), Cascading Style Sheets (CSS) and JavaScript.

A complete workflow of the steps from data acquisition in the laboratory, data validation/cleaning, data ingestion and finally the data query is shown in Figure 8.1. As new laboratory data is acquired, the database will be updated using the combined Bash/Python script (see section 8.2.2).

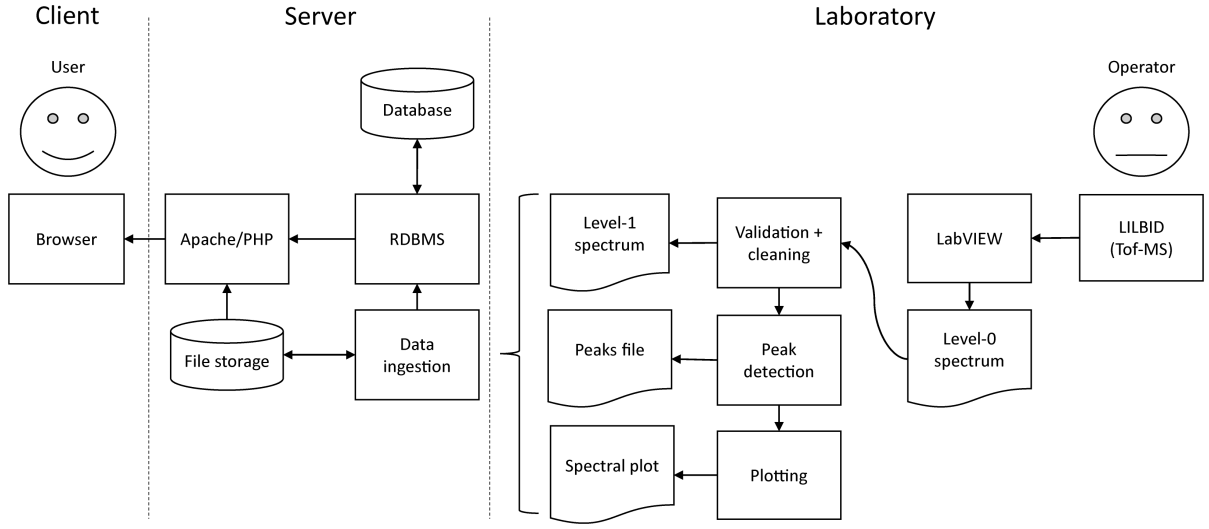

Figure 8.1: *Flowchart of the database system including (from right to left) data acquisition, data pre-processing and data ingestion. Processes shown to the right, with exception of the LILBID technique itself, are performed on the laboratory computer (sampling). Processes shown to the left are performed on the server (pre-processing, ingestion and data retrieval).*

8.2.4 Manual data post-processing

The level-1 mass spectra files are reorganized text files (Figure A.2) with a header that contains a unique spectral identifier (date and time) and information about experimental parameters (examined substances, solution, delay time, number of averaged spectra etc.). Below the header, the text files contain two columns with the x- and y- values (floats) of the mass spectra, with x representing mass (in u) and y representing intensity (in V). The time interval between two lines of the columns corresponds to the sampling interval of the measurement computer (1 ns; see section 8.2.1).

Software on the measurement computer converts the ions' flight times into their masses by use of a second order calibration equation. The applied delayed extraction method (see chapter 7) and variable initial ion velocities result in unavoidable mass shifts (deviances up to > 1 u) of the converted masses compared to the real ion masses in level-1 spectra during conversion of the ions' flight times into their masses (Christian et al., 2000), with increasing mass shifts for increasing ion masses.

For a reliable analysis of the mass spectra, it is critical to recalibrate the mass spectra to minimize the mass shifts. Recalibrated level-2 mass spectra are produced by using a semi-automatic Python script. The script calculates a polynomial function based on manually inserted real peak masses (x-values) for previously detected (shifted) peaks and fits the corresponding data file with this function.

The resulting level-2 spectra still often possess an uneven baseline due to instrumental, chemical and random background noise during the measurements (Urban and Štys, 2015). The noise can either produce fake peaks (fake mass lines) or hide small peaks in the mass spectra. To fully understand the mass spectra and further improve the spectral analysis, the noise needs to be subtracted. Several methods and programs exist that are capable of subtracting the baselines from mass spectra (Xu et al., 2011; Urban and Štys, 2015). We here use the commercial software OriginPro® to create baseline subtracted data (level-3) using the Asymmetric Least Squares Smoothing (ALS) algorithm (Eilers, 2003).

The peaks in the level-3 mass spectra are then labeled with their corresponding masses (x-values). Peak identification is performed either manually, or automatically using a software. Automatic peak detection routines can reliably detect peaks with significantly high amplitudes (y-values) but might overlook smaller peaks and detect false positives (fake peaks). For the reliable detection of small peaks, manual peak identification is indispensable. After peak detection, the mass spectra can be analyzed in detail and compared to mass spectra recorded in space.

When data is chosen for post-processing and graphical plots of level-2 or level-3 mass spectra are created (in PNG or PDF format), they replace the graphical plots of the level-1 mass spectra on the database server.

8.3 Results and discussion

8.3.1 The new LILBID spectral reference library

The spectral reference library currently contains more than 10,000 LILBID mass spectra recorded using a wide range of experimental parameters. Figure 8.2 shows the search interface of the spectral reference library. The data in the library can be searched using numerous experimental parameters, as described below, in order from upper left to lower right in the search interface.

Substance: The name of the analyte.

Matrix: The name of the solvent.

Peaks: The peaks in the mass spectra (x-values with significantly high y-values) created by the analyte, the solvent and physio-chemical interactions between both. The peaks are detected by a peak detection routine (see section 8.2.2). An error (±) can be applied because of the potential peak shifts in level-1 mass spectra (see section 8.2.4).

Date: The measurement date.

Ion Mode: Ion mode of the mass spectrometer, i.e. positive (cations) or negative (anions).

Plasma or Desorption: Mass spectra are recorded either in the 'plasma' regime (water molecules are broken) or in the desorption regime (water molecules are intact). For further information about the two regimes, we refer to chapter 7.

Numerical abundances of the most common elements in the used analytes' molecular structures. The most common elements are carbon (C), hydrogen (H), nitrogen (N), oxygen (O), sodium (Na), potassium (K), chlorine (Cl), phosphorus (P), and sulfur (S).

Laser intensity: The intensity of the laser (typically varying from 85 to 100 %).

Flashlamp Energy: The energy of the laser's flashlamp during laser pumping (typically between 5.30 and 5.46 J).

Energy Density: The laser's energy density results from the used laser intensity and flashlamp energy (typically between 400 and 1150 MW/cm^2.

Delay Time: The time between laser shot and ion acceleration (typically between 3.8 and 7.8 µs). A combination of delay time and energy density can be correlated to impact speeds of ice grains onto mass spectrometers in space (see chapter 7).

MCP: The voltage applied to the Microchannel Plate (MCP) detector (typically ranging from 1.40 to 1.55 kV).

Wavelength: The used wavelength of the Nd:YAG infrared laser (typically 2480 nm).

Number of Spectra: The number of averaged mass spectra used to achieve the respective mass spectrum stored on the database server (typically between 300 and 500).

The data can be filtered using either a single experimental parameter or a combination of multiple experimental parameters. When applying the filter, all matches will be shown in the results interface (Figure 8.3) and can be sorted by individual parameters. The level-1 mass spectra text files can be retrieved through their dates, which are the spectra's unique identifiers. Graphical plots of the mass spectra (level-1, level-2 or level-3) can be retrieved via the 'Images' column. A search function on the top right of the results interface lets one search for individual spectra within the results interface (Figure 8.3).

Other available databases (see section 8.1) can provide structural information or thermodynamic data about an analyzed single substance. In contrast, the LILBID spectral reference library contains mass spectra of single substances and mixtures of substances in variable background matrices recorded with varying sets of experimental parameters that are important for comparison with and interpretation of impact ionization mass spectra recorded in space.

The data in the LILBID spectral reference library can be searched for particular peaks in the mass spectra after processing with the peak detection routine (see section 8.2.2). If the baseline is extremely bumpy and varies by at least half an order of magnitude (caused by e.g. very salty measuring solutions or high MCP voltages) or if the dynamic range (ratio of the largest to smallest detected signal) of the recorded mass spectrum is clearly below 10^1, tiny peaks are potentially not detected and the routine

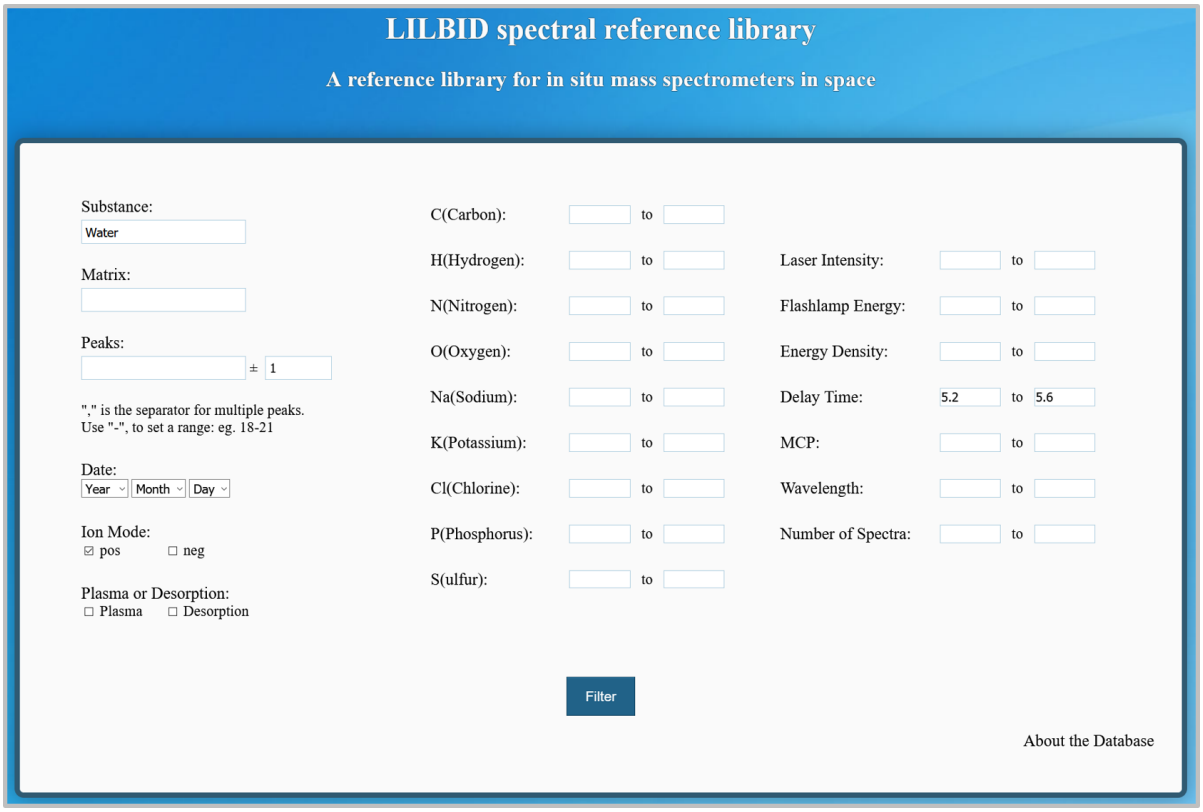

Figure 8.2: *Search interface of the LILBID mass spectral reference library. The library is capable of filtering via several adjustable setup parameters (e.g. laser intensity and delay time) as well as parameters that depend on the measuring solution (e.g. substance name and apparent peaks in the mass spectra). Here, as an example, given input parameters are I. Substance = Water, II. Ion Mode = positive, III. Delay Time = 5.2 – 5.6 µs. Filtering for these input parameters results in the interface shown in Figure 8.3.*

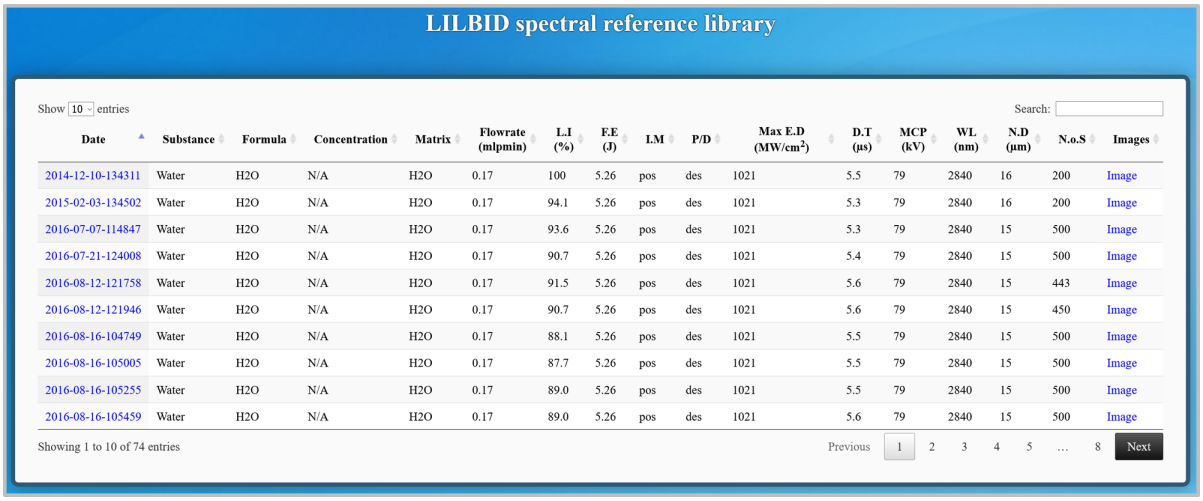

Date	Substance	Formula	Concentration	Matrix	Flowrate (ml/min)	L.I (%)	F.E (J)	I.M	P/D	Max E.D (MW/cm²)	D.T (µs)	MCP (kV)	WL (nm)	N.D (µm)	N.o.S	Images
2014-12-10-134311	Water	H2O	N/A	H2O	0.17	100	5.26	pos	des	1021	5.5	79	2840	16	200	Image
2015-02-03-134502	Water	H2O	N/A	H2O	0.17	94.1	5.26	pos	des	1021	5.3	79	2840	16	200	Image
2016-07-07-114847	Water	H2O	N/A	H2O	0.17	93.6	5.26	pos	des	1021	5.3	79	2840	15	500	Image
2016-07-21-124008	Water	H2O	N/A	H2O	0.17	90.7	5.26	pos	des	1021	5.4	79	2840	15	500	Image
2016-08-12-121758	Water	H2O	N/A	H2O	0.17	91.5	5.26	pos	des	1021	5.6	79	2840	15	443	Image
2016-08-12-121946	Water	H2O	N/A	H2O	0.17	90.7	5.26	pos	des	1021	5.6	79	2840	15	450	Image
2016-08-16-104749	Water	H2O	N/A	H2O	0.17	88.1	5.26	pos	des	1021	5.5	79	2840	15	500	Image
2016-08-16-105005	Water	H2O	N/A	H2O	0.17	87.7	5.26	pos	des	1021	5.5	79	2840	15	500	Image
2016-08-16-105255	Water	H2O	N/A	H2O	0.17	89.0	5.26	pos	des	1021	5.5	79	2840	15	500	Image
2016-08-16-105459	Water	H2O	N/A	H2O	0.17	89.0	5.26	pos	des	1021	5.6	79	2840	15	500	Image

Figure 8.3: *Results interface of the LILBID mass spectral reference library after filtering for example input parameters (see Figure 8.2). Formula: Chemical formula of the analyte. Concentration: Concentration of the analyte. Flowrate: Flow rate of the liquid beam. L.I: Laser intensity. F.E: Flashlamp energy. I.M: Ion mode. P/D: Plasma or desorption. Max E.D: Maximum possible energy density at the time of recording. D.T: Delay time. W.L: Wavelength of the laser. N.D: Diameter of the nozzle used to inject the liquid beam. N.o.S: Number of spectra.*

detects a sparse number of fake peaks instead. This algorithm will be further improved in the future.

Another future improvement will be to provide additional important information about the measured substances (solubility in water, toxicity etc.) without adding new columns to the DBMS to maintain the database as small and efficient as possible. To achieve this, clicking on the substance names in the database will redirect to their corresponding Wikipedia articles.

We also plan to implement a function to filter using the chemical families of the used analytes (e.g., salts, alcohols, ketones etc.).

8.3.2 Science case: Data post-processing of a LILBID mass spectrum and comparison with a CDA mass spectrum

Graphical plots of an example LILBID mass spectrum at different data processing stages (levels) are shown in Figure 8.4. The mass spectrum was recorded in the positive ion mode using water containing about 10^{-7} M NaCl as the analyte. The applied experimental parameters correspond to intermediate impact speeds (8-10 km/s) of ice grains onto spaceborne mass spectrometers (see chapter 7; Figure 8.5). Peaks in the mass spectrum represent cationic water species of the form $[(H_2O)_{0-3}H_3O]^+$ and cationic sodium-water species of the form $[(H_2O)_{0-2}Na]^+$.

The level-1 mass spectrum has a slightly uneven baseline and peak shifts of about 0.1 u from the correct isotopic masses. Uneven baselines and peak shifts can hinder analysis of more complex mass spectra (e.g. spectra of organic mixtures or high salinity solutions). In level-2 mass spectra, peak shifts are reduced and level-3 mass spectra are additionally baseline corrected, which aids peak detection and subsequent spectral analyses (Figure 8.4). After processing to level-3, and with the current mass resolution of the laboratory ToF-MS (600 – 800 m/Δm), it is often possible to resolve interfering species at the same integer mass with a mass difference of about 0.15 to 0.25 u (chapter 10).

So-called Type-1 mass spectra from ice grains recorded by the CDA in the Saturnian system show peaks that are almost exclusively related to cationic water species of the form $[(H_2O)_nH_3O]^+$ with n ranging from 0 to $>$ 10 (Postberg et al., 2008; Postberg et al., 2009a). In addition to cationic water species, occasional traces of sodium can be observed in Type-1 spectra. One such spectrum is shown in Figure 8.5. The much lower mass resolution of the CDA instrument (20-50 m/Δm; Srama et al., 2004) compared to the LILBID setup (600-800 m/Δm) is apparent. The spectrum shows the same water and sodium-water species as the laboratory LILBID spectrum (Figure 8.4) at similar relative abundances, with $[H_3O]^+$ at m/z 19 being slightly more abundant in the CDA spectrum and $[H_2O]_3H_3O^+$ at m/z 73 being slightly more abundant in the LILBID spectrum. For an even better quantitative match with flight mass spectra, laboratory spectra generated using different experimental parameters can be co-added (see chapter 7).

As well as water dominated LILBID mass spectra, more complex spectra, such as those from organic mixtures, salty solutions or even both

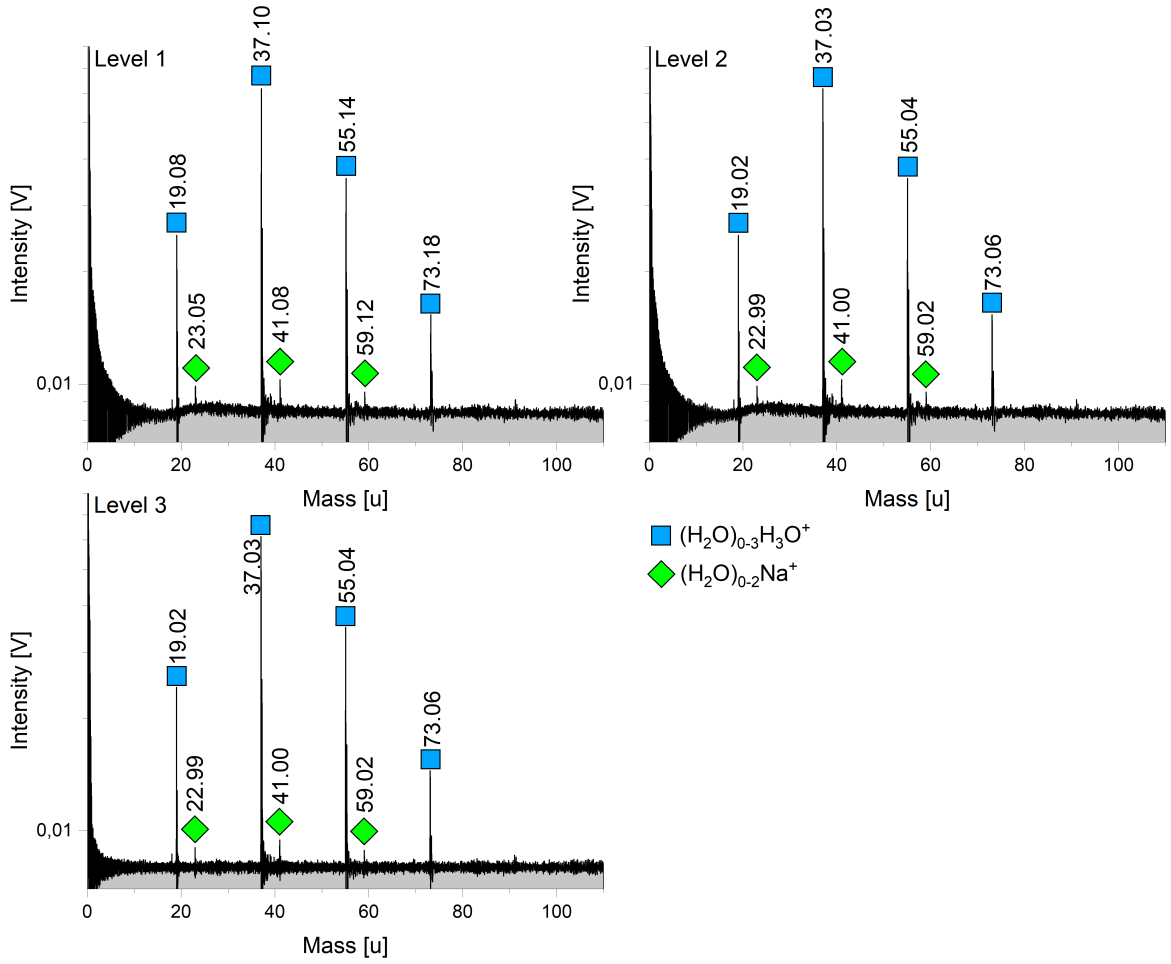

Figure 8.4: *Graphical plots of the same LILBID mass spectrum at different data processing stages (levels). The plots show a cation mass spectrum of water with an NaCl concentration of approximately 10^{-7} M generated using a delay time of 5.5 µs and a laser intensity of 98.5 %. The peaks are labeled with corresponding masses (x-values). Top left: The pre-processed data (level-1) shows a slightly bumpy baseline and peaks shifted from their real isotopic masses. The text file's header can be found in Figure A.2. Top right: The recalibrated data (level-2) shows a slightly bumpy baseline but corrected isotopic masses. Bottom left: The recalibrated and baseline corrected data (level-3) exhibits an even baseline and corrected isotopic masses.*

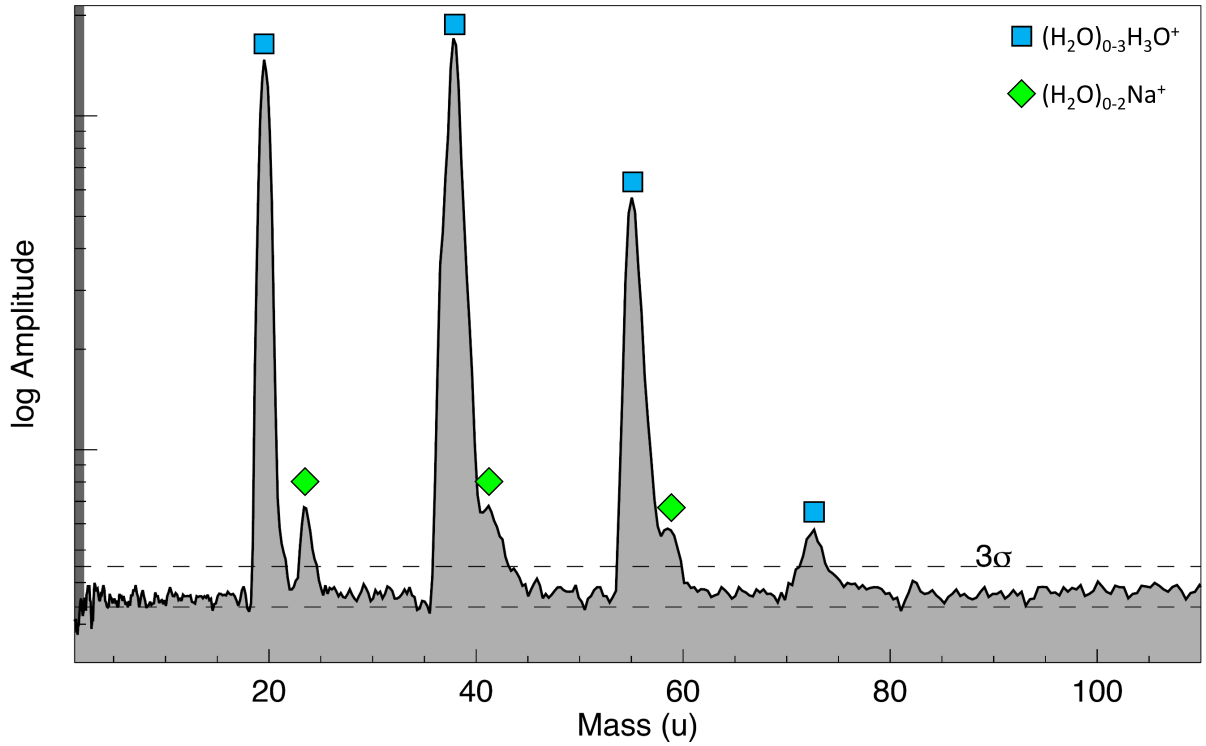

Figure 8.5: *Baseline corrected CDA mass spectrum of a nearly pure water ice grain containing traces of sodium (Type-1; Postberg et al. 2008, 2009a) recorded in the Saturnian system. The ice grain hit the mass spectrometer on the orbiting Cassini spacecraft at a relative speed of approximately 9 km/s. The spectrum shows the same water species, at similar relative abundances, as the LILBID mass spectrum in Figure 8.4.*

together can be compared to impact ionization mass spectra from space (e.g. Postberg et al., 2009a; Postberg et al., 2018a; Khawaja et al., 2019). The LILBID mass spectra can also be used to forecast the potential mass spectral appearance of all water soluble and many water insoluble substances that might appear in ice grains emitted by extraterrestrial active ocean worlds (e.g. as demonstrated in chapters 9 and 10).

8.4 Conclusions and outlook

The laboratory LILBID facility has been proven to simulate the spectra produced by ice grain impacts onto spaceborne mass spectrometers. Variations in spectra due to the ice grains' compositions and impact speeds can be accurately reproduced by adjusting appropriate experimental parameters (chapters 7, 9, and 10; Postberg et al., 2009a; Postberg et al., 2018a; Khawaja et al., 2019). Over 10,000 LILBID mass spectra of more than 200 substances, each with their associated experimental parameters, have been uploaded to a LILBID mass spectral reference library. The library, containing cation and anion mass spectra, filters the spectra for the used experimental parameters that can be compared to different properties of the encountered ice grains in space. Processing by a peak detection routine allows the mass spectra to be selected based on the appearance of particular peaks. Filtering by experimental parameters and peaks lets characteristic mass spectra be selected for further analysis.

LILBID data processing, mass spectral analysis and comparison of

LILBID data with data from space follow a predictable, repetitive pattern. This pattern can be executed more rapidly and efficiently, with reducing risk of user error, by use of the automated processing steps and database storage described above. The database therefore improves the analysis of mass spectra of ice grains recorded in space, from not only past missions (e.g. Cassini) but also future missions with higher resolution mass spectrometers, such as NASA's Europa Clipper (Howell and Pappalardo, 2020) in particular. Future data from space can straightforwardly be investigated without any delay. The database can also be used to compare LILBID data with many other types of mass spectrometric data, for example with electron ionization mass spectra from the NIST Chemistry WebBook (https://webbook.nist.gov/).

The database is designed to be continuously improved. The peak detection algorithm will be modified to detect very small peaks and exclude fake peaks even more reliably. We will add a function to filter the measured substances for chemical families and general information about the measured substances will be rapidly retrievable in future. Newly recorded spectra will be regularly uploaded to the database. The LabView component will be adapted to improve the header definition, so that manual data cleaning is no longer necessary. We plan to enhance the capabilities of the LILBID setup to also analyze neutral atoms created by the infrared laser hitting the water beam, which are suspected to be more abundant than ions in the impact cloud of ice grains. The database will then also contain LILBID analogue mass spectra applicable to neutral gas mass spectrometers, such as the Particle Environment Package - Neutral Ion Mass Spectrometer (PEP-NIM; Barabash et al. 2013) or the MAss Spectrometer for Planetary EXploration (MASPEX; Brockwell et al., 2016) on board ESA's Juice (Grasset et al., 2013) and NASA's upcoming Europa Clipper (Howell and Pappalardo, 2020) missions to the Jovian System, respectively.

The LILBID spectral reference library is currently accessible to group members at Freie Universität Berlin and a fully-functional version lacking access only to the raw data (available on request to collaborators) will be made available to the general public in the future.

Acknowledgements

The authors thank René Reviol and Ferdinand Stolz for fruitful discussions. The research leading to these results received funding from the German Research Foundation (DFG) projects PO 1015/3-1, /4-1, project AB 63/9-1 and from the European Research Council (ERC) under the European Union's Horizon 2020 research and innovation program (ERC Consolidator Grant 724908-Habitat OASIS). The mass spectra in the spectral reference library were recorded at the Institute of Earth Sciences, Ruprecht-Karls-Universität Heidelberg, Germany, at the Institute of Geological Sciences, Freie Universität Berlin, Germany and at the Wilhelm-Ostwald-Institute for Physical and Theoretical Chemistry, Universität Leipzig, Germany.

Author disclosure statement

No competing financial interests exist.

III. Experiments with amino acids, fatty acids, and peptides for the detection of biosignatures in ice grains from extraterrestrial ocean worlds

9 Analogue experiments for the identification of trace biosignatures in ice grains from extraterrestrial ocean worlds[1]

Summary

This is the abstract of the original publication and is titled "Summary" here to separate it from the overall abstract of this thesis given on page vii.

RELIABLE IDENTIFICATION of biosignatures, such as amino acids, fatty acids, and peptides, on extraterrestrial ocean worlds is a key prerequisite for space missions that search for life or its emergence on these worlds. One promising approach is the use of high-performance *in situ* impact ionization mass spectrometers to sample water ice grains emerging from ocean-bearing moons such as Europa or Enceladus. A predecessor of such detectors, the Cosmic Dust Analyzer on board the Cassini spacecraft, has proven to be very successful in analyzing inorganic and organic ocean constituents and with that characterizing the habitability of Enceladus ocean. However, biosignatures have not been definitively identified in extraterrestrial ocean environments so far. Here, we investigate with an analogue experiment the spectral appearance of amino acids, fatty acids, and peptides in water ice grains, together with their detection limits, as applicable to spaceborne mass spectrometers. We employ a laboratory-based laser induced liquid beam ion desorption technique, proven to simulate accurately the impact ionization mass spectra of water ice grains over a wide range of impact speeds. The investigated organics produce characteristic mass spectra, with molecular peaks as well as clearly identifiable, distinctive fragments. We find the detection limits of these key biosignatures to be at the µM or nM level, depending on the molecular species and instrument polarity, and infer that impact ionization mass spectrometers are most sensitive to the molecular peaks of these biosignatures at encounter velocities of 4–6 km/s.

Keywords: Enceladus, Europa, Plume, Extraterrestrial life, Mass spectrometry, Space missions

[1]This chapter as well as the corresponding supplementary information (appendix B) are published as: Klenner, F., Postberg, F., Hillier, J., Khawaja, N., Reviol, R., Stolz, F., Cable, M.L., Abel, B., and Nölle, L. (2020). Analog experiments for the identification of trace biosignatures in ice grains from extraterrestrial ocean worlds. *Astrobiology*, 20(2):179–189. DOI: 10.1089/ast.2019.2065

9.1 Introduction

One of the most compelling questions in planetary science is whether life might originate or be sustained on a world other than the Earth. In our own solar system, we may have the opportunity to test this hypothesis by exploring Mars or extraterrestrial ocean worlds such as Enceladus and Europa (Lunine, 2017; Hendrix et al., 2019). These moons of Saturn and Jupiter, respectively, host global, subsurface, liquid water oceans (Khurana et al., 1998; Thomas et al., 2016) with conditions possibly suitable for life or its emergence (Hand et al., 2007; Glein et al., 2018; McKay et al., 2018). The Cassini mission identified and sampled a plume of gas and water ice grains at Enceladus' South Pole via multiple flybys, confirming that the plume material was sourced from the interior ocean (Postberg et al., 2008; Postberg et al., 2009a; Waite et al., 2009; Hsu et al., 2015). A similar plume may also be present at Europa (Roth et al., 2014; Sparks et al., 2016; Sparks et al., 2017; Jia et al., 2018). Sampling the icy grains of these plumes may, therefore, be a straightforward and cost-effective means of assessing the composition of the extraterrestrial ocean beneath.

Impact ionization mass spectrometers, such as the Cosmic Dust Analyzer (CDA) (Srama et al., 2004) on the Cassini spacecraft or the Surface Dust Analyzer (SUDA) (Kempf et al., 2014) on board Europa Clipper, can measure the composition of plume ice grains by analyzing the mass spectra of ions generated by high-velocity (>1 km/s) impacts of these grains onto an impact target. The Cassini spacecraft revealed that $\sim$ 25 % of the ice grains emerging from Enceladus contain detectable organic material (Postberg et al., 2011a; Postberg et al., 2018b). Many of these exhibit signs of volatile aliphatic nitrogen- and oxygen-bearing, and aromatic compounds (Khawaja et al., 2019), and 1-4 % of the organic-rich ice grains even contain complex organic macromolecules at high ($\geq$0.5 wt %) concentrations (Postberg et al., 2018a). However, it is still unclear whether these organic materials contain biosignatures. This might be difficult to achieve with the limited mass resolution (20-50 m/Δm) and range (usually up to m/z 200) of Cassini's CDA (Srama et al., 2004) but will certainly be possible for SUDA (150-200 m/Δm up to m/z 500) at Europa (Kempf et al., 2014) and mass spectrometers on future Enceladus missions, such as the Enceladus Ice Analyzer (ENIA; $\sim$ 2000 m/Δm, up to m/z 2000) (Srama et al., 2015a; Reh et al., 2016).

Two classes of organic molecules that have been suggested to be potential biosignatures in extraterrestrial ocean environments are amino acids and fatty acids. Amino acids are found in meteorites (Cronin and Pizzarello, 1983) and can be generated abiotically, such as via Friedel-Crafts reactions during water-rock interaction (e.g. Menez et al., 2018) under conditions similar to those suspected to be found on Enceladus (Postberg et al., 2018b); however, abiotic synthesis follows the rules of thermodynamics and results in an excess of the simplest amino acid (glycine [Gly]) compared with the others (Higgs and Pudritz, 2009). In systems modified by biotic processes, more complex amino acids become prevalent, and Gly no longer is the most abundant amino acid present; therefore, the ratio of various amino acids (e.g., aspartic acid [Asp] and serine [Ser]) to Gly can

be considered as a biosignature (Dorn et al., 2011; Davila and McKay, 2014; Reh et al., 2016; Sherwood, 2016; Creamer et al., 2017). Similarly, the prevalence of peptides - polymers of two or more amino acids that combine to form proteins - may also indicate active biochemistry in an extraterrestrial ocean, as the rate of generation of these complex organic molecules must have exceeded the rate of decomposition via hydrolysis or other mechanisms. Indeed, the presence of specific amino acids such as Asp, Ser, and arginine (Arg) may indicate either active biotic or abiotic production, as these amino acids are degraded over relatively short geological timescales (<1 Ma) (Truong et al., 2019).

Fatty acids can also serve as biosignatures. These molecules are found in the lipid membranes of all known lifeforms, and they exhibit something known as the "Lego principle" - biological processes use a selected set of molecules (McKay, 2004). For most organisms, fatty acids are generated biochemically by the addition of two carbon atoms at a time, leading to an excess of fatty acids with an even number of carbon atoms; for *Archaea*, the addition is via a five-carbon isoprene subunit, leading to a carbon chain pattern divisible by five (Georgiou and Deamer, 2014). In abiotic (Fischer-Tropsch) synthesis, carbons are added one at a time, so no such pattern is observed. Assessment of the fatty acid distribution can, therefore, serve as a discriminator for biosignatures in an extraterrestrial ocean environment (Dorn et al., 2011; Reh et al., 2016; Sherwood, 2016).

The ability to detect and quantify amino acids, peptides, and fatty acids is important to determine the presence of life in an extraterrestrial ocean. In this work, we investigate and, in turn, simulate what the characteristic signals of these biosignatures would be in a spaceborne mass spectrometer if these substances were embedded in ice grains, and we infer the detection limits for these compounds for CDA-, SUDA-, or ENIA-like instruments sampling an Enceladus or Europa plume at hypervelocity.

9.2 Methods

9.2.1 Scientific approach

Impact ionization records time-of-flight (TOF) mass spectra of ions generated by high-velocity (≥1 km/s) impacts of individual grains onto a metal target (Postberg et al., 2011b; Srama et al., 2004; Kempf et al., 2014; Reh et al., 2016). The majority of TOF impact ionization mass spectrometers that have so far measured cosmic dust in situ, such as CDA on board Cassini (Srama et al., 2004) or the Dust Impact Mass Analyzer instruments (PUMA 1 and 2) on board the Vega missions (Kissel et al., 1986), are sensitive only to cations. The Cometary and Interstellar Dust Analyzer (CIDA) on Stardust was a notable exception (Brownlee et al., 2003), capable of producing anion mass spectra, and proposed impact ionization mass spectrometers, such as the SUDA (Kempf et al., 2014) or the ENIA (Mitri et al., 2018; Reh et al., 2016), will also have this capability.

At relevant impact speeds, the impact ionization process almost exclusively creates singly charged ions, and therefore the spectral peak positions (ion arrival times) are only dependent on the masses of the atoms and molecules. Previous work has shown spectral variations introduced

by varying ionization conditions due to different impact velocities of ice grains can be precisely reproduced with a laser-based analogue experiment (see chapter 7), as can the effects of varying grain compositions. By comparing laboratory spectra with those recorded in space (Postberg et al., 2009a; Postberg et al., 2011a; Postberg et al., 2018a; Khawaja et al., 2019), the compositions of the ice grains can be investigated in detail, because the compounds and concentrations measured in a water matrix with the analogue experiment are well known. In this work, we use the laser-based analogue experiment to investigate the mass spectral appearance of various amino acids, fatty acids, and peptides dissolved in H_2O to infer characteristic mass peaks, cleavages of the parent molecules, and resulting peak patterns. These laboratory data are archived in the form of an internal database (spectral reference library) and can be compared with results from previous and future space missions.

9.2.2 Experimental description

Figure 7.2 is shown in the original publication and has been removed here to avoid repetition.

The experimental setup utilized in Heidelberg and Leipzig for this work presented here (Figure 7.2) is described in detail in chapter 7, and, as such, we only provide a brief overview here.

The setup applies a technique known as laser induced liquid beam ion desorption (LILBID) (Karas et al., 1991; Karas et al., 2000). The impact ionization process of ice grains is simulated by intersecting a mm-sized water beam with a pulsed infrared (IR) laser (2840 nm, 20 Hz, 7 ns pulse length), which operates at adjustable laser intensities (0-100 %). When the water beam absorbs the laser energy, it is heated up and explosively disperses into atomic, molecular, and macroscopic fragments. Cations and anions can then be analyzed in a reflectron TOF-MS with a mass resolution of about 800 m/Δm and a mass range m/z > 10,000, after passing through a field-free drift region. The mass spectrometer uses the principle of delayed extraction (see chapter 7), in which setting a delay time before ion extraction allows the selection of ions as a function of their initial velocities, forming a gating system. The signals are detected (Photonis Chevron MCP-Set), amplified (Preamp 100, Kaesdorf), digitized (12 bit, Acqiris), and recorded with a LabVIEW controlled computer. Each mass spectrum presented here is the average of at least 500 individual spectra. To ensure reproducible spectra, the experimental setup is calibrated by using a solution of 10^{-6} M NaCl before every measurement at three different delay times and laser intensities.

9.2.3 Biosignature solutions

The tested compounds were prepared in aqueous solutions. Nine amino acids (Gly, alanine [Ala], Ser, threonine [Thr], Asp, lysine [Lys], glutamic acid [Glu], histidine [His], Arg, 50 ppmw each) were dissolved together to investigate the overall spectral appearance of a complex amino acid mixture. Aqueous solutions of Asp, Glu, Lys, tyrosine (Tyr), ornithine (Orn), and citrulline (Cit) were also measured individually (Figure 9.1 top and Supplementary Figures B.1-B.4). These amino acids were selected, because they have side chains covering a wide range of properties (pro-

teinogenic/nonproteinogenic, uncharged/charged, polar/nonpolar, hydrophilic/hydrophobic). All amino acids were measured in the cation mode of the mass spectrometer. Gly, Ser, His, Orn, Asp, Glu, Cit, and Tyr were additionally measured in the anion mode.

A mixture of fatty acids was prepared in a water-acetonitrile (50:50 vol) matrix because of the fatty acids' poor solubilities in water (especially the fatty acids with the higher carbon numbers $C_{\geq 17}$). We used the sodium salts (soaps) of the saturated fatty acids dodecanoic acid (12 carbon atoms, i.e., C_{12}), tridecanoic acid (C_{13}), tetradecanoic acid (C_{14}), pentadecanoic acid (C_{15}), hexadecanoic acid (C_{16}), heptadecanoicacid (C_{17}), octadecanoic acid (C_{18}), nonadecanoic acid (C_{19}), and eicosanoic acid (C_{20}). These fatty acids were selected, because the majority of hydrocarbon chains that are capable of assembling into stable bilayer membranes have lengths of 14-20 carbons (Georgiou and Deamer, 2014). We prepared a mixture with fatty acid concentrations of 5.5×10^{-6} M each. All fatty acids were measured by using the anion mode of the mass spectrometer.

The following five peptides were investigated in aqueous solutions: Glycine-aspartic acid (Gly-Asp), glycine- glutamic acid (Gly-Glu), histidine-serine (His-Ser), glycineproline- glutamic acid (Gly-Pro-Glu) all at concentrations of 2000 ppmw, and arginine-glycine-aspartic acid-serine (Arg- Gly-Asp-Ser) at a concentration of 1000 ppmw. The peptides were measured by using both polarity modes of the mass spectrometer.

In the second phase of the experimental campaign, we sequentially lowered the solution concentrations to infer detection limits for a selection of these biosignatures. A characteristic mass peak just exceeding a 3 σ signal to noise level was defined as the detection limit.

All substances (p.a.) were purchased from Sigma Aldrich, except the fatty acids' sodium salts, which were purchased from Nu-Check Prep (Elysian, MN). The solutions were freshly prepared with doubly distilled and deionized H_2O in 50-mL sample cups. Performing one effective measurement requires a sample volume of $\sim$ 0.5 mL. To quantify any contamination from the setup, spectra of pure deionized H_2O were recorded before every measurement.

9.3 Results

Each of the biosignature groups - amino acids, fatty acids, and peptides - was separately measured in a water or water–acetonitrile matrix to investigate their general spectral appearances and detection limits. In the following, amino acids (AAs) are abbreviated to their common three letter code, and fatty acids to their respective carbon number C_x, as identified in the previous section.

9.3.1 Amino acids

Figure 9.1 shows a cation mass spectrum of one individual amino acid (Glu) at a concentration of 50 ppmw (top) and a cation mass spectrum of nine different amino acids at the same concentration of 50 ppmw (bottom). For further spectra of individual amino acids see Supplementary

Figures B.1-B.4. Molecular peaks of all amino acids can be clearly resolved without interferences with the water matrix. Amino acids form protonated and deprotonated molecular peaks $[M + H]^+$/ $[M - H]^-$ in water matrix mass spectra. Most amino acids favor the protonation over deprotonation (Figure 9.1). The sensitivity of the method varies; some amino acids show higher peak amplitudes than others for a given concentration. Despite the fact that the molar concentrations in a 50 ppmw solution are higher for low-mass amino acids compared with those with higher masses (Supplementary Table B.1), molecular peaks of high mass amino acids generally show higher amplitudes than the low-mass amino acids used here. All amino acids produce $[NH_4]^+$ (18 u) and $[CH_2NH_2]^+$ (30 u) cations (Figure 9.1 and Supplementary Figures B.1-B.4). Further, fragments due to the loss of COOH are observed for all amino acids. Amino acids containing a carboxyl group and an additional hydroxyl group produce fragments of the form AA-COOH-H_2O. Most amino acids also produce fragments due to the loss of OH.

Table 9.1 shows the detection limits of the investigated amino acids. The method is very sensitive to, for example, Arg and Lys whereas it is less sensitive to Tyr and Ser. Cations of the protonated form of most amino acid molecules are detectable at lower concentrations, with the exception of Gly, Aps, and Glu where the detection limit for the deprotonated anion is lower. Sensitivity to different amino acids also varies with experimental parameters (delay time and laser energy) and, therefore, is expected to vary with the impact speeds of ice grains onto mass spectrometers in space (see chapter 7 and section 9.4).

9.3.2 Fatty acids

Fatty acids were measured in a water-acetonitrile (50:50 vol) matrix because of their poor solubilities in water. Acetonitrile is unreactive with water and produces no peaks at masses above 70 u that interfere with the fatty acid analytes. The anion mode of the mass spectrometer was utilized, because fatty acids strongly favor forming deprotonated molecular anions $[M - H]^-$ over protonated molecular cations $[M + H]^+$ (Figure 9.2). We measured one mixture with each fatty acid at a concentration of 5.5×10^{-6} M. In contrast to the amino acids, there is no sensitivity variation: The deprotonated molecular peaks show very similar amplitudes, reflecting the identical fatty acid concentrations (Figure 9.2).

There are conspicuous peaks at m/z 172 and 186. The exact origin of these two peaks is currently unclear. They are observed in the anion mass spectra of individual fatty acids (e.g., hexadecanoic acid as shown in Supplementary Figure B.6), with the m/z 186 peak typically larger than m/z 172 in the individual fatty acid mass spectra. As these individual mass spectra were obtained from acetonitrile-free solutions, the two peaks do not derive from acetonitrile; instead, they are associated with the fatty acid sodium salts. The two peaks could potentially arise from fragments due to a C_nH_{2n} cleavage from the fatty acids in combination with electron-capture ionization. In this process, a neutral molecule attaches to an electron to form a singly negative charged ion with the same

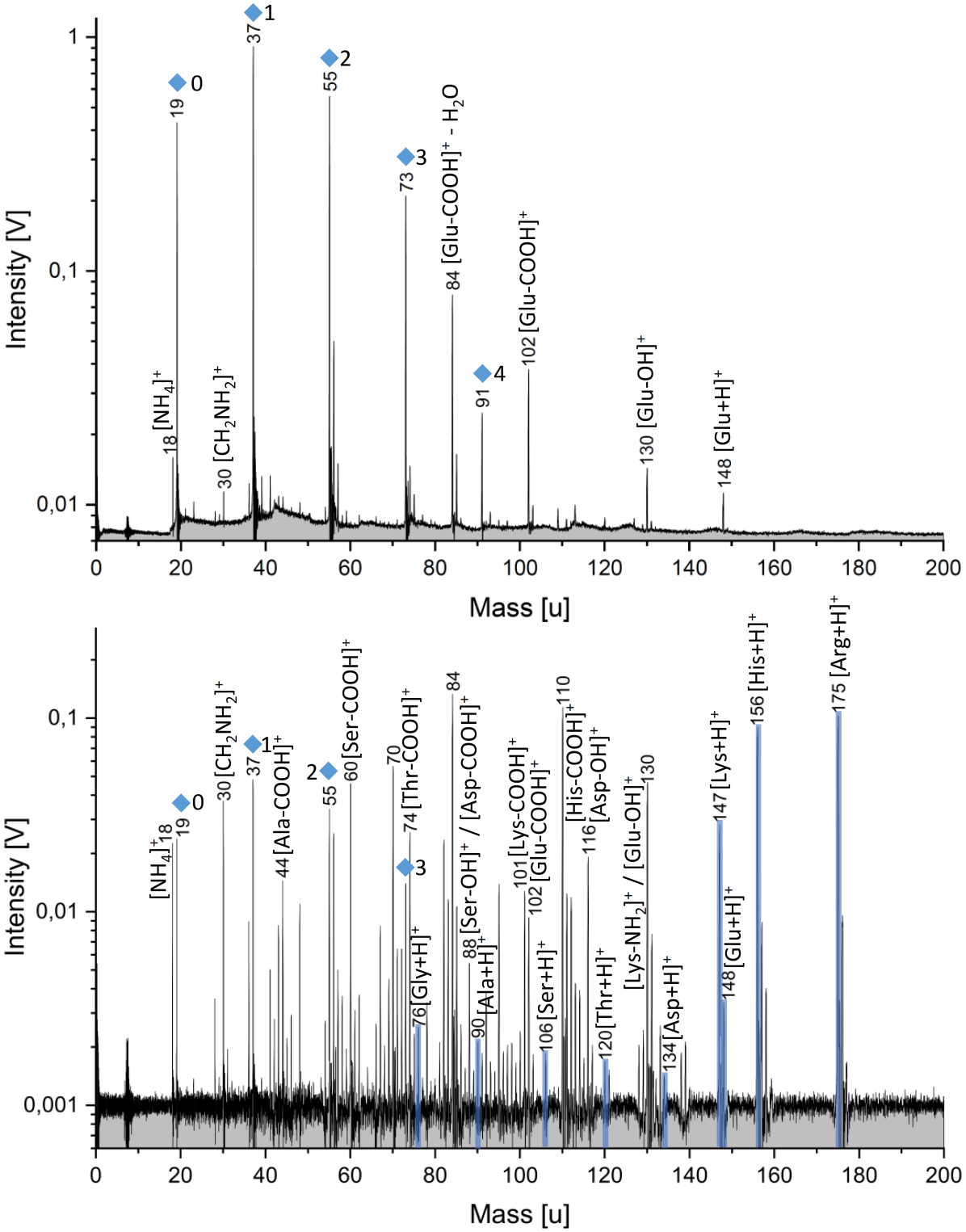

Figure 9.1: *Top: Laboratory mass spectrum (y-axis in logarithmic scale) of 50 ppmw Glu in positive detection mode. Glu fragments due to the loss of OH and COOH are observed. Glu-COOH additionally loses H_2O (observed at m/z 84). Bottom: Laboratory mass spectrum (y-axis in logarithmic scale; baseline corrected) of nine amino acids (50 ppmw each) in the positive detection mode. Molar concentrations can be found in Supplementary Table B.1. The protonated molecular peaks are highlighted in blue. Peaks, with varying intensities, corresponding to each amino acid can be detected. All amino acids produce $[NH_4]^+$ (18 u) and $[CH_2NH_2]^+$ (30 u) (see also Supplementary Figures B.1-B.4). The peak at m/z 84 derives from both Glu-COOH-H_2O and Lys-COOH-NH_3. The peak at m/z 70 represents $[Asp-COOH]^+ - H_2O$ as well as different fragments from Ser and Arg (see Supplementary Figure B.5). Mass peaks from the water matrix of the form $[(H_2O)_nH_3O]^+$ are marked by blue diamonds. The corresponding n is labeled beside the peaks. Ala, alanine; Arg, arginine; Asp, aspartic acid; Glu, glutamic acid; Gly, glycine; His, histidine; Lys, lysine; Ser, serine; Thr, threonine.*

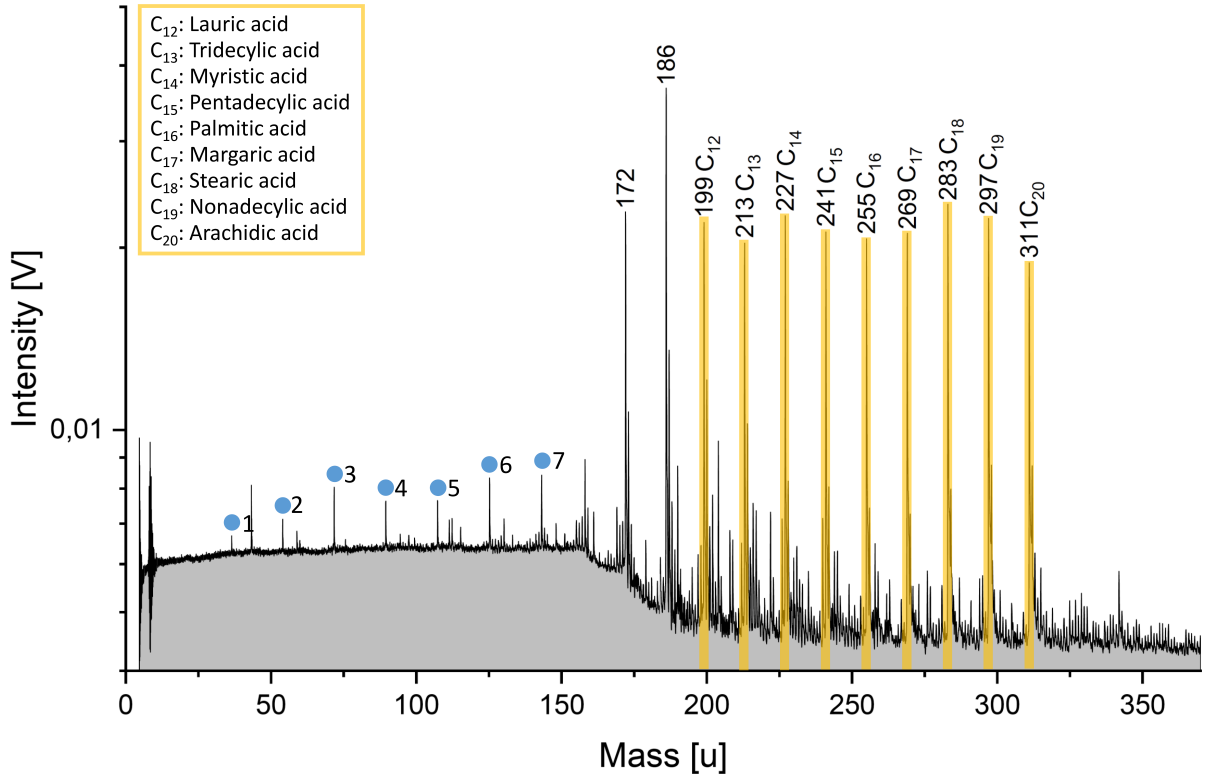

Figure 9.2: *Anion mass spectrum (y-axis in logarithmic scale) of fatty acids in a water-acetonitrile (50:50 vol) matrix. Deprotonated molecular peak intensities (highlighted in yellow) are approximately equal, consistent with the equal fatty acid concentrations of* 5.5×10^{-6} *M. Concentrations in ppmw can be found in Supplementary Table B.2. Mass peaks from the water matrix of the form* $[(H_2O)_nOH]^-$ *are marked by blue circles. The corresponding n is labeled beside the peaks. Peaks at m/z 172 and m/z 186 are observed; see text for further explanation.*

Table 9.1: Detection limits of amino acids in water.

Amino acid**	Molecular weight [u]	Detected ion* $[M+H]^+$	Detected ion* $[M-H]^-$	Detection limit [µM]
Gly	75			7
				1
Ser	105			10
				19
Orn	132			0.02
				15
His	155			0.01
				13
Cit	175			1
				6
Tyr	181			11
				11
Ala	89			2
Lys	146			0.001
Arg	174			0.001
Asp	133			0.1
Glu	147			0.1

* The respective cells of the detected ions are shaded.

** Ala = alanine; Arg = arginine; Asp = aspartic acid; Cit = citrulline; Glu = glutamic acid; Gly = glycine; His = histidine; Lys = lysine; M= molecule; Orn = ornithine; Ser = serine; Tyr = tyrosine.

integer mass as the neutral molecule (Hunt and Crow, 1978). To give an example, a CH_2 cleavage from dodecanoic acid (C_{12}) with a molecular weight of 200 u and subsequent electron capture ionization leads to a fragment with m/z 186, the mass of undecanoic acid (C_{11}). However, this explanation is unsatisfactory, given the absence of further fragmentation, the requirement of electron capture ionization, and the - in the case of dodecanoic acid at least - unusual fragmentation pathway, in which loss of a methyl group is followed by protonation, before electron capture. The two peaks at m/z 172 and m/z 186 may therefore instead either derive from undefined sodium- or sodium-water-complexed species arising from the used sodium salts or, even more likely, they could come from unknown contamination of the supplied fatty acid sodium salts.

Although detection limits have not yet been determined for each specific fatty acid, 0.02 µM ($\approx$ 5 ppbw) of each fatty acid can be easily detected (i.e., the intensities well exceed a 3 σ signal to noise level).

9.3.3 Peptides

Spectra of peptides in a water matrix show protonated and deprotonated molecular peaks, $[M+H]^+/[M-H]^-$. As with the single amino acids (see section 9.3.1), peptides favor the protonated form. Peptide spectra also show fragment peaks characteristic of their amino acid residues. Example cleavages are shown in Figures 9.3 and 9.4 for the tetrapeptide Arg- Gly-Asp-Ser and occur for all peptides discussed here. For other peptides see

Supplementary Figures B.7-B.10.

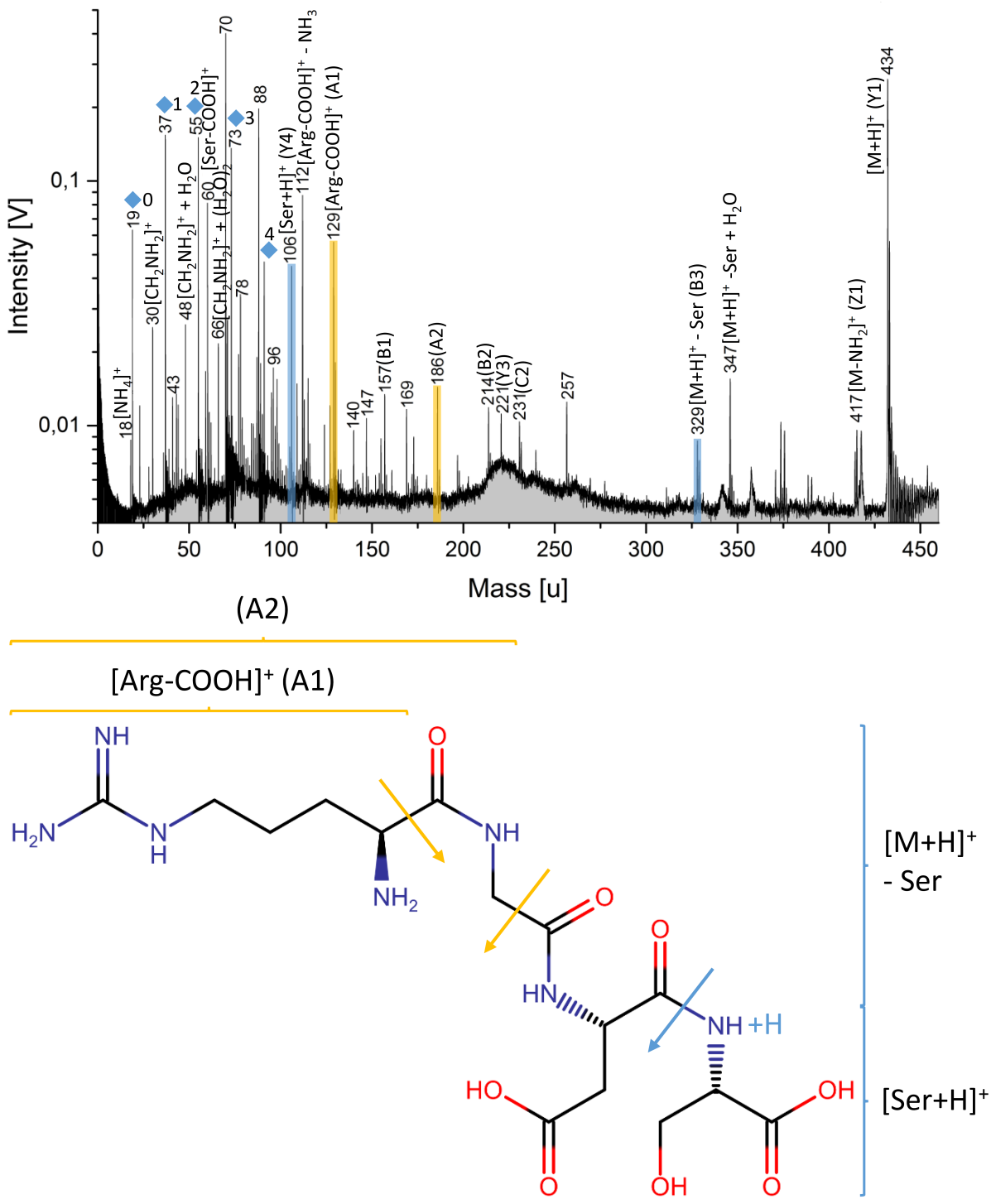

Figure 9.3: *Cation mass spectrum (y-axis in logarithmic scale) of* 23×10^{-4} *M (1000 ppmw) Arg-Gly-Asp-Ser (top) and the respective structural formula of the peptide (bottom). Important cleavages (arrows) are shown with different colors, and the resulting cation fragments are indicated in the mass spectrum. A prominent peak at m/z 70 is observed, as with the amino acid spectrum shown in Figure 9.1 (lower panel). Mass peaks, from the water matrix, of the form* $[(H_2O)_nH_3O]^+$*. are marked by blue diamonds. Peaks are labeled with the corresponding n. Common proteomics peptide sequencing nomenclature (Steen and Mann, 2004) is given in brackets, if applicable.*

Cleavage within the peptide usually occurs at specific bonds (Figures 9.3 and 9.4). Similar to the single amino acids, $[NH_4]^+$ (18 u)

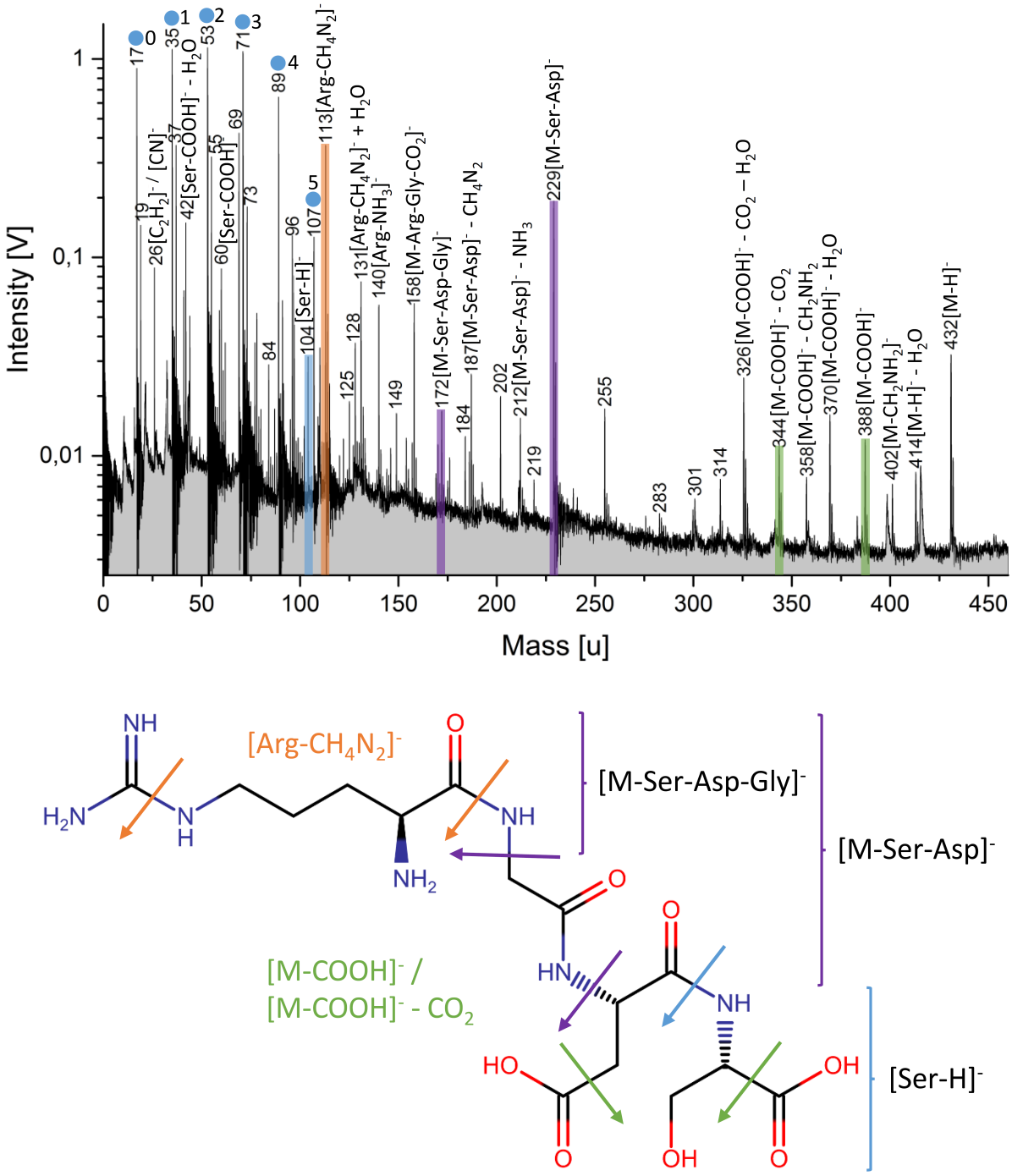

Figure 9.4: *Anion mass spectrum (y-axis in logarithmic scale) of* $23 \times 10^{-4} M$ *(1000 ppmw) Arg-Gly-Asp-Ser (top) and the respective structural formula of the peptide (bottom). Important cleavages (arrows) are shown with different colors, and the resulting anion fragments are indicated in the mass spectrum. Mass peaks from the water matrix of the form* $[(H_2O)_n OH]^-$ *are marked by blue circles, with corresponding n shown by each peak.*

and $[CH_2NH_2]^+$ (30 u) are always present. The cationic fragment $[M - NH_2]^+$, and anionic fragments of the form $[M - (COOH)_n]^-$, produced by cleavage of the carboxyl groups, are also observed. The residual mass can additionally lose water to form $[M - (COOH)_n - (H_2O)]^-$.

The terminal amino acids of all peptides can be identified. Similarly, cleavages of carbonyl groups next to the peptide bonds are observed for all peptides. From this cleavage, one of the terminal amino acids of the respective peptide regularly shows up as $[AA_{term1} - COOH]^+$ in cation spectra (Figure 9.3). For example, $[Arg–COOH]^+$ is observed in the spectrum of Arg-Gly-Asp-Ser. A cleavage of the terminal peptide bond on the opposite side of the peptide occurs in such a way that the respective terminal amino acid is detected as $[AA_{term2} + H]^+$ and $[AA_{term2} - H]^-$, in cation and anion mode, respectively (Figures 9.3 and 9.4). For example, $[Ser + H]^+$ and $[Ser - H]^-$ are present in the spectra of Arg-Gly- Asp-Ser. The remaining peptide fragment can be observed as $[M - AA_{term2}]^+$ in the cation spectrum (Figure 9.3).

Table 9.2 shows the detection limits of Arg-Gly-Asp-Ser and its various fragments. Cationic fragments are generally detectable at 10–20 × lower concentrations than anionic fragments.

Table 9.2: Detection limit of the peptide Arg-Gly-Asp-Ser and its fragments.

MS detection mode	Detected ion*	Ion mass [u]	Detection limit [µM]
Positive	$[CH_2NH_2]^+$	30	2
	$[Ser - COOH]^+$	60	12
	$[Ser - OH - H_2O]^+$ and $[C_4H_8N]^+$	70	0.2
	$[Ser - OH]^+$ and $[C_4H_8N + H_2O]^+$	88	1
	$[Ser + H]^+$	106	12
	$[Arg - COOH - NH_3]^+$	112	1
	$[Arg - COOH]^+$	129	0.2
	$[M - Ser + H_2O]^+$	347	12
	$[M - NH_2]^+$	417	1
	$[M + H]^+$	434	1
Negative	$[Ser - COOH - H_2O]^-$	42	23
	$[Ser - COOH]^-$	60	23
	$[Ser - H]^-$	104	230
	$[Arg - CH_4N_2]^-$	113	1
	$[M - Arg - Gly - CO_2]^-$	158	23
	$[M - Asp - Ser]^-$	229	23
	$[M - H]^-$	432	12

* Arg = arginine; Asp = aspartic acid; Gly = glycine; MS= mass spectrometer; Ser = serine.

9.4 Discussion

The amplitudes of molecular peaks from different amino acids at a given concentration can vary by more than an order of magnitude (Figure 9.1).

This is because the structures of individual amino acids vary in their side chains as well as in their chain lengths. The different side chains lead to different amplitudes, because the side chains possess a wide range of properties, with the logarithmic acid dissociation constant pK_a being the most important (e.g. Wu et al., 1992). The lowest detection limits (0.001 µM) are inferred for the amino acids with basic side chains (Lys and Arg), that is, relatively high pK_a values, because these molecules easily and efficiently form ions detectable by a mass spectrometer. In contrast, the molecular peaks of individual fatty acids at a given concentration are equally high (Figure 9.2), because the structures of the used fatty acids (C_{12}-C_{20}) vary only in their chain lengths and the fatty acids have very similar pK_a values. We conclude that the detection method is equally sensitive to these fatty acids, which are important for life (Georgiou and Deamer, 2014). The fatty acid abundance patterns reflect biosignatures without bias. This is why the dominant presence of even carbon number fatty acids is an even better biosignature than it was considered so far.

All amino acids show strong peaks at m/z 18 ($[NH_4]^+$) and m/z 30 ($[CH_2NH_2]^+$). Interestingly, about 3 % of the organic-bearing ice grains emitted by Enceladus' plumes and recorded by CDA show a similarly abundant signature of $[NH_4]^+$, together with an unspecified organic peak between m/z 26 and m/z 31 (Khawaja et al., 2019). Khawaja et al. (2019) concluded these to be from aliphatic nitrogen-bearing compounds at the mmol level (possibly amines, amides, or nitriles). Our results show that cation fragments from amino acids are also in agreement with these detected signatures.

In most cases, cationic (protonated) molecular peaks of amino acids and peptides as well as their cationic fragments can be detected at much lower concentrations than their anionic (deprotonated) molecular peaks and anionic fragments (Tables 9.1 and 9.2). This is because ion protonation of these organics is more likely than ion deprotonation. In contrast, fatty acid molecular and fragment peaks are more abundant in the anionic form than in the cationic form. This is why it is crucial to detect both cations and anions with future impact ionization instruments, such as the SUDA (Kempf et al., 2014) or the ENIA (Mitri et al., 2018; Reh et al., 2016), visiting ocean worlds.

According to a model by Steel et al. (2017), concentrations of individual amino acids in the Enceladus ocean could be up to 25 µM in an exclusively abiotic scenario. The total abiotic amino acid concentration would be 104 µM in a steady-state ocean and up to 90 µM are expected in a biotic scenario based on methanogens. Similarly, cell (individual cell mass: 2×10^{-14} g) concentrations of $\sim 8.5 \times 10^7$ cells/ cm^3 in the plume would be expected due to biotic production (Steel et al., 2017). The predicted amino acid concentrations are above the inferred detection limits in this work. Given the ability to accurately reproduce impact ionization mass spectra of water ice grains at different impact speeds from space with our LILBID experiment (see chapter 7) and the previously derived NaCl salt concentration in the Enceladus ocean by using the LILBID setup (Postberg et al., 2009a), we believe that the concentration behavior comparison of the organics is applicable.

A numerical model (Guzman et al., 2019) predicts concentrations of

individual amino acids in the Enceladus plume during mean levels of plume activity to be between 30 and 1000 µM in an abiotic scenario and ∼ 2 µM in a biotic scenario. According to our inferred amino acid detection limits and taking the higher dynamic range and the higher ion efficiency of future spaceborne impact ionization mass spectrometers into account, individual amino acids at the concentrations predicted by Guzman et al (2019) would be detectable on active ocean worlds undergoing similar or greater activity to Enceladus.

Cationic and anionic LILBID mass spectra of the investigated di-, tri-, and tetrapeptides show the peptides' molecular peaks and peaks characteristic of their amino acid residues. The terminal amino acids of the peptides can always be identified, independent of the total number of amino acids within each peptide. Therefore, our results can be extrapolated to longer oligopeptides, and possibly even polypeptides, provided that the mass range of the spaceborne mass spectrometer is sufficient for the respective molecule and its fragments.

Studies on fragmentation pathways of protonated peptides (Paizs and Suhai, 2005) demonstrated that peptides generally show predictable fragmentations and fragmentation pathways. Although we did not investigate fragmentation pathways in detail, some fragments described by Paizs and Suhai (2005) are also observed in our cation LILBID mass spectra, for example, water loss from Ser-containing peptides and ammonia loss from Arg-containing peptides. Ion beam irradiation of peptides that contain up to 25 amino acid residues (Bowie et al., 2002) indicates that peptides show characteristic fragmentation peaks related to their constituent amino acid residues in anion mass spectra. For example, the Ser residue undergoes a characteristic side chain cleavage resulting in a loss of CH_2O, converting Ser (molecular weight: 105 u) into Gly (molecular weight: 75 u). This cleavage is also observed in the LILBID anion mass spectra of Ser-containing peptides (Figure 9.4 and Supplementary Figure B.9).

The instrument sensitivity to different analytes varies with experimental parameters (delay time and laser energy), which can be correlated with impact speeds of icy grains onto detectors in space (see chapter 7). We can therefore infer, by comparison with the instrument parameters used here, and those required to simulate different speed regimes in space, that sensitivity to amino acids is maximized by using intermediate to high laser intensities and delay times equivalent to impact speeds of 4–10 km/s. The detection of fatty acids is maximized by using intermediate laser intensities and very high delay times, equivalent to impact speeds of 3–6 km/s, and the detection of peptides and their fragments is maximized by using low to intermediate laser intensities and intermediate to high delay times, equivalent to impact speeds of 4–8 km/s (see chapter 7). These speed ranges cover the expected flyby speeds of the Europa Clipper spacecraft (typically 4–4.5 km/s) and future Enceladus mission concepts such as the Enceladus Life Finder (ELF; 5km/s) (Reh et al., 2016).

9.5 Conclusion and outlook

The proven ability of the LILBID experiment to simulate the impact ionization mass spectra of water ice dominated grains (e.g. Postberg et al., 2009a; Postberg et al., 2011a; Postberg et al., 2018a; Khawaja et al., 2019; chapter 7) has been applied to the simulation of ice grains containing biosignatures. By generating spectral features arising from amino acids, fatty acids, and peptides in a water, or water-rich, matrix, we show that these constituents, if present at the µM or nM level, respectively, are likely to be readily identifiable in impact ionization mass spectra recorded in space.

Determination of laboratory detection thresholds for both cationic and anionic species, which are then transformed into recommended impact velocity regimes for a dust detector, aids in mission planning for future missions to icy moons such as Europa and Enceladus, such that the chances of detecting and identifying biomarkers within ice grains are maximized. From the settings used in our experiment, we conclude that the sensitivity of impact ionization detectors to the molecular peaks of all three biosignatures investigated here is optimal between 4 and 6 km/s. Therefore, we recommend encounter velocities within this speed range. However, higher velocity impacts are complementary, producing larger amplitude signals from molecular fragments that are often characteristic of their parent molecule and help constrain the overall molecular structure.

If protonated, most amino acids and peptides, as well as their cationic fragments, are generally detectable at lower concentrations than their anionic (deprotonated) counterparts, whereas deprotonated fatty acids are detectable at lower concentrations than their cationic (protonated) counterparts. Future space instruments, thus, ideally need to be capable of detecting both cations and anions to cover the complete range of biosignatures investigated here, that is, amino acids, fatty acids, and peptides.

Further work is underway to understand how the presence of salt and also other organic constituents in ice grains might affect the detection of these biosignatures and whether the abiotic and biotic signatures of organics remain distinguishable (see chapter 10). A correlation between the organics' concentrations and spectral peak appearances and amplitudes, in other words a quantitative calibration, in the mass spectra will be investigated in the future.

Acknowledgements

The authors thank Sascha Kempf for valuable discussions and Jan de Leeuw for the fruitful discussions about the peaks at m/z 172 and 186 in the fatty acid spectra. Some of this work was carried out at the Jet Propulsion Laboratory, California Institute of Technology, under a contract with the National Aeronautics and Space Administration.

Handling editor: Sherry Cady

Author disclosure statement

No competing financial interests exist.

Funding information

The research leading to these results received financial support from the German Research Foundation (DFG) projects PO 1015/2-1,/3-1,/4-1, project AB 63/9-1, and ERC Consolidator Grant 724908-Habitat OASIS.

10 Discriminating abiotic and biotic fingerprints of amino acids and fatty acids in ice grains relevant to ocean worlds[1]

Summary

This is the abstract of the original publication and is titled "Summary" here to separate it from the overall abstract of this thesis given on page vii.

IDENTIFYING AND DISTINGUISHING between abiotic and biotic signatures of organic molecules such as amino acids and fatty acids is key to the search for life on extraterrestrial ocean worlds. Impact ionization mass spectrometers can potentially achieve this by sampling water ice grains formed from ocean water and ejected by moons such as Enceladus and Europa, thereby exploring the habitability of their subsurface oceans in spacecraft flybys. Here, we extend previous high-sensitivity laser-based analogue experiments of biomolecules in pure water to investigate the mass spectra of amino acids and fatty acids at simulated abiotic and biotic relative abundances. To account for the complex background matrix expected to emerge from a salty Enceladean ocean that has been in extensive chemical exchange with a carbonaceous rocky core, other organic and inorganic constituents are added to the biosignature mixtures. We find that both amino acids and fatty acids produce sodiated molecular peaks in salty solutions. Under the soft ionization conditions expected for low-velocity (2–6 km/s) encounters of an orbiting spacecraft with ice grains, the unfragmented molecular spectral signatures of amino acids and fatty acids accurately reflect the original relative abundances of the parent molecules within the source solution, enabling characteristic abiotic and biotic relative abundance patterns to be identified. No critical interferences with other abiotic organic compounds were observed. Detection limits of the investigated biosignatures under Enceladus-like conditions are salinity dependent (decreasing sensitivity with increasing salinity), at the µM or nM level. The survivability and ionization efficiency of large organic molecules during impact ionization appears to be significantly improved when they are protected by a frozen water matrix. We infer from our experimental results that encounter velocities of 4–6 km/s are most appropriate for impact ionization mass spectrometers to detect and discriminate between abiotic and biotic signatures.

Keywords: Enceladus, Europa, Plume, Biomarkers, Mass spectrometry, Space missions

[1]This chapter as well as the corresponding supplementary information (appendix C) are published as: Klenner, F., Postberg, F., Hillier, J., Khawaja, N., Cable, M.L., Abel, B., Kempf, S., Glein, C.R., Lunine, J.I., Hodyss, R., Reviol, R., and Stolz, F. (2020). Discriminating abiotic and biotic fingerprints of amino acids and fatty acids in ice grains relevant to ocean worlds. *Astrobiology*, 20(10):1168–1184. DOI: 10.1089/ast.2019.2188

10.1 Introduction

The subsurface oceans of the Saturnian and Jovian moons Enceladus and Europa, respectively, harbor conditions that appear to be suitable for life or its emergence (Hand et al., 2007; Glein et al., 2018; McKay et al., 2018). Enceladus maintains a cryovolcanic plume (Goldstein et al., 2018; Postberg et al., 2018b; Spencer et al., 2018), and similar venting phenomena are potentially occurring on Europa (Roth et al., 2014; Sparks et al., 2016; Sparks et al., 2017; Jia et al., 2018; Huybrighs et al., 2020; Paganini et al., 2020). Measurements by the Cassini spacecraft indicate that a large fraction of the ice particles ejected into space formed from ocean water within Enceladus (Postberg et al., 2009a; Postberg et al., 2011a). Sampling these ice grains, therefore, provides a method for assessing the physical and chemical properties of the subsurface ocean as well as the ocean-core interface (Postberg et al., 2008; Postberg et al., 2009a; Postberg et al., 2018a; Hsu et al., 2015; Sekine et al., 2015; Khawaja et al., 2019; Glein and Waite, 2020).

Mass spectrometers such as the Cassini spacecraft's Cosmic Dust Analyzer (CDA) (Srama et al., 2004), the Surface Dust Analyzer (SUDA) (Kempf et al., 2014) being built for NASA's Europa Clipper mission, or instruments proposed for future missions to Enceladus (Lunine et al., 2015b; Reh et al., 2016; Mitri et al., 2018), such as the Enceladus Icy Jet Analyzer (ENIJA) (Srama et al., 2015a), subsequently renamed the Enceladus Ice Analyzer (ENIA), utilize the principle of impact ionization. In these instruments, ions are generated by hypervelocity ($\geq$ 1 km/s) impacts of nm- or µm-sized grains onto a metal target, forming an impact plasma from which time of flight (TOF) mass spectra are produced (Hillier et al., 2007; Postberg et al., 2009b; Postberg et al., 2011b; Wiederschein et al., 2015) (see chapter 7). The impact ionization process creates singly charged ions almost exclusively, and the spectral peak positions, that is, ion arrival times, therefore only depend on the atomic and molecular masses, together with the spectrometer's field configuration.

The controlled acceleration of µm-sized ice grains to hypervelocities in a laboratory environment for instrument calibration is extremely technically challenging, and techniques employing Laser-Induced Liquid Beam Ion Desorption (LILBID) (Karas et al., 1990; Karas et al., 1991; Karas et al., 2000) have instead been developed to simulate the process (Postberg et al., 2009a; Wiederschein et al., 2015; Taubner et al., 2020) (see chapter 7). Using such a LILBID analogue experiment, ice grain mass spectral variations as produced by different ice grain impact speeds recorded by CDA at Saturn have been reproduced (see chapter 7). In addition to the ability to reproduce noncompositional spectral variations, a further advantage with the analogue laser-desorption approach is that the compounds tested and their concentrations in the water matrix are known. This allows the compositions of ice grains detected in space to be investigated in detail by comparing them with the laboratory data (Postberg et al., 2009a; Postberg et al., 2018a; Khawaja et al., 2019).

Data obtained by Cassini's CDA instrument also revealed that $\sim$ 25 % (by number) of the ice grains formed from Enceladus' salty ocean contain organic material at detectable concentrations (Postberg et al., 2008;

Postberg et al., 2011a; Postberg et al., 2018b). Volatile organic constituents, including aliphatic oxygen- and nitrogen-bearing compounds, have been identified in the majority of these organic-bearing ice grains (Khawaja et al., 2019). It was found that 5-10 % of the organic-enriched ice grains contain even more complex organics derived from refractory macromolecules at high (±0.5 wt.-%) concentrations (Postberg et al., 2018a).

However, given the insufficient mass resolution of CDA, it is still unclear whether these ice grains contain biosignatures. The volatile organics are suggested to have been previously dissolved in the ocean (Khawaja et al., 2019). Their high vapor pressures enable efficient evaporation from Enceladus' oceanic water, and they subsequently undergo recondensation and adsorption onto water ice nucleation cores on cooling during ascent through the icy crustal cracks (Postberg et al., 2018b; Bouquet et al., 2019; Khawaja et al., 2019). In contrast, the refractory and probably hydrophobic macromolecules are hypothesized to originate from an organic layer floating on top of the ocean (Postberg et al., 2018a) (Figure 10.1).

Among potential biosignatures, amino acids and fatty acids are considered to be particularly diagnostic (McKay et al., 2018). Techniques such as laser-induced fluorescence have been proposed for detecting such biosignatures at low concentrations (e.g., 0.4 ppm of an amino acid in 3 µg of ice collected over an ∼150 km path) during plume traversing Enceladus flybys (Mathies et al., 2017). Recently, an experimental setup also applicable to ocean world space missions has demonstrated that amino acids and lauric acid can be identified in pure water by chemical ionization mass spectrometry, although the exact sensitivity of this technique remains to be determined (Waller et al., 2019).

High sensitivities to such compounds in pure water have been achieved with a LILBID setup (see chapter 9) by investigating the cation and anion spectra of various biogenic amino acids, fatty acids with 12 to 20 carbon atoms, and peptides with up to four amino acid residues in pure water. Molecular peaks and characteristic fragments were found to be clearly identifiable, with detection limits at the µM to nM level. Although most amino acids and peptides could be best identified in cation spectra, anion spectra were more suitable for the characterization of fatty acids. Molecular peaks of amino acids at a given concentration vary by more than an order of magnitude in intensity because of the different pK_a-values and proton affinities of individual amino acids. In contrast, molecular peaks of fatty acids at a given concentration are almost equally high (see chapter 9).

Building on the foundation of chapter 9, here we investigate two additional key aspects required for the characterization of these potential biosignatures if embedded in ice grains emerging from a subsurface ocean and ejected by an Enceladus-like plume.

(1) The example of Enceladean ice grains shows that some biosignatures might not be present in relatively pure water ice and instead will coexist with additional inorganic and organic constituents. We investigate the effects of ocean constituents other than water on the spectral appearances and on the detection limits of biosignatures.

(2) Both amino acids and fatty acids are also found in abiotic environments (Cronin and Pizzarello, 1983; Altwegg et al., 2016). However, the abundance ratios of specific amino acids and fatty acids that result from abiotic and biotic generation are distinctly different. We investigate abundances from both sources with the LILBID experiments to predict characteristic mass spectrometric fingerprints for abiotic and biotic cases in impact ionization mass spectrometers on future space missions.

The abiotic synthesis of amino acids in water–rock systems (Menez et al., 2018) follows the free energy of formation with the abundance of the simplest amino acid glycine exceeding those of other, more complex amino acids (Higgs and Pudritz, 2009). Because abiotic synthesis is generally inefficient, kinetically controlled reactions should favor the synthesis of simpler amino acids. In contrast, in biotic systems the more complex amino acids become prevalent and therefore the ratio of different amino acids to glycine can be used as a biosignature (Dorn et al., 2011; Davila and McKay, 2014; Reh et al., 2016; Sherwood, 2016; Creamer et al., 2017).

Fatty acids can also aid in the search for life, as they are commonly present in the lipid membranes of Earth life. For most organisms (bacteria and eukaryotes), fatty acids are biochemically produced by the addition of two carbon atoms at a time, resulting in an excess of unbranched, saturated fatty acids with an even number of carbon atoms, with hexadecanoic acid (C_{16}) and octadecanoic acid (C_{18}) dominating (Georgiou and Deamer, 2014). For archaea, carbon chains are constructed from isoprene units, and hence they exhibit a 5-carbon pattern (Berg et al., 2012). In contrast, in the abiotic (e.g., Fischer-Tropsch) synthesis of carbon chains, carbon atoms are added one at a time. The relative abundances of fatty acids with different backbone lengths can, therefore, serve as a discriminator for biosignatures (Summons et al., 2008; Dorn et al., 2011; Reh et al., 2016; Sherwood, 2016), although these patterns may be significantly less apparent in psychrophilic organisms that use more branched and unsaturated fatty acids to maintain membrane flexibility (M.J. Malaska, pers. comm., 2019[1]). In addition to mere detection, the ability to differentiate between biotic and abiotic signatures on extraterrestrial ocean worlds might therefore be crucial in the search for life.

The effects of ocean constituents other than water on the spectral appearance and detection limits for the key organic species mentioned earlier are of particular relevance to ocean worlds. Sodium salts, believed to be endogenous, have been observed not only on the surface of Europa (Trumbo et al., 2019) but also in particles emitted by Enceladus, where a large fraction of the ice grains detected in the plume are believed to be frozen ocean spray (called Type 3 grains). There, the nonwater constituents are dominated by sodium salts amounting to about 1 % of the ice grain's mass (Postberg et al., 2009a; Postberg et al., 2011a). These salts produce large quantities of cations and anions on impact ionization

[1]Personal communication of J.I. Lunine, who is a co-author of this study, with M.J. Malaska in 2019.

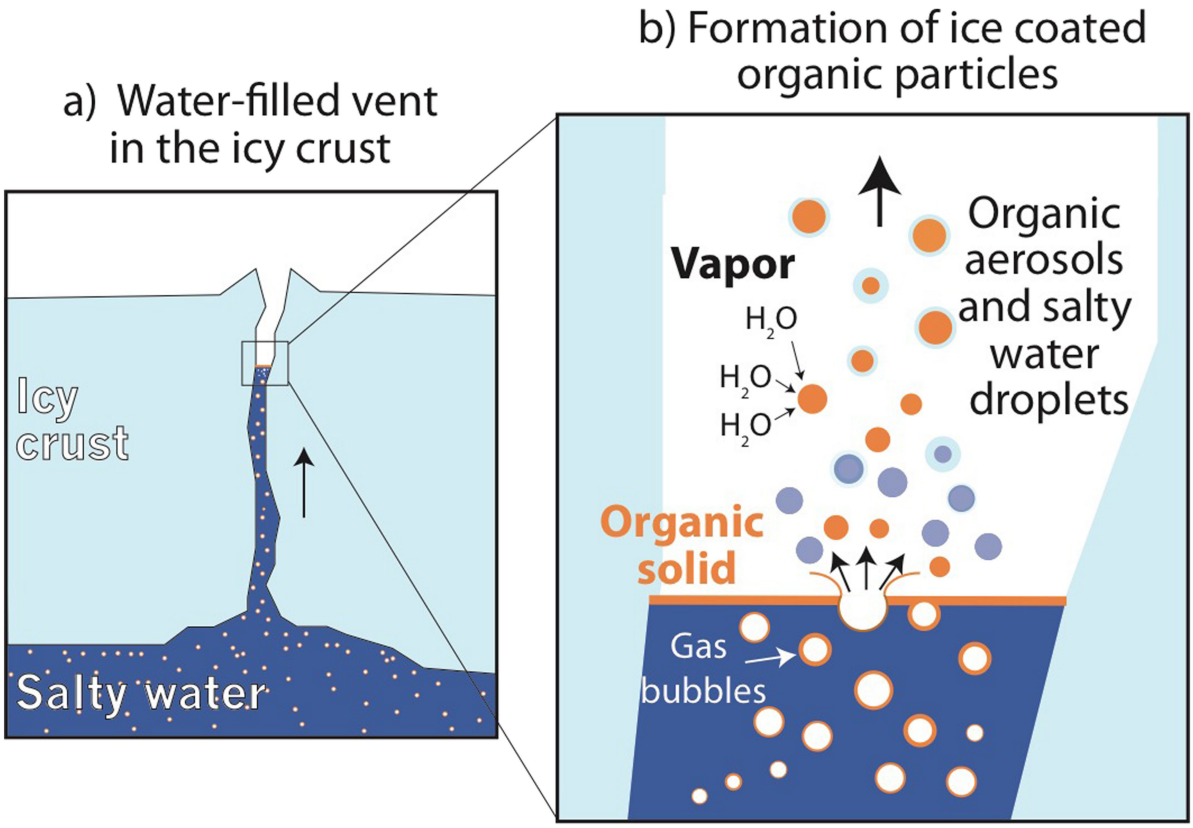

Figure 10.1: *Formation of ice grains from heterogeneous nucleation (not to scale) (from Postberg et al., 2018a with permission from Nature). (a) Ascending gas bubbles and thermal convection in the ocean transport organic material into water-filled cracks in the south polar ice crust. (b) Organics ultimately concentrate in a thin organic film/layer on top of the water table, located inside ice vents. When gas bubbles burst, they form aerosols made of organic material that later serve as condensation cores for the production of an icy crust from water vapor, thereby forming so-called HMOC-type ice particles containing organic hydrophobic macromolecules. Another effect of the bubble bursting is that larger, pure saltwater droplets form, which freeze and are later detected as salt-rich so-called Type 3 ice particles in the plume and Saturn's E ring. The figure implies the parallel formation of both organic and saltwater spray, but their formation could actually be separated in space (e.g., at different tiger stripes cracks) or time (Postberg et al., 2018b). HMOC, high mass organic cations.*

and may suppress the signals arising from less abundant dissolved constituents or modify their spectral appearance (Annesley, 2003; Piwowar et al., 2009). Amino acids are quite soluble (Dunn et al., 1933) and, if present, will dissolve in Enceladus' salty ocean and can be expected to reside in the salty Type 3 ice grains. Thus, in this work we investigate amino acids in an Enceladus-like salty ocean scenario and examine the effects of sodium salts on the mass spectral appearance as well as detection limits of the amino acids.

Although the Enceladean ocean is alkaline (e.g. Postberg et al., 2009a; Glein et al., 2015; Glein et al., 2018) and contains sodium (e.g. Postberg et al., 2009a), it is reasonable to assume that long-chain fatty acids, due to their low solubility in water, are not significantly dissolved in the ocean at temperatures close to 0°C, but instead are part of a phase-separated organic layer on top of the water surface as described in the work of Postberg et al. (2018a). After these components are aerosolized, they could serve as condensation cores for water vapor within the south polar ice vents, thereby growing a salt-poor outer ice layer on the grain (Postberg et al., 2018a; Postberg et al., 2018b). We, therefore, investigate appropriate mixtures of different fatty acids in a salt-poor solution and differentiate between biotic and abiotic signatures in the corresponding mass spectra.

In addition to potential biosignatures and salts, other organic species, most notably low-mass carboxylic acids, which are abundant in carbonaceous chondrites (Huang et al., 2005), could coexist in the ice grains. The latter species could be derived from a primordial reservoir in carbonaceous rock at the bottom of the ocean. We, therefore, investigate a complex mix of amino acids together with fatty acids and other organic background compounds, to identify potential interferences and infer how readily biosignatures from these key organic species can be detected in such a complex mixture.

10.2 Methods

Analogue mass spectra were generated by the LILBID mass spectrometer acting on water or water–acetonitrile matrixed solutions (see section 10.2.2). Here, the LILBID process, as well as the variety and concentrations of the solutions used are described.

10.2.1 Experimental

Figure 7.2 is shown in the original publication and has been removed here to avoid repetition.

The experimental setup used for this work (Figure 7.2) is described in detail in chapter 7 and we, therefore, provide only a brief overview here.

The technique used to simulate the impact ionization process of ice grains in space is as follows. A µm-sized liquid water beam is irradiated by a pulsed infrared laser (20 Hz and 7 ns pulse length) operating at a wavelength of $\sim$ 2850 nm and at variable laser intensities (0–100 %). The water beam absorbs the laser energy and explosively disperses into atomic, molecular, and macroscopic fragments, a portion of which is charged. After passing through a field-free drift region, cations and

anions are analyzed in a commercial reflectron TOF mass spectrometer. The mass spectrometer uses the principle of delayed extraction (see chapter 7). The delay time between laser shot and the switch-on of the acceleration voltages of the mass spectrometer, during which ions traverse the field-free region and enter the acceleration region, is adjusted, which allows the extraction of the ions as a function of their initial velocities. After amplifying and digitizing the detected signals, the final mass spectrum is recorded with a LabVIEW-controlled computer. The mass spectra presented here are each an average of typically 500 individual spectra, co-added to improve the signal to noise ratio. The experimental setup is intensity calibrated before every measurement by using a 10^{-6} M NaCl solution at three different delay times and laser intensities to ensure reproducible spectra. The mass spectra typically achieve a mass resolution of 600–800 m/Δm (full width at half maximum).

10.2.2 Biosignature solutions

Three main compositional scenarios have been investigated by using four different types of solution (i, ii, iii, and iv below). Later, amino acids are abbreviated to their common three letter codes (Table 10.1) and fatty acids to their respective carbon number C_n.

10.2.2.1 Amino acids in a salt-rich solution

2.2.1.1. Solution type i. Initially, 100 ppmw of the single amino acids His and Arg, each in a separate 0.1 M NaCl solution, were measured to investigate the general spectral appearance of amino acids under salty ocean conditions. Detection limits of each of the following 10 amino acids under such conditions were determined: Asp, Glu, His, Arg, Cit, Gly, Ser, Thr, Orn, and Tyr. A characteristic mass peak just exceeding a 3 σ signal to noise level was defined as the detection limit.

2.2.1.2. Solution type ii. These experiments were designed to investigate the mass spectra from ice grains that preserve the composition of a hypothetical abiotic ocean on Enceladus.

The abiotic abundances of amino acids and other soluble organic constituents are calculated under the simplified assumption that Enceladus' rocky core has a composition similar to primitive CR chondrites and that all water-soluble organics are unlikely to remain for long timescales in the highly porous, water-percolated (Choblet et al., 2017) rocky core, instead leaching into the ocean water. Organic abundances in CR2 and CR3 chondrites were reported by Glavin et al. (2011) and Pizzarello et al. (2012). We use the average concentrations (nmol/kg) of the seven most abundant amino acids, and those of the 14 other most abundant soluble organic compounds (Supplementary Table C.1), dissolving their total mass in the entire ocean volume. Estimates of the mass of the rocky core and the Enceladus ocean were obtained from the work of Waite et al. (2017). An example calculation and the resulting concentrations of the amino acids and carboxylic acids are summarized in Supplementary Data C.1 and Supplementary Table C.1. Concentrations of the most abundant inorganic substances were inferred by using values for the most abundant

salts (0.1 M NaCl, 0.015 M Na_2CO_3, and 0.015 M $NaHCO_3$) from Postberg et al. (2009a) and adopting an NH_3 concentration of 0.01 M (Waite et al., 2017).

10.2.2.2 Fatty acids in a salt-poor solution

2.2.2.1. Solution type iii. In contrast to amino acids, long-chain fatty acids are thought unlikely to be present at high concentrations in the salty ocean water because of their low water solubilities. They instead may accumulate in a thin organic film/layer on top of the water surface (Postberg et al., 2018a). Making combined solutions in the laboratory, at concentrations in pure water approaching the upper limit for the nine fatty acids ($C_{12–20}$), was found to be unfeasible and instead an acetonitrile–water mixture (50:50 vol) was used together with the sodium salts (soaps) of the fatty acids (as in chapter 9). This enabled the required concentrations to be achieved and also introduced small amounts of sodium into the solution, as might be expected in the organic layer on Enceladus (Postberg et al., 2018a) from physical mixing during the disruption of this layer (Figure 10.1).

Abundances of abiotically produced fatty acids in carbonaceous chondrites range from 100 ppbw to 5 pptw (Hayes, 1967; Lai et al., 2019); leaching from the chondrite-like core of Enceladus (Sekine et al., 2015) would generate dissolved free fatty acids (DFFAs) in the ocean in the $\sim$ 20–200 micromolar range (Waite et al., 2017). Abiotic fatty acid synthesis via, for example, Fischer-Tropsch-type processes (Loison et al., 2010) results in no preference for the production of odd or even carbon number fatty acids (see Section 10.1). We, therefore, consider the solution investigated in chapter 9, with each saturated fatty acid at a concentration of 5.5×10^{-6} M, as a possible lower bound. By contrast, many biochemically produced fatty acids show a clear preference for even carbon number fatty acids over odd carbon number fatty acids, with C_{16} and C_{18} showing the highest abundances (Georgiou and Deamer, 2014) (see Section 10.1). To investigate the spectral appearance of a simplified biotic versus an abiotic fatty acid fingerprint at comparable concentrations, a solution with the odd carbon number fatty acids (saturated) at a concentration of 5.5×10^{-6}; C_{12}, C_{14}, and C_{20} at a concentration of 55×10^{-6} M (10-fold greater than the odd-carbon background); and C_{16} and C_{18} at a concentration of 275×10^{-6} M (50-fold greater) was prepared and analyzed. Concentrations in ppmw can be found in Supplementary Table C.2. Due to the use of the sodium salts, this resulted in a $[Na]^+$ concentration of about 0.75 mM in the solutions used.

10.2.2.3 Complex biosignature mix

2.2.3.1. Solution type iv. We also investigate a more complex case in which amino acids and fatty acids enter the Enceladus ocean from biotic processes at depth. The fatty acids are assumed to migrate upward through the oceanic layer by thermal convection and bubble transport, thereby accumulating in an organic layer at the ocean's surface (Porco et al., 2017; Postberg et al., 2018a). Droplets formed from this layer may become the cores of salt-poor ice grains (Figure 10.1) after they are aerosolized from bubble bursting (Postberg et al., 2018a).

We based our concentration estimates on Earth's ocean as an analogue, as amino acid concentrations are determined by life as a system, which produces and consumes them. The presence of specific amino acids (e.g., aspartic acid and arginine) indicates either active biotic or abiotic production, because these amino acids are degraded over relatively short geological timescales (<1 Ma) (Truong et al., 2019). Ocean concentrations of dissolved free amino acids (DFAAs) are 10-20 nM in the deep ocean (Repeta, 2014), equivalent to about 1 ppbw Gly. The average concentration of DFFAs in ocean water is 5-80 µg/L or 5-80 ppbw (Zsolnay, 1977). We adjust this value based on enrichment of organics in marine sea spray aerosols, which was found to be a good analogue for organic-enriched ice grains from Enceladus (Postberg et al., 2018a). Bulk organic compounds are 100-1000 times enriched in marine aerosols compared with the surface ocean (Russell et al., 2010). From these, lipids and proteins will be even more (preferentially) enriched in sea spray aerosols (Burrows et al., 2014). For our biotic solution, we choose to enrich fatty acids by a factor of $\sim$ 100 and amino acids by a factor of$\sim$ 1000, yielding values slightly above or below 1 ppmw for each component.

To mimic abundance variations from biogenic fatty acids, we reduced the concentrations of fatty acids with odd carbon numbers and enhanced it 10-fold or 50-fold for fatty acids with even carbon numbers as previously done in Solution type iii. Ratios (varying from 0.25 to 1.5) of biogenic amino acids relative to Gly were approximated by using values for interstitial ocean water (Kawahata and Ishizuka, 1992). To account for other organics that may be likewise embedded in the ice grains (see section 10.1), we added the same 14 carboxylic acids as used for Solution type ii, plus propionic acid, each at higher concentrations than the biogenic compounds, to represent abiotic organic background components in a salt-poor solution. The concentrations of all substances used in Solution type iv are summarized in Supplementary Table C.3.

10.3 Results and spectral analysis

Measurement results for the four types of solutions (i, ii, iii, iv) are presented next. The laboratory results are archived in the form of an internal database (spectral reference library; see chapter 8) and can be compared with results from previous and future space missions.

10.3.1 General spectral appearance of amino acids and their detection limits in salty solutions (Solution type i)

In a typical cation mass spectrum of an amino acid (AA) in a salty solution (Solution type i), the spectral "background" produced by the NaCl solution consists of peaks of the form $[(H_2O)nNa]^+$, $[(NaOH)_nNa]^+$, $[(NaCl)_nNa]^+$ and mixed clusters of these species, for example, $[(NaOH)_n(H_2O)_mNa]^+$. These species were also observed by Postberg et al. (2009a), who performed LILBID experiments with pure salt solutions. We find that in this sodium-rich solution the AAs typically form neutral sodiated (sodium-complexed) molecules (AA_{Na}), in which a sodium ion

replaces a hydrogen ion (proton) in the amino acid molecule. This sodiated molecule is cationized by a $[Na]^+$ to form a disodiated adduct cation $[(AA_{Na})Na]^+$, as shown by His in Figure 10.2:

$$AA - [H]^+ + [Na]^+ \rightarrow AA_{Na} \tag{3}$$

$$AA_{Na} + [Na]^+ \rightarrow [(AA_{Na})Na]^+ \tag{4}$$

As one proton ($[H]^+$; 1u) is removed and two $[Na]^+$ (23u) are added, amino acid molecules in an NaCl-rich solution are detectable at masses of AA +45 u in the mass spectra. The most acidic amino acids (most notably Asp and Glu) have a characteristic trisodiated peak, in which an additional H is replaced by Na:

$$[(AA_{Na})Na]^+ - [H]^+ + [Na]^+ \rightarrow [(AA_{2Na})Na]^+ \tag{5}$$

This produces an additional molecular peak at AA +67 u in the mass spectra. One, or both, of these sodiated peaks may occur in an individual spectrum, as illustrated in Table 10.1. The disodiated and trisodiated peak amplitudes of different amino acids (AA +45 u and AA +67 u) vary within an order of magnitude for identical amino acid concentrations. The amino acids are clearly identifiable and, in general, neither quantitatively nor qualitatively influence the spectral appearance (e.g., peak amplitudes) of the salty matrix solution at the given concentrations (Supplementary Figure C.1).

The only exceptions are sodiated amino acids that may interfere with the ever-present salt–water peaks, for example, Arg + 45 u with $[(NaCl)_2(NaOH)_2Na]^+$ at m/z 219. Because of a significant peak asymmetry the mass resolution (600– 800 m/Δm) of the spectrometer used for this work is, however, sufficient to resolve interferences of this magnitude, such as the 0.19 u mass difference between Arg +45 u and $[(NaCl)_2(NaOH)_2Na]^+$ (Figure 10.3).

Table 10.1 shows the detection limits of amino acids in salty solutions. The detection limits were individually determined for each amino acid (apart from Gly, which was measured in a mixture) with the experimental parameters (laser intensity and delay time) optimized for greatest sensitivity to the amino acid under investigation. Trisodiated ions of Asp and Glu are detectable at the lowest concentrations in our experimental setup.

10.3.2 Amino acids at abiotic abundances in salty solutions with carboxylic acids (Solution type ii)

As in the case of Solution type i, $[(NaOH)_nNa]^+$, $[(NaCl)_nNa]^+$ and mixed clusters of these species, for example, $[(NaOH)_n(H_2O)_mNa]^+$ (Postberg et al., 2009a) from the inorganic spectral background are observable.

Table 10.1: Detection limits for the Laser-Induced-Liquid-Beam-Ion-Desorption results and molecular weights of amino acids in a salty 0.1 M NaCl solution. Note that detection limits of space instruments will likely be lower than these values (see main text).

Amino acid (three letter code)	Molecular weight [u]	Detected ion	Detection limit [µM]	Detection limit [ppmw]
Aspartic acid (Asp)	133	Asp +45 u	15	2
		Asp +67 u	4	0.5
Glutamic acid (Glu)	147	Glu +45 u	34	5
		Glu +67 u	3	0.5
Histidine (His)	155	His +45 u	13	2
		His +67 u	161	25
Arginine (Arg)	174	Arg +45 u	56	10
		Arg +67 u	5740	1000
Citrulline (Cit)	175	Cit +45 u	117	20
		Cit +67 u	286	50
Glycine (Gly)	75	Gly +45 u	270	20
Serine (Ser)	105	Ser +45 u	19	2
Threonine (Thr)	119	Thr +45 u	83	10
Ornithine (Orn)	132	Orn +45 u*	78	10
Tyrosine (Tyr)	181	Tyr +45 u	55	10
		Tyr +67 u	11	2

* We note that Orn produces an AA +67 u peak with an amplitude lower than AA + 45 u, although the detection limit was not determined. AA, amino acid.

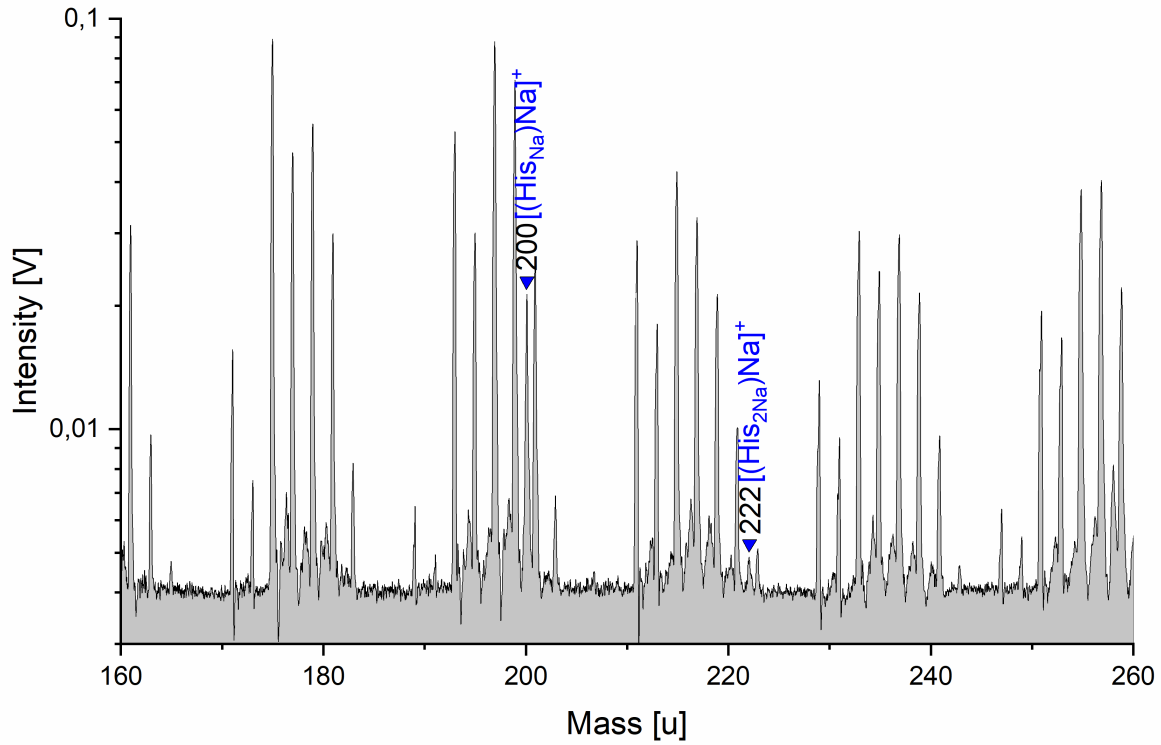

Figure 10.2: *Section of a baseline corrected cation mass spectrum of 100 ppmw His in 0.1 M NaCl (y-axis in logarithmic scale). The characteristic amino acid peaks are sodiated and detectable at His +45 u (m/z 200) and His +67 u (m/z 222). In addition to the amino acid peaks, the spectrum is dominated by salt peaks (unlabeled) from the matrix solution, with amplitudes often much higher than those of the amino acid (see text for further explanation).*

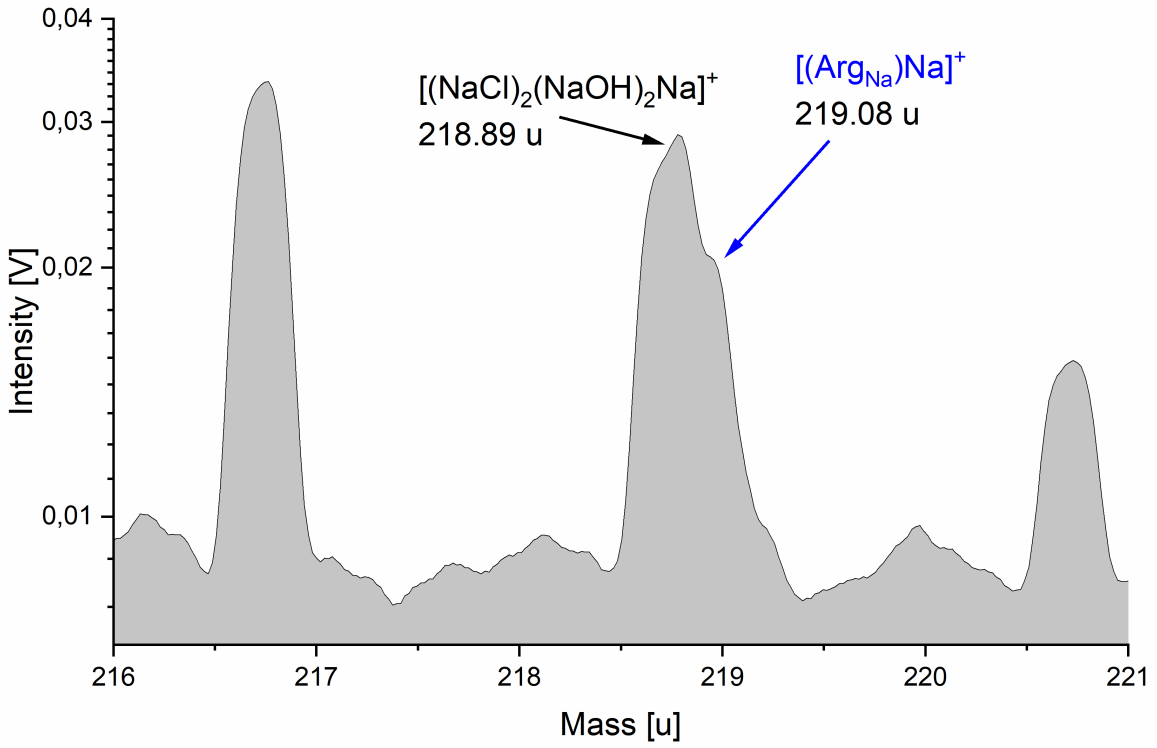

Figure 10.3: *A section of a cation mass spectrum (216–221 u) of 57 × 10^{-5} M (100 ppmw) arginine in 0.1 M NaCl (y-axis in logarithmic scale). Although the salt cluster species $[(NaCl)_2(NaOH)_2Na]^+$ at m/z 219 interferes with the sodiated $[(Arg_{Na})Na]^+$ (labeled blue), both species are identifiable. An extended mass range version of this spectrum is shown in Supplementary Figure C.1.*

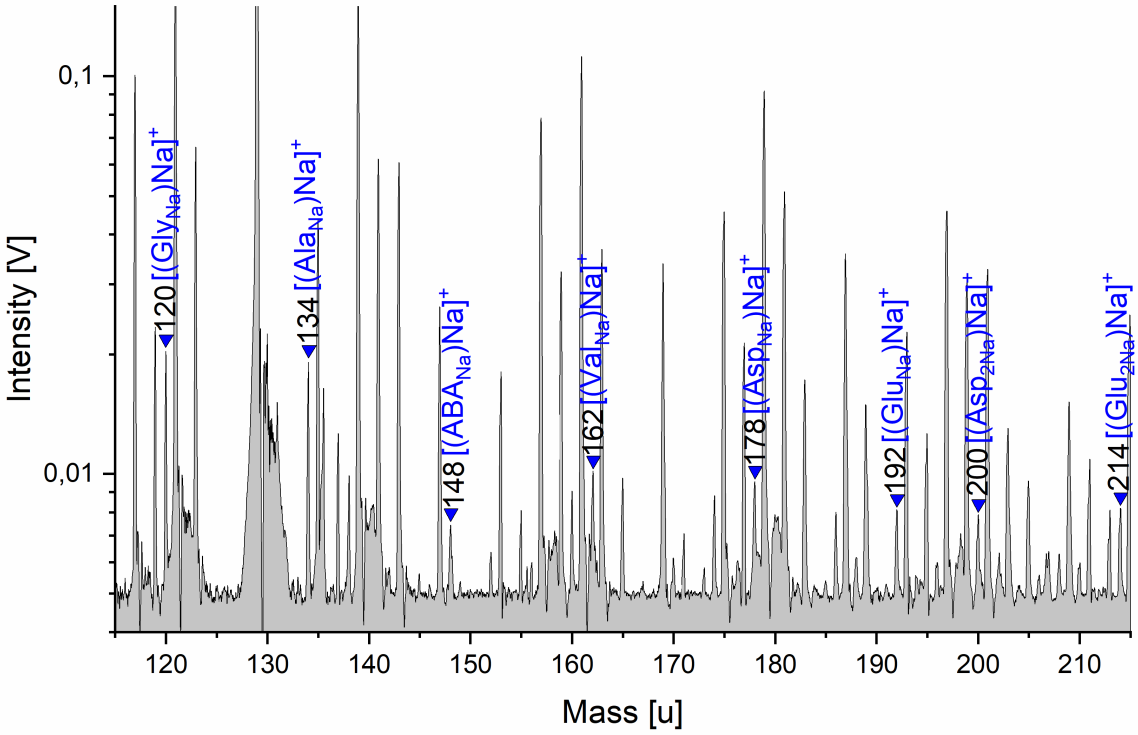

Figure 10.4: *Section (115–215 u) of a baseline-corrected laboratory cation mass spectrum (y-axis in logarithmic scale) of the seven most abundant amino acids (Gly, Ala, ABA, Ser, Val, Asp, and Glu) at abiotic concentration ratios in a salty Enceladus-like solution (Solution type ii) containing background compounds (carboxylic acids). Only Ser is undetectable at its inferred abiotic concentration of 2.9 × 10^{-5} M. Concentrations can be found in Supplementary Table C.1, together with the calculation of the concentrations in Supplementary Data C.1. The characteristic amino acid peaks are labeled in blue. In addition to the amino acid peaks, there are NaCl–water and Na_2CO_3-water peaks (unlabeled) from the matrix solution, with amplitudes often much higher than the amino acid peaks (see text for further explanation). No mass lines from the added carboxylic acids are observable.*

The characteristic sodiated peaks of Gly and Ala dominate the other sodiated amino acid peaks in the mass spectrum of the abiotic mix (Figure 10.4). Despite the low concentrations of the amino acids, the majority can be identified, with Ser as the exception. Typical amino acid fragments ($[NH_4]^+$, $[CH_2NH_2]^+$, $[AA-OH]^+$, $[AA-NH_2]^+$, and $[AA-COOH]^+$), as seen in low salinity solutions (see chapter 9), or their sodiated forms, are not observable in the spectrum of Solution type ii. If these fragments are, indeed, produced during laser desorption of this Solution type, they must be present only in very low quantities and/or interfere with more abundant species from the matrix solution. Here, we specifically note that the disodiated (M +45 u) peaks of the most abundant carboxylic acids — valeric acid and methylbutyric acid (molecular weights: 102 u) at a total concentration of 120 ppmw (considered likely to be detectable) — interfere with a salt species at m/z 147 ($[(Na_2CO_3)(H_2O)Na]^+$) and are unresolvable with the available mass resolution.

10.3.3 Fatty acids at abiotic and biotic concentration ratios (Solution type iii)

For comparison with the abiotic concentration ratios used in chapter 9 (Figure 10.5, upper panel), we measured fatty acids (sodium salts - see Section 10.2) at simulated biotic concentration ratios in a water–acetonitrile matrix (50:50 vol) (Figure 10.5, lower panel). Despite the different abundance ratios of the fatty acids, no indication of peak suppression or matrix effects was found. The deprotonated molecular peak amplitude pattern was found to match that of the abundance ratios of the fatty acids in the original solution, as observed with the abiotic case in chapter 9, confirming that no unexpected ion suppression effects on ion formation due to concentration imbalances of the different fatty acids occur. No clear preference in forming particular molecular peak ions was observed, despite the differing molecular masses of the fatty acids. Anions of the form $[M-2H+Na]^-$, as seen in, for example, electrospray ionization (ESI) experiments on dyes (Holčapek et al., 2007), were not found. Chlorinated adducts were also not observed, due to the absence of chlorine in the solution.

Detection limits for the fatty acids used here in salt poor solutions have been previously determined to be < 0.02 µM ($< \approx 5$ ppbw) (see chapter 9). In addition, some fatty acids were also tested in a salty solution (0.1 M NaCl). They were not detectable at the solubility limit (about 30 ppmw for hexadecanoic acid).

Sodiated dimers of the form $[C_{16,18}+C_{12,14,16,18,20}{-}2H+Na]^-$ can be clearly observed from species for which the combined fatty acid concentration exceeds $\approx 300 \times 10^{-6}$ M (Figure 10.5, lower panel). All dimers are identifiable as one of the fatty acids at the highest concentration of 275×10^{-6} M, that is, C_{16} and C_{18} in combination with another even carbon number fatty acid at a concentration of 55×10^{-6} or 275×10^{-6} M. The dimers were not observed in the abiotic case because of the lower fatty acid concentrations (each fatty acid at 5.5×10^{-6} M). Nonsodiated dimers were not observed.

There are conspicuous peaks at m/z 172 and m/z 186. The two peaks

were also observed in the abiotic case in chapter 9. Although their exact origin is unclear, these peaks are associated with the fatty acid samples (see Section 10.4).

10.3.4 Complex biotic mix of amino acids and fatty acids (Solution type iv)

Spectra arising from a low salinity solution of 8 amino acids, 9 fatty acids, and 15 carboxylic acids together at biotic concentration ratios were measured to simulate a spectrally demanding and complex mixture of organics in water ice grains with embedded biosignatures. Figures 10.6 and 10.7 show sections of mass spectra of this type of solution. The mass spectra were recorded in the cation (Figure 10.6) and anion (Figure 10.7) modes of the mass spectrometer, respectively.

Amino acids can be identified in such a complex mix by their protonated and deprotonated molecular peaks in the mass spectra, with sodiated species not expected to be observed owing to the low salinity of the background solution. Although the sensitivity of the method varies for different amino acids - reflecting differences in ion formation efficiency and therefore detection thresholds (see chapter 9) - amino acids other than Gly dominate the mass spectra of this biotic mixture. For example, Arg, Asp, and Lys show especially high peak amplitudes (Figures 10.6 and 10.7). Despite the differences in ion formation efficiency, we easily detect the characteristic spectral signatures, as initially applied to the solution to mimic biotic processes (e.g. Dorn et al., 2011). Extrapolating from the peak amplitudes, all amino acids would still be detectable even if an enrichment factor of 100 would have been chosen instead of 1000 (see section 10.2.2.3). Arg, Asp, and Lys would still be easily detectable with an enrichment factor of 10, likely even without any enrichment applied.

Fatty acids can be identified in such a complex mixture by their deprotonated molecular peaks ($[M-H]^-$) in the anion mode (Figure 10.7). The fatty acid biosignature abundance pattern, as seen in the mixture consisting only of fatty acids at biotic concentrations (Figure 10.5, bottom panel), is clearly observable and reflects the different biotic fatty acid concentrations. Even carbon number fatty acids are present in much higher abundances than odd carbon number fatty acids, as would be expected from biotic processes (e.g. Dorn et al., 2011). However, a general slight decline in sensitivity with increasing carbon number, due to the increasing poor solubility, can be observed. Extrapolating from the peak amplitudes, all fatty acids would still be detectable even if an enrichment factor of 10 would have been chosen instead of 100 (see section 10.2.2.3). Even numbered fatty acids would still be easily detectable without any enrichment applied.

Molecular peaks of the background carboxylic acids can also be identified, except decanoic acid (5 ppmw), propionic acid (2 ppmw), and formic acid (2 ppmw), which were present at the lowest concentrations of all background carboxylic acids. We, therefore, infer these three carboxylic acids to be present in the solution at abundances lower than their respective detection thresholds. Although present in higher concentrations, no

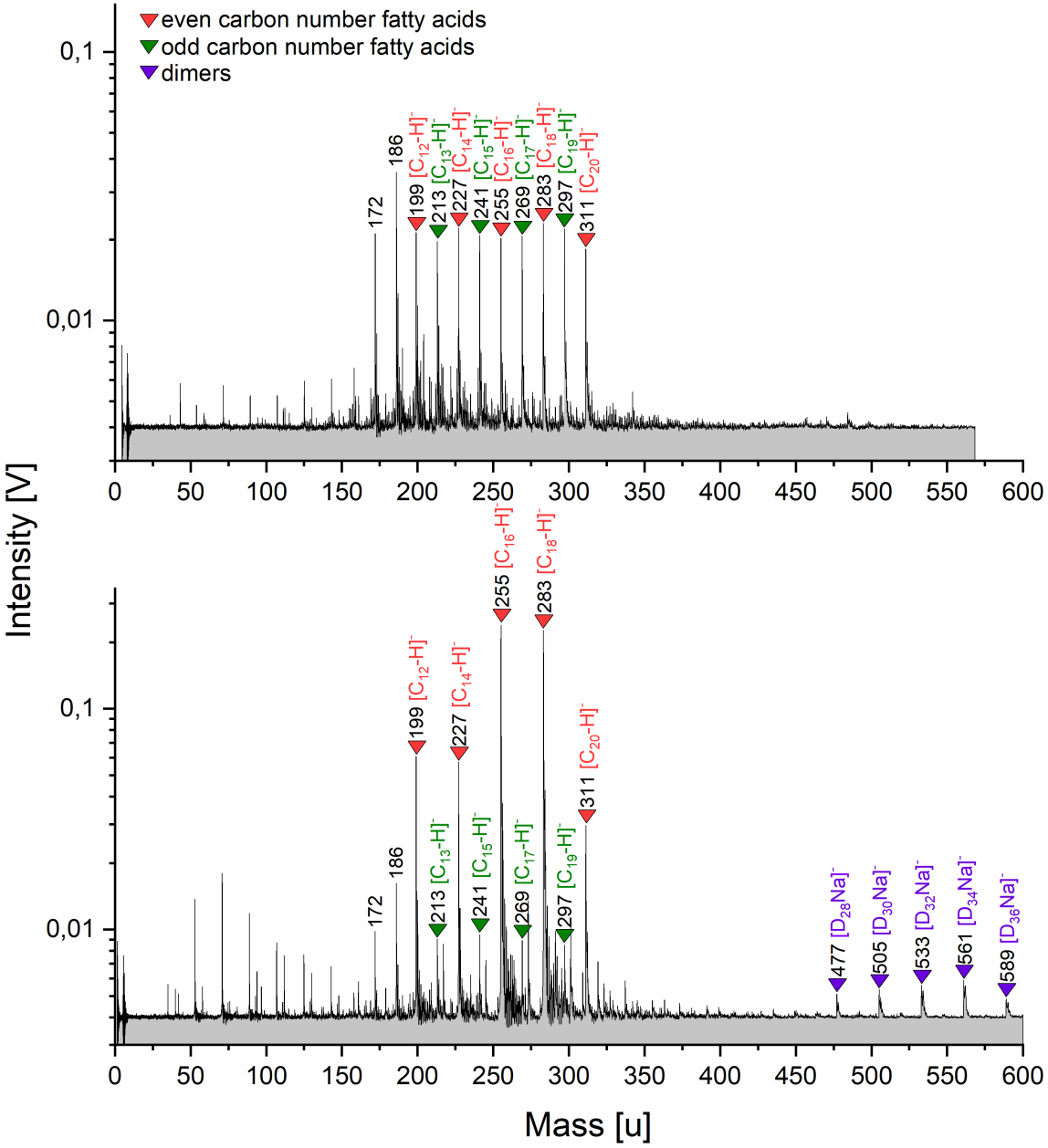

Figure 10.5: *Top: Baseline-corrected anion mass spectrum (y-axis in logarithmic scale) of fatty acids at abiotic concentration ratios in a water–acetonitrile matrix (50:50 vol) (adapted from chapter 9). The characteristic fatty acid peaks are labeled red and green for even and odd carbon number fatty acids, respectively. Deprotonated molecular peaks are equally intense, in agreement with the fatty acid equal concentrations of 5.5 × 10^{-6} M. Bottom: Baseline-corrected anion mass spectrum (y-axis in logarithmic scale) of fatty acids at biotic concentration ratios in a water–acetonitrile matrix (50:50 vol [Solution type iii]). Deprotonated molecular peak amplitudes reflect the concentration differences between odd and even carbon number fatty acids. Concentrations are 5.5 × 10^{-6} M for the odd carbon number fatty acids C_{13}, C_{15}, C_{17}, and C_{19}; 55 × 10^{-6} M for the even carbon number fatty acids C_{12}, C_{14}, and C_{20}; and 275 × 10^{-6} M for C_{16} and C_{18}. Concentrations in ppmw can be found in Supplementary Table C.2. Fatty acid dimers (sodiated) from the most abundant compounds are observed at m/z > 450. The total carbon numbers of the dimers are labeled in purple as D_{28}, D_{30}, D_{32}, D_{34}, and D_{36}.*

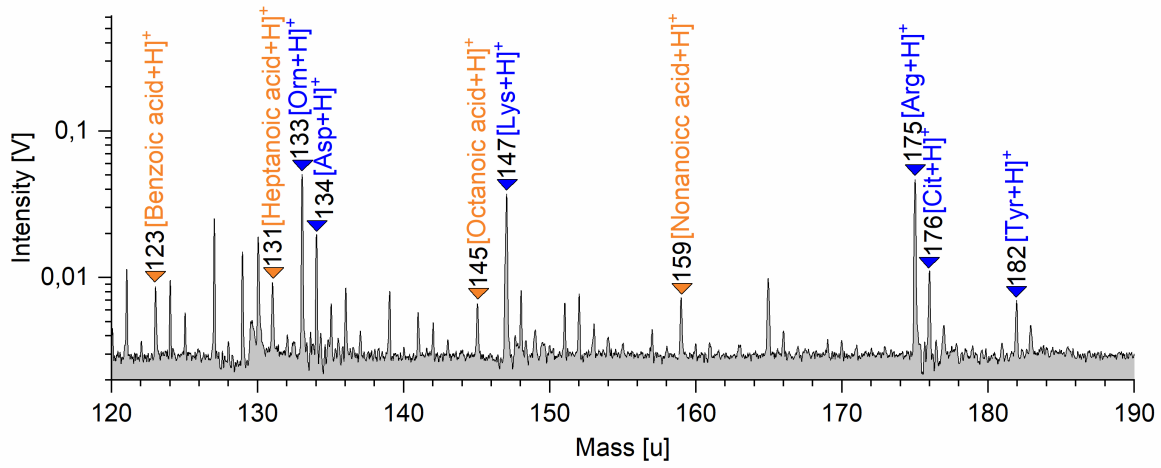

Figure 10.6: *Section of a baseline-corrected laboratory mass spectrum (120–190 u) recorded in the cation mode of the mass spectrometer (y-axis in logarithmic scale). The measured solution contains amino acids at relative abundances chosen to be representative for biotic processes as well as carboxylic acids as background components (Solution type iv). The concentrations can be found in Supplementary Table C.3. The amino acids (labeled blue) are clearly identifiable. Peaks from the background carboxylic acids are labeled orange. Unlabeled peaks of the background matrix are from water clusters ($[(H_2O)_nH_3O]^+$), Na–water clusters ($[(H_2O)_nNa]^+$), or water clusters of the organics ($[(H_2O)_n organic]^+$).*

interference of these abiotic organic compounds with any of the biogenic signals was observed.

10.4 Discussion

10.4.1 Salt-rich amino acid solutions

In this work, for the first time, analog mass spectra for amino acids potentially captured in salty ice grains from an ocean-bearing moon have been investigated. There are some fundamental differences in comparison with the previously investigated (see chapter 9) cationic mass spectra of amino acids in a salt-poor matrix.

Our results indicate that the protonated molecular peaks, which are strongest in a salt-poor medium, are suppressed (e.g., Piwowar et al., 2009) in the salt-rich case, with the strongest mass spectrometric signals from amino acids in Na-rich ocean water instead arising from sodiated cations (Figures 10.2 and 10.4). These appear at masses M(olecule) +45 u and M +67 u, respectively. In these complexes, one or two protons ($[H]^+$) are replaced by one or two sodium ions in the molecular structure and addition of another $[Na]^+$ cation provides a positive charge (Table 10.1) to the complex. Sodiation of organic molecules in a sodium-rich environment is a well-known process in ESI mass spectrometry (Newton and McLuckey, 2004; Concina et al., 2006). As in ESI, the polysodiated complexes in LILBID are likely to result from the substitution of carboxylic or amidic protons by Na^+, with the degree of sodiation dependent on the number of oxygen (from OH) and nitrogen atoms available in the molecule.

As in pure water the sensitivity of the method, and thus the detection limits, varies between different amino acids. The different side chains

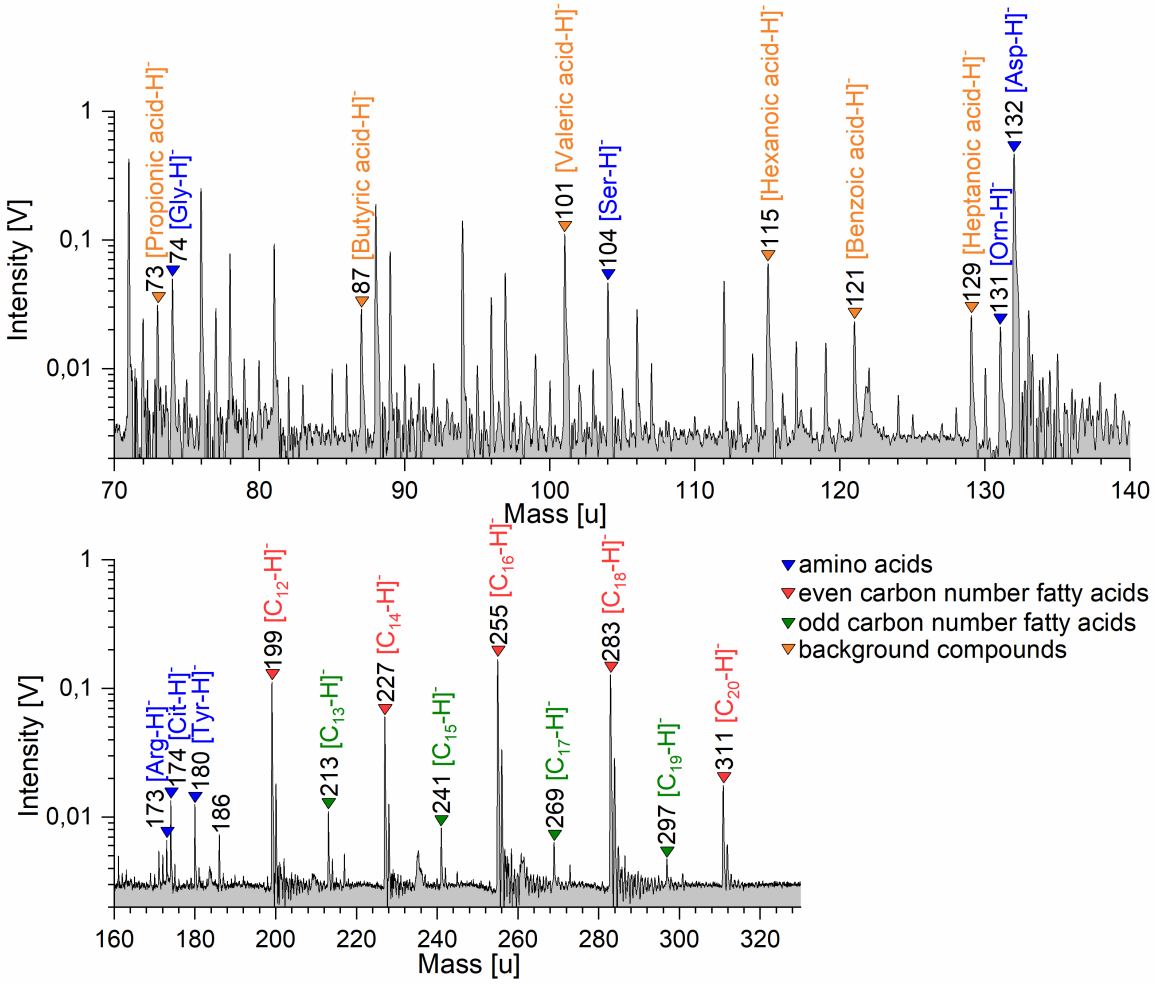

Figure 10.7: *Two sections of a baseline-corrected laboratory mass spectrum (70–140 u on the top panel and 160–350 u on the bottom panel) recorded in the anion mode of the mass spectrometer (y-axis in logarithmic scale). The solution contains amino acids and fatty acids at relative abundance ratios representative for biotic processes and carboxylic acids as background components (Solution type iv). The concentrations can be found in Supplementary Table C.3. A water–acetonitrile (50:50 vol) matrix was used, as the fatty acids are poorly water soluble. Amino acids (labeled blue) and fatty acids (labeled red and green) are clearly identifiable. Unspecified but fatty acid samples related peaks at m/z 172 and m/z 186 are observable as in Solution type iii. Peaks from the background carboxylic acids are labeled orange. Unlabeled peaks of the background matrix are from water clusters ($[(H_2O)_nOH]^-$), Cl–water clusters ($[(H_2O)_nCl]^-$), or water clusters of the organics ($[(H_2O)_n organic]^-$).*

confer a wide range of properties, with the logarithmic acid dissociation constant pK_a being the most relevant here (Wu et al., 1992). The more positive the pK_a, the less dissociation of the acid at any given pH, that is, the weaker the acid. In pure water, the lowest detection limits are determined to be those for Arg and Lys (1 nM) - amino acids with basic side chains and relatively high pK_a values (see chapter 9). In the salty matrix, we found the lowest detection limits (Table 10.1), those for sodiated Asp and Glu, to be about 3 µM (compared with about 0.1 µM for the relevant (nonsodiated) peaks in salt-poor water). Both amino acids have acidic side chains and relatively low pK_a values.

In general, sensitivity to those amino acids that have been investigated in both matrices drops between a factor of two (Ser) and five orders of magnitude (Arg) when a 1 % concentration of sodium salts is present. Experiments on NaCl-rich Gly solutions showed that the activity of Gly in the Gly-NaCl-H_2O system diminishes with increasing NaCl concentrations, giving rise to a so-called salt-in effect for amino acids (Sirbu and Iulian, 2010). We conclude that a high salt concentration also suppresses the characteristic organic peaks in our LILBID experiments. However, sensitivities vary significantly less between different sodiated amino acids (Table 10.1) compared with the sensitivity variations observed between protonated molecular species in a salt-poor matrix (Table 9.1). The salts (and NH_3) may function as a pH buffer in the solutions used here and, in turn, counter pH dependent effects on the different sensitivities to the amino acids and/or the ionic bonding of Na^+ to the amino acids might be more similar among different molecular structures than protonation of amino acid molecules.

Unlike identical measurements with amino acids at concentrations varying from 50 to 1000 ppmw in pure water (see chapter 9), in a salty solution no characteristic fragmentation of the amino acids was observed (whether sodiated or not) in the resulting mass spectra. The high salt concentration may have neutralized charged fragments or suppressed the fragmentation process of the organics. In the latter case, although out of the scope of this work, we hypothesize that uncomplexed amino acids may be less stable than the sodium complexes formed in a sufficiently $[Na]^+$-rich solution. This appears to differ from the case of ESI mass spectrometry, in which fragment cations of the form $[Na_2NH_2]^+$, $[NaOCNNa]^+$, and $[Na_3CN_2]^+$ can form from sodiated organic molecules, dependent on the elemental composition of the analyzed molecule (Shi et al., 2005).

In Solution type ii, several amino acids and salts, together with 14 carboxylic acids, were measured in the cation mode to simulate a more complex mixture, as might occur in Enceladus ocean. The goal was to investigate (a) interferences between mass lines and (b) matrix effects on the sensitivity for amino acids. Indeed, some of the peaks from sodiated amino acids have isobaric masses, at the integer level, with salt- and salt- water-derived peaks. However, the mass differences between these cationic species are relatively large, typically on the order of 0.15 to 0.2 u (Supplementary Figure C.2), and they can be readily resolved with a mass resolution of about $m/\Delta m = 1000$. For example, the disodiated Arg cation interferes with the salt cluster species $[(NaCl)_2(NaOH)_2Na]^+$ at m/z 219. The mass difference of 0.19 u between these two species can be

resolved with the laboratory reflectron (mass resolution of $m/\Delta m = 600$-800) used here (Figure 10.3).

Although some of the carboxylic acids were present in higher concentrations than most of the amino acids (e.g., valeric acid and methylbutyric acid at concentrations of almost 600 µM), no sodium complexes involving them were detectable in Solution type ii (cation mode). Their concentrations probably were below their detection limits in a salty matrix. This finding is in agreement with our nondetection of sodiated fatty acids at their solubility limit ($\sim$ 30 ppm for hexadecanoic acid) in a solution with identical salt compounds. They could, however, be identified in the negative mode in a low-salinity solution.

10.4.2 Fatty acids

If present in Enceladus ocean, the poorly soluble long-chain fatty acids will probably most easily enter the plume within salt-poor ice grains formed from an organic layer at the oceanic surface (Postberg et al., 2018a). Under such conditions, fatty acids produce characteristic deprotonated molecular peaks in anion mass spectra (Figures 10.5 and 10.7) even at trace concentrations of a few tens of nM (see chapter 9).

In the biotic mixture used for this work, with concentrations differing between fatty acids with even and odd carbon numbers, the peak amplitude pattern again matches that expected from the fatty acid concentrations (Figures 10.5 and 10.7). In contrast to amino acids, detection sensitivities vary by only a small amount between fatty acids ranging in size from 12 to 20 carbon atoms, with spectral peaks decreasing only slightly for identical concentrations with an increasing carbon number. This reflects the fact that, in contrast to amino acids, the fatty acids have very similar structures and pK_a values. This similarity enables the facile distinction between biotic and abiotic abundance patterns.

Even at low to intermediate sodium concentration in the solution ($\sim$ 0.75 mM from the sodium salts used), sodiated dimers of the fatty acids are observed (Figure 10.5), with amplitudes approximately two orders of magnitude lower than those of the deprotonated molecular peaks. A combined fatty acid concentration for two species of $\approx$ 300 µM is sufficient to create very clear dimer signals at the given $[Na]^+$ concentration and, extrapolating from the observed amplitudes (Figure 10.5), concentrations of 100 µM should still allow for a dimer detection. With increasing salinity, the sodiated dimers are likely to become more abundant than the deprotonated molecular anions, which may suffer from similar suppression effects as observed in the case of amino acids.

There are conspicuous peaks at m/z 172 and m/z 186 in all fatty acid mass spectra. These two peaks are also observed in chapter 9. The exact origin of these peaks is still unclear, but they are undoubtedly associated with the fatty acid samples. They may potentially be fragments due to C_nH_{2n} cleavage from the fatty acids in combination with electron capture ionization. The peaks could also represent undefined sodiated species. However, the most likely possibility is that the peaks derive from a specific but currently unknown contamination of the fatty acid sodium salts. For more details about the potential origin of these peaks, see chapter 9.

10.4.3 Complex biosignature mixtures

Two scenarios were investigated. The first (Solution type ii) simulated spectra arising from amino acids at putative abiotic abundances together with other abiotic organic compounds with added salts that are representative of Enceladus ocean composition. These were measured in the cation mode of the mass spectrometer. In the second scenario (Solution type iv), we investigated the spectra generated by biotic concentrations of fatty acids and amino acids in ice grains as may form from a putative organic film on the surface of Enceladus ocean. For the amino acids, biotic concentration ratios as they appear in Earth's ocean were used and enrichment factors inferred from similar processes on Earth's ocean then applied (section 10.2.2.3). The availability of amino acids in Enceladus ocean probably differs from that in Earth's ocean. However, as the most well-characterized, cold water, salty environment in which life flourishes, Earth's ocean currently represents the only example from which biotic amino acid abundance ratios can be derived for application to Enceladus. As in Solution type ii, a large number of potential abiotic organics were included in the simulant mixture. These parameters can be expected to produce the most complex, and therefore challenging, mass spectra for a biotic case. These spectra were obtained by using both positive and negative modes.

In both scenarios, the abiotic and biotic mass spectrometric fingerprints of the biosignatures could be successfully identified (Figures 10.4, 10.6, and 10.7). No unresolvable interferences with any of the amino acids and fatty acids in the solution were observed. In the analytically demanding salty solutions, sodiated amino acids can be identified down to $\sim$ 1 ppmw. The nondetection of Ser does, however, indicate that due to matrix effects the detection limits are slightly higher in comparison with those for a solution with just individual amino acids. In the salt-poor solution, the sensitivity to amino acids is much higher in most cases, as expected from the results in 9. There, 500 ppbw concentrations of Arg and Lys created very clear signals (signal to noise ratio $\approx$ 50 sigma for both amino acids) in the cation mode (Figure 10.6) whereas Asp and Ser are the dominant amino acid signals in the anion mass spectra (Figure 10.7).

In a similar way, spectra of fatty acid mixtures at biotic concentrations down to 100 ppbw reflect the biotic abundance pattern in which even carbon number fatty acids are clearly more abundant than odd carbon number fatty acids, even in a complex mixture where different organics could theoretically easily interfere with each other (Figure 10.7). However, a stronger dependence on the number of carbon atoms (i.e., C-number) was observed when compared to Solution type iii (Figure 10.5), with decreasing sensitivity toward higher carbon numbers. Extrapolating from the observed amplitudes, the biotic patterns would have been clearly identifiable in the mass spectra even at 10–100 times reduced concentrations in agreement with the detection limits found in chapter 9.

Chapter 7 shows that the experimental parameters of the LILBID analogue setup can be correlated with impact speeds of ice grains onto impact ionization mass spectrometer targets in space. By comparison be-

tween the experimental parameters used here (intermediate to high laser intensities and intermediate to high delay times) with amino acids and those required to simulate different impact speeds of the ice grains, we infer that instrument sensitivity to amino acids in grains formed from a salty ocean environment is maximized at impact speeds of 5–10 km/s. The slightly higher values compared with those in pure water agree with the observation that the sodiated amino acids, which are the characteristic peaks in a salty environment, resist fragmentation more than the protonated and deprotonated molecular species produced in a salt-poor matrix. We confirm the finding of chapter 9 that using very high delay times and intermediate laser intensities, equivalent to impact speeds of 3–6 km/s, maximizes the detection sensitivity for fatty acids.

Previous work has shown that organics (both refractory and volatile) in projectiles are capable of surviving the impact process at velocities of up to 5 km/s (e.g., Bowden et al., 2009; Burchell et al., 2014; New et al., 2020a). Further experiments, in which capsules containing aqueous amino acid solutions were subjected to impacts of steel projectiles at up to $\sim$ 2 km/s, showed that a large fraction (40–70 %) of the amino acids also survived (Blank et al., 2001). In the specific case of ice grains, modeling of particle impacts onto aluminum targets indicates that at relative velocities of up to 5 km/s, comparable with Enceladus plume transect velocities, little to no thermal degradation of entrained organics, such as amino acids, should occur (Mathies et al., 2017).

The LILBID technique is known to be capable of preserving and measuring delicate organic structures, such as intact membrane complexes (Morgner et al., 2007), as a function of applied laser intensity, with ultrasoft ionization occurring at low laser energies. However, the results presented in this work, and those of chapter 9, use higher laser energies that are typically more destructive, and yet show that a detectable fraction of organic molecules, in particular amino acids, fatty acids, and peptides, survive at equivalent impact speeds of > 5 km/s. The fragmentation of organic macromolecules during impacts of ice grains from Enceladus (Postberg et al., 2018a) shows similar behavior, with the characteristic (70–200 u) spectral signatures of the breakup of large (m $>$ 200 u) parent molecules only becoming detectable at impact speeds above 5 km/s and becoming more prominent at speeds > 10 km/s (Postberg et al., 2018a).

These laboratory and flight results are in good agreement with ab initio molecular dynamics simulations that show that even a few layers of water ice molecules can effectively protect organic molecules from impact fragmentation (Jaramillo-Botero et al., 2021). With ionization also promoted by a liquid or frozen water matrix (Wiederschein et al., 2015), the survivability and detectability of organics appears to be significantly improved in ice grains ejected into space by ocean-bearing moons, even if encountered at relative velocities above 5 km/s.

These relative speeds are of keen interest for feasibility studies of flying through the plume of Enceladus on ballistic trajectories. Cassini flew through the plume at speeds as low as 7.5 km/s, but plume transects at 4–5 km/s are possible (Reh et al., 2016; Mitri et al., 2018). Even slower speeds can be achieved, but grain impact speeds of greater than $\sim$ 3 km/s were required to generate sufficient ionization for the analysis of

plume material with Cassini's CDA. Thus, not only are plume transects below 3 km/s undesirable for this technique, but based on our work they also provide no improvements to the diagnostic capability of the mass spectrometry.

10.5 Conclusions

The proven ability of the LILBID experiment to simulate the impact ionization mass spectra of water–ice-dominated grains (e.g., Postberg et al., 2009a; Postberg et al., 2011a; Postberg et al., 2018a; Khawaja et al., 2019; chapter 7) has been applied to the simulation of ice grains containing biosignatures in biotic and abiotic concentration ratios. Potentially abiotic organic substances (such as simple carboxylic acids) and inorganic substances (salts and ammonia) have been added to investigate detection limits, potential mass spectral interferences, and suppression effects, with the aim of verifying whether abiotic and biotic spectral fingerprints can be clearly identified under complex conditions. A more precise quantitative determination of the biosignatures (e.g., calibration curves), however, is beyond the scope of this article and will be a goal of future work.

Enceladus' organics are principally believed to enter ice grains either from a solution in the ocean or from an organic layer on top of the ocean. Poorly soluble compounds can only originate from that layer and will be part of salt-poor ice grains (Type 2) (Postberg et al., 2018a; Khawaja et al., 2019), whereas organics with higher water solubility will also be incorporated into ice grains forming from salty ocean droplets (Type 3) (Postberg et al., 2009a). If present, free amino acids will be dissolved in the Enceladean ocean and are thus expected also to be found in salt-rich ice grains. All tested amino acids form sodiated cations that produce the most intense amino acids signal by far under these conditions. To discriminate between the characteristic sodiated mass peaks of amino acids and other dissolved organic species and extraneous peaks from near isobaric salt species, a future flight instrument will require a mass resolution of at least $m/\Delta m = 700$, and ideally $m/\Delta m > 1000$.

Amino acids generally favor forming cations, whereas fatty acids favor forming anions. A future flight instrument, therefore, ideally needs to be capable of detecting both cations and anions to cover the complete range of biosignatures investigated here.

Of the amino acids tested, Asp and Glu, via their sodium complexes, have been detected at the lowest concentrations (0.5 ppmw). Fatty acids and other carboxylic acids are not detected in such a high salinity environment at or below a level of 50 ppmw. In an environment of intermediate salinity, sodiated dimers of fatty acids, however, can be detected at a level of 0.1 mM, equivalent to $\sim$ 25 ppmw. By contrast, deprotonated anions from fatty acids and protonated cations from amino acids will dominate spectra from salt-poor water ices and are detectable down to the nanomolar or ppbw level, respectively (see chapter 9).

It is reasonable to assume that the observed suppression and complexation effects arising from interaction with the salty matrix will also affect other organic species. Recently, identified soluble organic compounds,

found in many salt-poor Type 2 grains, are believed to enter grains via condensation from the vapor phase (Khawaja et al., 2019). Such soluble organics should then also be incorporated into ocean spray, which is believed to form salty Type 3 ice grains rising through the Enceladus fractures (Postberg et al., 2009a; Postberg et al., 2011a). The work presented here, however, indicates that the detection and identification of such compounds in spectra generated by impacts of salty Type 3 grains might be more difficult than for the salt-poor grains.

The initial abundances of amino acids and fatty acids at given concentrations are reflected in the amplitudes of their molecular peaks, including the sodiated molecular peaks of amino acids in salty solutions. Abiotic and biotic fatty acid signatures within the ice grains are easily discernible. The ratios of various amino acids to Gly and the odd-even carbon number abundance pattern of fatty acids serve as biosignatures that can be readily distinguished from each other in mass spectra, even under demanding matrix conditions in a salt-poor as well as a salt-rich environment. Should they be present, these key organic species as well as their abiotic and biotic signatures are, therefore, likely to be identifiable in impact ionization mass spectra from ice grains recorded in space. Detection limits for space instrumentation with more efficient ion detectors and higher dynamic ranges than the experimental setup used here may be expected to be at least two orders of magnitude lower than the values reported here and in chapter 9. We conclude that in a salt-poor water ice matrix, all investigated biosignatures could then be detectable, as such, down to the nanomolar level, with amino acids in a salty environment detectable down to at least the micromolar level.

To simulate biotic concentrations, we used values from the only example we have: Earth's ocean. The concentrations and specific types of fatty acids and amino acids in an inhabited extraterrestrial environment will almost certainly be very different. Although our results demonstrate the ability to identify by using LILBID a large number of biogenic tracers at Earth-like concentrations, it is impossible to say whether this or any other method will be able to detect the concentrations of these substances in ice grains from an extraterrestrial ocean world.

It is important to note, however, that according to a recent work by Truong et al. (2019), concentrations of abiotic amino acids may be expected to be barely detectable. Specifically, aspartic acid and arginine have been shown to decompose within thousands, to at most a few million years in oceanic water and any detection of these compounds in material from ocean worlds will be strong evidence for a very efficient, probably extant generation mechanism. Another study implies high compatibility of amino acids in ice Ih during the freezing of an aqueous solution and suggests that the ice matrix protects amino acids from decomposition or racemization (Hao et al., 2018). The LILBID experiments conducted so far (this work, and chapter 9) show that such compounds can be reliably detected and identified at low concentrations, particularly arginine in a salt-poor matrix and aspartic acid in a salt-rich matrix.

In the future, the LILBID technique will be used to perform quantitative investigations of not only the biosignatures discussed in this work but also a wide range of other relevant organic compounds, in matrices

designed to mimic ice grains derived from a range of realistic oceanic compositions for Enceladus and Europa. The LILBID experiments on DNA extracted from bacterial cultures, as well as lysed and disrupted cellular material, are currently underway to investigate the mass spectral appearance of these biological materials after simulated impact ionization.

The results of this work also aid future space mission planning, with laboratory experimental parameters used to derive recommended impact velocity regimes and instrument configurations (see chapter 7) — for ice grain impacts onto spaceborne mass spectrometers — which maximize the chances of detecting biomarker compounds.

The survivability of organics appears to be significantly improved when large molecules are protected by a liquid or frozen water matrix, which simultaneously promotes ionization (Wiederschein et al., 2015). When using impact ionization mass spectrometers, the efficient detection of amino acids and fatty acids in ice grains present in plumes or ejecta emitted from Enceladus and Europa and the reliable identification of abiotic and biotic signatures of these organics is found to occur at encounter velocities of 3-8 km/s, with an optimal window at 4-6 km/s. At these speeds, in a water-rich matrix, even complex organic molecules remain largely intact, yet they are expected to efficiently form cations and anions from impact ionization, yielding the highest possible signal-to-noise ratio. This means that ballistic flythroughs of the Enceladus plume (and potential plumes of other ocean worlds) at these velocities will yield optimal diagnostic data on the presence and identity of potential biogenic compounds.

Acknowledgements

The authors thank Lenz Nölle for valuable discussions about the experimental results and Marie Dannenmann for discussions about future studies. Most of this work was carried out at the Institute of Earth Sciences, Heidelberg University. Some additional work was carried out at the Wilhelm-Ostwald-Institute, Leipzig University, and at the Jet Propulsion Laboratory, California Institute of Technology, under a contract with the National Aeronautics and Space Administration.

Handling editor: Sherry Cady

Author disclosure statement

No competing financial interests exist.

Funding information

The research leading to these results received funding from the German Research Foundation (DFG) projects PO 1015/2- 1,/3-1,/4-1, project AB 63/9-1 and from the European Research Council (ERC) under the European Union's Horizon 2020 research and innovation programme (ERC Consolidator Grant 724908-Habitat OASIS). JIL was supported by the

Distinguished Visiting Scientist Program at the NASA Jet Propulsion Laboratory during the course of the work.

IV. Conclusions and outlook

11 Conclusions

SAMPLING EMITTED ICE GRAINS in the vicinity of cryovolcanically active icy moons is a cost-effective means to investigate the subsurface oceans of these moons without requiring a landing mission. The oceans are analyzed with impact ionization mass spectrometers during spacecraft flyby encounters with µm-sized ice grains ejected from the moon's surface or subsurface. Detailed analyzes of the resulting impact ionization mass spectra require terrestrial calibration using Laser-Induced Liquid Beam Ion Desorption (LILBID) in the laboratory.

The goal of this thesis is to prepare for future space missions to extraterrestrial ocean worlds and improve spectral analysis of ice grain mass spectra recorded in space by using LILBID data. To achieve this goal, this thesis addressed four major scientific objectives (see section 6.2):

1. Can variations in the mass spectral appearance caused by differing impact speeds of ice grains onto space detectors be reproduced in the laboratory using LILBID?
2. The development of a comprehensive spectral reference library for existing and future LILBID mass spectra.
3. Will future impact ionization mass spectrometers be able to detect bioessential organic molecules, such as amino acids, fatty acids, and peptides, in ice grains emitted into space? If so, how sensitive are these instruments to these organics, i.e. what are the detection limits?
4. Will future impact ionization mass spectrometers be able to detect and discriminate between abiotic and biotic signatures of amino acids and fatty acids if mixed with a number of other organic and inorganic compounds in ice grains emitted from ocean worlds such as Enceladus and Europa? If so, what encounter speeds of spacecraft with the ice grains are most suitable for the detection of such acids?

This cumulative dissertation comprises three published, peer-reviewed articles in international scientific journals and one manuscript in preparation for submission to a peer-reviewed international scientific journal. The four self-contained articles (chapters 7 to 10 within Parts II and III) are complementary. The necessary steps to address the four scientific objectives were successfully completed within each article. Results were discussed and distinct conclusions drawn in the respective chapters. Overall conclusions are summarized in the following.

The impact ionization process is fundamentally linked to the impact speeds of the ice grains. Thus, spectral appearance is a function of not only ice grain composition but also impact speed onto the spaceborne mass spectrometer. The laboratory LILBID facility is capable of accurately reproducing impact ionization mass spectra generated by micron- and sub-micron-sized water ice grains encountered by spaceborne mass spectrometers at impact speeds ranging between < 3 and > 21 km/s.

This is accomplished by the selection of appropriate laser power densities and delay times of the gated mass spectrometer. The higher the laser's power density and the lower the delay time, the higher the simulated impact speed.

The experimental settings needed to simulate different ice grain impact speeds were inferred from a simple spectrum type (CDA Type 1; see section 3.1 and chapter 7) showing nearly pure water. These parameters suited to particular impact speeds can now be used as search parameters in a comprehensive spectral reference library developed during the course of this work, enabling spectra of more complex compounds, acquired under these conditions, to be rapidly located and investigated.

More than 10,000 cationic and anionic LILBID mass spectra of > 200 different organic and inorganic substances/mixtures have been successfully uploaded to a newly developed LILBID mass spectral reference library, an SQL-based database (chapter 8). Each spectrum is associated with the relevant experimental parameters allowing correlation with the parameters of the ice grains encountered in space. The reference library allows the collected data to be searched via the used experimental parameters and mass lines in the spectra returning matched spectra for analysis and comparison with flight mass spectra.

Future spacecraft data will be able to be rapidly analyzed by using the LILBID spectral reference library. The readiness of the spectral library, prior to the return of mission data, makes the reference library a fundamental tool for spectra analyzes because these can be planned and performed more systematically in much less time than for example analyses of CDA data from the Cassini mission (section 2.1). This is particularly relevant for future astrobiology investigations of ocean worlds in the Solar System (Figure 11.1), such as NASA's Europa Clipper mission designed to explore Europa's habitability (see section 4.2).

Bioessential compounds, namely amino acids, fatty acids, and peptides, have been tested with LILBID to predict their appearances and determine their detection limits in ice grain mass spectra recorded in space. The recorded spectra were uploaded to the spectral reference library and systematically analyzed. Characteristic spectral features of amino acids, fatty acids, and peptides are readily identifiable down to the µM or nM level in mass spectra recorded from aqueous solutions containing these molecules, even if other organic and inorganic background compounds are present. The relative abundances of these background compounds recreate the effect of a rocky core that extensively interacted with subsurface ocean water. Thus, these measurements represent the most realistic scenario for simulating the spectra from impact ionization of ice grains containing these biologically important molecules from extraterrestrial ocean worlds.

Poorly water soluble organics, such as fatty acids, if present in Enceladus' ocean (and possibly similarly in Europa's ocean), would be expected to enter ice grains from a thin, organic layer on top of the salty subsurface ocean and will therefore be incorporated into salt-poor ice grains (Type 2; Postberg et al., 2018a, Khawaja et al., 2019). These organics are expected to appear in mass spectra which exhibit only minor

salt peaks. In contrast, organics with higher water solubilities will enter ice grains from solution, in the salty ocean, and are therefore expected to be incorporated into ice grains forming from salty ocean droplets (Type 3; Postberg et al., 2009a). These organics will certainly appear in mass spectra together with prominent salt peaks.

Proteinogenic amino acids[1] are generally highly water soluble and are expected to be found in salt-rich Type 3 ice grains. The water solubility of peptides strongly depends on their amino acid residues, decreasing with an increasing number of hydrophobic amino acid residues (Narita et al., 1984; Sarma et al., 2018). Peptides, if present, can thus be expected to be found in both Type 2 and Type 3 ice grains. In fact, in recent laboratory experiments, peptide formation has been observed under simulated Enceladus hydrothermal conditions (Takahagi et al., 2019).

The tested organic molecules form protonated/deprotonated molecular peaks in salt-poor solutions that reflect the original relative abundances of the molecules in the source solutions. Peptides form fragments characteristic of their amino acid residues. Protonated amino acids and peptides, as well as their characteristic cationic fragments, are generally detectable at lower concentrations than their anionic counterparts. Deprotonated fatty acids are, however, detectable at lower concentrations than their cationic counterparts. A future flight instrument therefore ideally needs to be capable of detecting both cations and anions, in order to cover the complete range of biomolecules and their fragments investigated within Part III of this thesis. The SUrface Dust Analyzer (SUDA) on-board NASA's Europa Clipper spacecraft will have this dual polarity capability (see sections 4.2 and 4.3) .

Amino acids were also investigated in salt-rich matrices. Under these conditions, protonated and deprotonated molecular peaks, as observed in salt-poor matrices, are suppressed and the strongest mass spectral signals are produced by characteristic di- and tri-sodiated cations that still reflect the original relative abundances of the molecules in the source solutions, though with lower absolute amplitudes at a given concentration. Interferences between the sodiated molecules with near isobaric matrix compounds, particularly dominant salt species, in the mass spectra can be resolved with a mass resolution of > 1000 m/Δm. This would be comfortably possible with the Enceladus Ice Analyzer (ENIA) instrument included in the potential future Enceladus Life Finder (ELF) mission (see section 3.2).

The detection limits of the tested organics and their characteristic fragments strongly depend on the salinity of the matrix and are found to be about an order of magnitude higher in salt-rich solutions than in salt-poor solutions. Detection limits for space qualified impact ionization mass spectrometers possessing more efficient ion detectors and higher dynamic ranges than the LILBID facility are expected to be at least one order of magnitude lower than the values reported in this thesis.

It is reasonable to assume that the observed suppression and complexation effects arising from interactions with the salty matrix will also affect other organic species. These effects together with the higher de-

[1] Amino acids which are incorporated into proteins through biological processes.

tection limits in salt-rich solutions indicate that identification of organics might be more difficult in salt-rich Type 3 grains than in salt-poor Type 2 grains. To further evaluate this, a wide variety of organic compounds is currently being tested in salt-rich matrices with the LILBID setup (see section 12.2).

As peptides are polymers of two or more amino acids, any detection of peptides in the emitted ice grains would indicate active biochemistry within the respective moon's ocean, because the rate of generation of these molecules must have exceeded the rate of decomposition. However, amino acids and fatty acids can be produced either abiotically or biotically, although these result in significantly different abundance patterns of the organic molecules (Dorn et al., 2011; Sherwood, 2016; Creamer et al., 2017). These amino acid and fatty acid abundance patterns can be unambiguously detected and discriminated in LILBID mass spectra, even with numerous organic and inorganic background compounds in the solutions producing demanding matrix conditions. This means that future impact ionization mass spectrometers will very likely be capable of detecting amino acids, fatty acids, and peptides, if present in the emitted ice grains, and in turn discriminating between abiotic and biotic chemistry. Based on these finding, more measurements for the identification of biosignatures in ice grains, for example from DNA and lipids extracted from *Escherichia coli* cell cultures, as well as lysed and disrupted cellular material, are underway (see section 12.3).

Compounds measured with the LILBID apparatus and uploaded to the reference library are commonly tested using numerous combinations of laser power density and delay time. With varying experimental parameters, the sensitivity of the LILBID process, and by analogy the sensitivity expected for impact ionization mass spectrometers, to characteristic spectral signals from the tested compounds varies as well. Optimal encounter velocities for the detection of characteristic spectral features of target compounds, potentially embedded in the ice grains, can be predicted using LILBID data.

By comparing the experimental parameters used for the LILBID amino acid, fatty acid, and peptide experiments with those required to simulate spectra resulting from different impact speeds of ice grains onto spaceborne mass spectrometers, the investigated organics, as well as their characteristic abiotic and biotic abundance patterns, appear to be reliably identifiable when encountered by spacecraft at speeds between 3 and 8 km/s with an optimal window between 4 and 6 km/s. Therefore, spacecraft encounter velocities within this speed range are recommended (Figure 11.1).

It has been previously argued that impacts of ice grains onto metal targets of spaceborne mass spectrometers at these velocities would entirely destroy embedded organics and therefore only fragments of the parent molecules would appear in the mass spectra. This would make the successful characterization of organics in ice grains extremely challenging, if not impossible. This argument has been questioned by previous experimental studies showing that intact organic molecules are capable of surviving impacts at velocities up to 5 km/s

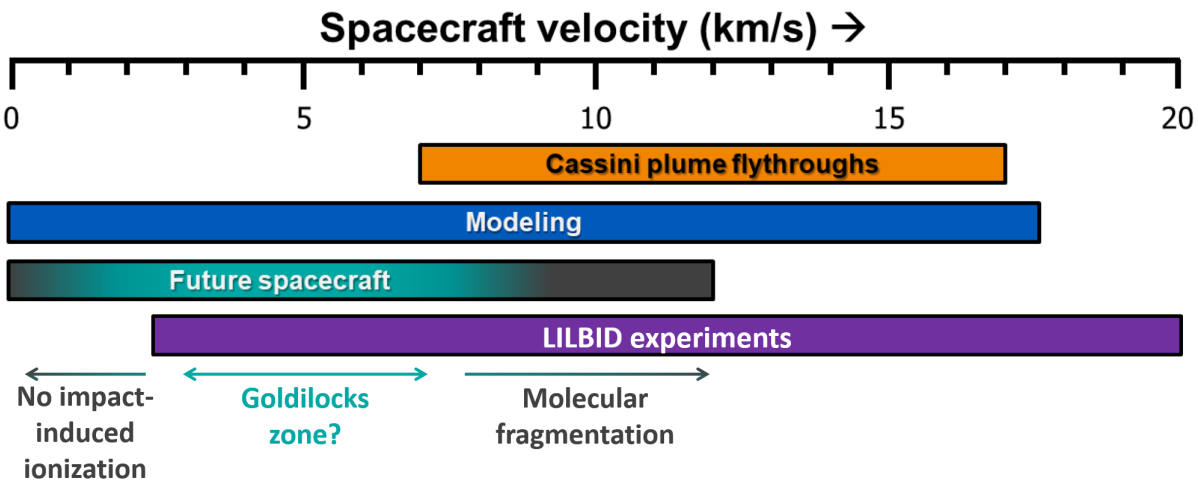

Figure 11.1: *A future astrobiology investigation targeting ice grains from Enceladus or Europa during spacecraft flybys requires velocities fast enough to ionize biomolecules, which are potentially encased in the ice grains, but slow enough to avoid significant fragmentation of these molecules. According to the work presented in this thesis, velocities of 4 - 6 km/s appear to be optimal for the detection and identification of potential biogenic molecules (figure adapted from Cable et al., 2020).*

(Bowden et al., 2009; Srama et al., 2009; Burchell et al., 2014; Hillier et al., 2014; New et al., 2020a; New et al., 2020b). Moreover, the findings of Postberg et al. (2018a) and Khawaja et al. (2019) prove that organic compounds, though probably fragments, embedded in ice grains can successfully be identified using impact ionization in space at speeds exceeding 5 km/s.

The LILBID analogue experiments in this thesis demonstrate that unfragmented parent molecules of amino acids, fatty acids, and peptides would survive ice grain impacts at velocities above 5 km/s. The frozen water matrix, in which organics from Enceladus and Europa are embedded, protects the organics from complete destruction, improving the probability of detecting and identifying the compounds using impact ionization in space.

These findings are in good agreement with ab initio molecular dynamics simulations which show that even a few layers of water ice molecules effectively protect organic molecules from fragmentation, by dissipating the energy from the impact (Jaramillo-Botero et al., 2021). The computer simulations, conducted with various organic compounds including amino acids and fatty acids, show that minimal to zero fragmentation of organics in ice grains occurs for impact speeds < 3 km/s. Impact speeds of between 4 and 6 km/s – the exact speed varies between the different organic molecules - represent velocity thresholds leading to 1 % fragmentation of the organics (Jaramillo-Botero et al., 2021). However, fragmentation of the organic parent molecules is often desirable for spectral analysis because the organics produce fragmentation patterns in the mass spectra characteristic of their organic families. Even if approximately 50 % of all parent molecules of a specific organic in one ice grain fragment during impact, characterization of this organic (e.g. determining its organic family) is still likely to be possible. It is important to note that, according to Jaramillo-Botero et al. (2021), impact speeds > 6.5 km/s are required

to fragment 50 % of arginine parent molecules, if they are embedded in at least a few layers of water ice.

Further LILBID measurements of organic compounds are currently being conducted or planned (see e.g. chapter 12). The LILBID facility will be enhanced to be able to analyze neutral atoms and molecules from an impact cloud (in addition to cations and anions). These spectra will then be uploaded to the database and serve as analogue data for neutral gas mass spectrometers, such as MASPEX aboard Europa Clipper (sections 3.2 and 4.2) or PEP-NIM (Barabash et al., 2013) aboard ESA's JUpiter ICy moons Explorer (JUICE; Grasset et al., 2013). The current Time-of-Flight mass spectrometer will possibly be complemented in the near future by an Orbitrap™-based mass spectrometer with drastically improved analytical capabilities (see section 12.1).

12 Outlook: Currently ongoing LILBID campaigns

BASED ON THE CONCLUSIONS of this thesis, many more laboratory measurement campaigns remain to be done; others, however, have already started. This chapter briefly summarizes three on-going experimental campaigns to which the PhD candidate contributes. Further recent laboratory measurement campaigns might be found in future theses of PhD candidates working in this research group (Nölle, 2020; Zou, 2020).

12.1 OLYMPIA - Combining LILBID and an Orbitrap™-based mass spectrometer

Orbitrap™, invented by Alexander Makarov in the late 1990s, is a high-resolution mass analyzer that combines a miniature design with modest power requirements and analytical properties far exceeding those of other mass analyzers, such as Time-of-Flight mass spectrometers (Makarov, 2000; Hu et al., 2005; Makarov et al., 2006; Zubarev and Makarov, 2013). Based on a so-called Kingdon trap (Kingdon, 1923), the Orbitrap™mass spectrometer traps ions in an electrostatic field. The ions orbit an axial electrode on stable orbits performing harmonic oscillations along this electrode with frequencies proportional to $(m/z)^{-1/2}$ (m: ion mass; z: ion charge). These oscillations are transformed into mass spectra using fast Fourier Transformation (FT). These mass spectra have a dynamic range greater than 10^3, a high mass accuracy (2-5 ppm)[1] and a very high mass resolution exceeding 100,000 m/Δm (Makarov, 2000; Hu et al., 2005; Makarov et al., 2006; Zubarev and Makarov, 2013). Combining such an Orbitrap™-based mass spectrometer with the LILBID facility would greatly enhance the capabilities of the resulting ice grain analogue mass spectra.

OLYMPIA (Orbitrap anaLYser MultiPle IonisAtion) is a laboratory setup capable of utilizing different ion sources with an Orbitrap™-based mass spectrometer to analyze the created ions. The feasibility of LILBID as an ion source is currently being tested in cooperation with the J. Heyrovský Institute of Physical Chemistry in Prague, the Laboratoire de Physique et Chimie de l'Environment et de l'Espace (LPC2E) in Orléans, the Wilhelm-Ostwald-Institute (WOI) for Physical and Theoretical Chemistry in Leipzig and the Leibniz Institute of Surface Engineering in Leipzig. The LILBID setup at WOI, which is similar to that in Berlin, could successfully be connected to an Orbitrap™-based mass spectrometer and various organic and inorganic compounds that were dissolved in water, frozen to ice, and ionized using laser desorption, were detected with this setup (Figure 12.1).

After these successful initial campaigns, the OLYMPIA setup has recently been tested at Freie Universität Berlin with the LILBID ion source used for the experiments within this thesis. Mechanical connection of the Orbitrap™-based mass spectrometer to the LILBID setup was successful

[1] The mass accuracy is a metric describing the difference between the measured mass of an ion and the real mass of that ion.

and spectra were recorded when firing the infrared laser onto a metal wire.[1] OLYMPIA will be at Freie Universität Berlin in 2021 and 2022 to systematically enhance its capabilities. The recorded high-resolution spectra will be uploaded to the mass spectral reference library.

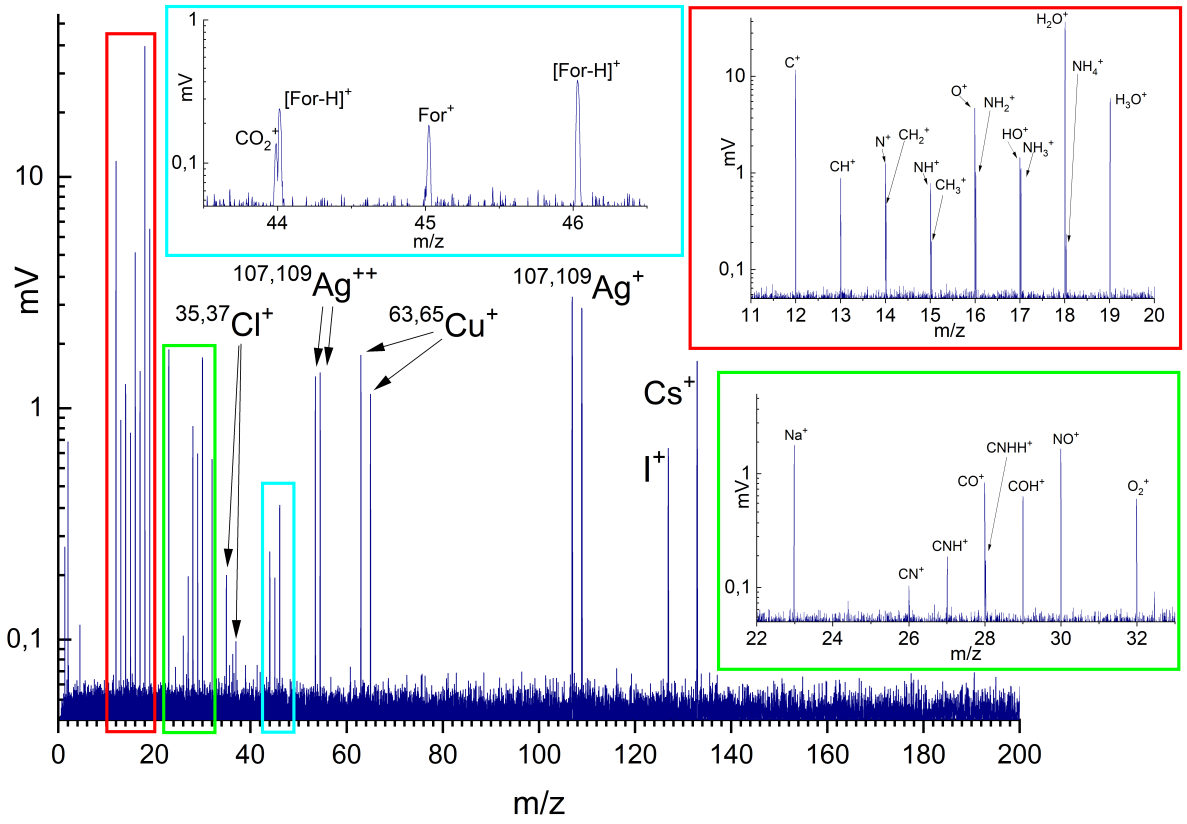

Figure 12.1: *A cationic mass spectrum (y-axis in logarithmic scale) of 10^{-3} M CsI, 10^{-3} M formamide, and 10^{-3} M arginine dissolved in water and frozen, recorded with the OLYMPIA setup. The water ice was mounted on a metal plate and ionized using laser desorption. Cesium (Cs) and iodine (I) ions as well as numerous organic fragments derived from formamide and arginine are observable. Note that an interference of carbon dioxide (CO_2^+) and the deprotonated formamide molecule at m/z 44 is clearly resolved in the spectrum. The mass resolution of OLYMPIA will be greatly increased in the future. Copper (Cu) and silver (Ag) are from the metal plate. Sodium (Na) contamination from preceding experiments is observable. Spectral analysis and graphical preparation were performed by the PhD candidate with friendly support of Illia Zymak (J. Heyrovský Institute of Physical Chemistry, Prague). The spectrum was recorded in Leipzig in October 2019.*

If the further development of OLYMPIA succeeds and reproducible mass spectra can be generated in the laboratory at Freie Universität Berlin, the ultimate goal is to support the construction and launch of an Orbitrap™-based mass spectrometer into space, to improve analyzes of ice grains emitted by extraterrestrial active ocean worlds.

12.2 Salt-rich organics measurements

The LILBID experiments in Part III of this thesis have shown that a salt-rich background significantly influences the spectral appearance of

[1] A metal wire yields many more ions than a water beam. Using this wire was the logical first step to align the ion optics of the Orbitrap™-based mass spectrometer.

potentially biogenic compounds indicating that organic substances could be detected in impact ionization mass spectra via their sodiated molecular peaks, if embedded in salt-rich ice grains. In fact, most of the organics from Enceladus and Europa are expected to be embedded in salt-rich ice grains. The salty matrix is expected to significantly affect the mass spectral appearance of the organics. Compounds from particular organic families, for example amino acids, are expected to be more easily detectable in cation mass spectra, whereas others, for example fatty acids, are expected to be more easily detectable in anion mass spectra. Compounds from various organic families, dissolved in salty solutions are currently being tested with the LILBID facility in the cation and anion mode of the mass spectrometer, to predict their spectral appearances and detection limits, in case they are embedded in salt-rich ice grains from Enceladus or Europa.

For example, linear alkylbenzenesulfonic acids (LAS) have been investigated to prepare for investigating compounds relevant to the icy moons, while at the same time ruling out a potential source of contamination on flight spectra because trace concentrations of these compounds are common in nearly every ecological niche on Earth (J. de Leeuw, pers. comm., 2019[1]). These acids easily form sodium dodecylbenzene sulfonates (Na-LAS) by attaching environmental $[Na]^+$ to its anionic $[SO_3]^-$ group. Two separate aqueous solutions have been prepared and measured using an LAS mixture (mainly C_{10} - C_{13} LAS)) in one solution and an Na-LAS mixture (mainly C_{10} - C_{13} LAS)) in the other solution, each of the mixtures at a total concentration of <1 wt.-%.[2] The sodium from the Na-LAS sample results in a sodium concentration of <30 mM in the second solution. Both the LAS and Na-LAS samples were donated by Jan de Leeuw from the Royal Netherlands Institute for Sea Research (NIOZ).

The resulting spectra show characteristic molecular peaks formed from protonated LAS molecules in the solution without sodium and disodiated LAS molecules in the sodium-rich solution (Figure 12.2). Unsodiated LAS fragments are only observed in the spectrum from the LAS solution without salts. One prominent sodiated fragment shows up in the Na-LAS spectrum at m/z 165. The absence of unsodiated fragments in the salt-rich case supports the finding within this thesis that, in LILBID, sodiated organic molecules might be more stable than unsodiated organic molecules.

Many more compounds, from various organic families, in salt-rich matrices are being investigated with the LILBID facility at Freie Universität Berlin. The recorded cation and anion spectra will be uploaded to the spectral reference library.

[1]Personal communication on August 27, 2019.

[2]The exact dissolved amount of the LAS and Na-LAS samples, respectively, is unknown.

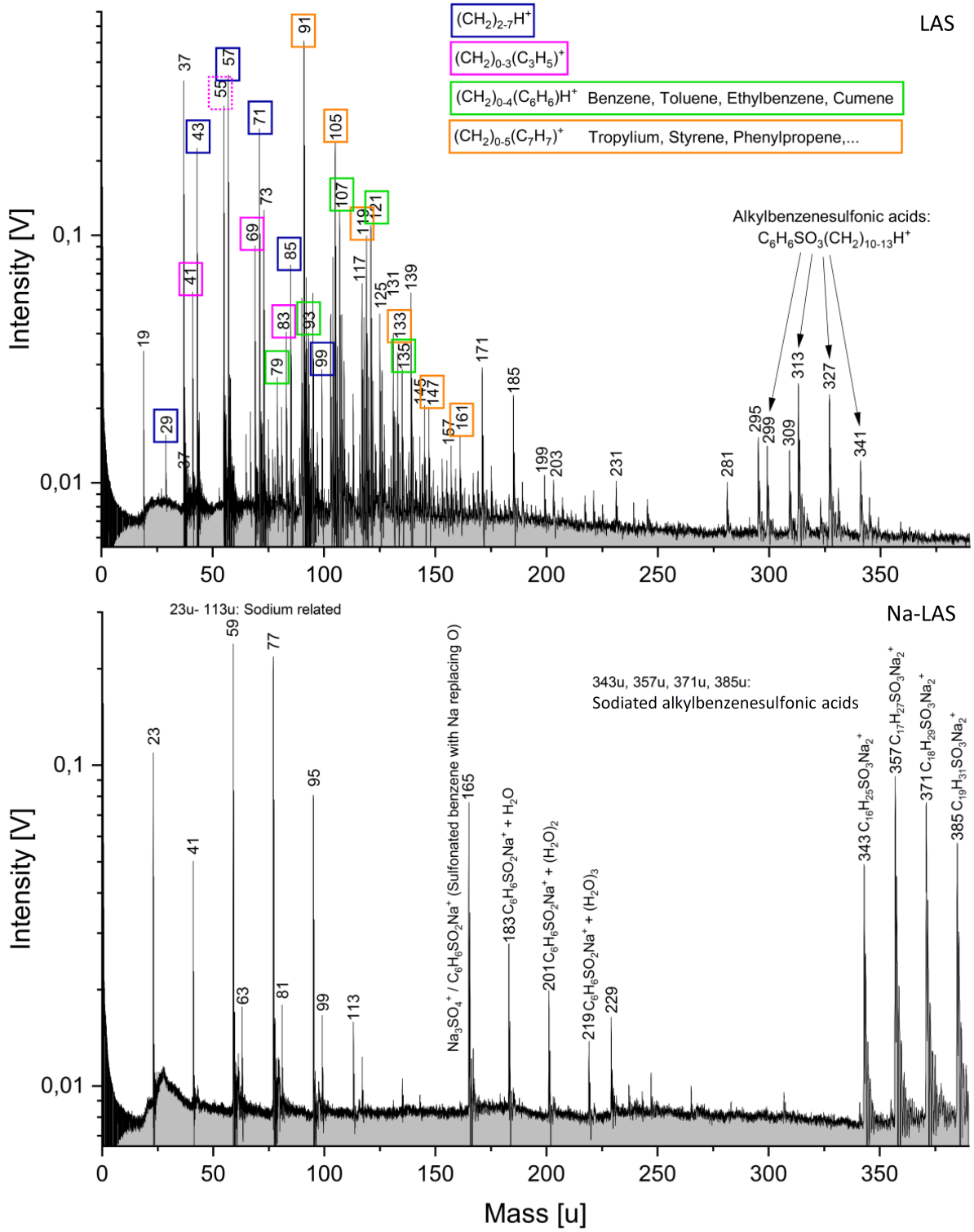

Figure 12.2: *Cation mass spectra (y-axes in logarithmic scale) of a mixture of four linear alkylbenzenesulfonic acids (LAS; top panel) and four sodium dodecylbenzene sulfonates (Na-LAS; bottom panel). Each mixture was measured at a total concentration of <1 wt.-% in H_2O. The individual protonated LAS can be observed at m/z 299, 313, 327, and 341 in the spectrum without sodium whereas disodiated LAS molecules form in the Na-rich solution producing peaks at m/z 343, 357, 371, and 385. Many more LAS fragments appear in the spectrum from the sodium free solution in comparison to that from the sodium-rich solution. The dashed box at m/z 55 indicates that the respective fragment ion interferes with a matrix water cluster ($[H_2O]_2H_3O^+$).*

12.3 Extended experiments for the detection of biosignatures on ocean worlds

Based upon the successful experiments presented within Part III of this thesis, experiments with actual biogenic compounds have already been started to predict the compounds' mass spectral appearances in impact ionization mass spectra of ice grains in space. *Escherichia coli (E.coli)*, a well known, widely distributed bacteria on Earth and are a commonly used model bacterium.

The first LILBID experiments with DNA and lipids extracted from *E.coli* cell cultures as well as lysed and disrupted cellular material show that DNA and lipids produce characteristic mass spectral signals (Dannenmann, 2020). An example spectrum of *E.coli* lipids is shown in Figure 12.3. The spectral appearance of saturated fatty acids, which here represent lipid fragments, is consistent with the findings in Part III of this thesis. As the lipids were extracted from biogenic cell cultures, fatty acids with even carbon numbers are more abundant than fatty acids with odd carbon numbers, with C_{16} and C_{18} being most abundant. Ice grain encounter speeds of 4 - 6 km/s with spacecraft are found to be optimal for the detection and identification of lipids and their fragments, with these optimal speeds increasing slightly proportional to increasing salt concentrations in the background matrix. These encounter speeds are consistent with the recommendation of this thesis for the optimal identification of biotic mass spectral signatures of fatty acids. For more information about the *E.coli* measurements, see Dannenmann (2020).

More LILBID experiments with a variety of biogenic materials are underway and will complement the spectral reference library in the near future.

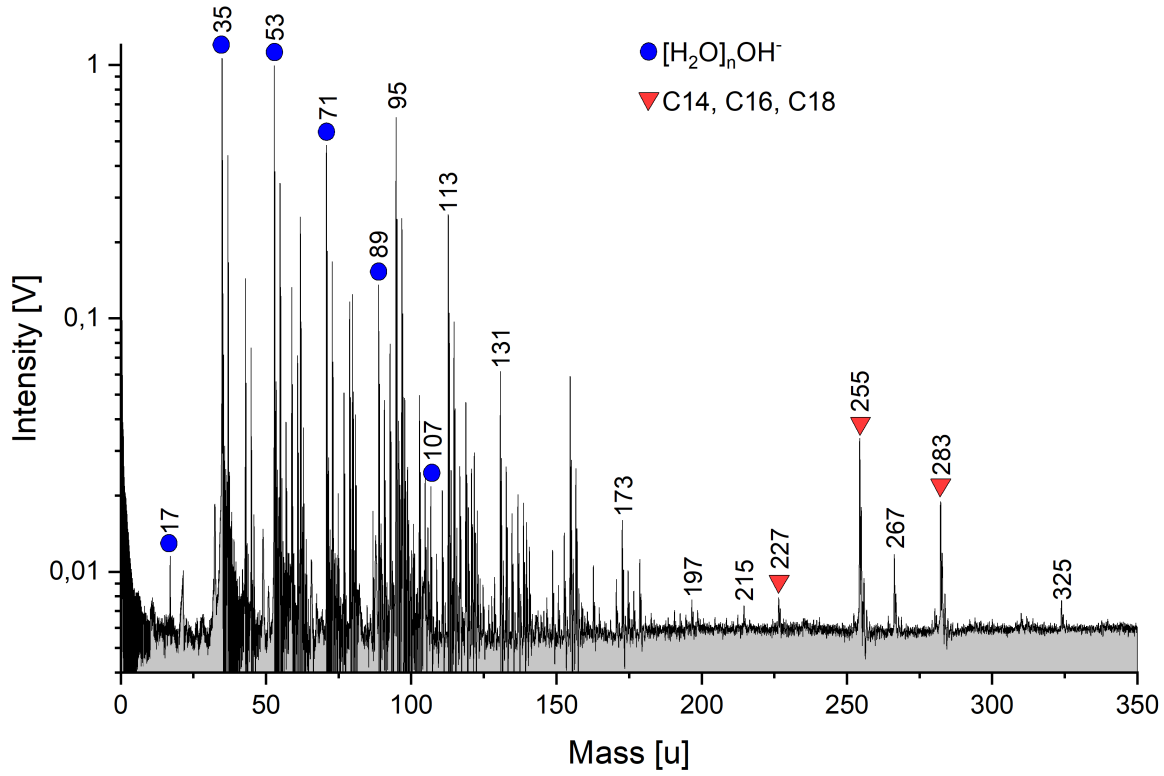

Figure 12.3: *A baseline corrected anion mass spectrum (y-axis in logarithmic scale) of 2.3 g/L (0.23 wt.-%) lipids extracted from E.coli cell cultures and dissolved in a water-isopropanol (50:50 vol) matrix. Linear saturated fatty acids with 14, 16, and 18 carbon atoms can be observed (red triangles), with C_{16} and C_{18} much more abundant than C_{14}. m/z 267 represents a cyclopropanated form of heptadecanoic acid (C_{17}). Blue circles show matrix water peaks of the form $[H_2O]_nOH^-$.*

Bibliography

Altobelli, N., Postberg, F., Fiege, K., Trieloff, M., Kimura, H., Sterken, V., Hsu, H.-W., Hillier, J., Khawaja, N., Moragas-Klostermeyer, G., et al. (2016). Flux and composition of interstellar dust at saturn from cassini's cosmic dust analyzer. *Science*, 352(6283):312–318.

Altwegg, K., Balsiger, H., Bar-Nun, A., Berthelier, J.-J., Bieler, A., Bochsler, P., Briois, C., Calmonte, U., Combi, M. R., Cottin, H., et al. (2016). Prebiotic chemicals—amino acid and phosphorus—in the coma of comet 67p/churyumov-gerasimenko. *Science Advances*, 2(5):e1600285.

Andersen, A., Kim, W., McClure, S., and Jun, I. (2020). Monte carlo evaluation of the europa clipper tid margin based on the variability of the jovian radiation environment with application for mission design. *Space Weather*, 18(2):e2019SW002340.

Anderson, J., Schubert, G., Jacobson, R., Lau, E., Moore, W., and Sjogren, W. (1998). Europa's differentiated internal structure: Inferences from four galileo encounters. *Science*, 281(5385):2019–2022.

Andersson, P. U., Ryding, M. J., Sekiguchi, O., and Uggerud, E. (2008). Isotope exchange and structural rearrangements in reactions between size-selected ionic water clusters, h 3 o+(h 2 o) n and nh 4+(h 2 o) n, and d 2 o. *Physical Chemistry Chemical Physics*, 10(40):6127–6134.

Angelis, G., Kordopati, G. G., Zingkou, E., Karioti, A., Sotiropoulou, G., and Pampalakis, G. (2020). Plausible emergence of biochemistry in enceladus based on chemobrionics. *Chemistry–A European Journal*, (in press).

Annesley, T. M. (2003). Ion suppression in mass spectrometry. *Clinical Chemistry*, 49(7):1041–1044.

Ashkenazy, Y. and Tziperman, E. (2020). Europa's dynamic ocean: Taylor columns, eddies, convection, ice melting and salinity. *arXiv preprint*, arXiv:2006.02242.

Auer, A. and Sitte, K. (1968). Detection technique for micrometeoroids using impact ionization. *Earth and Planetary Science Letters*, 4(2):178–183.

Balsiger, H., Altwegg, K., Bochsler, P., Eberhardt, P., Fischer, J., Graf, S., Jäckel, A., Kopp, E., Langer, U., Mildner, M., et al. (2007). Rosina–rosetta orbiter spectrometer for ion and neutral analysis. *Space Science Reviews*, 128(1-4):745–801.

Barabash, S., Wurz, P., Brandt, P., Wieser, M., Holmström, M., Futaana, Y., Stenberg, G., Nilsson, H., Eriksson, A., Tulej, M., et al. (2013). Particle environment package (pep). In *European Planetary Science Congress*, volume 8:EPSC2013–709.

Baross, J. A. and Hoffman, S. E. (1985). Submarine hydrothermal vents and associated gradient environments as sites for the origin and evolution of life. *Origins of Life and Evolution of the Biosphere*, 15(4):327–345.

Baum, W. A., Kreidl, T., Westphal, J. A., Danielson, G. E., Seidelmann, P. K., Pascu, D., and Currie, D. G. (1981). Saturn's e ring. *Icarus*, 47(1):84–96.

Bedford, D. (1971). Impact ionization of micro-particles at low velocities. *Journal of Physics A: General Physics*, 4(1):L14.

Beinsen, A. (2011). *Bildgebung und chemische Analytik mit Laserdesorptions-Massenspektrometrie im Bereich Forensik und Astrophysik*. PhD thesis, Georg-August-Universität Göttingen.

Berg, J. M., Tymoczko, J. L., and Stryer, L. (2012). Fatty acid metabolism. In Berg, J., Stryer, L., Tymoczko, J., and Gatto, G., editors, *Biochemistry*. New York: WH Freeman,.

Berg, O. E. and Richardson, F. F. (1969). The pioneer 8 cosmic dust experiment. *Review of Scientific Instruments*, 40(10):1333–1337.

Berkenkamp, S., Karas, M., and Hillenkamp, F. (1996). Ice as a matrix for ir-matrix-assisted laser desorption/ionization: mass spectra from a protein single crystal. *Proceedings of the National Academy of Sciences*, 93(14):7003–7007.

Billings, S. E. and Kattenhorn, S. A. (2005). The great thickness debate: Ice shell thickness models for europa and comparisons with estimates based on flexure at ridges. *Icarus*, 177(2):397–412.

Blank, J. G., Miller, G. H., Ahrens, M. J., and Winans, R. E. (2001). Experimental shock chemistry of aqueous amino acid solutions and the cometary delivery of prebiotic compounds. *Origins of Life and Evolution of the Biosphere*, 31(1-2):15–51.

Bouquet, A., Glein, C. R., and Waite Jr, J. H. (2019). How adsorption affects the gas–ice partitioning of organics erupted from enceladus. *The Astrophysical Journal*, 873:28.

Bowden, S. A., Parnell, J., and Burchell, M. J. (2009). Survival of organic compounds in ejecta from hypervelocity impacts on ice. *International Journal of Astrobiology*, 8(1):19–25.

Bowie, J. H., Brinkworth, C. S., and Dua, S. (2002). Collision-induced fragmentations of the (m-h)- parent anions of underivatized peptides: An aid to structure determination and some unusual negative ion cleavages. *Mass Spectrometry Reviews*, 21(2):87–107.

Brazelton, W. J., Schrenk, M. O., Kelley, D. S., and Baross, J. A. (2006). Methane-and sulfur-metabolizing microbial communities dominate the lost city hydrothermal field ecosystem. *Appl. Environ. Microbiol.*, 72(9):6257–6270.

Brockwell, T. G., Meech, K. J., Pickens, K., Waite, J. H., Miller, G., Roberts, J., Lunine, J. I., and Wilson, P. (2016). The mass spectrometer for planetary exploration (maspex). In *Aerospace Conference, IEEE, Big Sky, MT*, pages 1–17.

Brown, R. H., Baines, K. H., Bellucci, G., Bibring, J.-P., Buratti, B. J., Capaccioni, F., Cerroni, P., Clark, R. N., Coradini, A., Cruikshank, D. P., et al. (2004). The cassini visual and infrared mapping spectrometer (vims) investigation. *Space Science Reviews*, 115(1-4):111–168.

Brownlee, D., Burnett, D., Clark, B., Hanner, M., Horz, F., Kissel, J., Newburn, R., Sandford, S., Sekanina, Z., Tsou, P., et al. (1996). Stardust: Comet

and interstellar dust sample return mission. In *International Astronomical Union Colloquium*, volume 150, pages 223–226. Cambridge University Press.

Brownlee, D. E., Tsou, P., Anderson, J., Hanner, M., Newburn, R., Sekanina, Z., Clark, B., Hörz, F., Zolensky, M., Kissel, J., et al. (2003). Stardust: Comet and interstellar dust sample return mission. *Journal of Geophysical Research: Planets*, 108(E10):8111.

Burcar, B. T., Barge, L. M., Trail, D., Watson, E. B., Russell, M. J., and McGown, L. B. (2015). Rna oligomerization in laboratory analogues of alkaline hydrothermal vent systems. *Astrobiology*, 15(7):509–522.

Burchell, M. J., Bowden, S. A., Cole, M., Price, M. C., and Parnell, J. (2014). Survival of organic materials in hypervelocity impacts of ice on sand, ice, and water in the laboratory. *Astrobiology*, 14(6):473–485.

Burchell, M. J., Cole, M. J., McDonnell, J., and Zarnecki, J. C. (1999). Hypervelocity impact studies using the 2 mv van de graaff accelerator and two-stage light gas gun of the university of kent at canterbury. *Measurement Science and Technology*, 10(1):41–50.

Burrows, S. M., Ogunro, O., Frossard, A., Russell, L. M., Rasch, P. J., and Elliott, S. (2014). A physically based framework for modeling the organic fractionation of sea spray aerosol from bubble film langmuir equilibria. *Atmospheric Chemistry and Physics*, 14(24):13601–13629.

Cable, M., Waller, S., Hodyss, R., Hofmann, A., Malaska, M., Continetti, R., Jaramillo-Botero, A., Abel, B., Postberg, F., Miller, M., Burke, S., Belousov, A., Klenner, F., Tallarida, N., et al. (2020). Plume grain sampling at hypervelocity: Implications for astrobiology investigations. *Science White Paper for the Planetary Science and Astrobiology Decadal Survey 2023-2032*, July 2020:1–7.

Cadek, O., Tobie, G., Van Hoolst, T., Massé, M., Choblet, G., Lefèvre, A., Mitri, G., Baland, R., Běhounková, M., Bourgeois, O., and Trinh, A. (2016). Enceladus's internal ocean and ice shell constrained from cassini gravity, shape, and libration data. *Geophysical Research Letters*, 43(11):5653–5660.

Cameron, A. and Eggers Jr, D. (1948). An ion"velocitron". *Review of Scientific Instruments*, 19(9):605–607.

Camprubí, E., De Leeuw, J., House, C., Raulin, F., Russell, M., Spang, A., Tirumalai, M., and Westall, F. (2019). The emergence of life. *Space Science Reviews*, 215(8):56.

Carr, M. H., Belton, M. J., Chapman, C. R., Davies, M. E., Geissler, P., Greenberg, R., McEwen, A. S., Tufts, B. R., Greeley, R., Sullivan, R., et al. (1998). Evidence for a subsurface ocean on europa. *Nature*, 391(6665):363–365.

Cassini, G. D. (1685). Découverte de la lumière celeste qui paroist dans le zodiaque. *A Paris: de l'lmprimerie royale, par Sebastien Mabre-Cramoisy (ETH-Bibliothek Zürich)*, pages 1–68.

Charvat, A. and Abel, B. (2007). How to make big molecules fly out of liquid water: applications, features and physics of laser assisted liquid phase dispersion mass spectrometry. *Physical Chemistry Chemical Physics*, 9:3335–3360.

Charvat, A., Stasicki, B., and Abel, B. (2006). Product screening of fast reactions in ir-laser-heated liquid water filaments in a vacuum by mass spectrometry. *The Journal of Physical Chemistry A*, 110(9):3297–3306.

Choblet, G., Tobie, G., Sotin, C., Běhounková, M., Čadek, O., Postberg, F., and Souček, O. (2017). Powering prolonged hydrothermal activity inside enceladus. *Nature Astronomy*, 1(12):841–847.

Christian, N. P., Arnold, R. J., and Reilly, J. P. (2000). Improved calibration of time-of-flight mass spectra by simplex optimization of electrostatic ion calculations. *Analytical hemistry*, 72(14):3327–3337.

Collins, G. and Nimmo, F. (2009). Chaotic terrain on europa. In Pappalardo, R., McKinnon, W., and Khurana, K., editors, *Europa*, pages 259–281. University of Arizona Press Tucson, AZ.

Collins, G. C. and Goodman, J. C. (2007). Enceladus' south polar sea. *Icarus*, 189(1):72–82.

Concina, B., Hvelplund, P., Nielsen, A., Brøndsted Nielsen, S., Rangama, J., Liu, B., and Tomita, S. (2006). Formation and stability of charged amino acid clusters and the role of chirality. *Journal of the American Society for Mass Spectrometry*, 17(2):275–279.

Creamer, J. S., Mora, M. F., and Willis, P. A. (2017). Enhanced resolution of chiral amino acids with capillary electrophoresis for biosignature detection in extraterrestrial samples. *Analytical Chemistry*, 89(2):1329–1337.

Crick, F. H. and Orgel, L. E. (1973). Directed panspermia. *Icarus*, 19(3):341–346.

Cronin, J. and Pizzarello, S. (1983). Amino acids in meteorites. *Advances in Space Research*, 3(9):5–18.

Cuzzi, J. N., Burns, J. A., Charnoz, S., Clark, R. N., Colwell, J. E., Dones, L., Esposito, L. W., Filacchione, G., French, R. G., Hedman, M. M., et al. (2010). An evolving view of saturn's dynamic rings. *Science*, 327(5972):1470–1475.

Dachwald, B., Ulamec, S., Postberg, F., Sohl, F., de Vera, J.-P., Waldmann, C., Lorenz, R. D., Zacny, K. A., Hellard, H., Biele, J., et al. (2020). Key technologies and instrumentation for subsurface exploration of ocean worlds. *Space Science Reviews*, 216(5):83.

Dalai, P., Kaddour, H., and Sahai, N. (2016). Incubating life: Prebiotic sources of organics for the origin of life. *Elements*, 12(6):401–406.

Damer, B. and Deamer, D. (2020). The hot spring hypothesis for an origin of life. *Astrobiology*, 20(4):429–452.

Dannenmann, M. (2020). Analogue experiments with bacterial biosignatures for their potential detection on active ocean worlds. Bachelor's thesis, Freie Universität Berlin.

Davila, A. F. and McKay, C. P. (2014). Chance and necessity in biochemistry: Implications for the search for extraterrestrial biomarkers in earth-like environments. *Astrobiology*, 14(6):534–540.

de Pater, I., Martin, S. C., and Showalter, M. R. (2004). Keck near-infrared observations of saturn's e and g rings during earth's ring plane crossing in august 1995. *Icarus*, 172(2):446–454.

Doggett, T., Greeley, R., Figueredo, P., and Tanaka, K. (2009). Geologic stratigraphy and evolution of europa's surface. In Pappalardo, R., McKinnon, W., and Khurana, K., editors, *Europa*, pages 137–159. University of Arizona Press Tucson, AZ.

Dorn, E. D., Nealson, K. H., and Adami, C. (2011). Monomer abundance distribution patterns as a universal biosignature: examples from terrestrial and digital life. *Journal of Molecular Evolution*, 72(3):283–295.

Dougherty, M., Kellock, S., Southwood, D., Balogh, A., Smith, E., Tsurutani, B., Gerlach, B., Glassmeier, K.-H., Gleim, F., Russell, C., et al. (2004). The cassini magnetic field investigation. *Space Science Reviews*, 114(1-4):331–383.

Dougherty, M., Khurana, K., Neubauer, F., Russell, C., Saur, J., Leisner, J., and Burton, M. (2006). Identification of a dynamic atmosphere at enceladus with the cassini magnetometer. *Science*, 311(5766):1406–1409.

Drapatz, S. and Michel, K. (1974). On the intensity of rotational lines of h2 and hd from dense interstellar clouds. *Astronomy and Astrophysics*, 36:211–216.

Drolshagen, G., Svedhem, H., Grün, E., and Bunte, K. (2001). Measurements of cosmic dust and micro-debris in geo. *Advances in Space Research*, 28(9):1325–1333.

Dunn, M. S., Ross, F. J., and Read, L. S. (1933). The solubility of the amino acids in water. *Journal of Biological Chemistry*, 103(2):579–595.

Eilers, P. H. (2003). A perfect smoother. *Analytical Chemistry*, 75(14):3631–3636.

Elachi, C., Allison, M., Borgarelli, L., Encrenaz, P., Im, E., Janssen, M., Johnson, W., Kirk, R. L., Lorenz, R., Lunine, J., et al. (2004). Radar: The cassini titan radar mapper. *Space Science Reviews*, 115(1-4):71–110.

Esposito, L. W., Barth, C. A., Colwell, J. E., Lawrence, G. M., McClintock, W. E., Stewart, A. I. F., Keller, H. U., Korth, A., Lauche, H., Festou, M. C., et al. (2004). The cassini ultraviolet imaging spectrograph investigation. *Space Science Reviews*, 115(1-4):299–361.

Fegley Jr, B. and Zolotov, M. Y. (2000). Chemistry of sodium, potassium, and chlorine in volcanic gases on io. *Icarus*, 148(1):193–210.

Fiege, K., Trieloff, M., Hillier, J. K., Guglielmino, M., Postberg, F., Srama, R., Kempf, S., and Blum, J. (2014). Calibration of relative sensitivity factors for impact ionization detectors with high-velocity silicate microparticles. *Icarus*, 241:336–345.

Fielding, L. A., Hillier, J. K., Burchell, M. J., and Armes, S. P. (2015). Space science applications for conducting polymer particles: synthetic mimics for cosmic dust and micrometeorites. *Chemical Communications*, 51(95):16886–16899.

Flasar, F. M., Kunde, V., Abbas, M., Achterberg, R., Ade, P., Barucci, A., Bézard, B., Bjoraker, G., Brasunas, J., Calcutt, S., et al. (2004). Exploring the saturn system in the thermal infrared: The composite infrared spectrometer. *Space Science Reviews*, 115(1-4):169–297.

Fortes, A. (2000). Exobiological implications of a possible ammonia–water ocean inside titan. *Icarus*, 146(2):444–452.

Fortney, J. J., Helled, R., Nettelmann, N., Stevenson, D. J., Marley, M. S., Hubbard, W. B., and Iess, L. (2018). The interior of saturn. In Baines, K. H., Flasar, F. M., Krupp, N., and Stallard, T., editors, *Saturn in the 21st Century*, page 44–68. Cambridge University Press.

Franz, O. and Millis, R. (1975). Photometry of dione, tethys, and enceladus on the ubv system. *Icarus*, 24(4):433–442.

Friichtenicht, J. (1964). Micrometeroid simulation using nuclear accelerator techniques. *Nuclear Instruments and Methods*, 28(1):70–78.

Friichtenicht, J., Roy, N., and Becker, D. (1971). The cosmic dust analyzer: Experimental evaluation of an impact ionization model. In *International Astronomical Union Colloquium*, volume 13:299-310.

Fu, Q., Lollar, B. S., Horita, J., Lacrampe-Couloume, G., and Seyfried Jr, W. E. (2007). Abiotic formation of hydrocarbons under hydrothermal conditions: Constraints from chemical and isotope data. *Geochimica et Cosmochimica Acta*, 71(8):1982–1998.

Galilei, G. (1610). Siderius nuncius. *Astronomical Treatise*, pages published in New Latin on March 13, 1610.

Georgiou, C. D. and Deamer, D. W. (2014). Lipids as universal biomarkers of extraterrestrial life. *Astrobiology*, 14(6):541–549.

Glavin, D. P., Callahan, M. P., Dworkin, J. P., and Elsila, J. E. (2011). The effects of parent body processes on amino acids in carbonaceous chondrites. *Meteoritics & Planetary Science*, 45(12):1948–1972.

Glein, C., Postberg, F., and Vance, S. (2018). The geochemistry of enceladus: Composition and controls. In Schenk, P., Clark, R., C.J.A. Howet and, A. V., and Waite, J., editors, *Enceladus and the Icy Moons of Saturn*, pages 39–56. University of Arizona Press Tucson, AZ.

Glein, C. R., Baross, J. A., and Waite, J. H. (2015). The ph of enceladus' ocean. *Geochimica et Cosmochimica Acta*, 162:202–219.

Glein, C. R. and Waite, J. H. (2020). The carbonate geochemistry of enceladus' ocean. *Geophysical Research Letters*, 47(3):e2019GL085885.

Godfrey, D. A. (1988). A hexagonal feature around saturn's north pole. *Icarus*, 76(2):335–356.

Goguen, J. D., Buratti, B. J., Brown, R. H., Clark, R. N., Nicholson, P. D., Hedman, M. M., Howell, R. R., Sotin, C., Cruikshank, D. P., Baines, K. H., Lawrence, K. J., Spencer, J. R., and Blackburn, D. G. (2013). The temperature and width of an active fissure on enceladus measured with cassini vims during the 14 april 2012 south pole flyover. *Icarus*, 226(1):1128–1137.

Goldstein, D. B., Hedman, M., Manga, M., Perry, M., Spitale, J., and Teolis, B. (2018). Enceladus plume dynamics: From surface to space. In Schenk, P., Clark, R., C.J.A. Howet and, A. V., and Waite, J., editors, *Enceladus and the Icy Moons of Saturn*, pages 175–194. University of Arizona Press Tucson, AZ.

Goldsworthy, B., Burchell, M. J., Cole, M. J., Armes, S. P., Khan, M. A., Lascelles, S., Green, S. F., McDonnell, J., Srama, R., and Bigger, S. (2003). Time of flight mass spectra of ions in plasmas produced by hypervelocity impacts of organic and mineralogical microparticles on a cosmic dust analyser. *Astronomy & Astrophysics*, 409(3):1151–1167.

Gomez Casajus, L., Zannoni, M., Modenini, D., Tortora, P., Nimmo, F., Van Hoolst, T., Buccino, D., and Oudrhiri, K. (2020). Updated europa gravity field and interior structure from a reanalysis of galileo tracking data. *Icarus*, (in press):114187.

Graps, A., Grün, E., Svedhem, H., Krüger, H., Horányi, M., Heck, A., and Lammers, S. (2000). Io as a source of the jovian dust streams. *Nature*, 405(6782):48–50.

Grasset, O., Dougherty, M., Coustenis, A., Bunce, E., Erd, C., Titov, D., Blanc, M., Coates, A., Drossart, P., Fletcher, L., et al. (2013). Jupiter icy moons explorer (juice): An esa mission to orbit ganymede and to characterise the jupiter system. *Planetary and Space Science*, 78:1–21.

Greeley, R., Pappalardo, R. T., Prockter, L. M., Hendrix, A. R., and Lock, R. E. (2009). Future exploration of europa. In Pappalardo, R., McKinnon, W., and Khurana, K., editors, *Europa*, pages 655–695. University of Arizona Press Tucson, AZ.

Griffith, C. A., Owen, T., Miller, G. A., and Geballe, T. (1998). Transient clouds in titan's lower atmosphere. *Nature*, 395(6702):575–578.

Grün, E., Fechtig, H., Giese, R. H., Kissel, J., Linkert, D., Maas, D., McDonnell, J. A. M., Morfill, G. E., Schwehm, G., and Zook, H. A. (1992b). The ulysses dust experiment. *Astronomy and Astrophysics Supplement Series*, 92(2):411–423.

Grün, E., Fechtig, H., Hanner, M. S., Kissel, J., Lindblad, B.-A., Linkert, D., Maas, D., Morfill, G. E., and Zook, H. A. (1992a). The galileo dust detector. *Space Science Reviews*, 60:317–340.

Grüner, B. M., Hahne, H., Mazur, P. K., Trajkovic-Arsic, M., Maier, S., Esposito, I., Kalideris, E., Michalski, C. W., Kleeff, J., Rauser, S., et al. (2012). Maldi imaging mass spectrometry for in situ proteomic analysis of preneoplastic lesions in pancreatic cancer. *PloS ONE*, 7(6):e39424.

Guillot, T., Atreya, S., Charnoz, S., Dougherty, M. K., and Read, P. (2009). Saturn's exploration beyond cassini-huygens. In Dougherty, M. K., Esposito, L. W., and Krimigis, S. M., editors, *Saturn from Cassini-Huygens*, pages 745–761. Springer, Dordrecht.

Gurnett, D., Kurth, W., Kirchner, D., Hospodarsky, G., Averkamp, T., Zarka, P., Lecacheux, A., Manning, R., Roux, A., Canu, P., et al. (2004). The cassini radio and plasma wave investigation. *Space Science Reviews*, 114(1-4):395–463.

Gurnett, D., Persoon, A., Kurth, W., Groene, J., Averkamp, T., Dougherty, M., and Southwood, D. (2007). The variable rotation period of the inner region of saturn's plasma disk. *Science*, 316(5823):442–445.

Guzman, M., Lorenz, R., Hurley, D., Farrell, W., Spencer, J., Hansen, C., Hurford, T., Ibea, J., Carlson, P., and McKay, C. P. (2019). Collecting amino

acids in the enceladus plume. *International Journal of Astrobiology*, 18(1):47–59.

Halliwell, B. (2006). Reactive species and antioxidants. redox biology is a fundamental theme of aerobic life. *Plant Physiology*, 141(2):312–322.

Hand, K., Sotin, C., Hayes, A., and Coustenis, A. (2020). On the habitability and future exploration of ocean worlds. *Space Science Reviews*, 216:95.

Hand, K. P., Carlson, R. W., and Chyba, C. F. (2007). Energy, chemical disequilibrium, and geological constraints on europa. *Astrobiology*, 7(6):1006–1022.

Hand, K. P. and Chyba, C. F. (2007). Empirical constraints on the salinity of the europan ocean and implications for a thin ice shell. *Icarus*, 189(2):424–438.

Hand, K. P., Chyba, C. F., Priscu, J. C., Carlson, R. W., and Nealson, K. H. (2009). Astrobiology and the potential for life on europa. In Pappalardo, R., McKinnon, W., and Khurana, K., editors, *Europa*, pages 589–629. University of Arizona Press Tucson, AZ.

Hansen, C. J., Esposito, L., Stewart, A., Colwell, J., Hendrix, A., Pryor, W., Shemansky, D., and West, R. (2006). Enceladus' water vapor plume. *Science*, 311(5766):1422–1425.

Hao, J., Giovenco, E., Pedreira-Segade, U., Montagnac, G., and Daniel, I. (2018). Compatibility of amino acids in ice ih: Implications for the origin of life. *Astrobiology*, 18(4):381–392.

Hasegawa, S., Hamabe, Y., Fujiwara, A., Yano, H., Sasaki, S., Ohashi, H., Kawamura, T., Nogami, K.-I., Kobayashi, K., Iwai, T., et al. (2001). Microparticle acceleration for hypervelocity experiments by a 3.75 mv van de graaff accelerator and a 100kv electrostatic accelerator in japan. *International Journal of Impact Engineering*, 26(1-10):299–308.

Hayes, A. G. (2016). The lakes and seas of titan. *Annual Review of Earth and Planetary Sciences*, 44:57–83.

Hayes, A. G., Lorenz, R. D., and Lunine, J. I. (2018). A post-cassini view of titan's methane-based hydrologic cycle. *Nature Geoscience*, 11(5):306–313.

Hayes, J. M. (1967). Organic constituents of meteorites—a review. *Geochimica et Cosmochimica Acta*, 31(9):1395–1440.

Helfenstein, P. (2010). Tectonic overturn on enceladus. *Nature Geoscience*, 3(2):75–76.

Helled, R. and Guillot, T. (2013). Interior models of saturn: including the uncertainties in shape and rotation. *The Astrophysical Journal*, 767(2):113.

Helled, R., Schubert, G., and Anderson, J. D. (2009). Empirical models of pressure and density in saturn's interior: Implications for the helium concentration, its depth dependence, and saturn's precession rate. *Icarus*, 199(2):368–377.

Hemingway, D., Iess, L., Tajeddine, R., and Tobie, G. (2018). The interior of enceladus. In Schenk, P., Clark, R., C.J.A. Howet and, A. V., and Waite, J., editors, *Enceladus and the Icy Moons of Saturn*, pages 57–77. University of Arizona Press Tucson, AZ.

Hendrix, A. R., Hurford, T. A., Barge, L. M., Bland, M. T., Bowman, J. S., Brinckerhoff, W., Buratti, B. J., Cable, M. L., Castillo-Rogez, J., Collins, G. C., et al. (2019). The nasa roadmap to ocean worlds. *Astrobiology*, 19(1):1–27.

Henry, C. A. (2002). An introduction to the design of the cassini spacecraft. *Space Science Reviews*, 104(1-4):129–153.

Herschel, W. (1790). Account of the discovery of a sixth and seventh satellite of the planet saturn; with remarks on the construction of its ring, its atmosphere, its rotation on an axis, and its spheroidical figure. *Philosophical Transactions of the Royal Society of London*, 80:1–20.

Higgs, P. G. and Pudritz, R. E. (2009). A thermodynamic basis for prebiotic amino acid synthesis and the nature of the first genetic code. *Astrobiology*, 9:483–490.

Hillier, J., Schmidt, J., Hsu, H.-W., and Postberg, F. (2018). Dust emission by active moons. *Space Science Reviews*, 214:131.

Hillier, J. K., Green, S. F., McBride, N., Schwanethal, J. P., Postberg, F., Srama, R., Kempf, S., Moragas-Klostermeyer, G., McDonnell, J. A. M., and Grün, E. (2007). The composition of saturn's e ring. *Monthly Notices of the Royal Astronomical Society*, 377(4):1588–1596.

Hillier, J. K., McBride, N., Green, S., Kempf, S., and Srama, R. (2006). Modelling cda mass spectra. *Planetary and Space Science*, 54(9-10):1007–1013.

Hillier, J. K., Sternovsky, Z., Armes, S. P., Fielding, L. A., Postberg, F., Bugiel, S., Drake, K., Srama, R., Kearsley, A. T., and Trieloff, M. (2014). Impact ionisation mass spectrometry of polypyrrole-coated pyrrhotite microparticles. *Planetary and Space Science*, 97:9–22.

Hodgkinson, M. R., Webber, A. P., Roberts, S., Mills, R. A., Connelly, D. P., and Murton, B. J. (2015). Talc-dominated seafloor deposits reveal a new class of hydrothermal system. *Nature communications*, 6:10150.

Hoffmann, H., Seiß, M., Salo, H., and Spahn, F. (2015). Vertical structures induced by embedded moonlets in saturn's rings. *Icarus*, 252:400–414.

Holčapek, M., Volná, K., and Vaněrková, D. (2007). Effects of functional groups on the fragmentation of dyes in electrospray and atmospheric pressure chemical ionization mass spectra. *Dyes and Pigments*, 75(1):156–165.

Hornung, K. and Kissel, J. (1994). On shock wave impact ionization of dust particles. *Astronomy and Astrophysics*, 291:324–336.

Howell, S. M. and Pappalardo, R. T. (2020). Nasa's europa clipper—a mission to a potentially habitable ocean world. *Nature Communications*, 11:1311.

Howett, C., Spencer, J., Pearl, J., and Segura, M. (2010). Thermal inertia and bolometric bond albedo values for mimas, enceladus, tethys, dione, rhea and iapetus as derived from cassini/cirs measurements. *Icarus*, 206(2):573–593.

Howett, C., Spencer, J., Pearl, J., and Segura, M. (2011). High heat flow from enceladus' south polar region measured using 10–600 cm^{-1} cassini/cirs data. *Journal of Geophysical Research: Planets*, 116(E3).

Hsu, H.-W., Postberg, F., Sekine, Y., Shibuya, T., Kempf, S., Horányi, M., Juhász, A., Altobelli, N., Suzuki, K., Masaki, Y., Kuwatani, T., Tachibana, S., iti Sirono, S., Moragas-Klostermeyer, G., and Srama, R. (2015). Ongoing hydrothermal activities within enceladus. *Nature*, 519:207–210.

Hu, Q., Noll, R. J., Li, H., Makarov, A., Hardman, M., and Graham Cooks, R. (2005). The orbitrap: a new mass spectrometer. *Journal of Mass Spectrometry*, 40(4):430–443.

Huang, Y., Wang, Y., Alexandre, M. R., Lee, T., Rose-Petruck, C., Fuller, M., and Pizzarello, S. (2005). Molecular and compound-specific isotopic characterization of monocarboxylic acids in carbonaceous meteorites. *Geochimica et Cosmochimica Acta*, 69(4):1073–1084.

Hubbard, W. B., Dougherty, M. K., Gautier, D., and Jacobson, R. (2009). The interior of saturn. In Dougherty, M. K., Esposito, L. W., and Krimigis, S. M., editors, *Saturn from Cassini-Huygens*, pages 75–81. Springer, Dordrecht.

Hunt, D. F. and Crow, F. W. (1978). Electron capture negative ion chemical ionization mass spectrometry. *Analytical Chemistry*, 50(13):1781–1784.

Hussmann, H., Sohl, F., and Spohn, T. (2006). Subsurface oceans and deep interiors of medium-sized outer planet satellites and large trans-neptunian objects. *Icarus*, 185(1):258–273.

Hussmann, H. and Spohn, T. (2004). Thermal-orbital evolution of io and europa. *Icarus*, 171(2):391–410.

Huybrighs, H., Roussos, E., Blöcker, A., Krupp, N., Futaana, Y., Barabash, S., Hadid, L., Holmberg, M., Lomax, O., and Witasse, O. (2020). An active plume eruption on europa during galileo flyby e26 as indicated by energetic proton depletions. *Geophysical Research Letters*, 47:e2020GL087806.

Huygens, C. (1659). Systema saturnium, sive de causis mirandorum saturni phaenomenon, et comite ejus planeta novo. *The Hagae-Comitis*, pages 1–84.

Iess, L., Militzer, B., Kaspi, Y., Nicholson, P., Durante, D., Racioppa, P., Anabtawi, A., Galanti, E., Hubbard, W., Mariani, M., et al. (2019). Measurement and implications of saturn's gravity field and ring mass. *Science*, 364(6445):eaat2965.

Iess, L., Stevenson, D. J., Parisi, M., Hemingway, D., Jacobson, R. A., Lunine, J. I., Nimmo, F., Armstrong, J. W., Asmar, S. W., Ducci, M., and Tortora, P. (2014). The gravity field and interior structure of enceladus. *Science*, 344(6179):78–80.

Jaramillo-Botero, A., Cable, M., Hofmann, A., Hodyss, R., Malaska, M., and Lunine, J. (2021). Understanding hypervelocity sampling of biosignatures in space missions. *Astrobiology*, 21(in press).

Jia, X., Kivelson, M. G., Khurana, K. K., and Kurth, W. S. (2018). Evidence of a plume on europa from galileo magnetic and plasma wave signatures. *Nature Astronomy*, 2(6):459–464.

Johnson, C. M., Beard, B. L., and Roden, E. E. (2008). The iron isotope fingerprints of redox and biogeochemical cycling in modern and ancient earth. *Annual Review of Earth and Planetary Sciences*, 36:457–493.

Karas, M., Bachmann, D., Bahr, U., and Hillenkamp, F. (1987). Matrix-assisted ultraviolet laser desorption of non-volatile compounds. *International Journal of Mass Spectrometry and Ion Processes*, 78:53–68.

Karas, M., Bachmann, D., and Hillenkamp, F. (1985). Influence of the wavelength in high-irradiance ultraviolet laser desorption mass spectrometry of organic molecules. *Analytical Chemistry*, 57(14):2935–2939.

Karas, M., Bahr, U., Ingendoh, A., Nordhoff, E., Stahl, B., Strupat, K., and Hillenkamp, F. (1990). Principles and applications of matrix-assisted uv-laser desorption/ionization mass spectrometry. *Analytica Chimica Acta*, 241:175–185.

Karas, M., Bahr, U., Ingendoh, A., Nordhoff, E., Stahl, B., Strupat, K., and Hillenkamp, F. (1991). Principles and applications of matrix-assisted uv-laser desorption/ionization mass spectrometry. *Journal of Chromatography B*, 562:745–746.

Karas, M., Glückmann, M., and Schäfer, J. (2000). Ionization in matrix-assisted laser desorption/ionization: singly charged molecular ions are the lucky survivors. *Journal of Mass Spectrometry*, 35(1):1–12.

Kattenhorn, S. A. and Prockter, L. M. (2014). Evidence for subduction in the ice shell of europa. *Nature Geoscience*, 7(10):762–767.

Kawahata, H. and Ishizuka, T. (1992). Amino acids in interstitial waters from sites 790 and 791 in the izu-bonin island. *Proceedings of Ocean Drilling Program, Scientific results*, 126:531–540.

Kelley, D. (2005). From the mantle to microbes: The lost city hydrothermal field. *Oceanography*, 18(3):32–45.

Kelley, D. S., Karson, J. A., Blackman, D. K., and Fruh-Green, G. L. (2001). An off-axis hydrothermal vent field near the mid-atlantic ridge at 30 degrees n. *Nature*, 412(6843):145–149.

Kempf, S., Altobelli, N., Briois, C., Grün, E., Horanyi, M., Postberg, F., Schmidt, J., Srama, R., Sternovsky, Z., Tobie, G., and Zolotov, M. (2014). Suda: A dust mass spectrometer for compositional surface mapping for a mission to europa. In *European Planetary Science Congress*, volume 9:EPSC2014-229.

Kempf, S., Beckmann, U., Moragas-Klostermeyer, G., Postberg, F., Srama, R., Economou, T., Schmidt, J., Spahn, F., and Grün, E. (2008). The e ring in the vicinity of enceladus: I. spatial distribution and properties of the ring particles. *Icarus*, 193(2):420–437.

Kempf, S., Beckmann, U., and Schmidt, J. (2010). How the enceladus dust plume feeds saturn's e ring. *Icarus*, 206(2):446–457.

Kempf, S. et al. (2009). Dust spectroscopy of jovian satellite surface composition. In *European Planetary Science Congress*, volume 4:EPSC2009-472.

Kempf, S., Goode, W., Srama, R., and F, P. (2020). What does really happen in a dust impact? In *EGU General Assembly Conference Abstracts, EGU2020-20089*.

Kempf, S., Horányi, M., Hsu, H.-W., Hill, T.-W., Juhász, A., and Smith, H. T. (2018). Saturn's diffuse e ring and its connection with enceladus. In Schenk, P., Clark, R., C.J.A. Howet and, A. V., and Waite, J., editors, *Enceladus and the Icy Moons of Saturn*, pages 195–210. University of Arizona Press Tucson, AZ.

Kempf, S., Srama, R., Grün, E., Mocker, A., Postberg, F., Hillier, J. K., Horányi, M., Sternovsky, Z., Abel, B., Beinsen, A., et al. (2012). Linear high resolution dust mass spectrometer for a mission to the galilean satellites. *Planetary and Space Science*, 65(1):10–20.

Kempf, S., Sternovsky, Z., Horanyi, M., Hand, K. P., Srama, R., Postberg, F., Altobelli, N., Gruen, E., Gudipati, M. S., Schmidt, J., et al. (2019). The sufarce dust analyzer (suda): Compositional mapping of europa's surface. In *American Geophysical Union, Fall Meeting*, volume P53D–3500.

Khawaja, N., Postberg, F., Hillier, J., Klenner, F., Kempf, S., Nölle, L., Reviol, R., Zou, Z., and Srama, R. (2019). Low-mass nitrogen-, oxygen-bearing, and aromatic compounds in enceladean ice grains. *Monthly Notices of the Royal Astronomical Society*, 489(4):5231–5243.

Khawaja, N. A. (2016). *Organic compounds in Saturn's E ring and its compositional profile in the vicinity of Rhea*. PhD thesis, Ruprecht-Karls-Universität Heidelberg.

Khurana, K., Kivelson, M., Stevenson, D., Schubert, G., Russell, C., Walker, R., and Polanskey, C. (1998). Induced magnetic fields as evidence for subsurface oceans in europa and callisto. *Nature*, 395(6704):777–780.

Kingdon, K. (1923). A method for the neutralization of electron space charge by positive ionization at very low gas pressures. *Physical Review*, 21(4):408–418.

Kissel, J., Sagdeev, R., Bertaux, J., Angarov, V., Audouze, J., Blamont, J., Büchler, K., Evlanov, E., Fechtig, H., Fomenkova, M., et al. (1986). Composition of comet halley dust particles from vega observations. *Nature*, 321(6067):280–282.

Kivelson, M. G., Khurana, K. K., Russell, C. T., Volwerk, M., Walker, R. J., and Zimmer, C. (2000). Galileo magnetometer measurements: A stronger case for a subsurface ocean at europa. *Science*, 289(5483):1340–1343.

Kleinekofort, W., Avdiev, J., and Brutschy, B. (1996a). A new method of laser desorption mass spectrometry for the study of biological macromolecules. *International Journal of Mass Spectrometry and Ion Processes*, 152(2-3):135–142.

Kleinekofort, W., Pfenninger, A., Plomer, T., Griesinger, C., and Brutschy, B. (1996b). Observation of noncovalent complexes using laser-induced liquid beam ionization/desorption. *International Journal of Mass Spectrometry and Ion Processes*, 156(3):195–202.

Kliore, A., Anderson, J., Armstrong, J., Asmar, S., Hamilton, C., Rappaport, N., Wahlquist, H., Ambrosini, R., Flasar, F., French, R., et al. (2004). Cassini radio science. *Space Science Reviews*, 115(1-4):1–70.

Konn, C., Charlou, J.-L., Donval, J.-P., Holm, N., Dehairs, F., and Bouillon, S. (2009). Hydrocarbons and oxidized organic compounds in hydrothermal

fluids from rainbow and lost city ultramafic-hosted vents. *Chemical Geology*, 258(3-4):299–314.

Koschny, D. and Grün, E. (2001). Impacts into ice–silicate mixtures: Ejecta mass and size distributions. *Icarus*, 154(2):402–411.

Kovtun, Y. V. (2015). Mean energy of water molecule ionization by electron impact. *Technical Physics*, 60(8):1110–1118.

Krimigis, S., Mitchell, D., Hamilton, D., Livi, S., Dandouras, J., Jaskulek, S., Armstrong, T., Boldt, J., Cheng, A., Gloeckler, G., et al. (2004). Magnetosphere imaging instrument (mimi) on the cassini mission to saturn/titan. *Space Science Reviews*, 114(1-4):233–329.

Krivov, A. V., Sremčević, M., Spahn, F., Dikarev, V. V., and Kholshevnikov, K. V. (2003). Impact-generated dust clouds around planetary satellites: spherically symmetric case. *Planetary and Space Science*, 51(3):251–269.

Krüger, H., Krivov, A. V., and Grün, E. (2000). A dust cloud of ganymede maintained by hypervelocity impacts of interplanetary micrometeoroids. *Planetary and Space Science*, 48(15):1457–1471.

Lai, J. C.-Y., Pearce, B. K., Pudritz, R. E., and Lee, D. (2019). Meteoritic abundances of fatty acids and potential reaction pathways in planetesimals. *Icarus*, 319:685–700.

Laroche, M., Almeras, L., Pecchi, E., Bechah, Y., Raoult, D., Viola, A., and Parola, P. (2017). Maldi-tof ms as an innovative tool for detection of plasmodium parasites in anopheles mosquitoes. *Malaria Journal*, 16(1):5.

Lebreton, J.-P. and Matson, D. (2002). The huygens probe: Science, payload and mission overview. *Space Science Reviews*, 104(1-4):59–100.

Lebreton, J.-P., Witasse, O., Sollazzo, C., Blancquaert, T., Couzin, P., Schipper, A.-M., Jones, J. B., Matson, D. L., Gurvits, L. I., Atkinson, D. H., et al. (2005). An overview of the descent and landing of the huygens probe on titan. *Nature*, 438(7069):758–764.

Liao, Y., Nimmo, F., and Neufeld, J. A. (2020). Heat production and tidally driven fluid flow in the permeable core of enceladus. *Journal of Geophysical Research: Planets*, 125:e2019JE006209.

Ligier, N., Poulet, F., Carter, J., Brunetto, R., and Gourgeot, F. (2016). Vlt/sinfoni observations of europa: New insights into the surface composition. *The Astronomical Journal*, 151(6):163.

Loison, A., Dubant, S., Adam, P., and Albrecht, P. (2010). Elucidation of an iterative process of carbon–carbon bond formation of prebiotic significance. *Astrobiology*, 10(10):973–988.

Lorenz, R. D., Turtle, E. P., Barnes, J. W., Trainer, M. G., Adams, D. S., Hibbard, K. E., Sheldon, C. Z., Zacny, K., Peplowski, P. N., Lawrence, D. J., et al. (2018). Dragonfly: A rotorcraft lander concept for scientific exploration at titan. *Johns Hopkins APL Technical Digest*, 34(3):374–387.

Luisi, P. L. (2016). *The emergence of life: from chemical origins to synthetic biology*. Cambridge University Press, 2 edition.

Lunine, J., Waite, J., Postberg, F., Spilker, L., and Clark, K. (2015a). Enceladus life finder: The search for life in a habitable moon. In *EGU General Assembly Conference Abstracts, EGU2015-14923*.

Lunine, J., Waite, J., Postberg, F., Spilker, L., and Clark, K. (2015b). Enceladus life finder: The search for life in a habitable moon. In *46th Lunar and Planetary Science Conference*, volume 1525.

Lunine, J. I. (2017). Ocean worlds exploration. *Acta Astronautica*, 131:123–130.

Mager, F., Sokolova, L., Lintzel, J., Brutschy, B., and Nussberger, S. (2010). Lilbid-mass spectrometry of the mitochondrial preprotein translocase tom. *Journal of Physics: Condensed Matter*, 22(45):454132.

Makarov, A. (2000). Electrostatic axially harmonic orbital trapping: a high-performance technique of mass analysis. *Analytical chemistry*, 72(6):1156–1162.

Makarov, A., Denisov, E., Kholomeev, A., Balschun, W., Lange, O., Strupat, K., and Horning, S. (2006). Performance evaluation of a hybrid linear ion trap/orbitrap mass spectrometer. *Analytical Chemistry*, 78(7):2113–2120.

Maksyutenko, P., Rizzo, T. R., and Boyarkin, O. V. (2006). A direct measurement of the dissociation energy of water. *The Journal of Chemical Physics*, 125(18):181101.

Mamyrin, B. (1994). Laser assisted reflectron time-of-flight mass spectrometry. *International Journal of Mass Spectrometry and Ion Processes*, 131:1–19.

Mamyrin, B. (2001). Time-of-flight mass spectrometry (concepts, achievements, and prospects). *International Journal of Mass Spectrometry*, 206(3):251–266.

Mamyrin, B., Karataev, V., Shmikk, D., and Zagulin, V. (1973). The mass-reflectron, a new nonmagnetic time-of-flight mass spectrometer with high resolution. *Zhurnal Ehksperimental'noj i Teoreticheskoj Fiziki*, 64(1):82–89.

Martin, W., Baross, J., Kelley, D., and Russell, M. J. (2008). Hydrothermal vents and the origin of life. *Nature Reviews Microbiology*, 6(11):805–814.

Mathies, R. A., Razu, M. E., Kim, J., Stockton, A. M., Turin, P., and Butterworth, A. (2017). Feasibility of detecting bioorganic compounds in enceladus plumes with the enceladus organic analyzer. *Astrobiology*, 17(9):902–912.

Matson, D. L., Spilker, L. J., and Lebreton, J.-P. (2002). The cassini/huygens mission to the saturnian system. *Space Science Reviews*, 104(1-4):1–58.

Maxwell, J. C. (1859). On the stability of the motion of saturn's rings; an essay which obtained the adams' prize for the year 1856, in the university of cambridge. *Cambridge: Macmillan and Co.*, pages 297—-304.

McCollom, T. M. and Seewald, J. S. (2006). Carbon isotope composition of organic compounds produced by abiotic synthesis under hydrothermal conditions. *Earth and Planetary Science Letters*, 243(1-2):74–84.

McDermott, J. M., Seewald, J. S., German, C. R., and Sylva, S. P. (2015). Pathways for abiotic organic synthesis at submarine hydrothermal fields. *Proceedings of the National Academy of Sciences*, 112(25):7668–7672.

McEwen, A., Moore, J., Spilker, L., Barnes, J., Beauchamp, P., Bowman, J., Cable, M., Edgington, S., Hendrix, A., et al. (2019). Scientific goals for exploration of the outer solar system: Explore outer planet systems and ocean worlds. *OPAG Report*, v. 28 August 2019:1–79.

McKay, C., Davila, A., Glein, C., Hand, K., and Stockton, A. (2018). Enceladus astrobiology, habitability, and the origin of life. In Schenk, P., Clark, R., C.J.A. Howet and, A. V., and Waite, J., editors, *Enceladus and the Icy Moons of Saturn*, pages 437–452. University of Arizona Press Tucson, AZ.

McKay, C. P. (2004). What is life—and how do we search for it in other worlds? *PLoS Biology*, 2(9):e302.

McKinnon, W. B. (2015). Effect of enceladus's rapid synchronous spin on interpretation of cassini gravity. *Geophysical Research Letters*, 42(7):2137–2143.

Melwani Daswani, M. and Vance, S. D. (2020). Evolution of volatiles from europa's interior into its ocean. In *Goldschmidt Conference Abstracts*, volume 2020 1777.

Menez, B., Pisapia, C., Andreani, M., Jamme, F., Vanbellingen, Q., Brunelle, A., Richard, L., Dumas, P., and Refregiers, M. (2018). Abiotic synthesis of amino acids in the recesses of the oceanic lithosphere. *Nature*, 564:59–63.

Miljković, K., Hillier, J., Mason, N., and Zarnecki, J. (2012). Models of dust around europa and ganymede. *Planetary and Space Science*, 70(1):20–27.

Miller, M., Hodyss, R., Malaska, M., Hofmann, A., Waller, S., Belousov, A., Lambert, J., Madzunkov, S., Darrach, M., Jaramillo-Botero, A., Cable, M., and Continetti, R. (2019). Hypervelocity enceladus ice grain analogue production with the aerosol impact spectrometer. In *European Planetary Science Congress*, volume 13:EPSC-DPS2019-353-1.

Mitchell, C., Porco, C., and Weiss, J. (2015). Tracking the geysers of enceladus into saturn's e ring. *The Astronomical Journal*, 149(5):156.

Mitri, G., Postberg, F., Soderblom, J. M., Wurz, P., Tortora, P., Abel, B., Barnes, J. W., Berga, M., Carrasco, N., Coustenis, A., et al. (2018). Explorer of enceladus and titan (e2t): Investigating ocean worlds' evolution and habitability in the solar system. *Planetary and Space Science*, 155:73–90.

Mocker, A., Armes, S., Bugiel, S., Fiege, K., Gruen, E., Heines, B., Hillier, J., Kempf, S., and Srama, R. (2010). The heidelberg dust accelerator: Investigating hypervelocity particle impacts. In *American Geophysical Union, Fall Meeting*, volume P31B-1524.

Mocker, A., Hornung, K., Grün, E., Kempf, S., Collette, A., Drake, K., Horányi, M., Munsat, T., O'Brien, L., Sternovsky, Z., and Srama, R. (2013). On the application of a linear time-of-flight mass spectrometer for the investigation of hypervelocity impacts of micron and sub-micron sized dust particles. *Planetary and Space Science*, 89:47–57.

Moore, J., Spilker, L., Cable, M., Edgington, S., Hendrix, A., Hofstadter, M., Hurford, T., Mandt, K., McEwen, A., et al. (2020). Exploration strategy for the outer planets 2023-2032: Goals and priorities. *Outer Planets Assessment Group White Paper*, v. 30 April 2020:1–8.

Morgner, N., Barth, H.-D., and Brutschy, B. (2006). A new way to detect noncovalently bonded complexes of biomolecules from liquid micro-droplets by laser mass spectrometry. *Australian Journal of Chemistry*, 59(2):109–114.

Morgner, N., Barth, H.-D., Brutschy, B., Scheffer, U., Breitung, S., and Göbel, M. (2008). Binding sites of the viral rna element tar and of tar mutants for various peptide ligands, probed with lilbid: a new laser mass spectrometry. *Journal of the American Society for Mass Spectrometry*, 19(11):1600–1611.

Morgner, N., Kleinschroth, T., Barth, H.-D., Ludwig, B., and Brutschy, B. (2007). A novel approach to analyze membrane proteins by laser mass spectrometry: from protein subunits to the integral complex. *Journal of the American Society for Mass Spectrometry*, 18(8):1429–1438.

Narita, M., Ishikawa, K., Chen, J.-Y., and Kim, Y. (1984). Prediction and improvement of protected peptide solubility in organic solvents. *International Journal of Peptide and Protein Research*, 24(6):580–587.

NASA(url1) (2020). Quick facts — mission – nasa solar system exploration. `https://solarsystem.nasa.gov/missions/cassini/mission/quick-facts/`. Retrieved on May 25, 2020.

NASA(url2) (2020). About — mission – nasa's europa clipper. `https://europa.nasa.gov/mission/about/`. Retrieved on June 19, 2020.

Nealson, K. H. (1997). The limits of life on earth and searching for life on mars. *Journal of Geophysical Research: Planets*, 102(E10):23675–23686.

New, J., Mathies, R., Price, M., Cole, M., Golozar, M., Spathis, V., Burchell, M., and Butterworth, A. (2020a). Characterizing organic particle impacts on inert metal surfaces: Foundations for capturing organic molecules during hypervelocity transits of enceladus plumes. *Meteoritics & Planetary Science*, 55(3):465–479.

New, J. S., Kazemi, B., Price, M. C., Cole, M. J., Spathis, V., Mathies, R. A., and Butterworth, A. L. (2020b). Feasibility of enceladus plume biosignature analysis: Successful capture of organic ice particles in hypervelocity impacts. *Meteoritics & Planetary Science*, 55(8):1936–1948.

Newton, K. A. and McLuckey, S. A. (2004). Generation and manipulation of sodium cationized peptides in the gas phase. *Journal of the American Society for Mass Spectrometry*, 15(4):607–615.

Niedner-Schatteburg, G. and Bondybey, V. E. (2000). Ft-icr studies of solvation effects in ionic water cluster reactions. *Chemical reviews*, 100(11):4059–4086.

Nimmo, F. and Pappalardo, R. (2016). Ocean worlds in the outer solar system. *Journal of Geophysical Research: Planets*, 121(8):1378–1399.

Nölle, L. (2020). *Multidimensional scan of the Saturnian E ring based on the data record of Cassini's Cosmic Dust Analyser*. PhD thesis, Freie Universität Berlin, in preparation.

Nordheim, T., Hand, K., and Paranicas, C. (2018). Preservation of potential biosignatures in the shallow subsurface of europa. *Nature Astronomy*, 2(8):673–679.

Ojakangas, G. W. and Stevenson, D. (1986). Episodic volcanism of tidally heated satellites with application to io. *Icarus*, 66(2):341–358.

Opsal, R. B., Owens, K. G., and Reilly, J. P. (1985). Resolution in the linear time-of-flight mass spectrometer. *Analytical Chemistry*, 57(9):1884–1889.

Orgel, L. E. (1998). The origin of life—a review of facts and speculations. *Trends in biochemical sciences*, 23(12):491–495.

Padoan, A., Seraglia, R., Basso, D., Fogar, P., Sperti, C., Moz, S., Greco, E., Marchet, A., de Manzoni, G., Zambon, C.-F., et al. (2013). Usefulness of maldi-tof/ms identification of low-mw fragments in sera for the differential diagnosis of pancreatic cancer. *Pancreas*, 42(4):622–632.

Paganini, L., Villanueva, G. L., Roth, L., Mandell, A., Hurford, T., Retherford, K. D., and Mumma, M. J. (2020). A measurement of water vapour amid a largely quiescent environment on europa. *Nature Astronomy*, 4:266—-272.

Paizs, B. and Suhai, S. (2005). Fragmentation pathways of protonated peptides. *Mass Spectrometry Reviews*, 24(4):508–548.

Pappalardo, R., Senske, D., Korth, H., Klima, R., Vance, S., and Craft, K. (2017). The europa clipper mission: Exploring the habitability of a unique icy world. In *European Planetary Science Congress*, volume 11:EPSC2017-304.

Pappalardo, R. T., Belton, M. J., Breneman, H., Carr, M., Chapman, C. R., Collins, G., Denk, T., Fagents, S., Geissler, P. E., Giese, B., et al. (1999). Does europa have a subsurface ocean? evaluation of the geological evidence. *Journal of Geophysical Research: Planets*, 104(E10):24015–24055.

Pasch, H. and Schrepp, W. (2013). *MALDI-TOF mass spectrometry of synthetic polymers*. Springer Berlin Heidelberg, 1 edition.

Patel, R. (2015). Maldi-tof ms for the diagnosis of infectious diseases. *Clinical chemistry*, 61(1):100–111.

Peetz, O., Hellwig, N., Henrich, E., Mezhyrova, J., Dötsch, V., Bernhard, F., and Morgner, N. (2018). Lilbid and nesi: different native mass spectrometry techniques as tools in structural biology. *Journal of The American Society for Mass Spectrometry*, 30(1):181–191.

Phillips, C. B., Hand, K. P., Cable, M. L., Hofmann, A., and Craft, K. (2019). Update on the europa lander mission concept. In *50th Lunar and Planetary Science Conference*, volume 2132.

Piwowar, A. M., Lockyer, N. P., and Vickerman, J. C. (2009). Salt effects on ion formation in desorption mass spectrometry: an investigation into the role of alkali chlorides on peak suppression in time-of-flight-secondary ion mass spectrometry. *Analytical chemistry*, 81(3):1040–1048.

Pizzarello, S., Schrader, D. L., Monroe, A. A., and Lauretta, D. S. (2012). Large enantiomeric excesses in primitive meteorites and the diverse effects of water in cosmochemical evolution. *Proceedings of the National Academy of Science*, 109(30):11949–11954.

Porco, C., Baker, E., Barbara, J., Beurle, K., Brahic, A., Burns, J., Charnoz, S., Cooper, N., Dawson, D., Del Genio, A., et al. (2005). Cassini imaging science: Initial results on saturn's atmosphere. *Science*, 307(5713):1243–1247.

Porco, C. C., Dones, L., and Mitchell, C. (2017). Could it be snowing microbes on enceladus? assessing conditions in its plume and implications for future missions. *Astrobiology*, 17(9):876–901.

Porco, C. C., Helfenstein, P., Thomas, P. C., Ingersoll, A. P., Wisdom, J., West, R., Neukum, G., Denk, T., Wagner, R., Roatsch, T., Kieffer, S., Turtle, E., McEwen, A., Johnson, T. V., Rathbun, J., Veverka, J., Wilson, D., Perry, J., Spitale, J., Brahic, A., Burns, J. A., DelGenio, A. D., Dones, L., Murray, C. D., and Squyres, S. (2006). Cassini observes the active south pole of enceladus. *Science*, 311(5766):1393–1401.

Porco, C. C., West, R. A., Squyres, S., Mcewen, A., Thomas, P., Murray, C. D., Delgenio, A., Ingersoll, A. P., Johnson, T. V., Neukum, G., et al. (2004). Cassini imaging science: Instrument characteristics and anticipated scientific investigations at saturn. *Space Science Reviews*, 115(1-4):363–497.

Postberg, F., Clark, R., Hansen, C., Coates, A., Dalle Ore, C., Scipioni, F., Hedman, M., and Waite, J. (2018b). Plume and surface composition of enceladus. In Schenk, P., Clark, R., C.J.A. Howet and, A. V., and Waite, J., editors, *Enceladus and the Icy Moons of Saturn*, pages 129–162. University of Arizona Press Tucson, AZ.

Postberg, F., Grün, E., Horanyi, M., Kempf, S., Krüger, H., Schmidt, J., Spahn, F., Srama, R., Sternovsky, Z., and Trieloff, M. (2011b). Compositional mapping of planetary moons by mass spectrometry of dust ejecta. *Planetary and Space Science*, 59(14):1815–1825.

Postberg, F., Kempf, S., Hillier, J., Srama, R., Green, S., McBride, N., and Grün, E. (2008). The e-ring in the vicinity of enceladus ii. probing the moon's interior—the composition of e-ring particles. *Icarus*, 193:438–454.

Postberg, F., Kempf, S., Rost, D., Stephan, T., Srama, R., Trieloff, M., Mocker, A., and Goerlich, M. (2009b). Discriminating contamination from particle components in spectra of cassini's dust detector cda. *Planetary and Space Science*, 57(12):1359–1374.

Postberg, F., Kempf, S., Schmidt, J., Brilliantov, N., Beinsen, A., Abel, B., Buck, U., and Srama, R. (2009a). Sodium salts in e-ring ice grains from an ocean below the surface of enceladus. *Nature*, 459:1098–1101.

Postberg, F., Kempf, S., Srama, R., Green, S. F., Hillier, J. K., McBride, N., and Grün, E. (2006). Composition of jovian dust stream particles. *Icarus*, 183(1):122–134.

Postberg, F., Khawaja, N., Abel, B., Choblet, G., Glein, C. R., Gudipati, M. S., Henderson, B. L., Hsu, H.-W., Kempf, S., Klenner, F., et al. (2018a). Macromolecular organic compounds from the depths of enceladus. *Nature*, 558(7711):564–568.

Postberg, F., Schmidt, J., Hillier, J., Kempf, S., and Srama, R. (2011a). A salt-water reservoir as the source of a compositionally stratified plume on enceladus. *Nature*, 474(7353):620–622.

Preiner, M., Asche, S., Becker, S., Betts, H. C., Boniface, A., Camprubi, E., Chandru, K., Erastova, V., Garg, S. G., Khawaja, N., et al. (2020). The future of origin of life research: bridging decades-old divisions. *Life*, 10(3):20.

Quick, L. C., Barnouin, O. S., Prockter, L. M., and Patterson, G. W. (2013). Constraints on the detection of cryovolcanic plumes on europa. *Planetary and Space Science*, 86:1–9.

Raulin, F., McKay, C., Lunine, J., and T, O. (2010). Titan's astrobiology. In Brown, R., Lebreton, J. P., and Waite, J., editors, *Titan from Cassini-Huygens*, pages 215–233. Springer Netherlands.

Read, P., Dowling, T., and Schubert, G. (2009). Saturn's rotation period from its atmospheric planetary-wave configuration. *Nature*, 460(7255):608–610.

Reh, K., Cable, M. L., Clark, K., Lunine, J. I., Postberg, F., Spilker, L., and Waite, J. H. (2016). Enceladus life finder: The search for life in a habitable moon. In *Aerospace Conference, IEEE, Big Sky, MT*, pages 1–8.

Remoroza, C. A., Mak, T. D., De Leoz, M. L. A., Mirokhin, Y. A., and Stein, S. E. (2018). Creating a mass spectral reference library for oligosaccharides in human milk. *Analytical Chemistry*, 90(15):8977–8988.

Repeta, D. (2014). Chemical characterization and cycling of dissolved organic matter. In Hansell, D. A. and Carlson, C. A., editors, *Biogeochemistry of Marine Dissolved Organic Matter*, pages 21–63. Academic Press Elsevier.

Reviol, R., Postberg, F., Trieloff, M., Srama, R., and Abel, B. (2012). Simulation of tof spectra from cosmic ice particles in the laboratory by ir-fl-maldi. In *European Planetary Science Congress*, volume 7:EPSC2012-489-1.

Riley, J., Hoppa, G. V., Greenberg, R., Tufts, B. R., and Geissler, P. (2000). Distribution of chaotic terrain on europa. *Journal of Geophysical Research: Planets*, 105(E9):22599–22615.

Roberts, J. H. (2015). The fluffy core of enceladus. *Icarus*, 258:54–66.

Robidel, R., Le Mouélic, S., Tobie, G., Massé, M., Seignovert, B., Sotin, C., and Rodriguez, S. (2020). Photometrically-corrected global infrared mosaics of enceladus: New implications for its spectral diversity and geological activity. *Icarus*, 349(in press):113848.

Roth, L., Saur, J., Retherford, K. D., Strobel, D. F., Feldman, P. D., McGrath, M. A., and Nimmo, F. (2014). Transient water vapor at europa's south pole. *Science*, 343(6167):171–174.

Rushdi, A. I. and Simoneit, B. R. (2005). Abiotic synthesis of organic compounds from carbon disulfide under hydrothermal conditions. *Astrobiology*, 5(6):749–769.

Russell, L. M., Hawkins, L. N., Frossard, A. A., Quinn, P. K., and Bates, T. S. (2010). Carbohydrate-like composition of submicron atmospheric particles and their production from ocean bubble bursting. *Proceedings of the National Academy of Sciences*, 107(15):6652–6657.

Russell, M. J. and Hall, A. (1997). The emergence of life from iron monosulphide bubbles at a submarine hydrothermal redox and ph front. *Journal of the Geological Society*, 154(3):377–402.

Sánchez-Lavega, A., Colas, F., Lecacheux, J., Laques, P., Miyazaki, I., and Parker, D. (1991). The great white spot and disturbances in saturn's equatorial atmosphere during 1990. *Nature*, 353(6343):397–401.

Sarma, R., Wong, K.-Y., Lynch, G. C., and Montgomery Pettitt, B. (2018). Peptide solubility limits: Backbone and side-chain interactions. *The Journal of Physical Chemistry B*, 122(13):3528–3539.

Schenk, P., White, O., Byrne, P., and Moore, J. (2018). Saturn's other icy moons: Geologically complex worlds in their own right. In Schenk, P., Clark, R., C.J.A. Howet and, A. V., and Waite, J., editors, *Enceladus and the Icy Moons of Saturn*, pages 237–265. University of Arizona Press Tucson, AZ.

Schmidt, B., Blankenship, D., Patterson, G., and Schenk, P. (2011). Active formation of 'chaos terrain' over shallow subsurface water on europa. *Nature*, 479(7374):502–505.

Schmidt, J., Brilliantov, N., Spahn, F., and Kempf, S. (2008). Slow dust in enceladus' plume from condensation and wall collisions in tiger stripe fractures. *Nature*, 451(7179):685–688.

Schmidt, J., Ohtsuki, K., Rappaport, N., Salo, H., and Spahn, F. (2009). Dynamics of saturn's dense rings. In Dougherty, M. K., Esposito, L. W., and Krimigis, S. M., editors, *Saturn from Cassini-Huygens*, pages 413–458. Springer, Dordrecht.

Schubert, G., Anderson, J. D., Travis, B. J., and Palguta, J. (2007). Enceladus: present internal structure and differentiation by early and long-term radiogenic heating. *Icarus*, 188(2):345–355.

Schubert, G., Sohl, F., and Hussmann, H. (2009). Interior of europa. In Pappalardo, R., McKinnon, W., and Khurana, K., editors, *Europa*, pages 353–367. University of Arizona Press Tucson, AZ.

Seidelmann, P. K., Archinal, B. A., A'hearn, M. F., Conrad, A., Consolmagno, G., Hestroffer, D., Hilton, J., Krasinsky, G., Neumann, G., Oberst, J., et al. (2007). Report of the iau/iag working group on cartographic coordinates and rotational elements: 2006. *Celestial Mechanics and Dynamical Astronomy*, 98(3):155–180.

Sekine, Y., Shibuya, T., Postberg, F., Hsu, H.-W., Suzuki, K., Masaki, Y., Kuwatani, T., Mori, M., Hong, P. K., Yoshizaki, M., Tachibana, S., and Sirono, S.-i. (2015). High-temperature water–rock interactions and hydrothermal environments in the chondrite-like core of enceladus. *Nature Communications*, 6:8604.

Seng, P., Drancourt, M., Gouriet, F., La Scola, B., Fournier, P.-E., Rolain, J. M., and Raoult, D. (2009). Ongoing revolution in bacteriology: routine identification of bacteria by matrix-assisted laser desorption ionization time-of-flight mass spectrometry. *Clinical Infectious Diseases*, 49(4):543–551.

Shapiro, R. and Schulze-Makuch, D. (2009). The search for alien life in our solar system: strategies and priorities. *Astrobiology*, 9(4):335–343.

Shemansky, D., Yung, Y., Liu, X., Yoshii, J., Hansen, C. J., Hendrix, A. R., and Esposito, L. W. (2014). A new understanding of the europa atmosphere and limits on geophysical activity. *The Astrophysical Journal*, 797(2):84.

Sherwood, B. (2016). Strategic map for exploring the ocean-world enceladus. *Acta Astronautica*, 126:52–58.

Shi, T., Zhao, J., Shek, P. I., Hopkinson, A. C., and Siu, K. M. (2005). Carbonate, carbamate, urea, and guanidine as model species for functional groups in biological molecules a combined density functional theory and mass spectrometry examination of polysodiation and gas-phase dissociation. *Canadian Journal of Chemistry*, 83(11):1941–1952.

Showalter, M. R., Cuzzi, J. N., and Larson, S. M. (1991). Structure and particle properties of saturn's e ring. *Icarus*, 94(2):451–473.

Shu, A., Collette, A., Drake, K., Grün, E., Horányi, M., Kempf, S., Mocker, A., Munsat, T., Northway, P., Srama, R., et al. (2012). 3 mv hypervelocity dust accelerator at the colorado center for lunar dust and atmospheric studies. *Review of Scientific Instruments*, 83(7):075108.

Sim, K., Shaw, A. G., Randell, P., Cox, M. J., McClure, Z. E., Li, M.-S., Haddad, M., Langford, P. R., Cookson, W. O., Moffatt, M. F., and Kroll, J. S. (2015). Dysbiosis anticipating necrotizing enterocolitis in very premature infants. *Clinical Infectious Diseases*, 60(3):389–397.

Sirbu, F. and Iulian, O. (2010). The mixing effect of glycine with sodium chloride from activity coefficients investigations at t=(303.15 and 313.15) k. *Journal of Optoelectronics and Advanced Materials*, 12(5):1200–1205.

Slipher, E. and Slipher, V. (1914). Mimas and enceladus turn always the same face to saturn. *Lowell Observatory Bulletin*, 2(62):70–72.

Smith, B. A., Soderblom, L., Batson, R., Bridges, P., Inge, J., Masursky, H., Shoemaker, E., Beebe, R., Boyce, J., Briggs, G., Bunker, A., Collins, S. A., Hansen, C. J., Johnson, T. V., Mitchell, J. L., Terrile, R. J., Cook, A. F., Cuzzi, J., Pollack, J. B., Danielson, G. E., Ingersoll, A. P., Davies, M. E., Hunt, G. E., Morrison, D., Owen, T., Sagan, C., Veverka, J., Strom, R., and Suomi, V. E. (1982). A new look at the saturn system: The voyager 2 images. *Science*, 215(4532):504–537.

Soderlund, K. M., Kalousová, K., Buffo, J. J., Glein, C. R., Goodman, J. C., Mitri, G., Patterson, G. W., Postberg, F., Rovira-Navarro, M., Rückriemen, T., et al. (2020). Ice-ocean exchange processes in the jovian and saturnian satellites. *Space Science Reviews*, 216(5):80.

Sohl, F., Spohn, T., Breuer, D., and Nagel, K. (2002). Implications from galileo observations on the interior structure and chemistry of the galilean satellites. *Icarus*, 157(1):104–119.

Southworth, B., Kempf, S., and Schmidt, J. (2015). Modeling europa's dust plumes. *Geophysical Research Letters*, 42(24):10541–10548.

Spahn, F., Schmidt, J., Albers, N., Hörning, M., Makuch, M., Seiß, M., Kempf, S., Srama, R., Dikarev, V., Helfert, S., Moragas-Klostermeyer, G., Krivov, A. V., Sremčević, M., Tuzzolino, A. J., Economou, T., and Grün, E. (2006). Cassini dust measurements at enceladus and implications for the origin of the e ring. *Science*, 311(5766):1416–1418.

Sparks, W. B., Hand, K., McGrath, M., Bergeron, E., Cracraft, M., and Deustua, S. (2016). Probing for evidence of plumes on europa with hst/stis. *The Astrophysical Journal*, 829(2):121.

Sparks, W. B., Schmidt, B. E., McGrath, M. A., Hand, K. P., Spencer, J., Cracraft, M., and Deustua, S. E. (2017). Active cryovolcanism on europa? *The Astrophysical Journal Letters*, 839(2):L18.

Spencer, J. and Nimmo, F. (2013). Enceladus: An active ice world in the saturn system. *Annual Review of Earth and Planetary Sciences*, 41(1):693–717.

Spencer, J., Nimmo, F., Ingersoll, A., Hurford, T., Kite, E., Rhoden, A., Schmidt, J., and Howett, C. (2018). Plume origins and plumbing: From ocean to surface. In Schenk, P., Clark, R., C.J.A. Howet and, A. V., and Waite, J., editors, *Enceladus and the Icy Moons of Saturn*, pages 163–174. University of Arizona Press Tucson, AZ.

Spencer, J., Pearl, J., Segura, M., Flasar, F., Mamoutkine, A., Romani, P., Buratti, B., Hendrix, A., Spilker, L., and Lopes, R. (2006). Cassini encounters enceladus: Background and the discovery of a south polar hot spot. *Science*, 311(5766):1401–1405.

Spencer, J. R., Tamppari, L. K., Martin, T. Z., and Travis, L. D. (1999). Temperatures on europa from galileo photopolarimeter-radiometer: nighttime thermal anomalies. *Science*, 284(5419):1514–1516.

Spilker, L. (2018). The scientific achievements of the cassini-huygens mission. In Ko, C., Yu, P., and Chang, C., editors, *Serendipities in the Solar System and Beyond, Vol. 513*, pages 131–146. Astronomical Society of the Pacific.

Spilker, L. J. (2019). Cassini-huygens' exploration of the saturn system: 13 years of discovery. *Science*, 364:1046–1051.

Srama, R., Ahrens, T. J., Altobelli, N., Auer, S., Bradley, J. G., Burton, M., Dikarev, V. V., Economou, T., Fechtig, H., Görlich, M., Grande, M., Graps, A., Grün, E., Havnes, O., Helfert, S., Horanyi, M., Igenbergs, E., Jessberger, E. K., Johnson, T. V., Kempf, S., Krivov, A. V., Krüger, H., Mocker-Ahlreep, A., Moragas-Klostermeyer, G., Lamy, P., Landgraf, M., Linkert, D., Linkert, G., Lura, F., McDonnell, J. A. M., Möhlmann, D., Morfill, G. E., Müller, M., Roy, M., Schäfer, G., Schlotzhauer, G., Schwehm, G. H., Spahn, F., Stübig, M., Svestka, J., Tschernjawski, V., Tuzzolino, A. J., Wäsch, R., and Zook, H. A. (2004). The cassini cosmic dust analyzer. *Space Science Reviews*, 114:465–518.

Srama, R., Kempf, S., Moragas-Klostermeyer, G., Altobelli, N., Auer, S., Beckmann, U., Bugiel, S., Burton, M., Economomou, T., Fechtig, H., et al. (2011). The cosmic dust analyser onboard cassini: ten years of discoveries. *CEAS Space Journal*, 2(1-4):3–16.

Srama, R., Kobayashi, M., Krüger, H., Arai, T., Kimura, H., Trieloff, M., Agarwal, J., Li, Y., Postberg, F., Khawaja, N., Hillier, J., et al. (2019). Dust astronomy with destiny plus at 1 au. In *EGU General Assembly Conference Abstracts, EGU2019-9105*.

Srama, R., Postberg, F., Henkel, H., Klopfer, T., Li, Y., Reviol, R., Khawaja, N., Klenner, F., Moragas-Klostermeyer, G., Nölle, L., Soja, R., Sternovsky, Z., Kempf, S., and Trieloff, M. (2015b). Enija : Search for life with a high-resolution tof-ms for in-situ compositonal analysis of nano- and micron-sized dust particles. In *EGU General Assembly Conference Abstracts, EGU2015-13456*.

Srama, R., Postberg, F., Henkel, H., Klopfer, T., Li, Y., Simolka, J., Bugiel, S., Kempf, S., Hillier, J., Khawaja, N., Trieloff, M., Abel, B., Moragas-Klostermeyer, G., Strack, H., Schmidt, J., Soja, R., Sternovsky, Z., and

Spohn, T. (2015a). Enceladus icy jet analyzer (enija) : Search for life with a high resolution tof-ms for in situ characterization of high dust density regions. In *European Planetary Science Congress*, volume 10:EPSC2015-769.

Srama, R., Woiwode, W., Postberg, F., Armes, S. P., Fujii, S., Dupin, D., Ormond-Prout, J., Sternovsky, Z., Kempf, S., Moragas-Klostermeyer, G., et al. (2009). Mass spectrometry of hyper-velocity impacts of organic micrograins. *Rapid Communications in Mass Spectrometry*, 23(24):3895–3906.

Sremčević, M., Krivov, A. V., Krüger, H., and Spahn, F. (2005). Impact-generated dust clouds around planetary satellites: model versus galileo data. *Planetary and Space Science*, 53(6):625–641.

Steel, E. L., Davila, A., and McKay, C. P. (2017). Abiotic and biotic formation of amino acids in the enceladus ocean. *Astrobiology*, 17(9):862–875.

Steen, H. and Mann, M. (2004). The abc's (and xyz's) of peptide sequencing. *Nature Reviews Molecular Cell Biology*, 5(9):699–711.

Stolz, F. (2016). *Liquid Micro Jets in Interaction with Intense Infrared Laser Beams for Chemical Analysis and Novel Applications*. PhD thesis, Universität Leipzig.

Stübig, M. (2002). *New insights in impact ionization and in time-of-flight mass spectroscopy with micrometeoroid detectors by improved impact simulations in the laboratory*. PhD thesis, Ruprecht-Karls-Universität Heidelberg.

Summons, R. E., Albrecht, P., McDonald, G., and Moldowan, J. M. (2008). Molecular biosignatures. *Space Science Reviews*, 135:133–159.

Takahagi, W., Seo, K., Shibuya, T., Takano, Y., Fujishima, K., Saitoh, M., Shimamura, S., Matsui, Y., Tomita, M., and Takai, K. (2019). Peptide synthesis under the alkaline hydrothermal conditions on enceladus. *ACS Earth and Space Chemistry*, 3(11):2559–2568.

Taubner, R.-S., Olsson-Francis, K., Vance, S. D., Ramkissoon, N. K., Postberg, F., de Vera, J.-P., Antunes, A., Casas, E. C., Sekine, Y., Noack, L., Barge, L., Goodman, J., Jebbar, M., Journaux, B., Karatekin, Ö., Klenner, F., et al. (2020). Experimental and simulation efforts in the astrobiological exploration of exooceans. *Space Science Reviews*, 216:9.

Thomas, P. C. (2010). Sizes, shapes and derived properties of the saturnian satellites after the cassini nominal mission. *Icarus*, 208(1):395–401.

Thomas, P. C., Tajeddine, R., Tiscareno, M. S., Burns, J. A., Joseph, J., Loredo, T. J., Helfenstein, P., and Porco, C. (2016). Enceladus's measured physical libration requires a global subsurface ocean. *Icarus*, 264:37–47.

Timmermann, R. and Grün, E. (1991). Plasma emission from high velocity impacts of microparticles onto water ice. In Levasseur-Regourd, A. and Hasegawa, H., editors, *Origin and Evolution of Interplanetary Dust*, page 375-378. Springer, Dordrecht: Astrophysics and Space Science Library.

Tobie, G. (2015). Enceladus' hot springs. *Nature*, 519(7542):162–163.

Tobie, G., Čadek, O., and Sotin, C. (2008). Solid tidal friction above a liquid water reservoir as the origin of the south pole hotspot on enceladus. *Icarus*, 196(2):642–652.

Tobie, G., Choblet, G., and Sotin, C. (2003). Tidally heated convection: Constraints on europa's ice shell thickness. *Journal of Geophysical Research: Planets*, 108(E11):5124.

Trumbo, S. K., Brown, M. E., and Hand, K. P. (2019). Sodium chloride on the surface of europa. *Science Advances*, 5(6):eaaw7123.

Truong, N., Monroe, A. A., Glein, C. R., Anbar, A. D., and Lunine, J. I. (2019). Decomposition of amino acids in water with application to in-situ measurements of enceladus, europa and other hydrothermally active icy ocean worlds. *Icarus*, 329:140–147.

Urban, J. and Štys, D. (2015). Noise and baseline filtration in mass spectrometry. In *International Conference on Bioinformatics and Biomedical Engineering*, pages 418–425. Springer.

Vance, S., Hand, K., and Pappalardo, R. (2016). Geophysical controls of chemical disequilibria in europa. *Geophysical Research Letters*, 43(10):4871–4879.

Vance, S. and Melwani Daswani, M. (2020). Serpentinite and the search for life beyond earth. *Philosophical Transactions of the Royal Society A*, 378(2165):20180421.

Verbiscer, A. J., Skrutskie, M. F., and Hamilton, D. P. (2009). Saturn's largest ring. *Nature*, 461(7267):1098–1100.

Waite, J., Lewis, W., Kasprzak, W., Anicich, V., Block, B., Cravens, T. E., Fletcher, G., Ip, W.-H., Luhmann, J., McNutt, R., et al. (2004). The cassini ion and neutral mass spectrometer (inms) investigation. *Space Science Reviews*, 114(1-4):113–231.

Waite, J., Lewis, W., Magee, B., Lunine, J., McKinnon, W., Glein, C., Mousis, O., Young, D., Brockwell, T., Westlake, J., Nguyen, M., Teolis, B., Niemann, B., McNutt, R., Perry, M., and Ip, W. (2009). Liquid water on enceladus from observations of ammonia and ar-40 in the plume. *Nature*, 460:487–490.

Waite, J. H., Combi, M. R., Ip, W.-H., Cravens, T. E., McNutt, R. L., Kasprzak, W., Yelle, R., Luhmann, J., Niemann, H., Gell, D., et al. (2006). Cassini ion and neutral mass spectrometer: Enceladus plume composition and structure. *Science*, 311(5766):1419–1422.

Waite, J. H., Glein, C. R., Perryman, R. S., Teolis, B. D., Magee, B. A., Miller, G., Grimes, J., Perry, M. E., Miller, K. E., Bouquet, A., et al. (2017). Cassini finds molecular hydrogen in the enceladus plume: evidence for hydrothermal processes. *Science*, 356(6334):155–159.

Waller, S. E., Belousov, A., Kidd, R. D., Nikolić, D., Madzunkov, S. M., Wiley, J. S., and Darrach, M. R. (2019). Chemical ionization mass spectrometry: Applications for the in situ measurement of nonvolatile organics at ocean worlds. *Astrobiology*, 19(10):1196–1210.

Wattenberg, A., Sobott, F., Barth, H.-D., and Brutschy, B. (1999). Laser desorption mass spectrometry on liquid beams. *European Mass Spectrometry*, 5(2):71–76.

Whitehouse, D. (2009). *Renaissance Genius: Galileo Galilei & His Legacy To Modern Science*. Sterling Publishing Company, Inc., NY.

Wiederschein, F. (2009). *Investigation of Laser-Induced-Liquid-Beam-Ion-Desorption (LILBID) with Molecular Dynamics Simulations.* PhD thesis, Georg-August-Universität Göttingen.

Wiederschein, F., Vöhringer-Martinez, E., Beinsen, A., Postberg, F., Schmidt, J., Srama, R., Stolz, F., Grubmüller, H., and Abel, B. (2015). Charge separation and isolation in strong water droplet impacts. *Physical Chemistry Chemical Physics*, 17(10):6858–6864.

Wu, Y., Koch, W., Berezansky, P., and Holland, L. (1992). The dissociation constant of amino acids by the conductimetric method: I. pk 1 of mopso-hcl at 25° c. *Journal of Solution Chemistry*, 21(6):597–605.

Xu, Z., Sun, X., and Harrington, P. d. B. (2011). Baseline correction method using an orthogonal basis for gas chromatography/mass spectrometry data. *Analytical Chemistry*, 83(19):7464–7471.

Young, D., Berthelier, J., Blanc, M., Burch, J., Coates, A., Goldstein, R., Grande, M., Hill, T., Johnson, R., Kelha, V., et al. (2004). Cassini plasma spectrometer investigation. *Space Science Reviews*, 114(1-4):1–112.

Zahnle, K., Schenk, P., Levison, H., and Dones, L. (2003). Cratering rates in the outer solar system. *Icarus*, 163(2):263–289.

Zhong, N., Cui, Y., Zhou, X., Li, T., and Han, J. (2015). Identification of prohibitin 1 as a potential prognostic biomarker in human pancreatic carcinoma using modified aqueous two-phase partition system combined with 2d-maldi-tof-tof-ms/ms. *Tumor Biology*, 36(2):1221–1231.

Zimmer, C., Khurana, K. K., and Kivelson, M. G. (2000). Subsurface oceans on europa and callisto: Constraints from galileo magnetometer observations. *Icarus*, 147(2):329–347.

Zolotov, M. Y. and Kargel, J. S. (2009). On the chemical composition of europa's icy shell, ocean, and underlying rocks. In Pappalardo, R., McKinnon, W., and Khurana, K., editors, *Europa*, pages 431–457. University of Arizona Press Tucson, AZ.

Zou, Z. (2020). *Investigation of Enceladus ocean composition from the composition of salt-rich ice grains emitted by its cryo volcanic plume.* PhD thesis, Freie Universität Berlin, in preparation.

Zou, Z., Postberg, F., Hillier, J., Khawaja, N., Klenner, F., and Nölle, L. (2020). Compositional heterogeneity amongst salt-rich grains emitted from enceladus' subsurface ocean. In *EGU General Assembly Conference Abstracts, EGU2020-18970.*

Zsolnay, A. (1977). Inventory of nonvolatile fatty acids and hydrocarbons in the oceans. *Marine Chemistry*, 5(4-6):465–475.

Zubarev, R. A. and Makarov, A. (2013). Orbitrap mass spectrometry. *Analytical Chemistry*, 85:5288–5296.

Appendices

A Supplementary Information, chapter 8

```
#date=2019-11-08-113032
#fullscale=2.000000
#solution=Water_H2O_pure_NA_0.19mlpmin_98.5%_FL5.38J_pos
#plasmaordesorption=des
#plasmacriterion=m16greater0.02
#energydensity=1152
#delaytime=055
#mcp=150
#wavelength=2840
#focusdiameter=210
#focusdiameterdesc=10_90
#laserpower=50
#waterjetposition=B
#nozzlediameter=16
#numberofspectra=490
#masscalibrationa=0.349710
#masscalibrationb=-0.226610
#masscalibrationc=0.392110
##mcal_form=att+bt+c
##########
0.39211000      0.00806038
0.39188374      0.00822231
0.39165818      0.00819951
0.39143332      0.00834288
0.39120916      0.00828671
0.39098569      0.00840915
```

Figure A.1: *Header and the first few x- and y-values of a raw data text file (level-0). The header starts with the date as unique spectral identifier and contains several experimental parameters. The "solution=" line contains information about different experimental parameters, which have to be separated onto individual lines before feeding the data to the database. This is achieved by using a Python script. The reorganized text file can be found in Figure A.2.*

```
#Substance=Water
#Formula=H2O
#Concentration=pure
#Matrix=NA
#Flowrate=0.19mlpmin
#Laser Intensity=98.5%
#Flashlamp energy=FL5.38J
#Ion mode=pos
#date=2019-11-08-113032
#fullscale=2.000000
#solution=Water_H2O_pure_NA_0.19mlpmin_98.5%_FL5.38J_pos
#plasmaordesorption=des
#plasmacriterion=m16greater0.02
#energydensity=1152
#delaytime=055
#mcp=150
#wavelength=2840
#focusdiameter=210
#focusdiameterdesc=10_90
#laserpower=50
#waterjetposition=B
#nozzlediameter=16
#numberofspectra=490
#masscalibrationa=0.349710
#masscalibrationb=-0.226610
#masscalibrationc=0.392110
##mcal_form=att+bt+c
##########
0.39211000      0.00806038
0.39188374      0.00822231
0.39165818      0.00819951
0.39143332      0.00834288
0.39120916      0.00828671
0.39098569      0.00840915
```

Figure A.2: *Header and the first few x- and y-values of a reorganized level-1 text file. The corresponding unorganized level-0 file can be found in Figure A.1. The "solution=" line is split into eight lines, each containing a single experimental parameter. The newly created eight lines are added to the header above the "date" line, which is the unique spectral identifier. The reorganized level-1 files can be ingested to the database system.*

Table A.1: Our currently used software versions.

Software	Version
LabVIEW	14.0.1f3
Python	2.7.6
Matplotlib	1.2.0
OriginPro®	9.8.0.200

B Supplementary Information, chapter 9

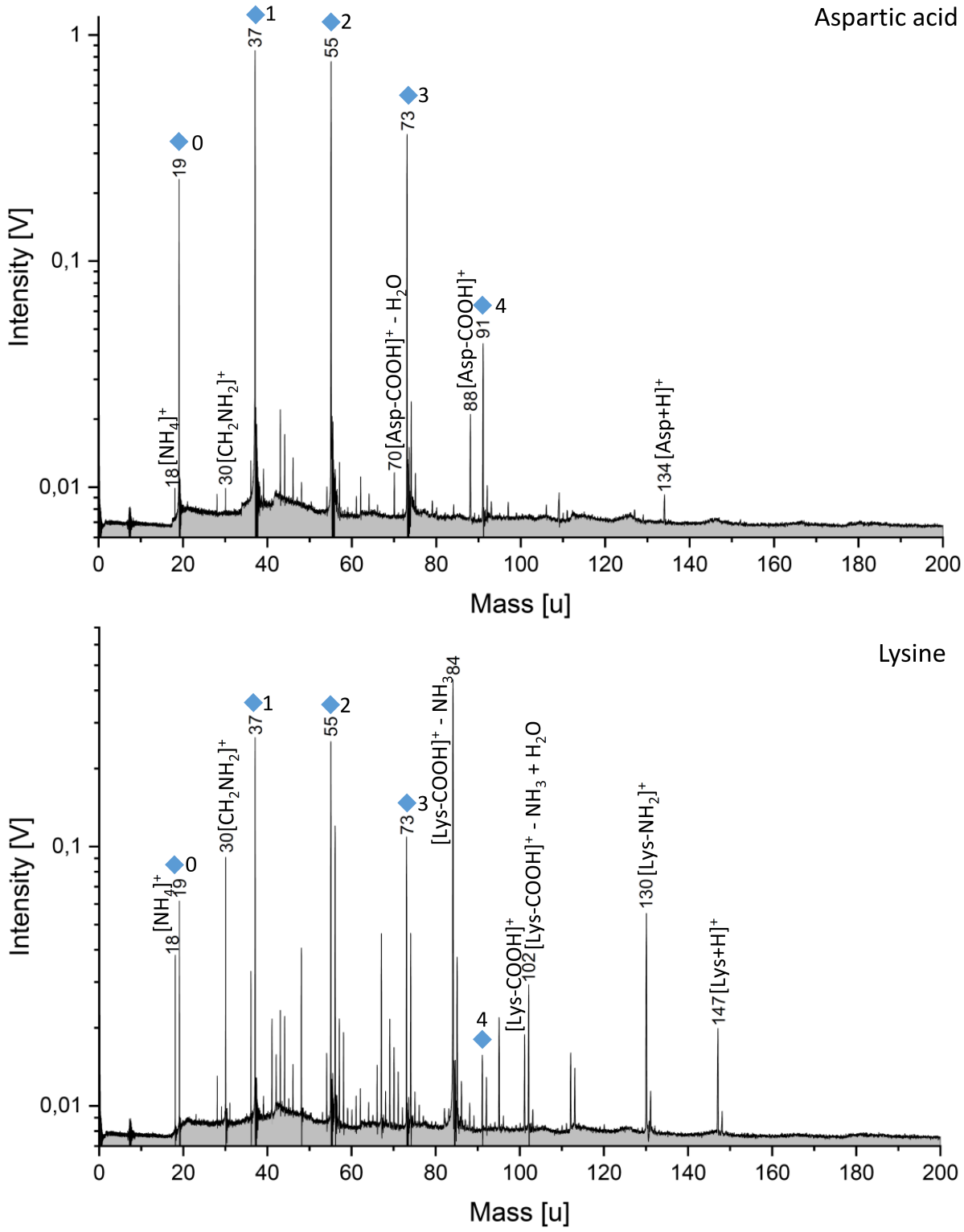

Figure B.1: *Cation mass spectra (y-axis in logarithmic scale) of 50 ppmw Asp and Lys in H_2O. The spectra were obtained by using a laser intensity of 94 % and at a delay time of 5.0 µs. All amino acids investigated here form protonated molecular peaks and the typical fragments $[NH_4]^+$ and $[CH_2NH_2]^+$. Amino acid spectra also exhibit fragments due to the loss of COOH. Here, the Lys spectrum shows the respective cleavage in combination with a loss of NH_2. Water peaks of the form $[(H_2O)_nH_3O]^+$ are labeled with blue diamonds. The corresponding n is labeled besides the symbol. Asp, aspartic acid; Lys, lysine.*

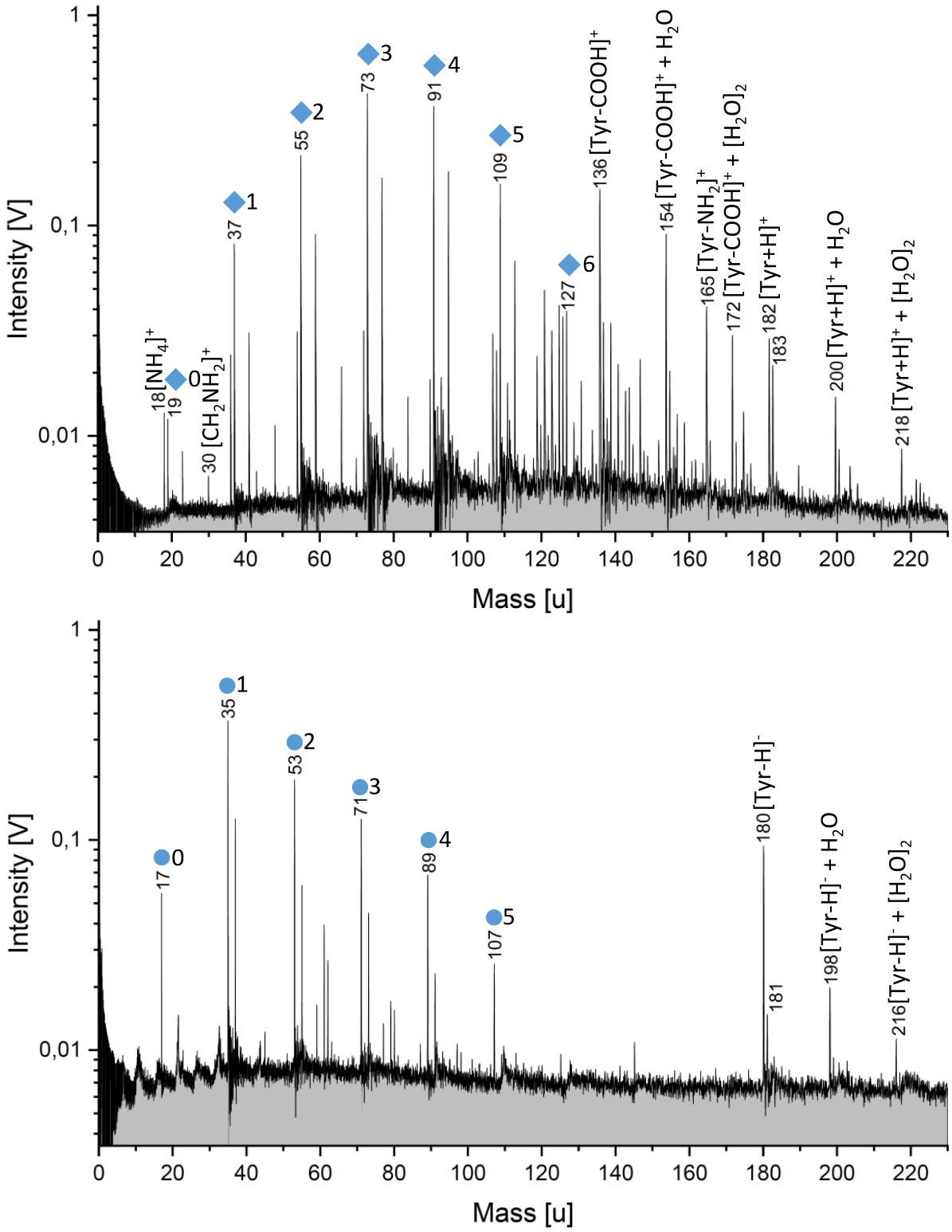

Figure B.2: *Cation (top) and anion (bottom) mass spectra (y-axis in logarithmic scale) of 380 ppmw Tyr in H_2O. The spectra were obtained by using a laser intensity of 93.2 % and at a delay time of 6.3 µs. Tyr forms both a protonated and a deprotonated molecular peak. The typical fragments $[NH_4]^+$ and $[CH_2NH_2]^+$ are also observed. Tyr also produces fragments due to the loss of COOH and NH_2 in cation mass spectra. Tyr shows water clustering in both cation and anion mass spectra. Its Tyr-COOH fragment shows water clustering in the cation mass spectrum. Water peaks of the forms $[(H_2O)_nH_3O]^+$ and $[(H_2O)_nOH]^-$ are labeled with blue diamonds and blue circles, respectively. The corresponding n is labeled beside the symbol. Tyr, tyrosine.*

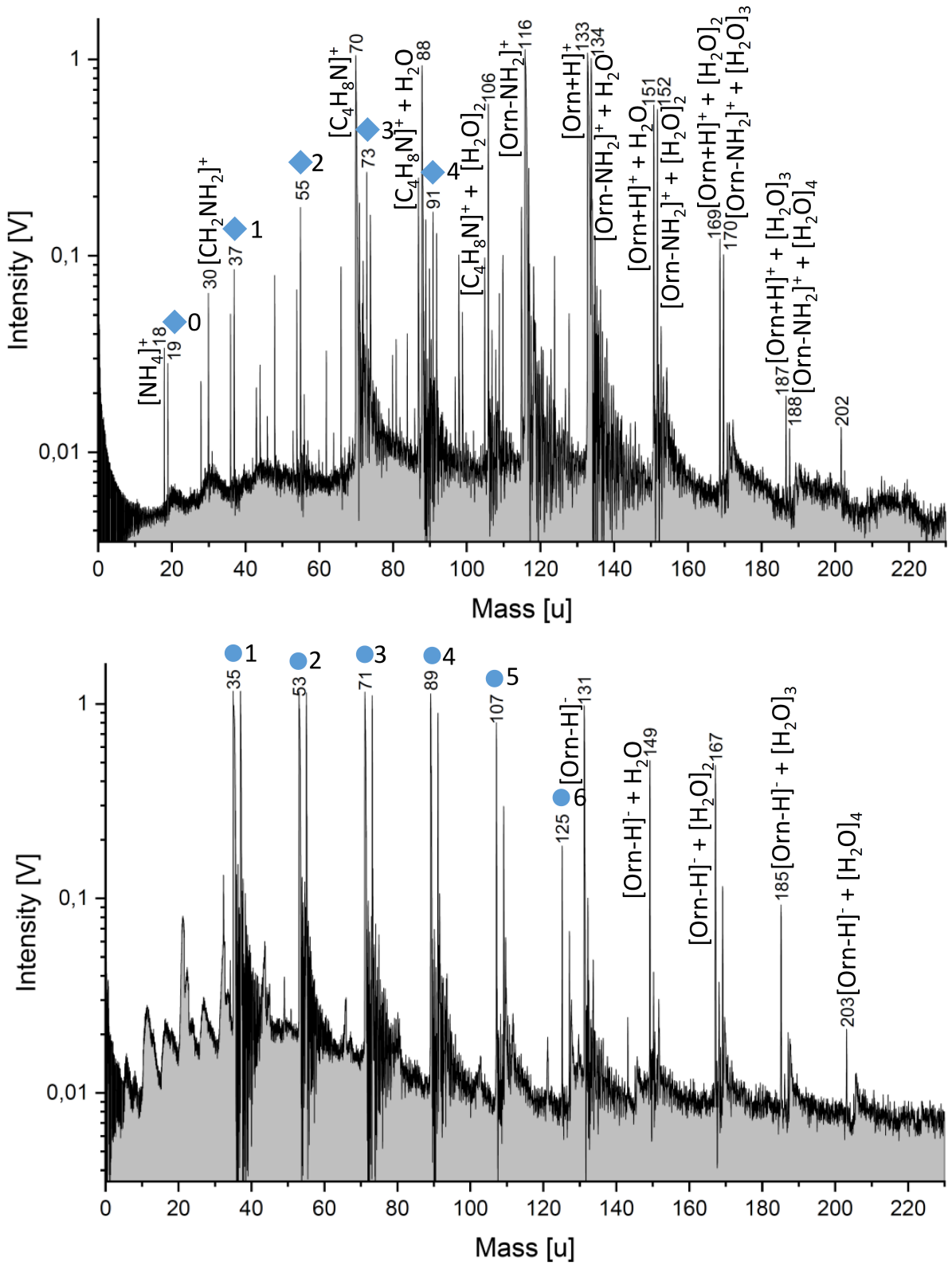

Figure B.3: *Cation (top) and anion (bottom) mass spectra (y-axis in logarithmic scale) of 1000 ppmw Orn in H_2O. The spectra were obtained by using a laser intensity of 93.2 % and at a delay time of 6.3 µs. Orn forms both a protonated and a deprotonated molecular peak. The typical fragments $[NH_4]^+$ and $[CH_2NH_2]^+$ are observed. Orn also produces a fragment due to the loss of NH_2 in the cation mass spectrum. An additional cleavage of $COOH_2$ from this fragment leads to a $[C_4H_8N]^+$ peak at m/z 70. Orn undergoes water clustering in both cation and anion mass spectra, and $[C_4H_8N]^+$ clusters with water are visible in the cation mass spectrum only. Water peaks of the forms $[(H_2O)_nH_3O]^+$ and $[(H_2O)_nOH]^-$ are labeled with blue diamonds and blue circles, respectively. The corresponding n is labeled beside the symbol. Orn, ornithine.*

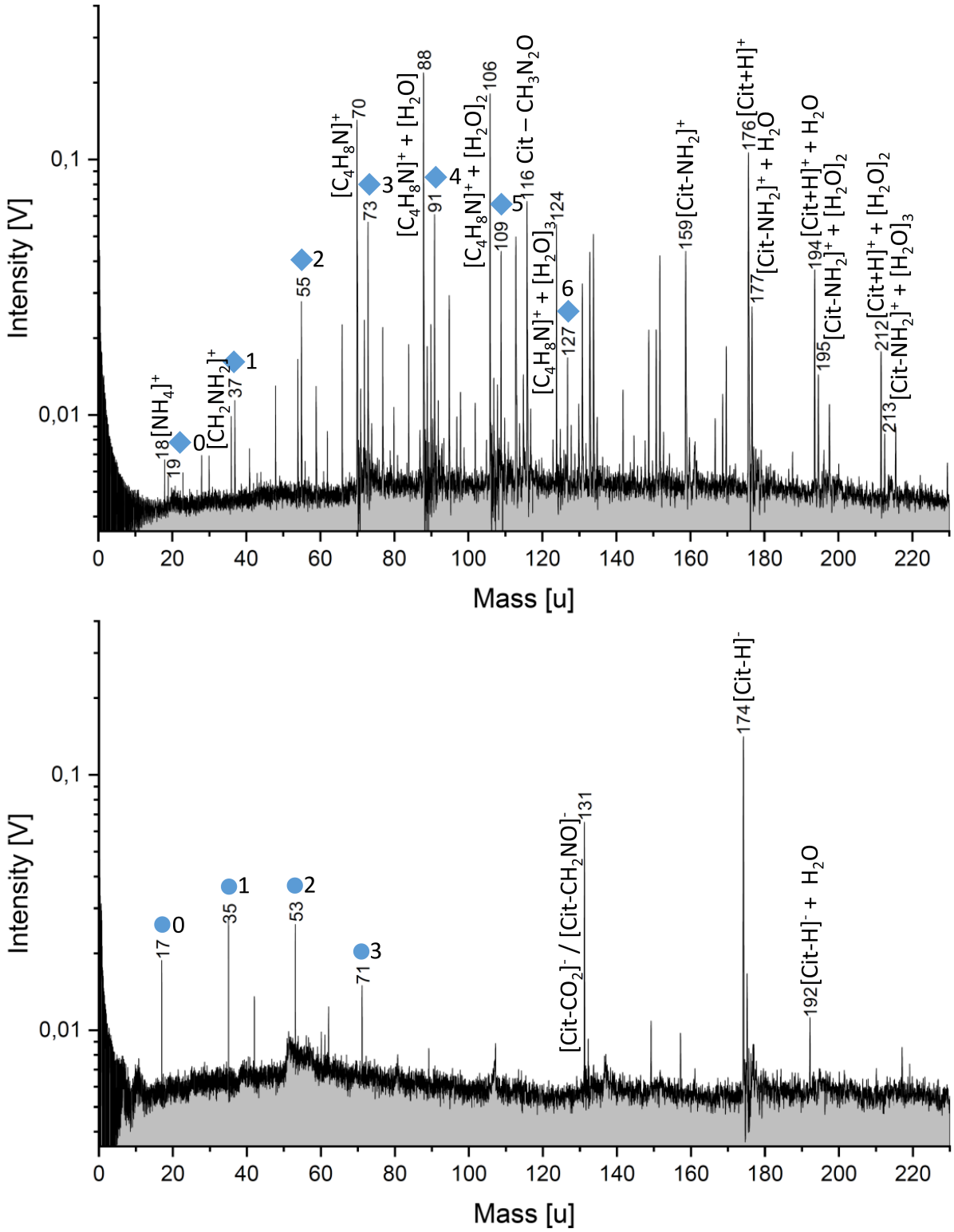

Figure B.4: *Cation (top) and anion (bottom) mass spectra (y-axis in logarithmic scale) of 1000 ppmw Cit in H_2O. The spectra were obtained by using a laser intensity of 93.2 % and at a delay time of 6.3 µs. Cit forms both a protonated and a deprotonated molecular peak. The typical fragments $[NH_4]^+$ and $[CH_2NH_2]^+$ are observed. Cit also produces a cation fragment due to the loss of NH_2 and CH_3N_2O. A prominent peak at m/z 70 is visible ($[C_4H_8N]^+$). A cleavage of CO_2 from Cit leads to a peak at m/z 131 in the anion mass spectrum. Cit exhibits water clustering in both cation and anion mass spectra, with m/z 70 forming clusters with water in cation mass spectra. Water peaks of the forms $[(H_2O)_nH_3O]^+$ and $[(H_2O)_nOH]^-$ are labeled with blue diamonds and blue circles, respectively. The corresponding n is labeled beside the symbol. Cit, citrulline.*

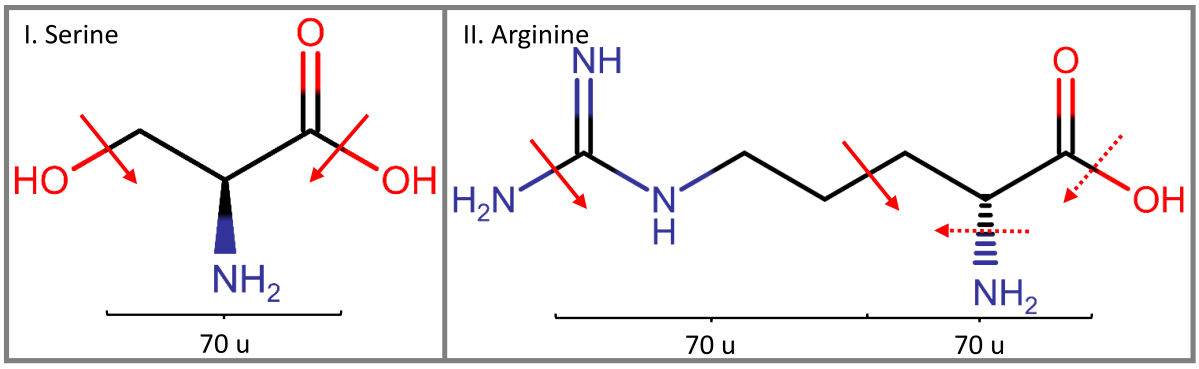

Figure B.5: *Origin of the prominent mass peak at m/z 70 in Figure 9.1. In addition to* $[Asp - COOH]^+ - H_2O$*, this peak represents amino acid fragments of Ser and Arg, which derive from different cleavages (shown with red arrows): I. Cleavage of both hydroxy groups of Ser. II. Cleavage between the third and the fourth carbon atom within Arg and additional* NH_2 *or OH loss, respectively. Dashed arrows indicate that only one of these cleavages happens. Arg, arginine; Ser, serine.*

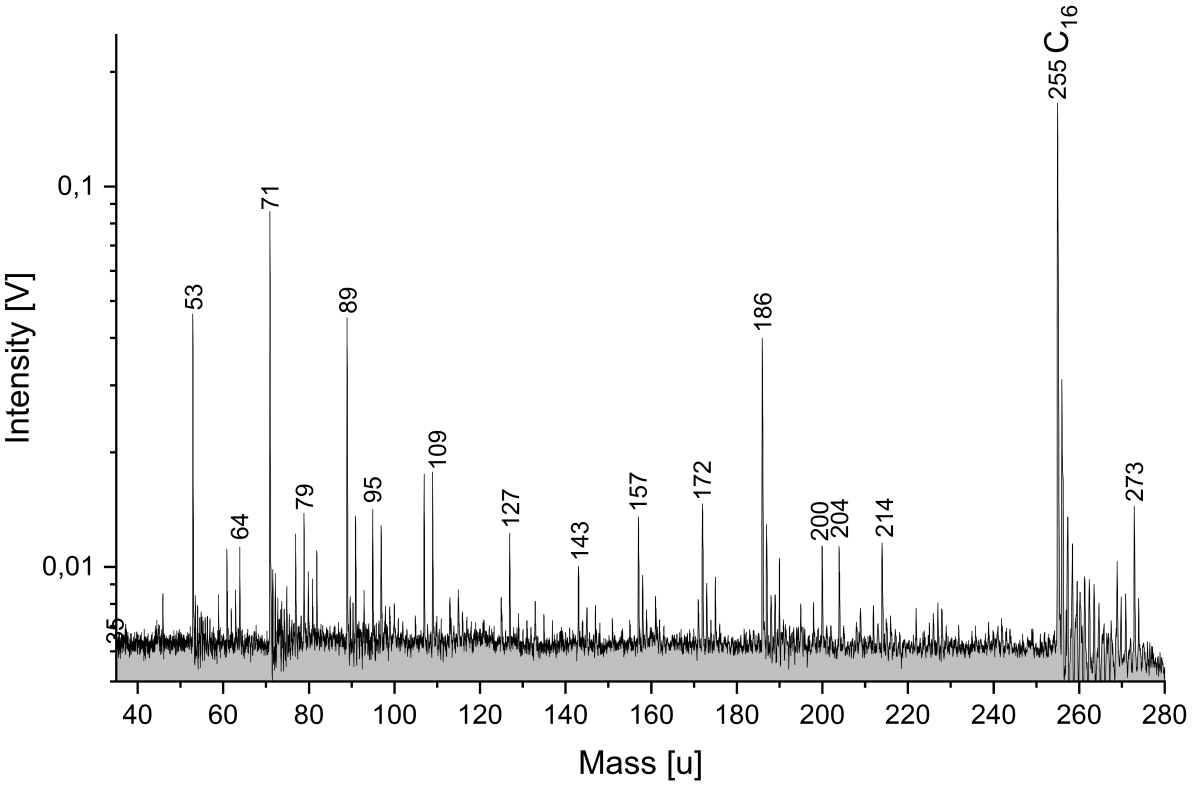

Figure B.6: *An anion mass spectrum (y-axis in logarithmic scale) of 26 ppmw* (10^{-4} *M) hexadecanoic acid* (C_{16}) *in* H_2O*. Apart from the molecular peak at m/z 255, further peaks related to the fatty acid sample at m/z 172 and m/z 186 are observable.*

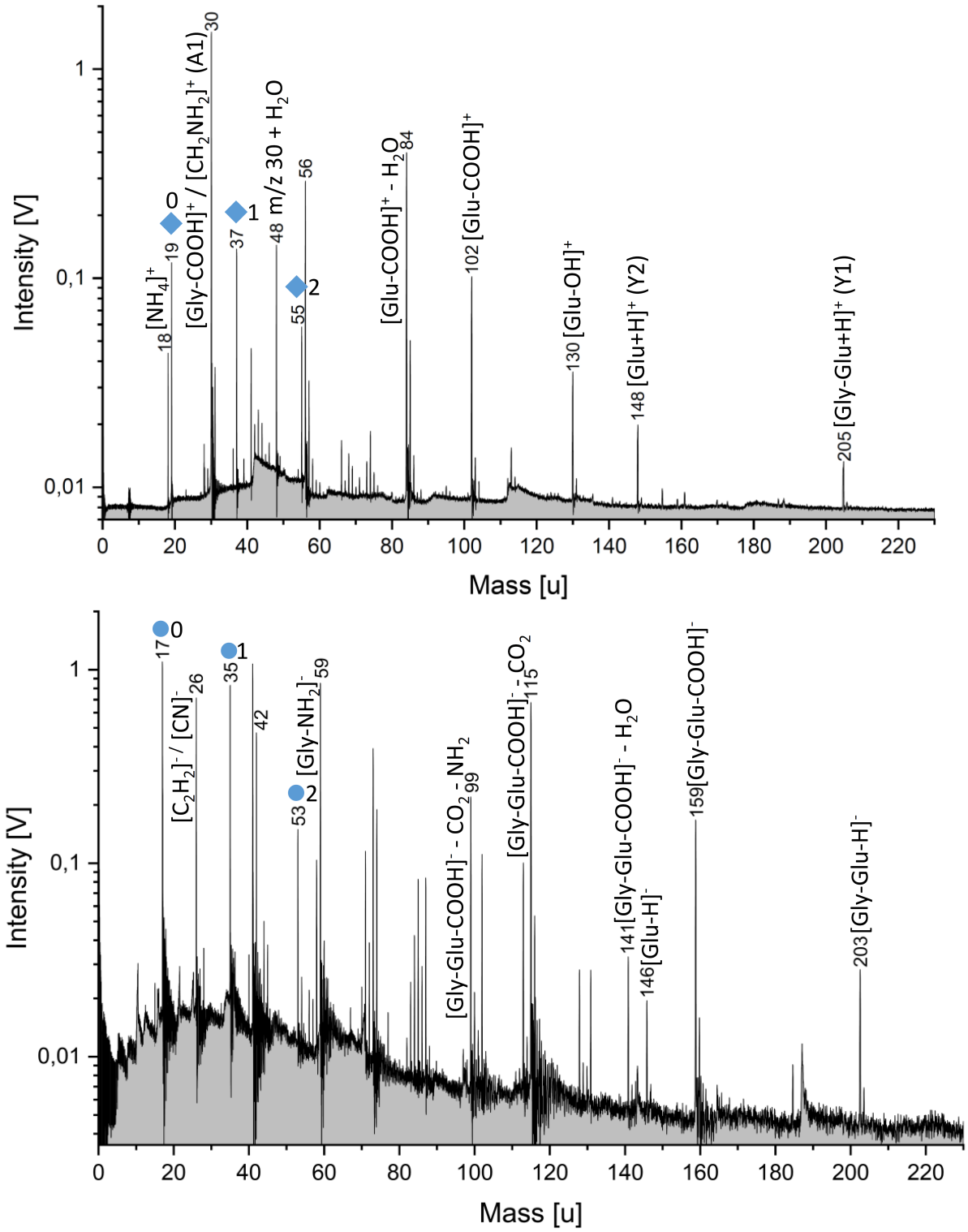

Figure B.7: *Cation (top) and anion (bottom) mass spectra (y-axis in logarithmic scale) of 2000 ppmw Gly-Glu. The mass spectra were obtained at a laser intensity of 96.2 % and delay times of 4.7 µs (cation mass spectrum) and 5.1 µs (anion mass spectrum). Characteristic cleavages of the peptide (explained in section 9.3) are observed. Apart from the peptide molecule, both amino acid residues Gly and Glu can be identified. Water peaks of the forms* $[(H_2O)_nH_3O]^+$ *and* $[(H_2O)_nOH]^-$ *are labeled with blue diamonds and blue circles, respectively. The corresponding n is labeled besides the symbol. Glu, glutamic acid; Gly, glycine.*

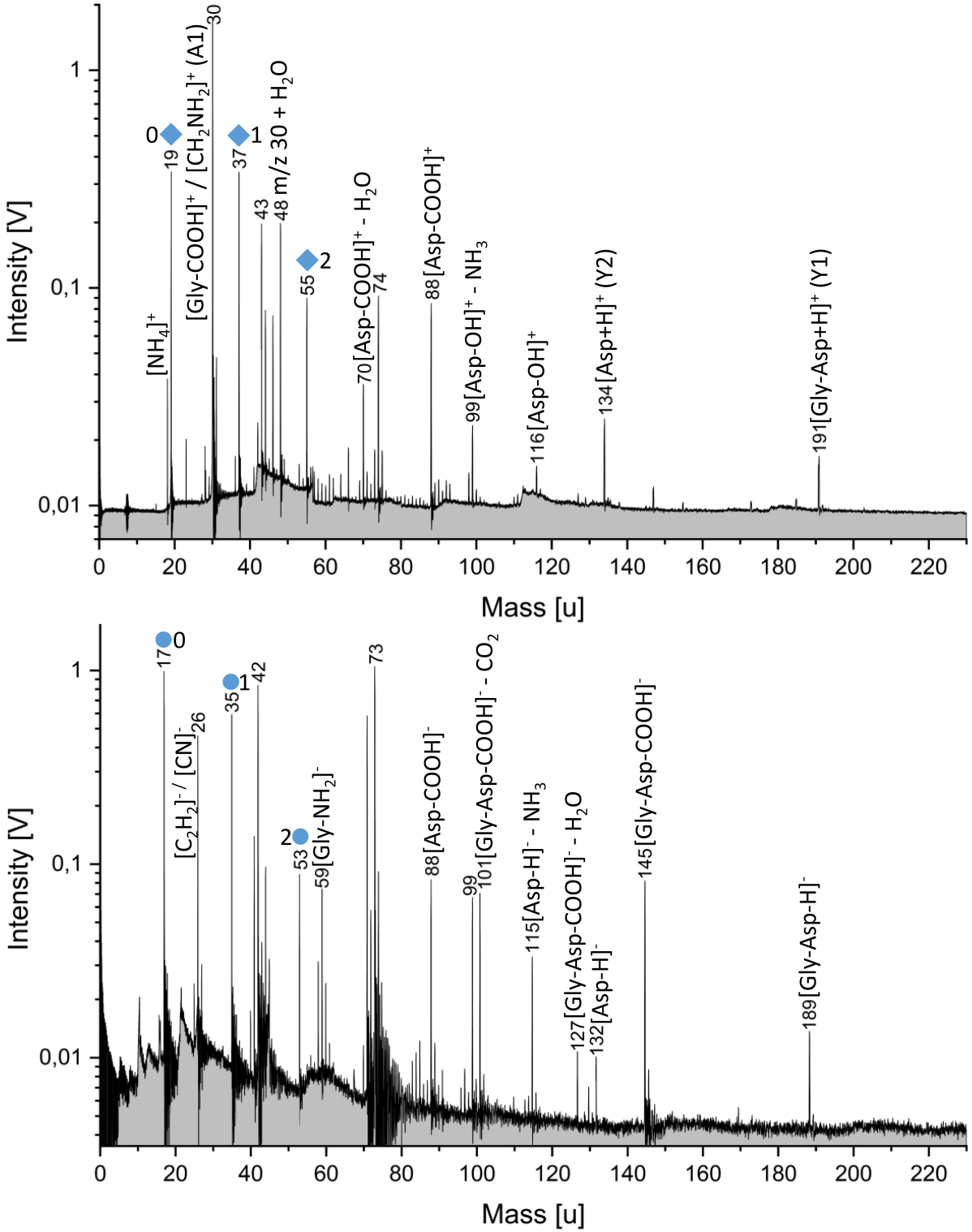

Figure B.8: *Cation (top) and anion (bottom) mass spectra (y-axis in logarithmic scale) of 2000 ppmw Gly-Asp. The mass spectra were obtained at a laser intensity of 96.2 % and delay times of 4.7 µs (cation mass spectrum) and 5.1 µs (anion mass spectrum). Characteristic cleavages of the peptide (explained in section 9.3) are observed. Apart from the peptide molecule, both amino acid residues Gly and Asp can be identified. Water peaks of the forms* $[(H_2O)_nH_3O]^+$ *and* $[(H_2O)_nOH]^-$ *are labeled with blue diamonds and blue circles, respectively. The corresponding n is labeled beside the symbol.*

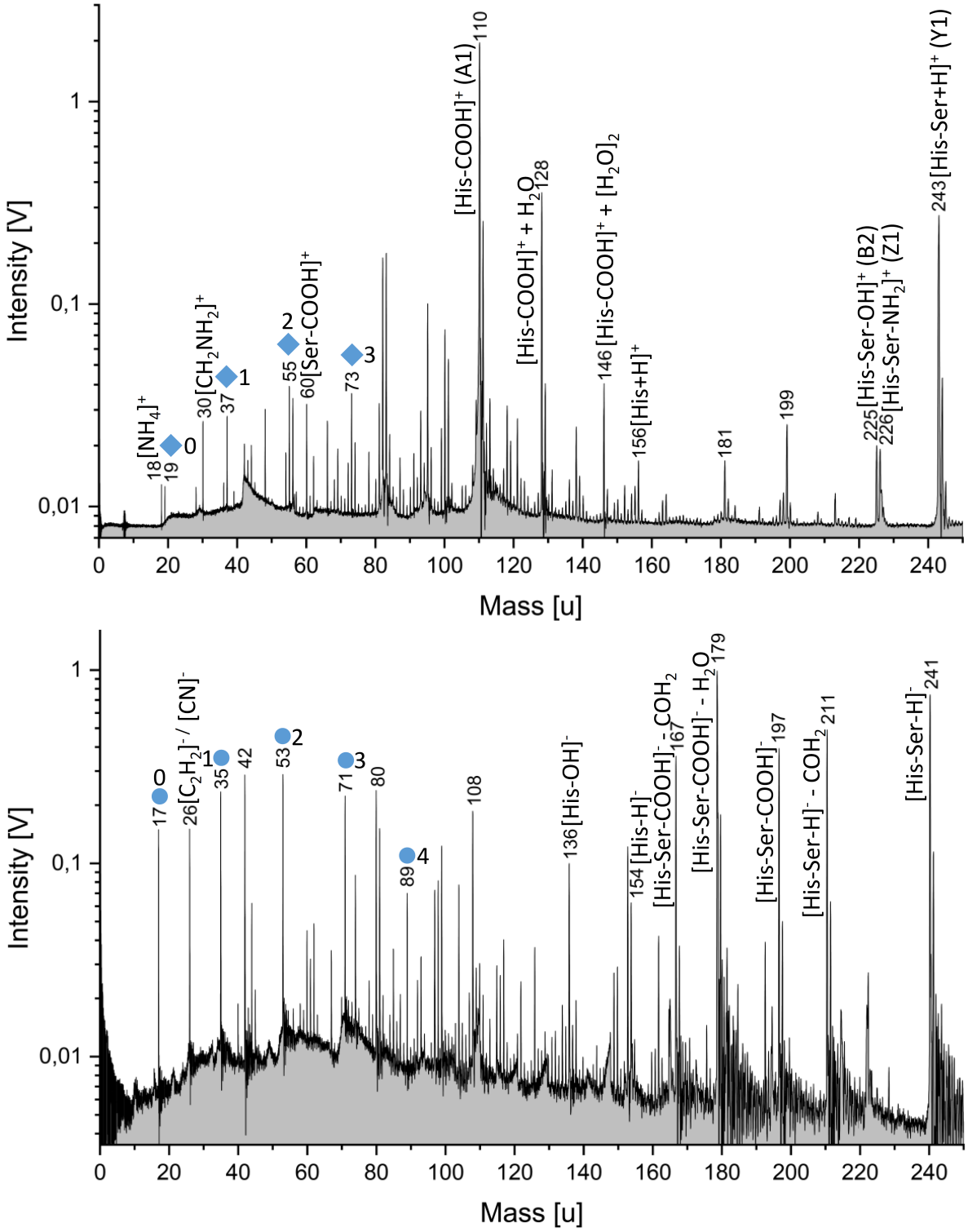

Figure B.9: *Cation (top) and anion (bottom) mass spectra (y-axis in logarithmic scale) of 2000 ppmw His-Ser. The mass spectra were obtained at a laser intensity of 93.2 % and delay times of 5.5 µs (cation mass spectrum) and 6.0 µs (anion mass spectrum). Characteristic cleavages of the peptide (explained in section 9.3) are observed. Apart from the peptide molecule, both amino acid residues His and Ser can be identified. Water peaks of the forms* $[(H_2O)_nH_3O]^+$ *and* $[(H_2O)_nOH]^-$ *are labeled with blue diamonds and blue circles, respectively. The corresponding n is labeled beside the symbol. His, histidine.*

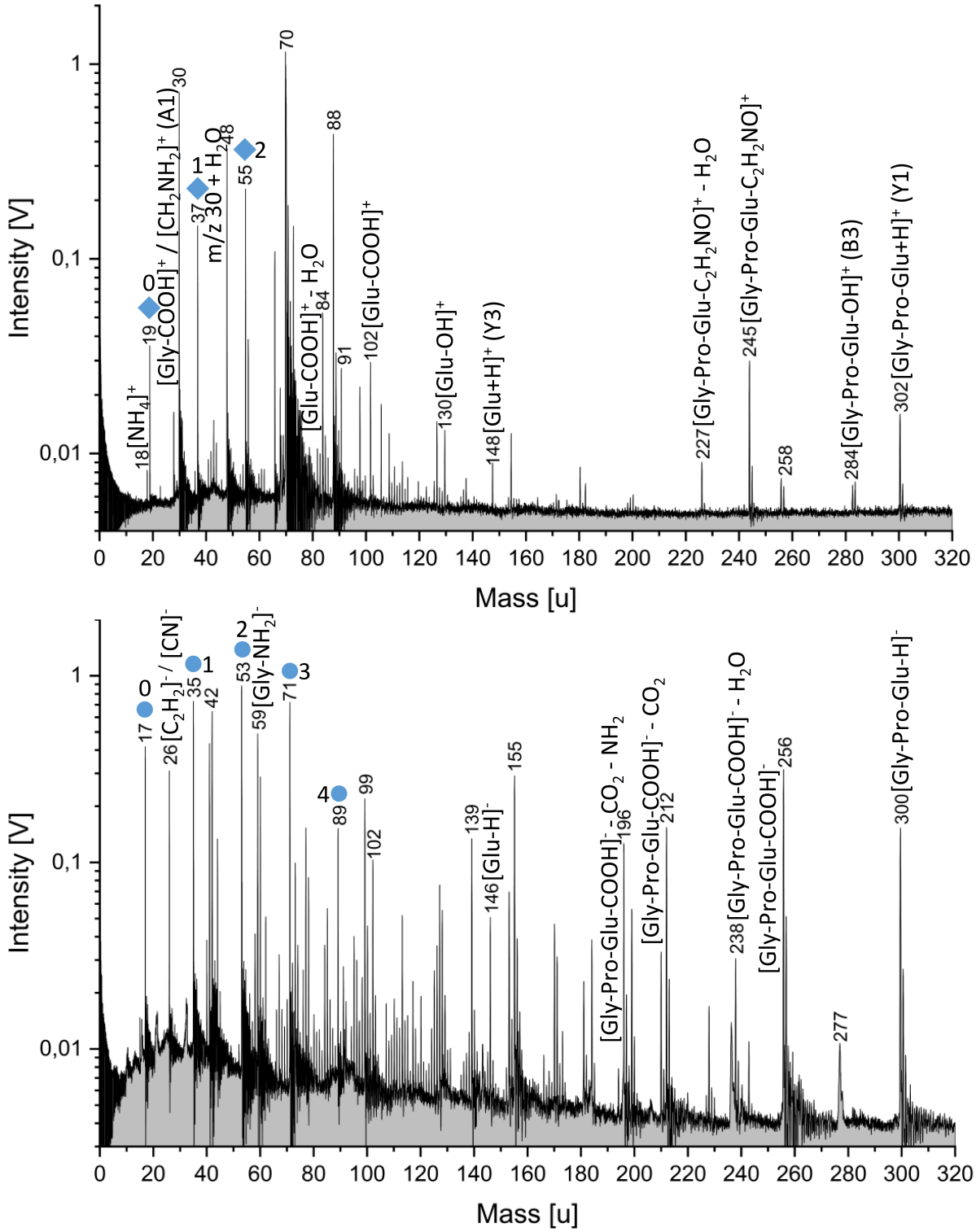

Figure B.10: *Cation (top) and anion (bottom) mass spectra (y-axis in logarithmic scale) of 2000 ppmw Gly-Pro-Glu. The mass spectra were obtained at a laser intensity of 93.2 % and a delay time of 6.0 µs (both spectra). Characteristic cleavages of the peptide (explained in section 9.3) are observed. Apart from the peptide molecule, both terminal amino acid residues Gly and Glu can be identified. A prominent peak at m/z 70 is observable in the cation mass spectrum. This peak is most likely associated with Pro, as it is not observable in the cation mass spectrum of Gly-Glu (Supplementary Figure B.7 top panel). Water peaks of the forms* $[(H_2O)_nH_3O]^+$ *and* $[(H_2O)_nOH]^-$ *are labeled with blue diamonds and blue circles, respectively. The corresponding n is labeled beside the symbol.*

Table B.1: Molar concentrations of the nine amino acids at a concentration of 50 ppmw used for the mass spectra in Figure 9.1.

Amino acid*	**Molecular weight [u]**	**Concentration [10^{-5}M]**
Gly	75	67
Ala	89	56
Ser	105	48
Thr	119	42
Asp	133	38
Lys	146	34
Glu	147	34
His	155	32
Arg	174	29

* Ala = alanine; Arg = arginine; Asp = aspartic acid; Glu = glutamic acid; Gly = glycine; His = histidine; Lys = lysine; Ser = serine; Thr = threonine.

Table B.2: Concentrations in ppmw of the nine fatty acids at a concentrations of 5.5×10^{-6} M used for the mass spectrum in Figure 9.2.

Fatty acid	**Molecular weight [u]**	**Concentration [ppmw]**
Lauric acid (C_{12})	200	1.23
Tridecylic acid (C_{13})	214	1.35
Myristic acid (C_{14})	228	1.43
Pentadecylic acid (C_{15})	242	1.51
Palmitic acid (C_{16})	256	1.59
Margaric acid (C_{17})	270	1.69
Stearic acid (C_{18})	284	1.76
Nonadecylic acid (C_{19})	298	1.86
Arachidic acid (C_{20})	312	1.93

C Supplementary Information, chapter 10

C.1 Calculation of the amino acid concentrations in Supplementary Table C.1 (Solution type ii) using Glutamic acid (Glu) as an example

Published Glu concentrations in a selection of CR chondrites (Glavin et al., 2011; Pizzarello et al., 2012) are 1.6, 8.2, 16.4, 9.4, and 16.7 µmol/kg, means 10.46 µmol/kg on average; 10.46 µmol/kg equates to 1.54 mg/kg. Using two different estimates of the total core mass of Enceladus: I. 8.38×10^{19} kg and II. 6.3×10^{19} kg (Waite et al., 2017) gives the total amino acid mass on Enceladus:

I. 1.54 mg/kg $\times$ 8.38×10^{19} kg = 1.29×10^{14} kg
II. 1.54 mg/kg $\times$ 6.3×10^{19} kg = 9.69×10^{13} kg

With two different estimates of the ocean mass of the Enceladean ocean: I. 3.2×10^{19} kg and II. 1×10^{19} kg (Waite et al., 2017) the concentration of Glu in the Enceladean ocean is calculated as follows (assuming water-rock interaction):

I. 1.29×10^{14} kg/3.2×10^{19} kg = 4.03 ppmw
II. 9.69×10^{13} kg/1×10^{19} kg = 9.69 ppmw

4.03 and 9.69 ppmw means 6.86 ppmw on average.

A conservative concentration toward the lower end of this range, 5 ppmw, was chosen for the abiotic mix.

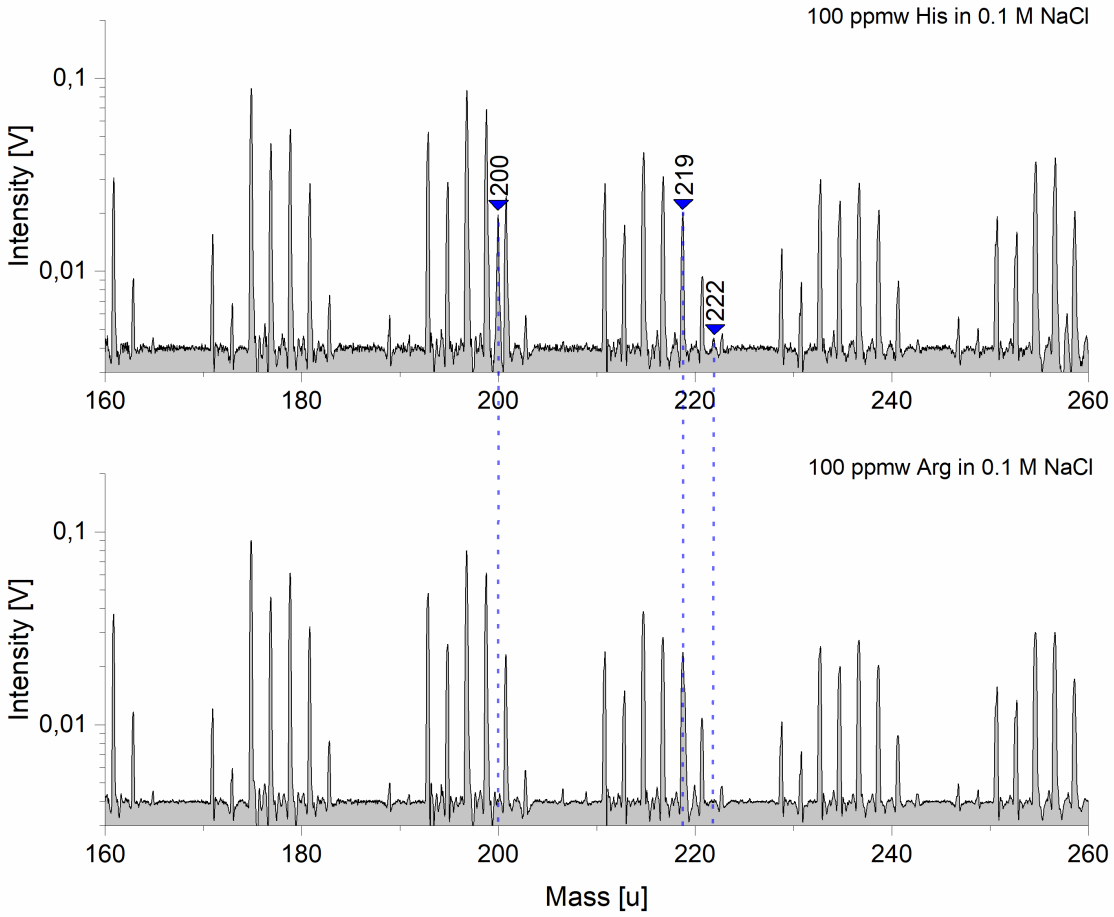

Figure C.1: *Sections (160–260 u) of baseline-corrected cation mass spectra (y-axis in logarithmic scale) of 100 ppmw His in 0.1 M NaCl (top) and 100 ppmw Arg in 0.1 M NaCl (bottom). The two solutions differ only in the amino acid (His or Arg) used. Both spectra show identical peaks from the matrix solution with nearly identical amplitudes. His is clearly identifiable as disodiated cation* $[(His_{Na})Na]^+$ *at m/z 200 and as trisodiated cation* $[(His_{2Na})Na]^+$ *at m/z 222 (top). The disodiated arginine cation* $[(Arg_{Na})Na]^+$ *interferes with the salt species* $[(NaCl)_2(NaOH)_2Na]^+$ *from the matrix solution at m/z 219 (bottom). This interference can be resolved with the available mass resolution of 600–800* $m/\Delta m$ *because of a significant peak asymmetry (Figure 10.3).*

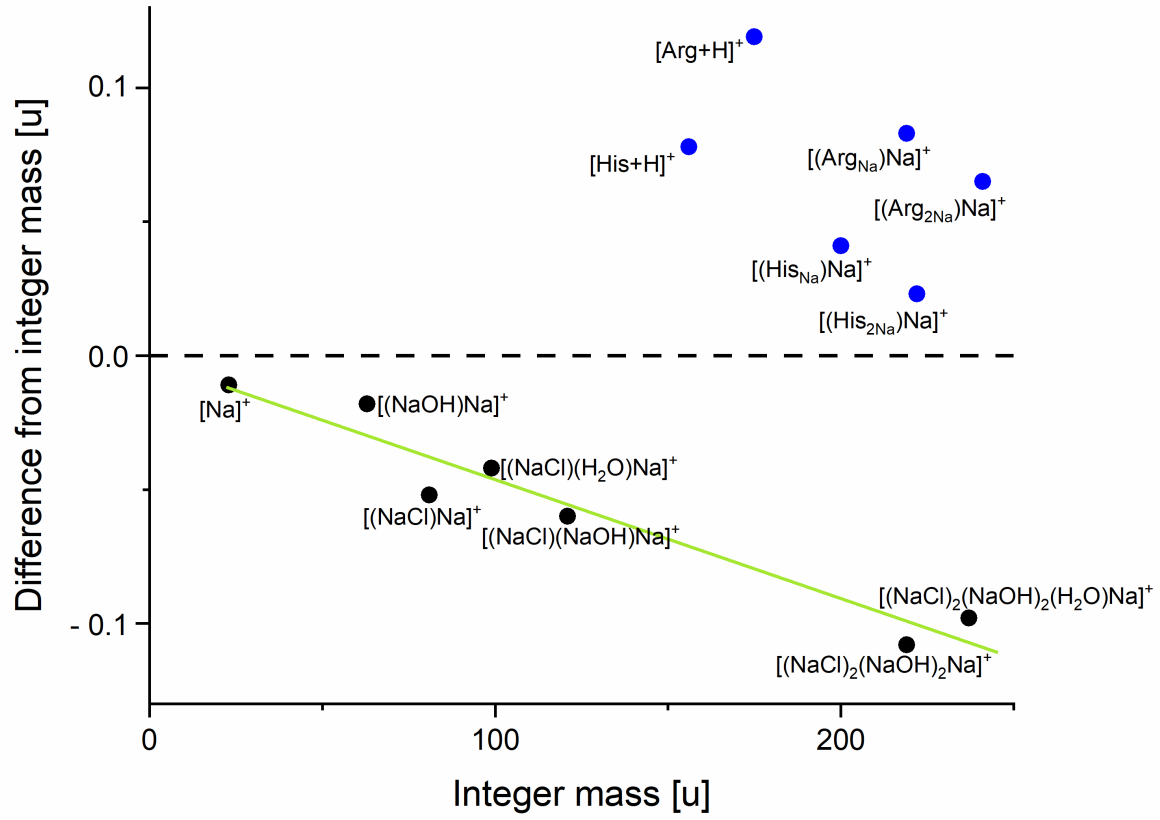

Figure C.2: *Masses on the integer level vs. exact differences from integer masses of the most common isotopes of typical salt species as seen in LILBID spectra of salt-rich solutions (black dots) and unsodiated as well as sodiated species of two amino acids (His and Arg; blue dots). Salt species from a salty background solution have a negative offset with respect to the integer mass. The masses of these salt and (unsodiated and sodiated) amino acid species near the same integer mass typically differ by about 0.15–0.2 u. The green trend line (applied to the salt species) highlights that the salt species' negative mass differences increase with mass.*

Table C.1: Concentrations in the abiotic amino acid mix (Solution type ii) used for the mass spectrum in Figure 10.4. For calculations of the concentrations, see the section on Biosignature solutions in the main text and Supplementary Data C.1.

Amino acid*	**Molecular weight [u]**	**Concentration [µmol/L]**	**Concentration [ppmw]**
Gly	75	2000	150
Ala	89	1685	150
Val	117	641	75
ABA	103	388	40
Glu	147	34	5
Ser	105	29	3
Asp	133	15	2
Carboxylic acid*	**Molecular weight [u]**	**Concentration [µmol/L]**	**Concentration [ppmw]**
Valeric acid	102	588	60
Methylbutyric acid	102	588	60
Hexanoic acid	116	259	30
Acetic acid	60	250	15
Heptanoic acid	130	231	30
Butyric acid	88	227	20
Octanoic acid	144	208	30
Nonanoic acid	158	190	30
Methylpentanoic acid	116	172	20
Ethylhexanoic acid	144	139	20
Benzoic acid	122	82	10
Formic acid	46	43	2
Ethylbutyric acid	116	43	5
Decanoic acid	172	29	5
Matrix component	**Molecular weight [u]**	**Concentration [M]**	
NaCl	58	0.1	
Na_2CO_3	106	0.015	
$NaHCO_3$	84	0.015	
NH_3	17	0.01	

* Amino acids and carboxylic acids are separately listed in order of decreasing concentrations in µmol/L.

Table C.2: Fatty acid concentrations in biotic concentration ratios used for the mass spectrum in Figure 10.5.

Fatty acid*	**Molecular weight [u]**	**Concentration [µmol/L]**	**Concentration [ppmw]**
C_{16}	256	275	70
C_{18}	284	275	78
C_{12}	200	55	11
C_{14}	228	55	13
C_{20}	312	55	17
C_{13}	214	5.5	1.2
C_{15}	242	5.5	1.3
C_{17}	270	5.5	1.5
C_{19}	298	5.5	1.6

* The fatty acids are listed in order of decreasing concentrations in µmol/L.

Table C.3: Concentrations of the biotic organic mixes (Solution type iv) used for the mass spectra in Figures 10.6 and 10.7.

Amino acid*	**Molecular weight [u]**	**Concentration [µmol/L]**	**Concentration [ppmw]**
Ser	105	29	3
Gly	75	27	2
Tyr	181	11	2
Cit	175	11	2
Asp	133	8	1
Orn	132	8	1
Arg	174	3	0.5
Lys	146	3	0.5
Fatty acid*	**Molecular weight [u]**	**Concentration [µmol/L]**	**Concentration [ppmw]**
C_{16}	256	20	5
C_{18}	284	18	5
C_{12}	200	5	1
C_{14}	228	4	1
C_{20}	312	3	1
C_{13}	214	0.5	0.1
C_{15}	242	0.4	0.1
C_{17}	270	0.4	0.1
C_{19}	298	0.3	0.1
Background compound*	**Molecular weight [u]**	**Concentration [µmol/L]**	**Concentration [ppmw]**
Methylbutyric acid	102	539	55
Valeric acid	102	392	40
Hexanoic acid	116	259	30
Acetic acid	60	250	15
Butyric acid	88	227	20
Methylpentanoic acid	116	216	25
Octanoic acid	144	208	30
Nonanoic acid	158	158	25
Heptanoic acid	130	154	20
Ethylhexanoic acid	144	139	20
Benzoic acid	122	82	10
Ethylbutyric acid	116	43	5
Formic acid	46	43	2
Decanoic acid	172	29	5
Propionic acid	74	27	2
NaCl	58	9	0.5

* Fatty acids were only used for the mass spectra in Figure 10.7. Amino acids, fatty acids and carboxylic acids are separately listed in order of decreasing concentration in µmol/L.

D Other published articles in collaboration with the PhD candidate

Published articles, which were written in collaboration with the PhD candidate during the time of his PhD in addition to those in Parts II and III are listed below:

1. Postberg, F., Khawaja, N., Abel, B., Choblet, G., Glein, C.R., Gudipati, M.S., Henderson, B.L., Hsu, H.-W., Kempf, S., **Klenner, F.**, Moragas-Klostermeyer, G., Magee, B., Nölle, L., Perry, M., Reviol, R., Schmidt, J., Srama, R., Stolz, F., Tobie, G., Trieloff, M., and Waite, J.H. (2018). Macromolecular organic compounds from the depths of Enceladus. *Nature*, 558(7711):564-568. DOI: 10.1038/s41586-018-0246-4.

2. Khawaja, N., Postberg, F., Hillier, J., **Klenner, F.**, Kempf, S., Nölle, L., Reviol, R., Zou, Z., and Srama, R. (2019). Low-mass nitrogen-, oxygen-bearing, and aromatic compounds in Enceladean ice grains. *Monthly Notices of the Royal Astronomical Society*, 489(4):5231-5243. DOI: 10.1093/mnras/stz2280.

3. Khawaja, N. and **Klenner, F.** (2019). Astrobiology – a roadmap for Pakistan. *MIT Technology Review PK*, 5(2):6-9. www.technologyreview.pk/astrobiology-a-roadmap-for-pakistan.* **Not peer-reviewed.*

4. Taubner, R.-S., Olsson-Francis, K., Vance, S.D., Ramkissoon, N.K., Postberg, F., de Vera, J.-P., Antunes, A., Casas, E.C., Sekine, Y., Noack, L., Barge, L., Goodman, J., Jebbar, M., Journaux, B., Karatekin, Ö., **Klenner, F.**, Rabbow, E., Rettberg, P., Rückriemen-Bez, T., Saur, J., Shibuya, T., and Soderlund, K.M. (2020). Experimental and simulation efforts in the astrobiological exploration of exooceans. *Space Science Reviews*, 216:9. DOI: 10.1007/s11214-020-0635-5.

5. Cable, M., Waller, S., Hodyss, R., Hofmann, A., Malaska, M., Continetti, R., Jaramillo-Botero, A., Abel, B., Postberg, F., Miller, M., Burke, S., Belousov, A., **Klenner, F.**, Tallarida, N., Lambert, J., Fuerstenau, S., and Ulibarri, Z. (2020). Plume grain sampling at hypervelocity: Implications for astrobiology investigations. *Science White Paper for the Planetary Science and Astrobiology Decadal Survey 2023-2032*, submitted on July 13, 2020:1-7.* **Not peer-reviewed.*

E Conference/workshop appearances related to chapters 7, 9 and 10

Conference/workshop abstracts, which rely on the three published articles within Parts II and III (chapters 7, 9 and 10) of this thesis are listed below:

The PhD candidate received several awards and travel grants in the occasion of these conferences and workshops. A complete list of awards and travel grants can be found in the PhD candidate's Curriculum Vitae (appendix F).

1. **Klenner, F.**, Reviol, R., and Postberg, F. (2017) Reproducing impact ionization mass spectra of E and F ring ice grains at different impact speeds. *European Planetary Science Congress (EPSC) Vol. 11*, Riga, Latvia, Abstract EPSC2017-1010-1.

2. **Klenner, F.**, Postberg, F., Stolz, F., Reviol, R., and Khawaja, N. (2017) Mass spectrometry of astrobiologically relevant organic material - Implications on future space missions to ocean worlds in the outer Solar System. *51st ESLAB Symposium: 'Extreme Habitable Worlds', Noordwijk, Netherlands*.

3. **Klenner, F.**, Postberg, F., and Stolz, F. (2017) Analogue mass spectra of astrobiological relevant organic material for in situ space detectors. *Ices in the Solar System workshop*, Madrid, Spain, Abstract booklet page 47/82.

4. **Klenner, F.**, Postberg, F., Stolz, F., Khawaja, N., and Reviol, R. (2018) Analog mass spectra of astrobiologically relevant organic material for spaceborne mass spectrometers and their future implications. *European Planetary Science Congress (EPSC) Vol. 12*, Berlin, Germany, Abstract EPSC2018-1262.

5. **Klenner, F.**, Postberg, F., Stolz, F., Khawaja, N., and Reviol, R. (2018) Analog mass spectra of astrobiologically relevant organic material for spaceborne mass spectrometers. *18th European Astrobiology Network Association (EANA) conference*, Berlin, Germany.

6. **Klenner, F.**, Postberg, F., Khawaja, N., and Reviol, R. (2018) The Heidelberg analog experiment for spaceborne mass spectrometers. *Advances in Space Mass Spectrometry for the Search of Extraterrestrial Signs of Life conference*, Orléans, France.

7. **Klenner, F.**, Postberg, F., Hillier, J., Khawaja, N., and Stolz, F. (2019) Experiments for the identification of biosignatures in ice grains from extraterrestrial ocean worlds. *European Planetary Science Congress (EPSC)-AAS Division for Planetary Sciences (DPS) Joint Meeting Vol. 13*, Geneva, Switzerland, Abstract EPSC-DPS2019-1754-1.

8. **Klenner, F.**, Postberg, F., Hillier, J., Khawaja, N., and Reviol, R., and Srama, R. (2019) Calibrating impact ionization detectors for hypervelocity water ice grains from ocean worlds. *European Planetary Science Congress (EPSC)-AAS Division for Planetary Sciences (DPS) joint meeting Vol. 13*, Geneva, Switzerland, Abstract EPSC-DPS2019-250-1.

9. **Klenner, F.**, Postberg, F., Hillier, J., Khawaja, N., and Stolz, F. (2019) Experiments for the identification of biosignatures in ice grains from extraterrestrial ocean worlds. *Goldschmidt conference*, Barcelona, Spain, Abstract 2019 1711.

10. **Klenner, F.**, Postberg, F., Hillier, J., Khawaja, N., Cable, M.L., Abel, B., Kempf, S., Lunine, J., and Glein, C.R. (2020) A method to discriminate between abiotic and biotic processes on cryovolcanically active ocean worlds. *European Geosciences Union (EGU) General Assembly (virtual)*, Vienna, Austria, Abstract EGU2020-9105.*

11. Khawaja, N., **Klenner, F.**, Hillier, J., Postberg, F., Dannenmann, M., and Zou, Z. (2020) Exploring the biogeochemistry of extraterrestrial active ocean worlds. *Molecular Origins of Life conference (virtual)*, Munich, Germany, Abstract booklet page 91/190.*

12. **Klenner, F.**, Postberg, F., Hillier, J., Khawaja, N., Dannenmann, M., Cable, M.L., and Abel, B. (2020) Discriminating abiotic and biotic chemistry on active ocean worlds. *Goldschmidt conference (virtual)*, Honolulu, USA, Abstract 2020 1334.*

13. **Klenner, F.**, Khawaja, N., Hillier, J., Zou, Z., Dannenmann, M., and Postberg, F. (2020) Exploring Enceladus and other ocean worlds using mass spectrometry. *American Geophysical Union Fall Meeting (virtual)*, San Francisco, USA, Abstract accepted for presentation on October 6, 2020.*

** These conferences were held virtually because of the worldwide Covid-19 pandemic, which began during the course of this thesis.*

F Curriculum Vitae

Due to privacy protection, the PhD candidate's Curriculum Vitae (CV) has been removed from the online version of this dissertation. The CV is included on the following two pages in the printed version.

Eidesstattliche Erklärung

Hiermit erkläre ich, dass ich die vorliegende Dissertation mit dem Thema

Experiments for the Detection of Biosignatures in Ice Grains by Space Missions to Enceladus and Europa

selbstständig verfasst und angefertigt habe und keine anderen als die angegebenen Quellen und Hilfsmittel verwendet habe. Geistiges Eigentum anderer Autoren wurde als solches gekennzeichnet.

Des Weiteren versichere ich, dass ich an keiner anderen Stelle ein Prüfungsverfahren beantragt bzw. die Dissertation in dieser oder anderer Form an keiner anderen Fakultät als Dissertation vorgelegt habe.

Berlin, den 20.11.2020 _____

(Fabian Klenner)

Danksagung

Der lange Weg vom Beginn der Promotion in Heidelberg über den Umzug nach Berlin, die Umsetzung der Messkampagnen, Auswertung der Daten, bis hin zur fertigen Dissertation wäre nicht ohne die Unterstützung, guten Ideen und Motivation vieler anderer möglich gewesen.

Mein erster großer Dank gilt Prof. Dr. Frank Postberg für die spannenden, zielgerichteten Aufgabenstellungen und die durchgehend engagierte Betreuung. Neben deiner Bereitschaft, jederzeit über Fragen und Anregungen zu diskutieren, hat die gute Arbeitsatmosphäre, unter anderem bedingt durch unsere regelmäßigen gruppeninternen "social Events", erheblich zum Gelingen meiner Dissertation beigetragen. Der zuvor beschriebene lange Weg war für mich deshalb sehr angenehm zu gehen. Ich danke dir auch für deine Geduld und Zeit, die es zweifelsfrei erfordert, eine Promotion zu betreuen. Während dieser Zeit durfte ich sehr vieles lernen und meine Fähigkeiten erweitern. Auch dass ich meine Ergebnisse auf zahlreichen Konferenzen vorstellen durfte, ist nicht selbstverständlich.

Einen weiteren besonderen Dank spreche ich Dr. Jon Hillier für die unermüdliche Unterstützung in Laborangelegenheiten aus. Obwohl die Tätigkeiten im und um das Labor sehr zeitintensiv sind, machen sie Spaß. Durch dich wurde die Laborarbeit für mich auf ein ganz neues Level angehoben. Besonders danke ich dir auch für unzählige ergebnisreiche Diskussionen und das Korrektur lesen englischer Texte.

Auch bedanke ich mich bei Prof. Dr. Jürgen Schmidt. Danke, dass du diese Dissertation gelesen und beurteilt haben wirst.

Ein weiterer großer Dank gilt Dr. Nozair Khawaja. Du hast mir mit deiner uneingeschränkten Hilfsbereitschaft sehr auf diesem Weg geholfen. Wir durften bisher zahlreiche Konferenzen miteinander teilen und ich freue mich schon sehr auf die nächsten. Du hast mir die Möglichkeit gegeben, mit dir das Astrobiology Network of Pakistan (ABNP) zu gründen und mir hierdurch einige neue Perspektiven und Möglichkeiten aufgezeigt.

Prof. Dr. Bernd Abel und Dr. Ferdinand Stolz danke ich für die unkomplizierte Zusammenarbeit und die Messkampagnen, die ich in Leipzig durchführen durfte. Ich seid stets motiviert und ich freue mich auf viele weitere Jahre guter Zusammenarbeit.

Den Co-Autoren meiner Veröffentlichungen danke ich für die gute Zusammenarbeit, das konstruktive Feedback und das Ermöglichen neuer Projekte. Insbesondere danke ich Dr. Morgan Cable (NASA's Jet Propulsion Laboratory). Durch dich hat sich mein Blick nun noch mehr in Richtung Astrobiologie und "hypervelocity impacts" gerichtet. Auch danke ich Prof. Dr. Sascha Kempf (University of Colorado, Boulder). Dein kritisches, konstruktives Feedback, sei es in Diskussionen, Mails oder zu Veröffentlichungen, ist immer enorm hilfreich.

Mit meinem Kollegen und Freund Simon Linti teile ich das coolste Büro an der FU. Dir danke ich vor allem für all unsere privaten Unternehmungen und Gespräche. Ich freue mich schon darauf, im Sommer unser Boot aufzurüsten und auf dem Schlachtensee zu paddeln. Lenz Nölle danke ich für viele weiterführende Gespräche, die gemeinsamen Konferenzen und die ständige Hilfsbereitschaft.

Es ist toll, dass wir den Weg vom Bachelorstudium bis hin zur Promotion parallel gehen dürfen. Ich wünsche euch beiden weiterhin viel Erfolg bei euren Promotionen.

Weiterhin danke ich Zenghui Zou (ehemals im coolsten Büro der FU) für angenehme Gespräche und die Unterstützung in Laborangelegenheiten. Viel Erfolg beim Endspurt deiner Promotion.

Muhammad Umair danke ich neben privaten Unterhaltungen für die Entwicklung der LILBID-Datenbank. Deine Programmierfähigkeiten vereinfachen die Auswertung der Labordaten ungemein. Auch danke ich Sebastian Walter für das Optimieren der Datenbank und viele andere IT Angelegenheiten.

Für die Hilfe beim Laborumzug von Heidelberg nach Berlin danke ich René Reviol. Ohne deine Unterstützung wäre das Setup nicht so schnell nach Wiederaufbau in Berlin funktionsfähig gewesen. Maryse Napoleoni danke ich für die Hilfe und Geduld bei den Laborarbeiten in den letzten Monaten.

Ein Dank auch an das gesamte OLYMPIA-Team um Dr. Christelle Briois (LPC2E, Université d'Orléans) und Dr. Ján Žabka (J. Heyrovský Institute of Physical Chemistry, Prag). Durch die gute Organisation des ganzen Teams, die ertragreichen Versuche tagsüber und die hin und wieder langen Nächte (z.B. unser Grillabend in Berlin) sind die Messkampagnen angenehm und machen Spaß.

Marie Dannenmann, Miriam Pavlista und Janine Bönigk danke ich für die Möglichkeit, Biosignaturen von lebenden Organismen zu untersuchen. Der biologische Anstrich, den ihr unserer Forschungsgruppe verschafft, ist sehr wertvoll.

Ich empfinde meinen Kollegen der Forschungsgruppe Planetologie und Fernerkundung gegenüber große Dankbarkeit. Eure Unterstützung, die netten Gespräche und "social Events" werde ich für immer in guter Erinnerung behalten.

Tiefsten Herzens danke ich meiner Familie, meinen Freunden und "Szívem" für die Motivation, unbezahlbare Momente und euren bedingungslosen Glauben an mich. Danke für alles.